CHARACTERISATION AND DEVELOPMENT OF ADVANCED STRUCTURAL ALLOYS FOR NUCLEAR FUSION REACTORS

By

TAY JONATHAN ZACHARY SPARKS

A thesis submitted to the University of Birmingham for the degree of DOCTOR OF PHILOSOPHY

School of Metallurgy and Materials
College of Engineering and Physical Sciences

University of Birmingham

September 2023

ABSTRACT

The breeder blanket fulfils a crucial function in the design of future magnetically confined fusion reactors, allowing for harvest of energy emitted from the fusion reaction and production of tritium fuel. Several designs are considered for the breeder blanket, which employ different structural materials as supports for the breeding material. As a result of the breeder blanket's proximity to the fusion plasma and bombardment by high energy fusion neutrons, candidate materials must exhibit resistance to high temperature and irradiation degradation, and easy component recycling after appreciably long lifetimes.

Front-runner candidate structural materials include the reduced activation ferritic martensitic steel EUROFER97, an oxide dispersion strengthened variant of EUROFER97, and the vanadium alloy, V-4Cr-4Ti. In this work high energy synchrotron X-ray diffraction during tensile testing is employed to characterise the microstructural evolution of these candidate structural materials at elevated temperature by way of the changing X-ray diffraction patterns collected during testing. Such characterisation allows for the determination of fundamental elastic properties (single crystal elastic constants, elastic modulus, Poisson's ratio, etc) and evaluation of the dislocation density behaviour during deformation. Experimental characterisation of the high temperature elastic properties supplements and supports modelling work necessary in the development of breeder blanket structures, and dislocation density evolution shows the cause of temperature dependency in the EUROFER97/ODS EUROFER97 steels during tensile and cyclic testing through consideration of the constitutive flow stress and dislocation recovery

mechanisms. The final experimental chapter looks beyond the currently considered candidate structural materials, considering the effect of tantalum addition on the mechanical properties of vanadium-based alloys, given tantalum's excellent high temperature properties and low activation. A pilot scheme of laboratory scale V-Ti-(Cr)-Ta alloys were arc melted and heat treated – their mechanical properties assessed relative to V-4Cr-4Ti by means of micro- and macro- indentation hardness testing.

The 2020-2050 period is anticipated to be an important period for the development of fusion as an energy source, with several key fusion projects slated for fulfilment within this window. The results presented in this work can be used to contrast the high temperature performance of current candidate structural materials, and the basic mechanical properties of a proposed next generation structural material class against the existing.

ACKNOWLEDGEMENTS

My journey pursuing a PhD has been a long and challenging one, and I would like to take this opportunity to express my deepest thanks to all those who have supported me.

My first thanks must go to my supervisors Dr Biao Cai and Dr Yiqiang Wang, who have offered constant support, advice, and insight throughout the past four years. I will be forever thankful for the opportunity you gave me to pursue this topic, the support you have offered me, and for all the help you have given me in expanding my knowledge and understanding.

My thanks also go to my co-supervisors Dr Yu-Lung Chiu, whose help in organising access to training and equipment was vital, and Dr Michael Gorley, whose comments and feedback helped shape and direct the project.

Beyond my supervisors, I would like to express my gratitude to the current and former staff and researchers of the University of Birmingham, School of Metallurgy and Materials who were instrumental in supporting my experimental work; particularly Amy Jade Newell, Simon Cannon, Grant Holt, Dr Ludwig Schneider, Theresa Morris, Uthman Mahmud, Dr Hiroto Kitaguchi, Dr Rebekah Tipping, Professor Paul Bowen, Dr Mark Duffield, Wanxuan Teng, Dr Ela Young, Dr Zihan Song, and Dr Lei Tang. I must also offer my grateful thanks to contacts within the UK Atomic Energy Authority who offered me their advice and assistance: Dr Matthew Carrington, Dr Duc Nguyen-Manh, and Dr Slava Kuksenko.

I gratefully acknowledge the financial support for my project provided by the University of Birmingham and the UK Atomic Energy Authority.

Access offered by Diamond Light Source (Oxford, UK) on the I12 beamline under proposals EE19251 and MG30778 is gratefully acknowledged, and the support provided by beamline scientists throughout beamtime and data analysis made this work possible, particular thanks go to Dr Oxana Magdysyuk and Dr Thomas Connolley.

Finally, a very special thank you to my friends and family who have offered their friendship, love and support over the course of my project. My friends – Liam Knight, Rhys Jenkins, Lauren Powell, and Lucy Hargrave – who helped me escape stress and made lockdown bearable, my siblings – Sorrel, Cali, Arron, and Matthew – who have always been there to support me and cheer me on, my partner – Kit Ross – who has been my rock and comfort through the highs and lows and has helped me more than I can say, and my parents who have offered unwavering support, and who I have always been able to turn to for advice.

My sincerest thanks to you all.

NOMENCLATURE

SYMBOLOGY

$\boldsymbol{F}_{[E/P]}$	Deformation gradient [elastic/plastic]
$\boldsymbol{L}_P$	Plastic component of spatial gradient of total deformation velocity
$\boldsymbol{m}_S$	Unit vector describing normal to a given active slip plane
$\boldsymbol{n}_S$	Unit vector describing slip direction of a given active slip plane
$\dot{\gamma}_S$	Shear rate across an active slip plane
$\dot{\gamma}_0$	Reference shear rate parameter
n	Rate sensitivity of slip parameter
τ_S	Resolved shear stress across an active slip plane
τ_{eff}	Effective shear stress
g_S	Resistance to shear slip across an active slip plane
$v_{[S]}$	Dislocation velocity [across an active slip plane]
v_0	Velocity factor describing dislocation movement attempt frequency and distance
C_{ij}	Elastic tensor components
S_{ij}	Compliance tensor components
I	Intensity
μ_G	Pseudo-Voigt function Gaussian fraction
x	Diffractogram x-axis [2θ, q, or d]
β_G	Pseudo-Voigt fitting Gaussian broadening parameter
β_C	Pseudo-Voigt fitting Lorentzian broadening parameter
β_T	Total X-ray Diffraction Peak Broadening
β_i	Instrumentally Induced X-ray Diffraction Peak Broadening
β_S	Sample Diffraction Peak Broadening
h_0	XRD background intensity
ε_{hkl}	Lattice strain experienced by the {h,k,l} indexed grain family

q_{hkl}^{0}	diffractogram peak position prior to load being applied
q_{hkl}	diffractogram peak position under strain
d_{hkl}	d-spacing of the {h,k,l} indexed grain family under strain
d_0	Initial d-spacing of the {h,k,l} indexed grain family prior to load
G_{hkl}	Diffraction shear modulus of the {h,k,l} indexed grain family
α	Kroner model fitting parameter
β	Kroner model fitting parameter
γ	Kroner model fitting parameter
η	Cubic shear modulus
μ	Cubic shear modulus
A_{hkl}	Cubic elastic anisotropy factor of the {h,k,l} indexed grain family
K_M	Polycrystalline bulk modulus
υ_{hkl}	Diffraction elastic ratio of the {h,k,l} indexed grain family
$E_{\parallel hkl}$	Diffraction elastic constant of the {h,k,l} indexed grain family parallel to the load direction
$E_{\perp hkl}$	Diffraction elastic constant of the {h,k,l} indexed grain family perpendicular to the load direction
Z	Zener anisotropy factor
a	Lattice parameter
B	Polycrystalline bulk modulus
G	Polycrystalline shear modulus
E	Polycrystalline elastic modulus
G_{VRH}	Voigt-Reuss-Hill polycrystalline shear modulus
G_{Voigt}	Voigt polycrystalline shear modulus
G_{Reuss}	Reuss polycrystalline shear modulus
T	Temperature
ΔK	X-ray diffractogram peak full width half maximum
D_0	Diffraction domain size
m	Effective outer radius of dislocations
b	Burgers vector
K	X-ray diffractogram peak centroid position

$\rho^{[m]}$	[Mobile] Dislocation density
C'	Tetragonal shear modulus
T_C	Curie temperature
T_m	Melting temperature
σ_y	Yield stress
σ_{xxx}	Strengthening contributions
k	Elemental strengthening coefficient
K_H	Hall-Petch coefficient
D	Grain size
d	Average particle size
L	Average particle spacing
ν	Poisson’s ratio
M	Taylor factor
$\delta_B D_B$	Grain boundary diffusion pre-exponential term
f	Particle volume fraction
θ	Dislocation forest strengthening parameter
k_b	Boltzmann constant
R	Molar gas constant
Q_B	Grain boundary diffusion activation energy
Ω	Atomic volume
$\dot{\varepsilon}$	Strain rate
t	Time after load release during cyclic loading
C_S	Friedel cross-slip pre-exponential factor
C_C	Friedel climb pre-exponential factor
$Q_{0,S}$	Friedel cross-slip activation energy
$Q_{0,C}$	Friedel climb activation energy
V_S	Friedel cross-slip activation volume
V_C	Friedel climb activation volume
ρ_E	Edge type dislocation density
ρ_S	Screw type dislocation density

v_D	Debye frequency
$\{A, B, C, D\}_V$	Verdier fitting parameters
$\{A, B, C, D\}_F$	Friedel fitting parameters
α_T	Linear thermal expansion coefficient
R_S	Thermal stress fracture resistance parameter
σ_U	Ultimate tensile strength
HV	Vickers hardness
F	Indentation peak load force
h	Indentation displacement
h_c	Indenter contact depth
h_{max}	Indentation maximum load depth
ε_g	Indenter geometry parameter
h_T	Maximum gradient tangential depth
S_C	Contact stiffness
S_S	Sample stiffness
S_f	Indenter frame stiffness
E_r	Reduced modulus of indentation
A_p	Projected area of indenter contact
E_{IT}	Sample indentation modulus
$H_{IT,0}$	Indentation hardness
η_{el}	Elastic fraction of work done during indentation
W_{el}	Elastic work done during indentation
W_T	Total work done during indentation
C_{h00}	Average contrast factor of {h,0,0} peak
C	Average contrast factor of {h,k,l} peak
q	Contrast factor determination parameter

INITIALISMS

BCC	Body Centred Cubic
BCT	Body Centred Tetragonal
CLAM	China Low Activation Martensitic
CNA	Castable Nanostructured Alloy
DBTT	Ductile to Brittle Transition Temperature
DCLL	Dual Coolant Lithium Lead
DEC	Diffraction Elastic Constant
DFT	Density Functional Theory
DLS	Diamond Light Source
E97	EUROFER97
EBSD	Electron Backscatter Diffraction
EDS	Energy Dispersive Spectroscopy
ETMT	Electro-Thermal Mechanical Testing
EU-DEMO	European Demonstration Power Plant
FCC	Face Centred Cubic
FWHM	Full Width Half Maximum
HCCB	Helium Cooled Ceramic Breeder
HCLL	Helium Cooled Lithium Lead
HCPB	Helium Cooled Pebble Bed
HE	High Energy
HEA	High Entropy Alloy
HIP	Hot Isostatic Pressing
I12-JEEP	I12 Joint Engineering, Environmental and Processing
ITER	International Thermonuclear Experimental Reactor
JET	Joint European Torus
LLCB	Lithium Lead Ceramic Breeder
LV	Lithium/Vanadium
LVDT	Linear Variable Differential Transformer
MS	Molten Salt

mWH	Modified Williamson-Hall
NIFS	National Institute for Fusion Science
ODS	Oxide Dispersion Strengthened
PAW	Projector Augmented Wave
PBE	Perdew-Burke-Enzerhof
RAFM	Reduced Activation Ferritic Martensitic
RT	Room Temperature
SCEC	Single Crystal Elastic Constant
SEM	Scanning Electron Microscope
SRO	Short Ranged Order
STEP	Spherical Tokamak for Energy Production
SWIP	South Western Institute of Physics
SWOT	Strength Weakness Opportunity Threat
TBM	Test Blanket Module
TBR	Tritium Breeding Ratio
V44	V-4Cr-4Ti
VASP	Vienna Ab Initio Simulation
WCCB	Water Cooled Ceramic Breeder
WCLL	Water Cooled Lithium Lead
XCT	X-ray Computed Tomography
XRD	X-Ray Diffraction
YS	Yield Stress

TABLE OF CONTENTS

LIST OF PUBLICATIONS

Published papers:

- **Tay Sparks**, Duc Nguyen-Manh, Pengfei Zheng, Jan S. Wróbel, Damian Sobieraj, Michael Gorley, Thomas Connolley, Christina Reinhard, Yiqiang Wang , Biao Cai, *Mechanical characterisation of V-4Cr-4Ti alloy: Tensile tests under high energy synchrotron diffraction*, Journal of Nuclear Materials, 569 (2022) https://doi.org/10.1016/j.jnucmat.2022.153911

- **Tay Sparks**, Michael Gorley, Jan Hoffmann, Yu-Lung Chiu, Thomas Connolley, Michael Rieth, Yiqiang Wang, Biao Cai, *In-situ synchrotron investigation of the elastic and tensile properties of oxide dispersion strengthened EUROFER97 steel*, Acta Materialia, 271 (2024) https://doi.org/10.1016/j.actamat.2024.119876

Papers in preparation:

- **Tay Sparks**, Michael Gorley, Yu-Lung Chiu, Thomas Connolley, Michael Rieth, Yiqiang Wang, Biao Cai, *High energy X-ray synchrotron characterisation of EUROFER97-2 steel under high temperature tensile and ratcheting testing*. To be submitted to Journal of Nuclear Materials

- **Tay Sparks**, Michael Gorley, Pengfei Zheng, Yiqiang Wang, Biao Cai, *Preparation and hardness testing of laboratory scale vanadium-based tantalum alloys.* To be submitted to Fusion Engineering and Design

Results of this work were presented at the following conferences:

- “Mechanical Characterisation of V-4Cr-4Ti Tensile Tests Under High Energy Synchrotron Diffraction” included as a poster session presentation at the **International Conference on Fusion Reactor Materials 2020 (ICFRM-20)**

- “Oxide Dispersion Strengthening of Eurofer97 Steel for fusion” included as a presentation at the Institute of Materials, Minerals, and Mining **5th Postgraduate Research Symposium on Ferrous Metallurgy (IOM3 PGR Symposium 2022)**

- “In-Situ Synchrotron Investigation of the Elastic and Tensile Properties of Oxide Dispersion Strengthened Eurofer97 steel” included as a poster at the **32nd Symposium on Fusion Technology 2022 (SOFT2022)**

LIST OF FIGURES

LIST OF TABLES

CHAPTER 1 INTRODUCTION

1.1.Motivation and Background

Over the past century the global energy landscape has changed drastically; energy consumption skyrocketing, bringing with it an existential threat to the world's population in the form of rampant climate change. As is shown in Figure 1.1, in the first twenty years of the 21st century alone, yearly worldwide energy consumption has seen an increase of almost 50% compared to the year 2000 level, and coal, natural gas, and oil still account for upwards of 80% of total consumption [1]. Meanwhile, 91 countries have made commitments to a Net Zero or climate neutral initiative, twenty-two of which have put in place legally binding targets to be fulfilled by at least 2050 [2]. The push towards Net Zero is multifaceted; carbon capture technologies to mitigate CO_2 emissions, improved energy efficiencies to lower energy requirements, and widespread behavioural changes to lower demand all have their role to play [3]. However, in order to meet the 2050 target it is clearly necessary that the energy supply shift away from strongly carbon emitting fuels. The demand for abundant clean energy is stronger than ever before, and nuclear fusion is poised to meet this demand, provided its promise can be realised.

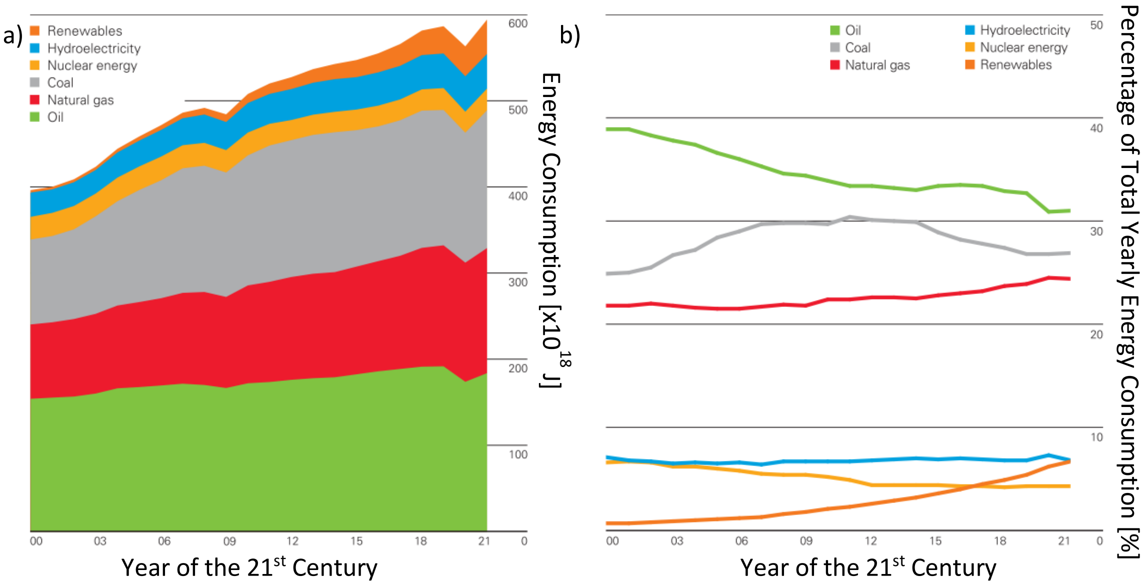

Figure 1.1 Global energy consumption for the period 2000-2021, shown as a) a stacked plot of contributing energy sources, and b) changing proportion of contribution of each energy source. After [1]

The realities of fusion power on the industrial scale remain to be seen, but early demonstration reactors are currently anticipated to produce net electricity to the grid on the order of 200-700 Mwe [4], [5]. The projected total levelized cost of electricity produced by fusion compared to established energy sources is shown in Figure 1.2. This data is modelled on the basis of yearly electricity production over energy source infrastructure lifetime, offset by external costs (environmental, health affecting, resource depleting, etc), and demonstrates the relative promise of fusion reactors in comparison to more well-established energy sources [6].

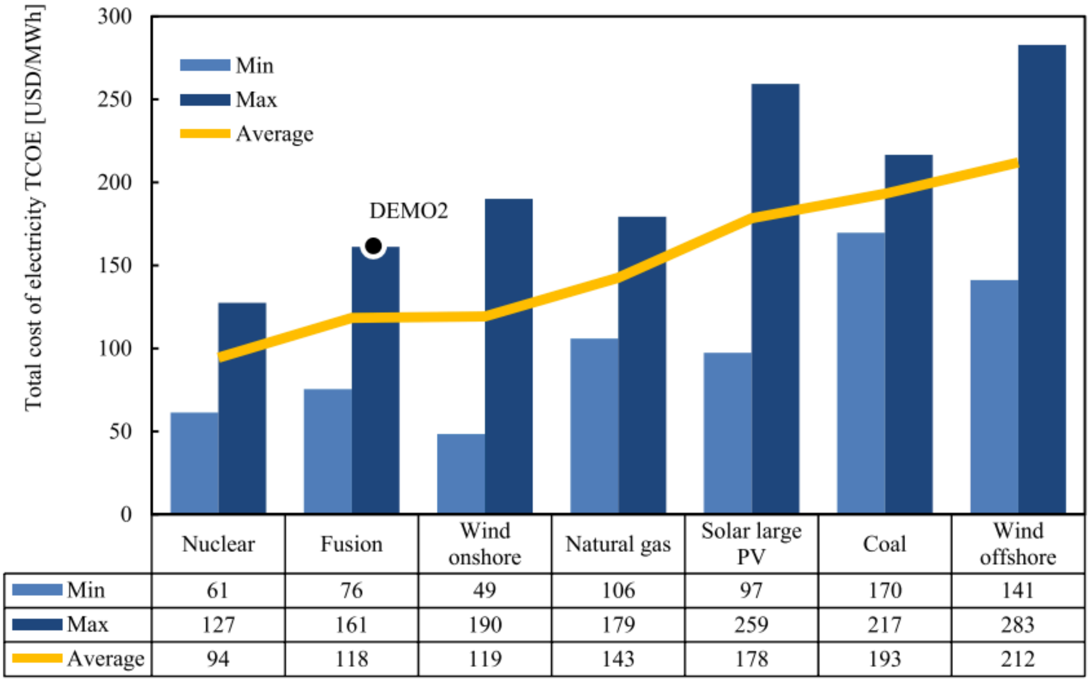

	Nuclear	Fusion	Wind onshore	Natural gas	Solar large PV	Coal	Wind offshore
Min	61	76	49	106	97	170	141
Max	127	161	190	179	259	217	283
Average	94	118	119	143	178	193	212

Figure 1.2 Total levelized cost, including external costs, of electricity produced by varying energy source. Recreated from [6]

Whilst the journey towards realising commercial nuclear fusion has seen significant research and global collaboration, key decisions remain to be made, with several major nuclear fusion reactors currently in the design phase. The challenges still to be overcome to facilitate the realisation of fusion are significant, and important among these is the materials challenge the fusion vessel poses.

The breeder blanket is the reactor component responsible for fusion product energy capture and conversion to harvestable energy, achieved as a result of coolant cycling through the breeder blanket structure. The irradiation doses and high temperatures which breeder blanket structural components (14 MeV neutron flux: 0.5-3x10^{14} ncm^{-2}s^{-1}, peak steady state heat flux: <2-7 MWm^{-2} [7]) can be expected to withstand impose strict candidate criteria, namely: resistance to irradiation induce embrittlement at low/moderate temperatures, resistance to thermal creep at high temperature, acceptable activation behaviour to allow component recycling, and sustained high temperature strength. In addition, effective operating temperatures of structural materials dictate compatible coolant systems, with important consequences for energy extraction and thermal efficiency of reactor design.

Attractive breeder blanket concepts include helium cooled pebble bed (HCPB), molten salt (MS) and lithium-vanadium (LV) designs, which introduce reduced activation ferritic martensitic (RAFM) steels, oxide dispersion strengthened (ODS) RAFM steels, and refractory vanadium alloys respectively as structural materials. These designs facilitate operation at 500-610°C, and response to deformation at high temperature is therefore a fundamental behaviour requiring quantification and microstructurally-based mechanistic characterisation. Microstructural response to deformation informs modelling/design relevant macroscopic properties, and high energy X-ray diffraction employed in-situ permits precise characterisation of lattice and dislocation response to deformation across the sample volume.

1.2. Thesis Outline

In this thesis the mechanical properties of candidate structural materials for use in nuclear fusion reactors are investigated. This thesis considers several generations of structural material design – using in-depth microstructural techniques to characterise the deformation properties of candidate structural materials, before looking beyond current candidate materials to the next generation of structural materials which may be considered.

- Chapter 2 presents the background to nuclear materials: providing context to the environmental factors which inform materials selection, and presenting existing understanding of candidate structural materials.
- The results of Chapter 3 (under review at Acta Materialia) concern the RAFM steel, EUROFER97, and ODS EUROFER97; in-situ synchrotron X-ray diffraction tensile testing allowed for characterisation of dislocation density and character, and elastic properties with increasing temperature, these properties allowing for an evaluation of individual strengthening contributions governing high temperature strength of these alloys.
- Chapter 4 (in preparation) concerns deformation behaviour of batch 2 EUROFER97 steel: in-situ X-ray diffraction of elevated temperature tensile testing is utilised to determine EUROFER97 dislocation evolution and recovery, in-situ X-ray tomography is employed to characterise the deformation behaviour of the alloy, and scanning electron microscopy fractography is used to image post fracture samples.
- Chapter 5 (previously published in the Journal of Nuclear Materials) concerns V-4Cr-4Ti, the current front runner V-based alloy considered for use in nuclear fusion reactors, presenting the results of in-situ X-ray diffraction tensile testing of this alloy at elevated temperature. Results of density functional theory based simulation of the elastic properties of V-4Cr-4Ti are included as a point of comparison to the experimentally determined results.

- Chapter 6 presents the results of a test pilot batch of V-Ti-Ta-Cr alloys, fabricated as a potential improvement over the V-4Cr-4Ti alloy, and mechanically characterised using micro and macro indentation techniques.
- Finally, Chapter 7 summarises the main findings and consequences of the work presented, finishing by considering future work required in this field.

In this way, this thesis aims to expand current understanding through (i) experimental characterisation of fundamental elastic properties of existing structural materials, (ii) identification of mechanistic dislocation behaviour in candidate RAFM/ODS RAFM steels and (iii) establishing basic understanding of an initial foray into next generation structural material development.

CHAPTER 2 LITERATURE REVIEW

2.1 Nuclear Fusion Energy

For over half a century, research has been conducted with the aim of realising fusion energy on Earth [8], but the fusion process has been providing Earth with energy for over four billion years. Fusion is the process which powers the Sun, and the high atomic mass elements which make up our universe owe their creation to the fusion reactions taking place within stars. Fusion occurs when atomic nuclei at extremely high energy collide, smaller nuclei combining to produce a heavier nuclide and a high energy by-product. The basis of the energy emitted during the fusion reaction comes from the strong nuclear force; provided the binding energy per nucleon of the product is significantly greater than that of the reactants, the mass defect increases and thus (through the mass-energy equivalence) energy is liberated from the fusion reaction. The variation of binding energy per nucleon with atomic weight is shown in Figure 2.1, demonstrating the increased binding energy towards iron and associated energy release by fusion/fission.

While fusion offers a high energy yield, there is a large energy barrier to be overcome, resulting from the strong repulsion experienced by like charged particles, such as the nuclei considered in fusion reactions. Nuclei involved in fusion must therefore be extremely high energy to overcome the Coulomb barrier.

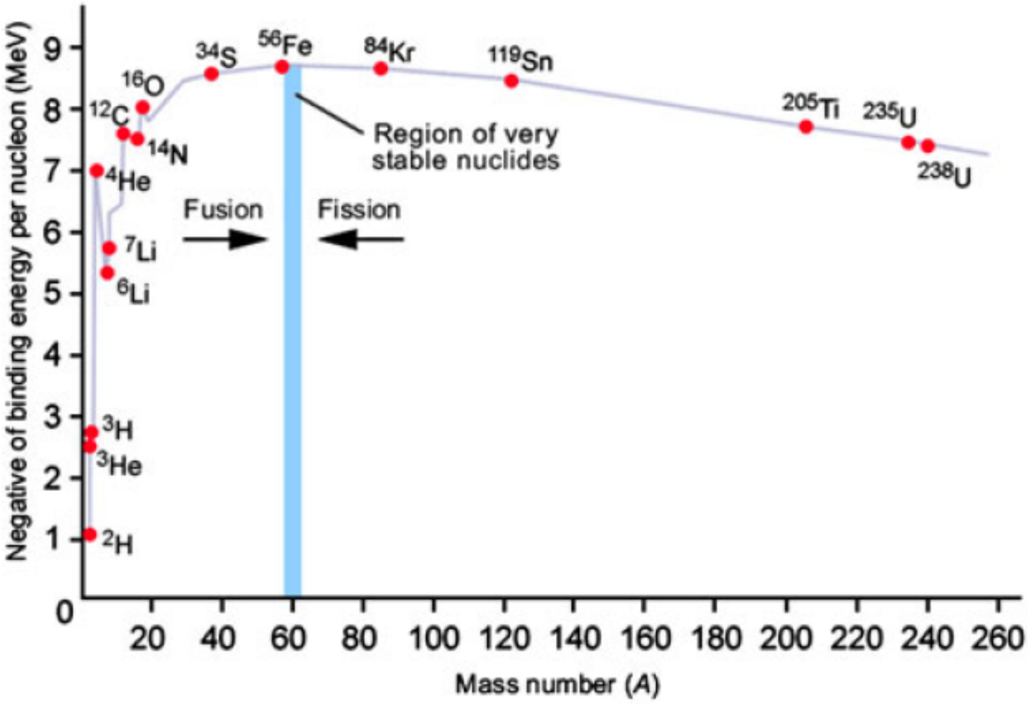

Figure 2.1 Variation of binding energy per nucleon with elemental mass number, demonstrating stabilisation of nuclei towards ^{56}*Fe. After* [9]

2.2 Harnessing Fusion

The proposition of bringing the process that powers the Sun to Earth is a complex one, and there are many competing concepts for how this might be achieved. There are two popular categories that fusion reactor concepts can be broken into, based on the reaction confinement technology utilised: magnetic confinement and inertial confinement. Inertial confinement is based around the principle of extreme compression to overcome the Coulomb barrier between reactants. This compression is achieved through laser impulse triggered ablation of a fuel pellet, by which the surface of the pellet rapidly evaporates, providing an intense thrust towards the centre of the pellet from all sides, compressing the internal fuel [10]. Such approaches have enjoyed some notable recent success [11], but the difficulties of efficient laser energy conversion, appropriate specimen geometries and repetition rate limit global interest in this technique. Inertial confinement deals primarily with solid fuel; plasma forming only temporarily at the centre of the laser ablation induced micro-implosions. This is in contrast to magnetic confinement-based technologies, which utilise sustained term high energy plasmas.

As a collection of nuclei, fusion plasma is highly charged. As a result of this, plasma is subject to manipulation by applied magnetic forces, and this is the basis of magnetic confinement. There are two primary classes of reactor design to consider within magnetically confined fusion: tokamak reactors and stellarators. Both designs contain the fusion plasma within a torus, cycling plasma round the containment vessel during operation. Tokamak reactors utilise two magnetic fields, designed to i) constrict the plasma (poloidal magnets) and ii) induce a current within the plasma (toroidal magnets). Stellarators meanwhile use geometrically contorted magnetic coils to produce a twisted magnetic field which forces the plasma around the containment vessel. Stellarators offer notable advantages over tokamak reactors, in that the contorted magnetic field sidesteps the issue of plasma instability caused by the tokamak's plasma current [12], and less power injection is required to maintain plasma energy [13]. However, these advantages are offset by the greatly increased complexity of stellarator design and manufacture, which has led to the tokamak being more generally favoured.

The fusion reactions considered for utilisation in commercial reactors concern the isotopes of hydrogen, tritium (^3H) and deuterium (^2H), hereafter referenced as T and D respectively. Deuterium is a stable isotope of hydrogen naturally present in sea water as “heavy water” at an abundance of approximately 1 deuterium atom in every 6700 hydrogen atoms [14], and tritium is a radioactive isotope of hydrogen with a half-life of 12.3 years naturally produced only in very low concentrations by cosmic radiation of hydrogen in the atmosphere [14]. The reactions with associated product energy are collected in Equations (2.1) (*D-T* reaction), and (2.2) and (2.3) (*D-D* reaction) [15].

$$D + T \rightarrow \alpha(3.52MeV) + n(14.1MeV) \tag{2.1}$$

$$D + D \underset{50\%}{\longrightarrow} T(1.01MeV) + p(3.03MeV) \tag{2.2}$$

$$D + D \underset{50\%}{\longrightarrow} {}^{3}He(0.82MeV) + n(2.45MeV) \tag{2.3}$$

The *D-T* reaction is the aim of the current fusion roadmap due to its higher power density and lower required critical temperature of operation [16]. However, the utilisation of *D-T* plasmas is hindered by the available inventory of tritium; once in operation, a tritium breeding ratio (TBR) >1.05-1.1 is generally required to maintain the plasma [17]–[19]. Breeder blankets are employed in fusion reactor designs to produce *T* from the absorption of fusion product neutrons by lithium:

$$n + {}^{6}Li \rightarrow {}^{4}He(1.05MeV) + T(2.73MeV) \tag{2.4}$$

$$n + {}^{7}Li \ \rightarrow T + {}^{4}He + n - 2.47\ MeV \tag{2.5}$$

Regardless of the TBR that can be reached however, a suitable *T* inventory is still required for reactor start-up. Given the extremely limited inventory of naturally occurring tritium, and the size and number of upcoming large scale fusion reactors, this problem is a significant one. It is here that the *D-D* reaction may be of particular interest, as it produces both *T* (equation (2.2)) and neutrons capable of producing more *T* (equation (2.3)). It has therefore been suggested that a period of *D-D* or highly diluted *D-T* plasma operation prior to steady state operation may be profitable, allowing build-up of a suitable *T* inventory.

The promise of nuclear fusion as an energy source for the future is by now well known: clean, plentiful energy not reliant on non-renewable resources or changing weather patterns. The 2020-2050 period is now poised to be the time for significant strides to be made in realising energy producing fusion power plants. Several key fusion projects are projected to come online over this period; the International Thermonuclear Experimental Reactor's (ITER's) first plasma intended for 2025 with high power operation slated for 2035/6 [20], the Spherical Tokamak for Energy Production's (STEP's) construction aiming to be completed by 2040 [21], and the construction of EUropean DEMOnstration power plant (EU-DEMO) currently intended to begin in the early 2040's [19].

In particular, ITER and EU-DEMO are significant milestones on the path to a fusion power plant, the combined effort of 35 countries over 17 years of design [20]. ITER will report a Q factor greater than 10, producing around 500 MW of fusion power from plasma pulses between 300 and 500 s in duration, utilising a 1:1 *D-T* fuel [20]. The importance of such operations can be put in context by comparison to the Joint European Torus (JET), which has produced a peak fusion power over its lifetime of 16 MW and set (in February of 2022) a maximum pulse time of 5 s utilising a *D-T* plasma, which returned a Q factor of 0.33 [22]. ITER operations will therefore provide unequalled opportunity for research and development orders of magnitude closer to the conditions expected in realised fusion reactor power plants. Beyond this, the importance of projects such as EU-DEMO and STEP in realising the promise of fusion powered energy to the grid, incorporating and adapting research results from the wealth of research that has come before, is evident. As these projects move out of pre-conceptual design, it is important to consider the state of research that has led to this point, and to solidify understanding to support upcoming design decisions.

2.3 Fusion Reactor Structural Design

D-T fusion plasma requires an operating temperature of 10-20 keV [15], [23], and whilst the operating temperature of the reactor vessel drops off dramatically outside the mass of magnetically confined plasma, radiative heat from the fusion plasma means the reactor walls are still anticipated to experience operating heat power flux density typically between 0.1 and 7 MWm^{-2} [24]. Alongside the considerations of temperature, high energy neutrons (emitted as part of the fusion reaction (2.1)) bombard the reactor walls. In order to harvest energy from the fusion reaction, these neutrons must be arrested and their energy captured. These constraints pose a difficult materials challenge, and it is evident that high temperature performance, and resistance to the effects of long-term irradiation are crucial to selecting appropriate reactor materials candidates.

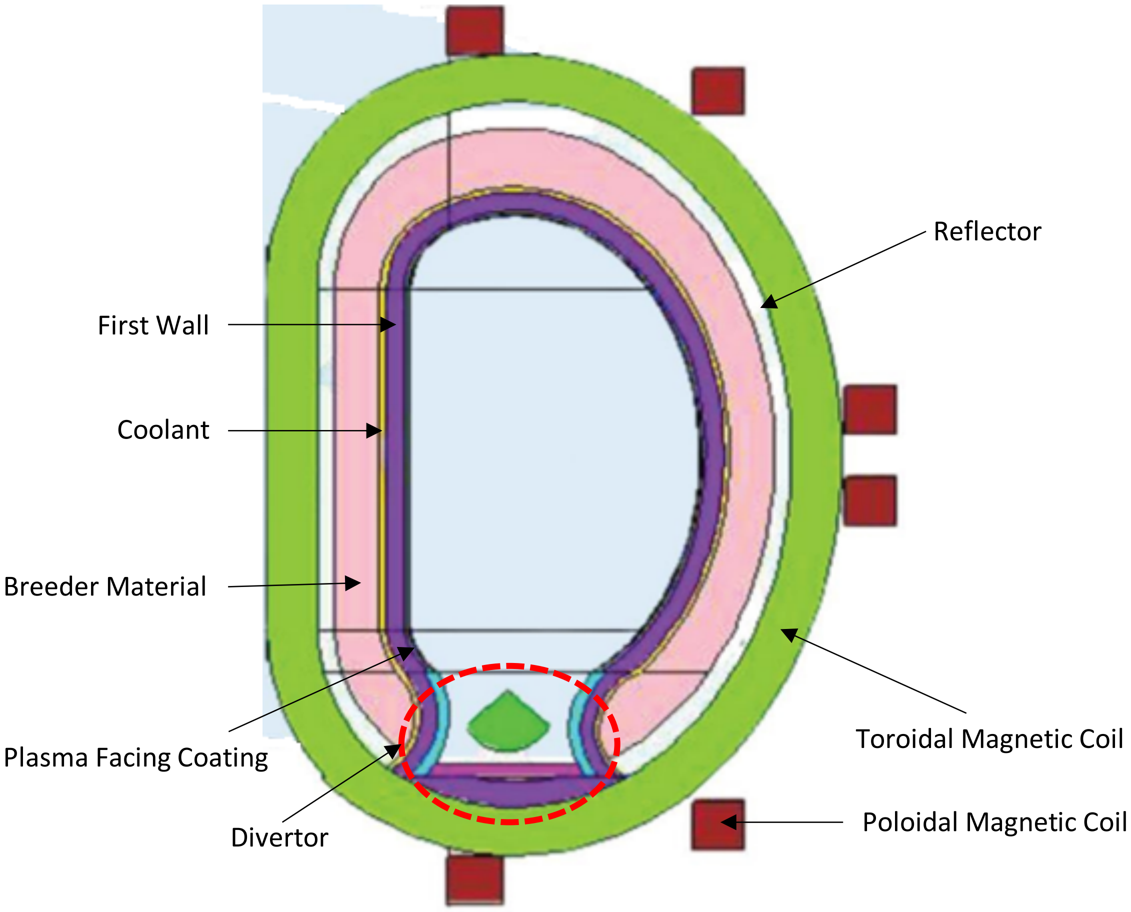

Figure 2.2 Cross section of tokamak fusion reactor (helium cooled lithium lead breeder blanket design included in schematic). After [25]

There are, of course, many components of the reactor vessel with varying requirements, which cannot be considered as a monolith. A cross-section of the tokamak reactor vessel is included in Figure 2.2. The first wall/blanket and the divertor are the components closest to the fusion plasma, and so will experience the highest thermal and neutron fluxes. The divertor is a trench running along the base of the reactor vessel for the purpose of removing helium ash and impurities from the fusion plasma. The first wall/blanket comprises the inner surface of the reactor vessel and serves to a) protect the rest of the reactor vessel from the thermal and neutron irradiation produced by the fusion plasma, and b) allow the energy of the emitted neutrons to be harvested.

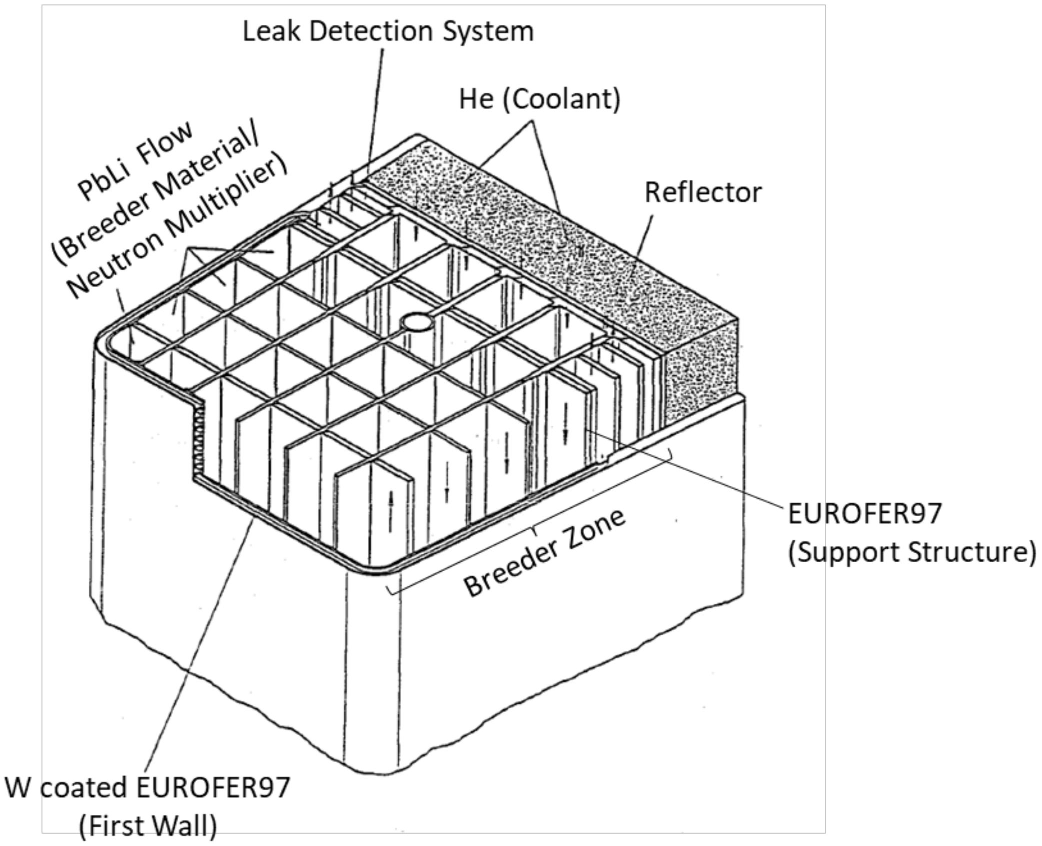

Figure 2.3 Isometric cut away of breeder blanket module. Figure displays outboard segment of dual coolant lithium lead breeder blanket modules for EU DEMO, modified from [26]

The first wall/blanket is normally comprised of many individual cassettes, an example of which is shown in Figure 2.3. The breeder material indicated in Figure 2.3 allows for the generation of tritium from the interaction of incident neutrons with lithium (described in Equations (2.4) and (2.5)). In fact, there are many competing breeder blanket designs. The critical components of breeder blanket designs are the tritium breeder (source of Li6 for T production), the neutron multiplier (increases quantity of emitted neutrons to counteract those lost in contact with non-breeder components), the coolant (removes heat from the breeder blanket for energy generation and to prevent structural overheating), and the structural materials employed (breeder blanket support). Breeder blanket concepts, including critical components and key considerations, are collected in Table 2.1.

Each design carries its own strengths and weaknesses, and are, from a conceptual level, worthy of investigation. Current interest lies towards the lithium-lead reactor designs, with six test blanket module designs slated for testing at ITER: a water cooled lithium lead (WCLL) design, a dual coolant lithium lead (DCLL) design, a water cooled ceramic breeder (WCCB) design, a helium cooled pebble bed (HCPB) design, a helium cooled ceramic breeder (HCCB) design, and a lithium lead ceramic breeder (LLCB) design [18], [27], [28]. Beyond ITER, the EU-DEMO Breeding Blanket Project initially proposed four concepts: HCPB, DCLL, WCLL, and helium cooled lithium lead (HCLL) designs. In a recent Fusion Roadmap revision has been focussed to concern only HCPB and WCLL, on the basis of ease of interfacing between breeder blanket and tokamak structure, as well as maturity and development of the four technologies in the years since proposal [18]. Lithium-lead is not without its own problems however: the accumulation of Pb activation products within the lithium-lead eutectic (notably long-lasting Po), and corrosion of structural components. The simplicity of self-cooling designs – such as Lithium/Vanadium (LV) and Molten Salt (MS) designs – make them attractive, in addition to the high operating temperature of the coolants considered. Breeder blanket design is still an open question; structural material choice a key consideration within this, and material compatibility issues (working temperature, corrosion, magnetohydrodynamics, etc) must be appropriately considered.

Table 2.1 Breeder blanket concept designs for future fusion reactors [17], [18], [29]–[31]

Breeder Blanket Concept	Tritium Breeder Material	Neutron Multiplier	Coolant (inlet/outlet temp)	Structural Material	Key considerations
Water Cooled Lithium Lead (WCLL)	PbLi	Pb in PbLi	Water 285/325°C	RAFM	• Low coolant high temperature, low thermal efficiency
Helium Cooled Lithium Lead (HCLL)	PbLi	Pb in PbLi	He 300/500°C	RAFM	• PbLi flow functions as tritium extraction mechanism, not coolant • He coolant requires high pressure and pump speeds
Dual Coolant Lithium Lead (DCLL)	PbLi	Pb in PbLi	He and PbLi He: LT 250/350°C HT 250/550°C PbLi: LT 275/425°C HT 480/700°C	RAFM/ ODS RAFM	• Structure is He cooled while breeder zone is self cooled – PbLi flow rate increased relative to HCLL • Exists as low temperature (LT) and high temperature (HT) design. HT design requires SiC-composite flow channel inserts providing increased thermal insulation between PbLi and structure, increasing PbLi operating temperature leading to increased efficiency • Reduced magnetohydrodynamic concerns • Requires thermal isolation between structure and breeder
Helium Cooled Pebble Bed (HCPB)	Li-containing Ceramic Pebbles	Be	He 300/500°C	RAFM	• High thermal efficiency • Presence of Be limits high temperature operation and introduces handling concerns • Pebble breeder requires cooling plates which necessitate complex thin, pressure altering cooling plates • Requires separate tritium extraction flow
Lithium Vanadium (LV)	Liquid Li	N/A	Liquid Li 400/600°C	Vanadium Alloys	• Simple design – negates need for multiplier, and self cools • Requires insulating layer to prevent magnetohydrodynamic pressures • Corrosion compatibility issues at high temperature
Molten Salt (MS)	Molten FLiBe salt	Be in FLiBe	FLiBe 510/610°C	ODS RAFM	• Reduced magnetohydrodynamic concerns • Low tritium solubility • Poor heat transfer properties

2.4 Candidate Structural Materials

Considering the high heat and neutron fluxes structural materials will be subjected to, candidate structural materials can be established on the basis of high temperature mechanical performance, resistance to thermal creep, activation properties, and resistance to degradation under irradiation. A variety of structural materials have been considered as candidates in this arena, roughly comprising three generations of materials design. The primary classes of material considered for structural application within fusion reactor design being reduced activation ferritic martensitic (RAFM) steels, oxide dispersion strengthened (ODS) RAFM steels, silicon carbide, vanadium alloys, and – recently – refractory metal high entropy alloys (HEA's), comparison in structural material operating temperatures is shown in Figure 2.4.

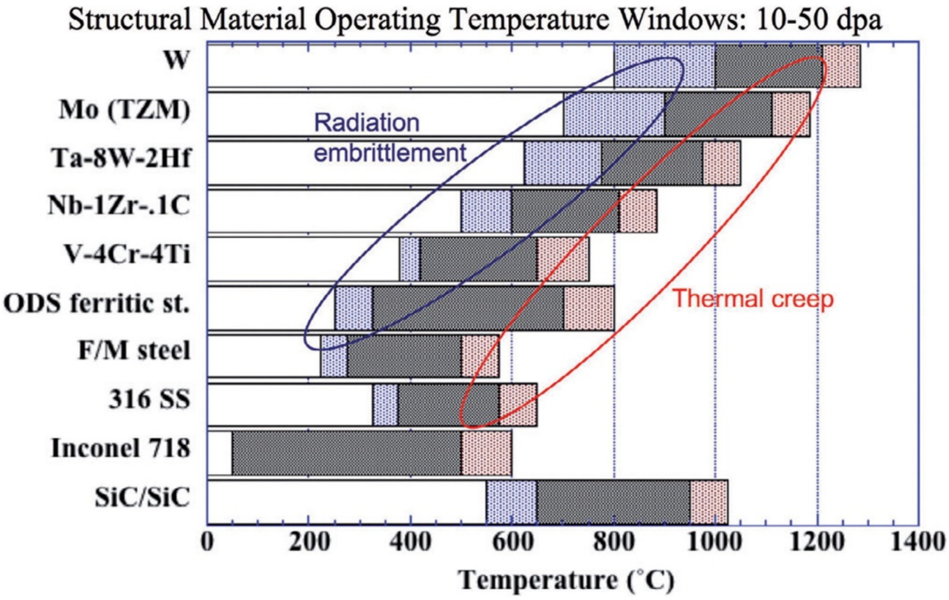

Figure 2.4 Candidate structural material operating temperature window at 10-50 dpa, limited by low temperature radiation embrittlement, and high temperature thermal creep. After [32]

2.4.1 Reduced Activation Ferritic Martensitic Steels

Given its widespread and historical use across many and diverse structural applications, steel was a natural jumping off point for the identification of fusion structural materials. A wealth of data had long been established concerning the mechanical performance of varying grades of steel in extreme environmental conditions. High chromium steels (9%wt-13%wt) are well regarded for structural application – chromium content high enough to enhance corrosion resistance and provide solid solution strengthening, yet low enough to avoid significantly raised ductile to brittle transition temperature (DBTT). Chromium content of 9wt% has been shown to maximise toughness and creep strength [33].

In order to avoid problems with handling and recycling, the elements selected for microalloying were filtered on the basis of activation. Common steel additions such as molybdenum and niobium are replaced with tungsten and tantalum to meet shallow land burial criteria, and cobalt, nickel, copper, and aluminium content are carefully controlled [34]. Such steels are therefore referred to as Reduced Activation Ferritic Martensitic (RAFM) steels, and the RAFM steels which currently draw the most interest are the Japanese F82H, and the European EUROFER97. EUROFER97 has composition 9CrWVTa, based upon the conventional alloy, T91 (Fe-9Cr-1Mo-0.2V-0.08Nb). The target composition of EUROFER97 is presented in Table 2.2.

Table 2.2 Target composition of EUROFER97, Fe balance [35], [36]. *Radiologically undesired elements are indicated with an **

Alloying Element	Minimum content (wt%)	Maximum content (wt%)	Target content (wt%)
Cr	8.5	9.5	9
W	1.0	1.2	1.1
Mn	0.2	0.6	0.4
V	0.15	0.25	0.2
Ta	0.10	0.14	0.12
C	0.09	0.12	0.11
N_2	0.015	0.045	0.030
O_2		0.01	<0.01
P		0.005	<0.005
S		0.005	<0.005
B		0.002	<0.001
Si*		0.05	<0.05
Al*		0.01	<0.01
Ti*		0.02	<0.01
Co*		0.01	<0.005
Cu*		0.01	<0.005
Mo*		0.005	<0.005
Ni*		0.01	<0.005
Nb*		0.005	<0.001
{As+Sn+Sb+Zr}*		0.05	<0.05

2.4.1.1 RAFM Fabrication and Microstructure

After their conception in 1982 [34], RAFM steel production has progressed; most commonly by vacuum induction melting, followed by a secondary refinement to remove impurities and inclusions. EUROFER97 heats as large as 2000 kg have been produced for the EU, provided in a variety of forms, and as of 2021 four batches of EUROFER97 (coded EUROFER97/2, EUROFER97/3, etc) have been produced by Böhler Edelstahl GmbH, Austria and Saarschmiede, Germany [37]. After refinement by vacuum arc remelting, heats undergo differing heat treatments depending on final product form. The microstructure of EUROFER97 (and RAFM steels in general) is highly dependent upon initial heat treatment; austenitization at temperatures exceeding 1000°C has been reported to lead to a notable increase in mean grain size by 5-10 microns [38], [39]. This has been linked to the presence or dissolution of carbides during austenitization: martensite lath packets are known to form and be bounded by prior austenite grains. When present, precipitates pin grain growth during austenitization, suppressing prior austenite grain size, and hence martensite grain size [40]. Conversely, if austenitization is performed at temperatures high enough to allow precipitate dissolution, grain growth is uninhibited in this way. Cooling rate utilised between heat treatment steps must also be considered, a cooling rate slower than roughly 2 °C/min has been to shown to allow the austenite phase to decay to soft ferrite and large carbides [37], rather than the desired hardened martensite. Tempering of martensite produced promotes ductility and leads to the formation of carbides across the material – a temperature close to the onset of austenitization is required for martensite softening, and selection of tempering temperature can have large knock on effects for ductile to brittle transition temperature [37]. Generally, blocks are normalised at 980-1040°C for 15-30 minutes, air cooled to room temperature, tempered at 750-60°C for 90-120 minutes, and finally air cooled to room temperature again [36], [37], [41].

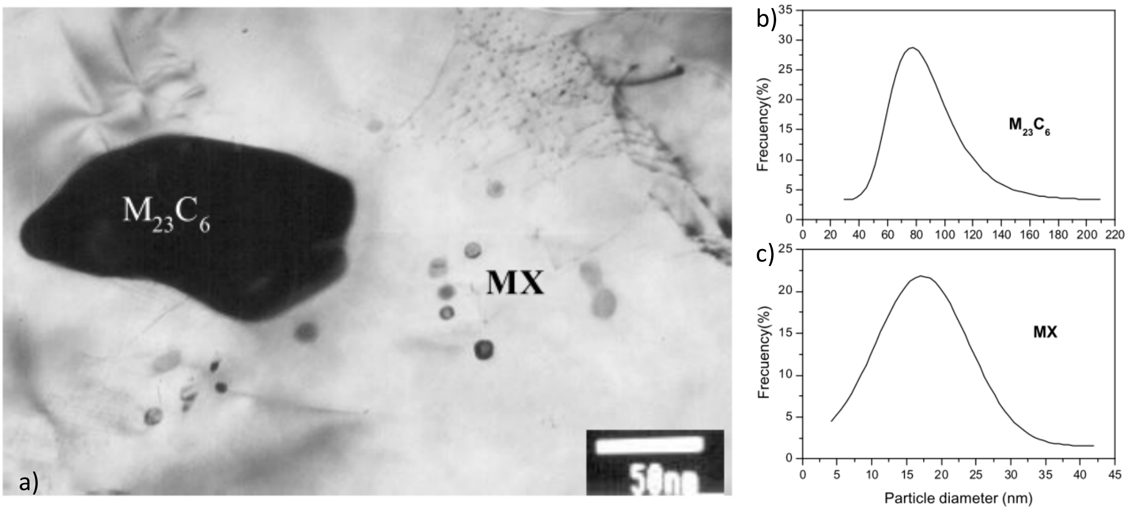

Figure 2.5 a) Transmission Electron Microscopy micrograph of classes of precipitates found within as-received EUROFER97. b)/c) Probability distribution curve illustrating the size distribution of these precipitates. After [42]

Following this fabrication, EUROFER97 exhibits an exclusively martensite structure, consisting of fine lath subgrains with high dislocation density, decorated with precipitates [43], [44]. Large Cr rich $M_{23}C_6$ carbides decorate grain and subgrain boundaries, with a size between 50-300 nm dependent upon growth site – the size of such carbides formed at lath boundaries being suppressed [44]. In contrast smaller V and Ta rich MX carbonitride precipitates are found both at grain/subgrain boundaries and across the lath [43], forming as spherical or plate-like precipitates 8-60 nm in size [42], [44]. Examples of the classes of precipitate observed in the as-received EUROFER97 are collected in Figure 2.5.

2.4.1.2 RAFM's Under High Temperature and Irradiation

Unirradiated EUROFER97 processed by the treatment described above exhibits a DBTT of approximately -70°C [37], [45], [46] – an appropriately low transition temperature which allows for thermal cycling during reactor operations without risk of component embrittlement. However, the DBTT is very sensitive to irradiation dose, particularly at moderate-low irradiation temperatures; experiments at irradiation temperatures between 250°C and 450°C found a large shift in DBTT was produced for those tests performed below an irradiation temperature of 350°C [39] (depicted in Figure 2.6). Experiments at irradiation temperatures around 300°C showed that DBTT reached ambient temperatures (>0°C) from doses as low as 7 dpa [47]. The irradiation induced shift in DBTT is initially very sensitive to dose [48], [49], but begins to flatten out at doses above 30 dpa, as shown in Figure 2.6. EUROFER97 samples exposed to irradiation temperatures 250-350°C exhibited significant radiation hardening and an accompanying decrease in elongation; this hardening quantified as an increase in yield strength at room and elevated temperature of over 200 MPa for samples exposed to dosages from 2.5 dpa [50]–[52]. The temperature dependency of irradiation hardening has been linked to the size and density of irradiation induced defects in test EUROFER97 samples. Transmission Electron Microscopy investigation of EUROFER97 irradiated at temperatures of 250°C and 300°C (dose 13-15 dpa) showed the presence of a high number density (10^{22}-10^{23} m^{-3}) of nanoscale b ½ <111> type dislocation loops, average size <10 nm [53]. These fine densely distributed defects slow the movement of dislocations throughout the material, strengthening the base material, with maximum strengthening effect reported at 300°C. Above 350°C, the density of observed dislocation loops rapidly falls off, the average size of dislocation loops grows, and the loop type shifts to predominantly b<110>. The temperature dependent irradiation hardening and susceptibility to embrittlement imposes a lower limit on the operating temperature window of EUROFER97 of 350°C, which raises compatibility concerns with proposed WCLL breeder designs.

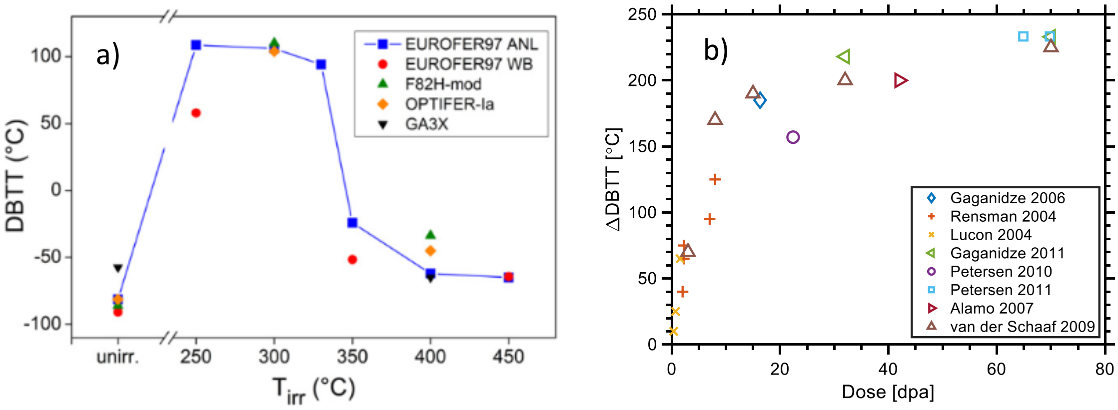

Figure 2.6 a)DBTT of select RAFM steels following irradiation at 300^{o}C with average dose 16.3 dpa. After Gaganidze et al (2013) [48] *b) shift in DBTT induced by irradiation of select RAFM steels at varying dosage for irradiation temperature 300-350^{o}C (data* [39], [47], [49], [54], [55].

One of the key benefits of ferritic martensitic steels, which lead to initial interest in their employment in fusion/fission environments, is their resistance to void swelling compared to austenitic steels previously favoured. The basis for this comes from the difference in dislocation bias between the two classes of steel, body centred cubic (BCC)/body centred tetragonal (BCT) structured (ferritic/martensitic) steel showing a lower dislocation bias and higher self-diffusion rate, leading to increased swelling resistance relative to face centred cubic (FCC) (austenitic) steel [56]. Ferritic/martensitic steels have been shown to exhibit an initially very low swelling rate, before ultimately transitioning to a steady state swelling rate two to four times smaller than austenitic steels [57].

EUROFER97 shows little significant change after high temperature (>500°C) ageing over <1000 hours [46], [58], [59]; ultimate tensile strength, yield strength, and elongation showing negligible change up to ageing 10,000 hours at 600°C [58]. Indeed, the most notable mechanical change recorded between as received and aged EUROFER97 samples is an increase in the DBTT of 20-25°C, previously linked to microstructural changes at elevated temperature [60]. Breakdown of lath subgrains was observed in 10,000h aged samples at 500/600°C, with the onset of recrystallisation at these temperatures. This has been linked to the coarsening of large $M_{23}C_6$ carbides at elevated temperature, producing an increased interparticle separation and hence lowering their efficiency in pinning subgrain boundary migration. Very large $M_{23}C_6$ carbides (300-1500 nm) have been reported to negatively affect the low temperature toughness of high chromium heat resistant steels: as these precipitates are brittle they act as stress concentrators, promoting the formation of microcracks during deformation [61]. This is in contrast to the nanosized MX carbonitrides, however, which exhibit much higher stability – demonstrating no significant change in size over annealing at 650°C for over 17,000 h [62]. Long term high temperature heating also leads to the formation of the Laves phase, the Laves phase starting to form from grain boundaries after annealing at 500°C for >100,000 hours, or from $M_{23}C_6$ carbides after annealing at 550°C for >20,000 hours [62]. Annealing of EUROFER97 at temperatures beyond 550°C saw the Laves Phase replaced by Z-phase, nucleating from VN type MX particles. It should be noted, the formation of high temperature phases is very sensitive to alloy chemical composition, Laves phase forming at areas rich with tungsten (grain boundaries as the result of diffusion, carbides as the result of the tungsten concentrated structure) [63]. Significant differences were therefore seen between EUROFER97 and other RAFM steels with only minor changes in elemental composition: China Low Activation Martensitic (CLAM) steel (composition within EUROFER97 specified bounds, but for slightly enriched tungsten content of 1.5wt%) saw Laves phase particles form only after ageing at 550°C for 10,000 hours [63], an RAFM steel (composition within EUROFER97 specified bounds, with augmented tungsten content of 1.53wt% and depressed tantalum content of 0.062wt%) saw Laves phase formation and coarsening after ageing at 550°C from 1250 hours [64], and F82H IEA (composition Fe-7.87Cr-1.98W-0.19V-0.1Mn-0.09C-0.07Si-0.04Ta) saw Laves phase formation from >1000 hours at 550°C and <1000 hours above 550°C – the Laves phase critically not giving way to Z-phase even at 650°C ageing over 100,000 hours [65].

The factors described result in a limit on the operating temperature: the loss of precipitate strengthening through the coarsening of $M_{23}C_6$ carbides, the loss of sub-boundary strengthening with the onset of recrystallisation, and the consumption of fine MX precipitates caused by the formation of Laves phase, all result in a corresponding drop in creep strength of EUROFER97 at 550°C [33].

2.4.2 Oxide Dispersion Strengthened RAFM's

Naturally, materials design has developed alongside other nuclear fusion technologies, and in order to widen the operating temperature window of proposed RAFM's, oxide dispersion strengthened (ODS) RAFM's have been produced. These alloys utilise diffuse populations of stable oxide nanoparticles to pin movement of dislocations and hence increase resistance to high temperature creep. The introduction of thermally stable oxides is intended to mitigate the cyclic softening observed in RAFM's with the coarsening of $M_{23}C_6$ precipitates at moderate temperatures (450^{o}C) [66]. Oxides of varying chemical composition have been investigated over the years, with oxides of yttria and titanium (as Y_2O_3, TiO_2, and complex Y-Ti-O oxides) attracting particular interest. Oxide content between 0.25 wt% and 0.5 wt% is commonly used.

2.4.2.1 ODS Steels: Fabrication and Microstructure

At present, ODS RAFM samples are produced almost exclusively by hot isostatic pressing (HIP'ing) of high purity mechanically alloyed powders of yttrium oxide and inert gas atomised EUROFER97. HIP'ing produces isotropic microstructure with respect to nanoparticle distribution and grain orientation. ODS EUROFER97 has been manufactured on a large scale in several distinct batches. First generation ODS EUROFER97 was fabricated in 0.3wt% and 0.5wt% yttria variants, produced by mechanical alloying (at Plansee, Austria) of inert gas atomised EUROFER97 (provided by Starck), and consolidation by hot isostatic pressing [35], [67]. Mechanical characterisation of the fabricated 0.3wt% yttria bars demonstrated suitable tensile properties (discussed in Section 2.4.2.2 ODS Steels: Under High Temperature and Irradiation) but poor impact properties; recording a DBTT between 60°C and 100°C [35], [67], well outside acceptable limits. The 0.5wt% yttria bars showed less favourable results, the strengthening effect less pronounced compared to EUROFER97, and the total elongation dramatically reduced [68].

The second generation ODS EUROFER was produced as a collaboration between Plansee and FZK, produced by the hot isostatic pressing of mechanically alloyed steel with 0.3wt% Y_2O_3 powder, followed by homogenising hot rolling, austenitisation and tempering [69], [70]. The second batch succeeded in recreating the excellent high temperature strength properties of the first, whilst reducing the DBTT to between -40°C and -80°C [70]. The subsequent “EU Batch” was produced by Plansee following the same fabrication route, the primary exception being the batch was water quenched to 450°C following austenitisation – ie above the martensite start temperature (M_S~350°C) [71], [72]. Large scale fabrication of ODS RAFM steels has processed almost exclusively by HIP’ing, but over recent years, research into production of ODS RAFM steels via additive manufacturing has also been seen [73].

In contrast to the entirely tempered martensitic structure of non-ODS RAFM, ODS RAFM steels present a mixed structure; balance between ferrite and martensite dictated by chromium content [74] and alloy fabrication parameters [71]. The structure of ODS EUROFER97 is heavily dependent upon fabrication heat treatment, commonly reported as either a predominantly martensitic structure, decorated with retained ferrite [75], or purely ferritic. Ferritic structure was reported both in the first generation [67], [68], [76], [77], second generation [78] and EU batch ODS 0.3wt% EUROFER97 [79], [80].

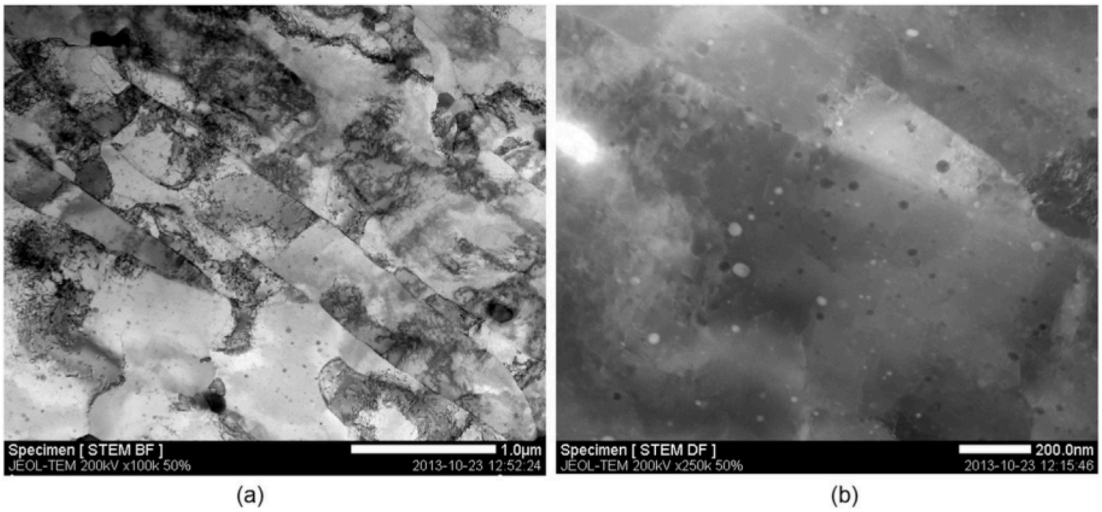

Figure 2.7 Nanoparticle distribution in ODS EUROFER97, annealed at 800 ℃ for 4320 h, demonstrating the varied size of nanoparticles present, captured using scanning transmission electron microscopy in the a) bright field and b) dark field. Recreated from [81]

The size and distribution of Y_2O_3 nanoparticles within the alloy (an example of which is shown in Figure 2.7) is dependent upon fabrication route: HIP'ed ODS EUROFER97 reporting nanoparticles with diameter 2-30 nm (mean size 12 nm) with a bimodal distribution of nanoparticles (2-10nm and 4-30nm areas) as-received [67], [82], [83], and hot rolling of the HIP'ed ODS EUROFER97 caused further inhomogeneity in nanoparticle distribution, producing stripes free of nanoparticles entirely [84]. In ferritic-martensitic ODS EUROFER97, the bimodal distribution of nanoparticles has been suggested to correspond to the phase – ferritic grains collecting high densities of fine nanoparticles, martensite grains collecting low densities of coarse nanoparticles [85]. In addition to the Y_2O_3 particles introduced during HIP'ing, ODS EUROFER97 is decorated with intragranular $M_{23}C_6$ carbides enriched – as in base EUROFER97 – with chromium [76].

2.4.2.2 ODS Steels: Under High Temperature and Irradiation

The major motivation in the development of ODS RAFM steels is their increased high temperature creep strength. Tensile testing of 0.3wt% ODS EUROFER97 across all batches at temperatures up to 700°C showed the 0.3wt% Y_2O_3 alloy demonstrated significantly improved mechanical performance (yield strength, ultimate tensile strength, and uniform elongation) relative to EUROFER97 [72]. Larson-Miller analysis of creep testing of EUROFER97 and 0.3wt% Y_2O_3 ODS EUROFER97 found the ODS sample able to effectively withstand temperatures roughly 65°C higher for equivalent applied stresses and rupture times [86]. The effect of long-term heating and load on 9Cr ODS F/M steels have been investigated in ageing and creep studies [87], [88]. These works found the microstructure and mechanical properties of this alloy class to be almost unaffected by thermal ageing at 700°C for over 10,000 h [88], or long term creep (74

MPa at 750°C for over 45,000 h & 104 MPa at 700°C for over 46,000 h [87]). Microscopic analysis of samples following testing found ODS nanoparticles retained thermal stability and promoted the retention of populations of dense dislocations, the only notable microscopic change observed being the coarsening of intragranular carbides.

The microstructure of ODS EUROFER97 arrived at through thermomechanical processing and carbon control has important consequences for impact properties. At low temperatures, ferritic ODS EUROFER97 exhibits lower fracture toughness than martensitic ODS EUROFER97, whilst at moderate temperature (100-500°C) the opposite is true, and at high temperature (>500°C) grain size effects are thought to dominate [71].

At high and low irradiation temperatures (high:400-550°C low:40°C [89]), deformation properties (considered as DBTT, uniform elongation, and yield stress) of ODS EUROFER97 were almost unchanged from its unirradiated state for doses up to 16.3 dpa [89]–[92]. However, irradiation studies of ODS EUROFER97 have demonstrated the same susceptibility to moderate temperature irradiation embrittlement as EUROFER97. A shift in DBTT greater than 50°C was observed in ODS EUROFER97 samples exposed to doses of even 1 dpa at irradiation temperatures of 300°C [90], [93], which brought the DBTT close to ambient temperatures (>0°C). The DBTT (analysed through master curve reference temperature, T_0) increased by 85°C for generation II ODS EUROFER97 under an irradiation temperature of 300°C, and exposed to dose 1.5dpa, a shift more than double that of base EUROFER97 [94].

Microstructural TEM characterisation of ODS EUROFER97 showed irradiation induced defects were present even from low irradiation temperatures and doses, “black dot” defects seen at irradiation temperature 40°C [89]. These defects provide less effective strengthening than the Y_2O_3 particles, being observed on the order of 1.5-5 nm, and with a density lower than that of the oxide particles [89]. The distribution of defects follows a bimodal distribution, seen alongside the aforementioned bimodal grain structure, and in keeping with the distribution of ODS particles, with coarse ODS particles (5-18 nm) collecting in fine grained regions, and fine ODS particles (<4 nm) collecting in larger grains [76].

As irradiation temperature increases, the defects seen evolve from black dot defects to self-interstitial atom dislocation loops. During neutron irradiation testing of EU batch ODS EUROFER97, dislocation loops with size 5-20 nm started to be seen at irradiation temperature 300°C from doses 1-3 dpa, the number density of defects highly dependent upon dose [92], [95]. The extensive irradiation hardening seen at this temperature is attributed to the size and density of black dot defects, which effectively impede the motion of dislocations. The size of observed dislocation loops increased to 20-40 nm under irradiation temperature of 450°C and 550°C, forming dislocation networks which interact only weakly with ODS particles, and the number density of black dot defects falls significantly [92]. In addition to the formation of defects, neutron irradiation of high Cr ODS steels has been reported to coarsen and reduce density of oxide nanoparticles through oxide dissolution and Oswald ripening [96], [97].

Taking into account the temperature windows of the breeder blanket concepts for which ODS EUROFER97 is considered, this irradiation low temperature hardening embrittlement poses a significant challenge to design adoption [98]

2.4.3 Refractory Alloys

2.4.3.1 Refractory Metals and their Alloys

The refractory metals (Figure 2.8) are a class of materials grouped due to their high melting temperatures (>1800°C). While various definitions exist, the core refractory metals commonly include vanadium, chromium, niobium, molybdenum, hafnium, tantalum, tungsten and rhenium. In addition to their high melting temperature, they exhibit excellent wear resistance and strength at high temperature, making the refractory metals an obviously attractive class of material for use as fusion structural materials.

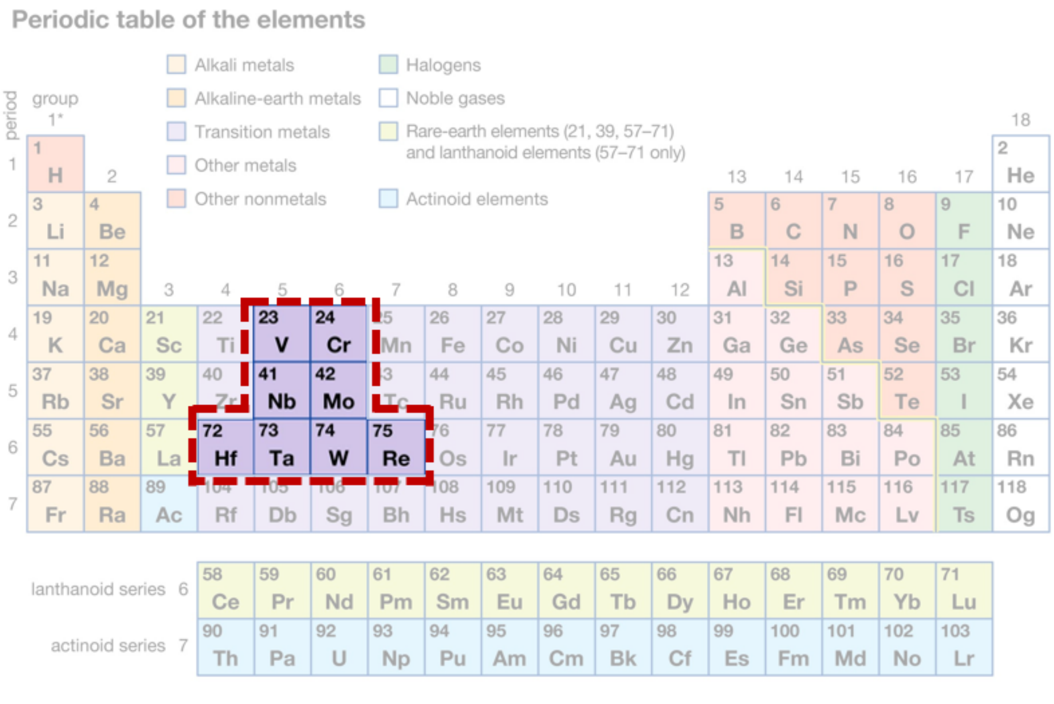

*Numbering system adopted by the International Union of Pure and Applied Chemistry (IUPAC). © Encyclopædia Britannica, Inc.

Figure 2.8 Figure highlighting the position of the refractory metals on the periodic table. Adapted from [99]

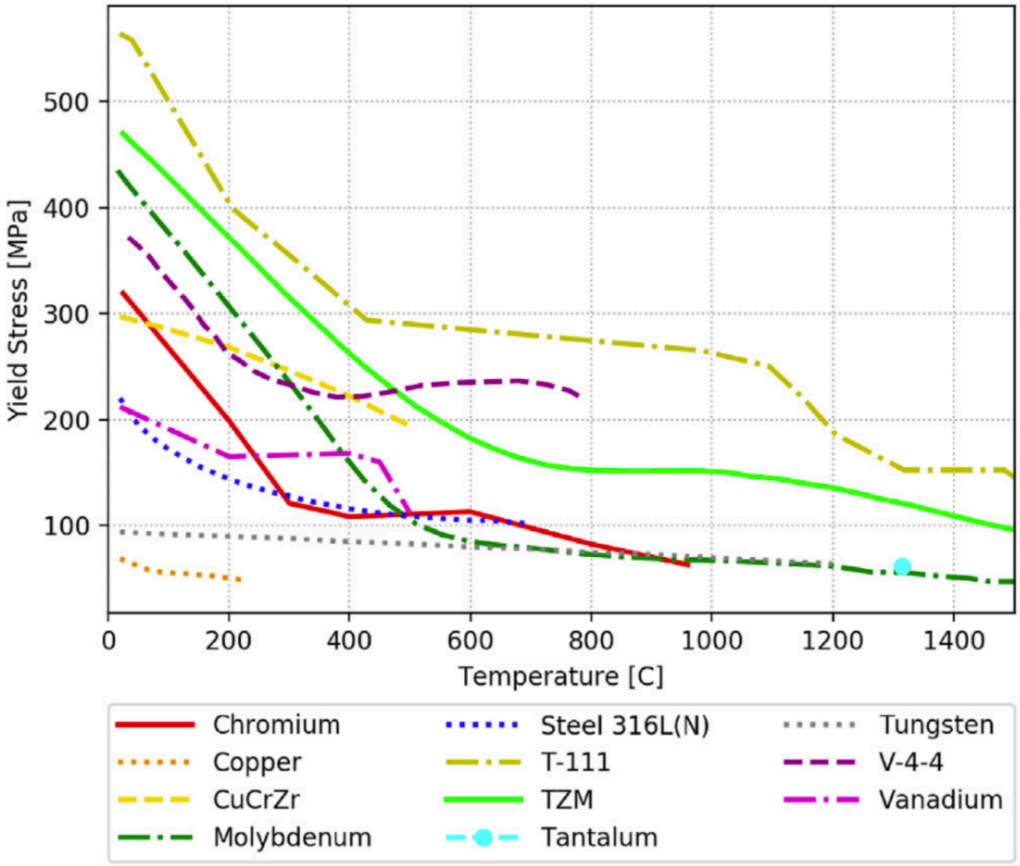

Figure 2.9 Temperature dependent strength behaviour of refractory metals/alloys – 316L steel included as reference point. Recreated from [100]

Despite their suitable high temperature properties (Figure 2.9), not all refractory metals should be considered for use within the nuclear field. Niobium and molybdenum do not meet the criteria of low activation established to meet the limit for hands on handling for over 10,000 years [100], [101], severely limiting recyclability and handling of materials post lifetime. The relative decay of dose rate for refractory metals are compared in Figure 2.10. Hafnium meanwhile exhibits an unfavourably high neutron cross section for high energy neutrons, and a concentration of hafnium as low as 3 %wt has been reported to lower the tritium breeder ratio by 10% [102].

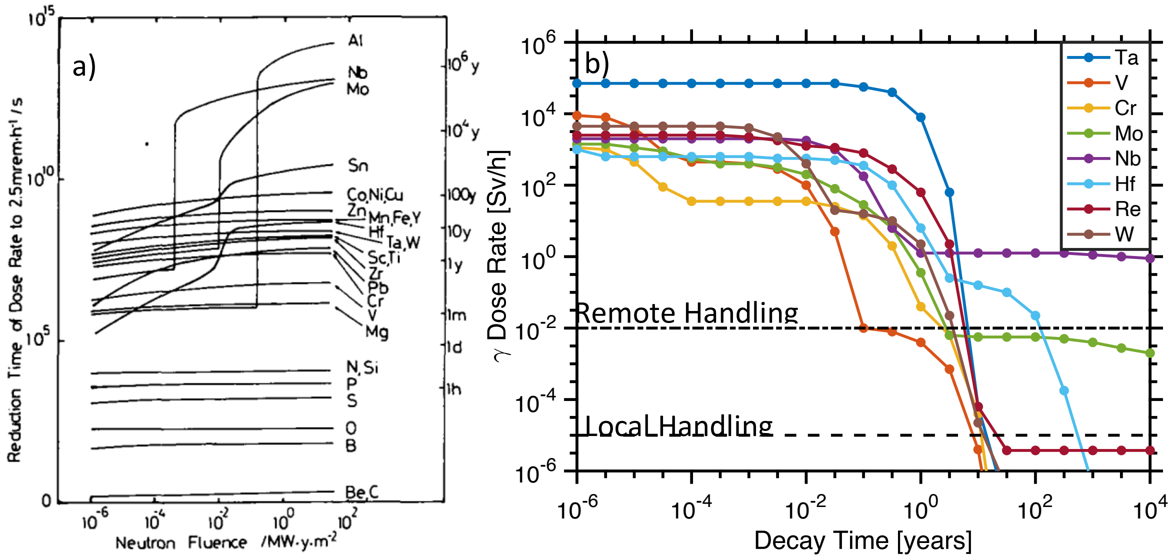

Figure 2.10 Recycling limits of refractory metals: a) time taken to reach 25μSvh^{-1}as a function of neutron fluence, after [103]*, and b) modelled decay of contact dose rate for refractory metals over time following exposure to neutron fluences simulating reactor blanket conditions (remote and hands on handling limits indicated), data taken from* [104]

Unfortunately, ambient temperature ductility proves a weakness for many refractory metals. Chromium has long been used as a microalloying element to improve the strength and corrosion resistance of steels, but as a material it exhibits very poor deformability, even above its ductile to brittle transition temperature [23]. Tungsten is well known for its exceptional high temperature performance, and is used as a first wall material in most fusion reactor designs. However, tungsten's high DBTT and susceptibility to irradiation embrittlement make it ill-suited to broader application [105]–[107].

The remaining refractory metals (vanadium and tantalum) may be deemed more favourable candidates. Tantalum reports high ductility, high thermal conductivity low thermal expansion, excellent corrosion resistance, and good fabricability [108]–[110]. Despite this, pure tantalum has been shown to exhibit heightened void swelling at irradiation temperatures around 600°C [111], meaning the use of pure tantalum in a structural capacity would require a high lower operating temperature. Alloying of tantalum presents an interesting opportunity, however. The tantalum-based alloy was T-111, a tantalum-8%wt tungsten-2%wt hafnium alloy which was first considered for space applications. The alloy exhibited excellent ductility and formability, and produced suitable high temperature tensile results [112], [113]. Little irradiation data exists for the T-111 alloy, but testing at 450°C and 600°C showed no void swelling and some evidence of densification [114], [115]. Issues with ease of production given scarcity of hafnium and tantalum, susceptibility to creep at moderate temperatures, has limited interest in this alloy during recent years.

Conversely, interest in vanadium-based alloys has grown over recent years. Vanadium exhibits excellent activation properties, and alloys of vanadium have been found to present high strength over appropriate operating temperatures and ductility at ambient temperatures [116]–[118]. Vanadium micro-alloyed with chromium and titanium (V-4%wt Cr-4%wt Ti) is a particularly promising candidate for fusion reactor structural applications.

Addition of chromium has been found to produce solid solution strengthening, significantly increasing the thermal creep resistance at even low concentrations as a result of dislocation pinning [116]. Similarly, the presence of low concentrations of titanium in vanadium alloys has been shown to improve the resistance of vanadium alloys to irradiation induced swelling [119]. Titanium has been found to exhibit tight binding with vacancies, resulting in the formation of titanium-vacancy complexes which effectively trap irradiation induced defects, preventing the cascade of such defects through the matrix [120]. In addition, the precipitation of Ti(CON) precipitates results in precipitate strengthening of the vanadium alloy. Indeed, a recent study by Shen et al. (2022) suggests the strengthening provided by titanium outstrips that provided by chromium [121]. Concentrations of chromium and titanium between 0% - approximately 20% respectively were initially investigated [122], resulting in two important determinations. Firstly that the greatest reduction in swelling was found at around 5% Ti by weight [119], and secondly that whilst increasing Cr content did improve alloy strength properties, a total alloy content above 10% was found to increase the DBTT of the alloy from -190°C to -30°C [116], [123], [124]. Thus V-4Cr-4Ti represents an optimisation of the favourable effects of Cr and Ti addition, whilst avoiding the issue of increased DBTT.

2.4.3.2 V-4Cr-4Ti: Fabrication and Microstructure

Unlike the high chromium RAFM steels otherwise considered for fusion structural applications, there is no existing infrastructure or established fabrication route for the production of large-scale vanadium alloys, necessary for the supply of industrially useful components. This poses a significant challenge to the long-term adoption of vanadium alloys in fusion design, and several fabrication methods have been proposed over the course of vanadium alloy research.

The first large scale V-4Cr-4Ti ingot (ID USDOE832665) recorded composition comprising 3.8 wt.% Cr and 3.9 wt% Ti, with >1400 wppm impurity, of which O contributed 310 wppm, and Si 783 wppm, mass 500 kg [125]. The ingot was produced by consumable electrode arc melting of constituent elements, followed by hot working during which the ingot was encapsulated in a contaminant protecting stainless steel jacket. Following extrusion at 1150°C, the ingot was warm rolled at 400°C to desired dimensions with two hour intermediate annealings at 1050-1070°C between rolling, final annealing at 1050°C to allow recrystallization [125]. Prior to this, 50 kg ingots of V-4Cr-4Ti had been produced by a very similar processing route – differences being the use of cold rolling in place of warm rolling, in order to avoid the formation of vanadium oxides [126].

Effort to limit unintended interstitial impurity content has dictated more current V-Cr-Ti alloy fabrication. The impurities introduced in the largest concentrations during fabrication are most commonly C, N, and O, and these can significantly alter the hardness of vanadium alloys. C, N, and O exist in vanadium alloys as interstitial impurities, acting as potent solid solution strengthening agents – with an increase in O content from 50 ppm to 2200 ppm having been seen to increase ultimate tensile strength by up to a factor of five [127]. However, with this strengthening comes a substantial hardening effect, which significantly degrades the ductility of the alloy [128].

Given the negative impact of interstitial impurities on the irradiation resistance and weldability of the V-4Cr-4Ti alloy it is unsurprising that one of the current fabrication routes, introduced in 2000 [129], is designed to keep the C/O/N impurity levels as low as possible. This fabrication route, employed by the National Institute for Fusion Science (NIFS) in Japan, limited the introduction of these impurities by canning the cold-rolled ingots in Zr or Nb foils during hot working. The foils act as getters, diverting any potential contamination from the ingot, and in this way oxygen level was effectively reduced, producing ingots with oxygen level 130-180 wppm [130]. Whilst the reduced concentration of impurity present in the NIFS-HEAT alloys has been shown to reduce weld embrittlement when compared to the US832665 alloy [131], this reduction has also induced some degradation of high temperature mechanical properties of the base alloy [132]. As previously mentioned, the C/O/N interstitials present in V-4Cr-4Ti alloys act as solid solution strengthening agents, and so the reduced concentration of these impurities in the NIFS-HEAT alloys leads to purification softening, manifesting as a reduction of yield strength and rupture time at elevated temperature (>700°C) [132].

As well as its effect on irradiation induced swelling, titanium has the added benefit of gettering interstitial impurities introduced into the alloy during fabrication. These precipitates are of the form Ti(CON), and effectively remove the interstitial impurities previously mentioned, leading to a reduction in the solid solution hardening experienced by the alloy. The introduction of titanium reduces the dependency of hardness upon impurity level post-annealing, indicating impurities no longer contribute to solid solution strengthening to the same degree [133]. It should be noted that as-melted ingots have very sparse populations of Ti precipitates, and thus the as-melted V-4Cr-4Ti does not experience the benefit of Ti gettering.

The mobility of oxygen within the vanadium matrix is fairly good, assisted further by the addition of chromium, meaning that precipitates begin to form in the region 400-600°C [130], [134]. Ti precipitates have the FCC crystal structure, meaning they are semi-coherent with the underlying bcc vanadium matrix [134], and as a result of this these precipitates preferentially form in-grain so as to maximise coherence [135]. Beyond 600°C the precipitates formed will coarsen and eventually – at temperatures in excess of 900°C – dissolve, releasing gettered impurities back into the matrix. This introduces particular issues regarding the weldability of V-4Cr-4Ti; titanium precipitates in the alloy are dissolved during welding, leading to an increased concentration of impurity localised to the weld. Consequently welds in the alloy are far more brittle than the base alloy, as a high concentration of impurities arrests the motion of dislocations through the weld, reducing ductility [131].

2.4.3.3 V-4Cr-4Ti: Under High Temperature and Irradiation

Base vanadium exhibits excellent high temperature properties, properties that are improved in the V-4Cr-4Ti alloy. Tensile testing of the standard condition (cold rolled and annealed at 100°C for 2 h) V-4Ti-4Cr at elevated temperature demonstrates an initially sharp fall in strength up to ~200°C, followed by stable yield stress (200-300 MPa depending on impurity content) and steadily decreasing elongation from 300°C to 700°C [136]–[139]. Beyond this point, yield stress again falls at temperatures above 800°C with an increased dependency upon strain rate, and this has been attributed to the onset of work softening [140]. These trends are shown graphically in Figure 2.11.

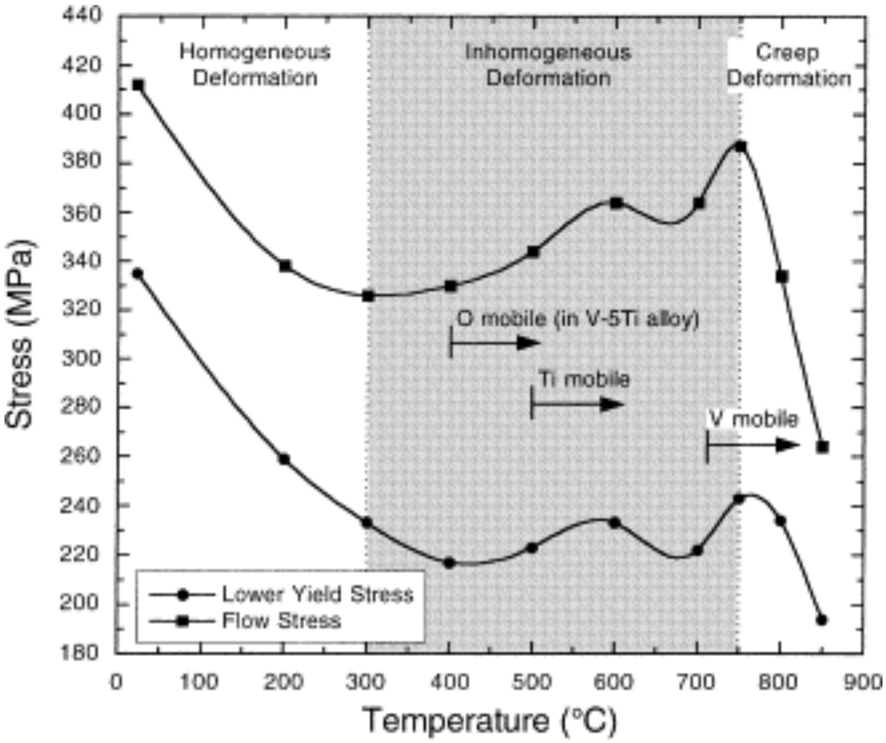

Figure 2.11 Variation of yield and flow stress of V-4Cr-4Ti with test temperature, demonstrating three regimes of deformation, recreated from [138]. *Sample prepared from standard condition plate with impurity content C+O+N 475 ppm, deformed at strain rate* 10^{-3} s^{-1}

Thermomechanical treatment of the alloy has been employed in an effort to improve the strength properties further, solution annealing, ageing, and cold working investigated to control grain size, precipitate size and distribution, and dislocation density. Standard condition V-4Cr-4Ti exhibits mean grain size ~20 um [124], [137], [138], but grain structure can be transformed to ~30 um equiaxed grains by solution annealing at 1100°C for 1 hour and 600°C ageing for 20 hours [137], [141]. Solution annealed aged V-4Cr-4Ti demonstrates higher room and elevated temperature strength than standard condition [137], [141], attributed to the dissolution of coarse Ti(C,O,N) precipitates, reprecipitated as more strengthening finer precipitates. Strength properties were further enhanced by subsequent cold rolling, which introduced higher dislocation densities, and produced an elongated grain structure. Creep testing of the solution annealed aged cold rolled samples demonstrated longer lifetime to fracture than standard condition V-4Cr-4Ti, and a steady creep rate that was the same or lower [137], [142], [143]. In fact, the lowest creep rate was found for samples solution annealed, cold rolled and then aged; dislocations introduced during cold working were decorated by fine precipitates introduced during subsequent ageing, producing a large population of thermally stable dislocations [142], [143]. This is in contrast to the dislocation density of the aged then cold worked sample, which exhibited similar dislocation density to standard condition V-4Cr-4Ti after ageing/creep testing [144], and for which there is a high density of relatively coarse precipitate found at grain boundaries [141].

Cold rolling physically breaks up larger Ti precipitate clusters formed during hot working, removing large precipitates which act as fracture initiation points, and in this way a greater degree of working is thought to improve the ductility of vanadium alloys [130]. However, it has been well recorded that the precipitate distribution produced by cold rolling is directional, leading to bands with a high number density of precipitates. As a result of the dislocation population introduced during cold rolling, precipitate coarsening during annealing is suppressed: precipitate size and distribution stable up to ageing 80 hours at 750°C [144]. The banded distribution of precipitates promotes a banded grain structure - with fine grains being produced during subsequent recrystallisation in areas with high precipitate density following cold rolling and coarse grains elsewhere, demonstrated in Figure 2.12 [105].

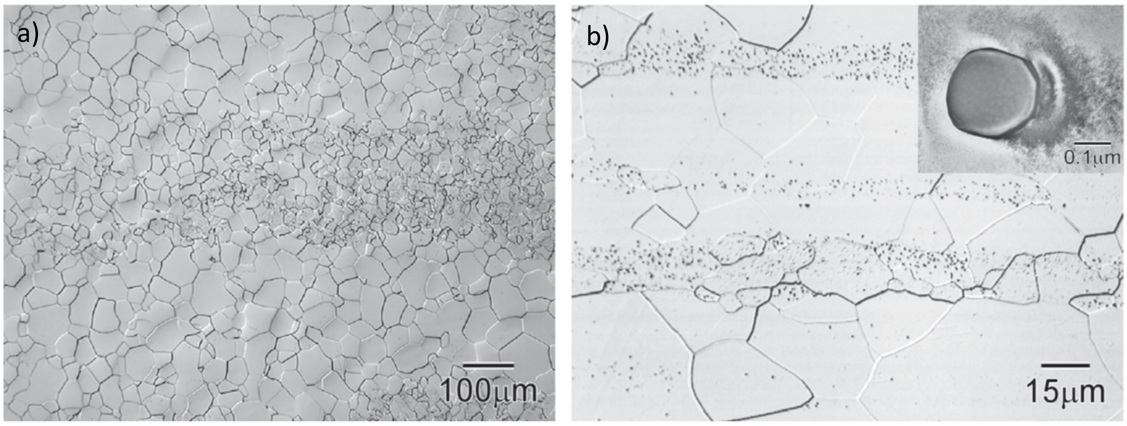

Figure 2.12 Optical metallographic micrographs of V-4Cr-4Ti grain structure demonstrating a) banded grain structure induced by cold rolling, b) banded precipitate distribution in fine grained regions with TEM micrograph of Ti(CON) precipitate inset, after [105]

Neutron irradiation testing of the standard condition USDOE832665 ingot [145] showed the V-4Cr-4Ti alloy to be very sensitive to low temperature neutron irradiation. The DBTT of V-4Cr-4Ti samples was brought to ambient temperature (>0°C) under irradiation temperatures 235-420°C for 0.5 dpa doses [145], [146] with heavy hardening seen around irradiation temperatures of 300°C [145]. At low temperatures the presence of titanium leads to the formation of fine, radiation induced precipitates (RIPs) with interstitial impurities [147]–[150]. The presence of such fine precipitates arrests the movement of dislocations through the alloy, and therefore reduces the ductility of the alloy. These RIPs are conjectured [148] to form as a result of enhanced oxygen uptake by the presence of irradiation induced vacancies, or else due to surface oxide layer dissolution into bulk - RIP prevalence having been found to be largely independent of initial impurity concentration.

In addition, interstitial impurities have been found to stabilise dislocation loops which form in the alloys during irradiation [151]. These dislocation loops act as obstacles to dislocation movement much like the aforementioned impurities and hence lead to alloy embrittlement. By stabilising these loops, impurities both as precipitates and in solid solution contribute to low temperature irradiation embrittlement. The irradiation embrittlement dictates a lower temperature limit to the operating window for V-4Cr-4Ti, whilst susceptibility to thermal creep provides the upper limit. Improving the resistance to creep would allow operation at higher coolant temperatures which would increase reactor efficiency and bring coolant temperatures above the lower window limit. Augmentation of the V-4Cr-4Ti alloy to improve its high temperature properties is therefore an attractive proposition, and one that has received much attention.

2.4.3.4 Improved Vanadium Alloys

Yttrium has proved a focus of vanadium-based alloy research as it allows for the control of grain structure and the generation of thermally stable fine precipitates, beyond what is capable in V-4Cr-4Ti. Yttrium has been investigated both as an addition to V-Cr-Ti based alloys, and as the sole alloying element in V-Y alloys. As a result of yttrium's extremely high oxygen affinity YO_x precipitates form rapidly in yttrium vanadium alloys, and remain stable throughout solidification, acting as nucleation points for grains - leading to a refined grain structure - and preferentially forming over Ti(CON) in the case of titanium containing alloys [152]; leaving titanium to provide solid solution strengthening. As such, yttrium is considered a better getter of interstitial impurities than titanium, resulting in vanadium-yttrium alloys with good ductility, and less susceptibility to irradiation embrittlement. The control of grain size has been shown to have significant effects on the creep behaviour of vanadium alloys; large grains (>10 um) do not effectively mitigate creep as fewer grain boundaries mean fewer arresting sites for dislocations, and small grains (<1 um) allows for creep via grain boundary sliding [153]. One difficulty that has presented itself as to the suitability of yttrium as an alloying element is its effect on Charpy impact upper shelf energy. Yttrium addition to V-4Cr-4Ti at 0.3 wt% was found to degrade the upper shelf impact energy by the formation of larger scale yttrium incursions which acted as fracture initiation points [154], [155]. Ultimately, addition of even trace amounts of yttrium has been shown to produce thermally stable fine precipitates whilst refining the alloy grain structure, and though at larger concentrations fracture susceptibility has increased, this is a promising area of research which bears more scrutiny.

Given their good mechanical strength at high temperatures the other refractory metals may also be considered as potential alloying elements in vanadium alloys [23]. In order to keep radioactivity concerns to a minimum, niobium and molybdenum must be taken out of consideration due to their higher activation, but research has begun as to the effects of other refractory metals. Tungsten has been investigated as a substitute to chromium due to its well reported excellent thermomechanical properties, with the alloy compositions most commonly under investigation being V-6W-1Ti and V-6W-4Ti [156]–[158]. Research in this area has shown that introduction of tungsten improves mechanical properties (yield stress and total elongation) at room temperature whilst having little impact on hardness, and that these alloys experience less age hardening than solution annealed V-4Cr-4Ti [158]. Whilst these results are important, and do suggest tungsten may be a suitable replacement for chromium in vanadium structural alloys, further research is required to determine the effect of tungsten addition on high temperature mechanical properties.

Tungsten is also employed in the design of vanadium alloys utilising the dispersion forming properties of zirconium to produce improved mechanical properties - alloys of the form V-Me(Cr,W)-Zr [159], [160]. The carbides formed by zirconium are on the order of 0.1-0.3 um and have high thermal stability, and as a result of this effectively suppress the recrystallisation of the alloy post-cold working up to temperatures of 1200°C, leading to increased plasticity at low temperature [160]. Further work must therefore be directed towards developing appropriate thermomechanical working to keep this increased low temperature plasticity whilst also gaining the improved high temperature strength induced by recrystallisation.

As has already been discussed, tantalum is a refractory metal with suitable high temperature properties and attractive low activation properties. Historically, V-Ta binary alloys [161]–[166] and V-Ta-Cr ternary alloys [161], [167] have shown excellent retained high temperature strength and good fabricability. Indeed, testing against like compositions the strengthening effect of tantalum addition was shown to be greater than that of chromium or tungsten beyond 900°C [165], V-16Ta creep tested at 700°C recorded creep properties on the order of similarly alloyed V-Ti binary alloys [163], and V-10Ta-10/15Cr alloys exhibited a reduction in tensile strength of only approximately 100MPa between room temperature and 700°C [167]. Recently the possibility of tantalum as an alloying element has begun to attract renewed interest, with new work into the oxidation and thermodynamic properties of V-Ti-Ta alloys [168]–[170], and impact and tensile properties of V-xTa-4Cr-4Ti alloys [171], [172]. This work provides a solid indication that the addition of tantalum is feasible, and in fact may have some unique advantages over currently considered alloys - V-4Ti-7Ta exhibiting better oxidation resistance than V-4Cr-4Ti [168]. The work performed into V-Ti-Cr-Ta alloys thus far has utilised tantalum content 4-35wt%: samples were tested in the as-rolled and annealed state with tensile, hardness, and Charpy impact testing having been reported. The results from this work are extremely promising: tantalum addition has been shown to increase room and elevated temperature strength at all concentrations, increase high temperature elongation, and no increase in DBTT has been observed for content <8 wt% [171], [172]. The addition of low wt% Ta content to V-based alloys therefore remains an open question, with significant promise for improvement over currently considered standards.

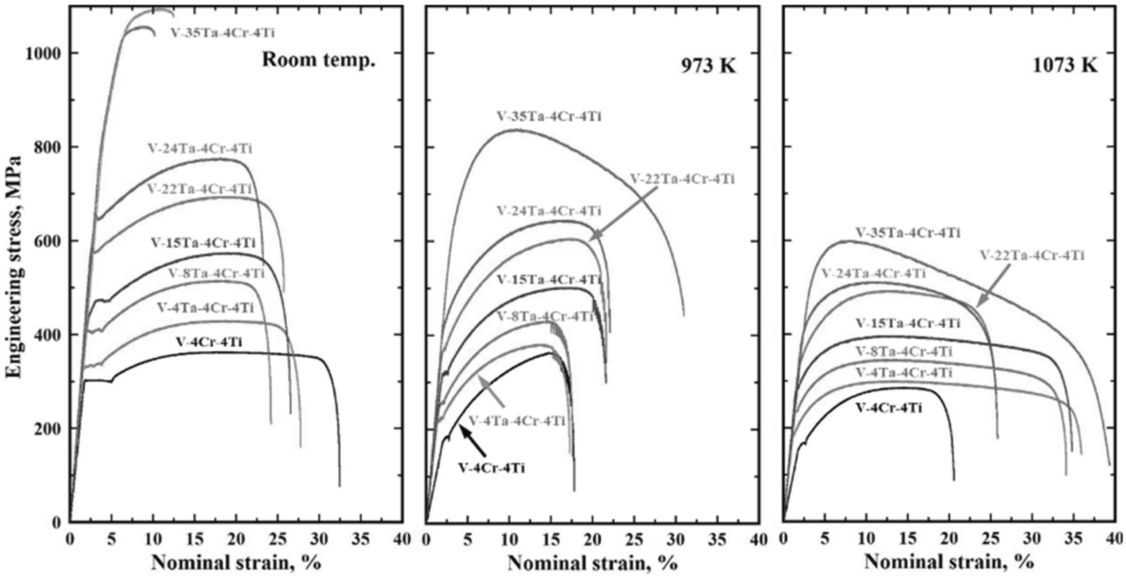

Figure 2.13 Stress-strain curves of V-4Cr-4Ti-xTa alloys at room and elevated temperature, demonstrating high temperature strengthening of even low (4 wt%) Ta content. Recreated from [171]

2.4.3.5 Refractory High Entropy Alloys

In addition to the alloys discussed above, high entropy alloys (HEAs) have recently begun to attract attention as potential structural candidates [173]. By careful consideration of the constituent elements, alloys with excellent composite properties can be produced, this being known as the Cocktail Effect. The diffusion rates allowable through a HEA are greatly retarded by the highly irregular energy landscape. This means the coarsening of precipitates is reduced as diffusion of solute through the matrix is slowed [174], [175], and also increases the tolerance of the alloy to irradiation - equal, low mobilities of interstitial and vacancy induced defects resulting in an increased likelihood of annihilation [176]. In a similar way the variation in atomic size and bonding character moving from site to site produces a large degree of lattice distortion which effectively inhibits the progression of dislocations through the HEA lattice.

As a result of these advantages, several HEA's composed primarily of refractory elements (V, Ta, W, and Cr) have been investigated over recent years [177]–[180], and these alloys have been shown to exhibit highly suitable thermomechanical and irradiation resistant properties. These alloys have exhibited phenomenal high temperature strength, the $V_{35}Ti_{35}Fe_{15}Cr_{10}Zr_5$ alloy produced by Xian et al. [177] demonstrating a yield strength >500 MPa higher than that of V-4Cr-4Ti over reactor operating temperatures. It should be noted also that the presence of vanadium in HEAs has the potential to induce a phase transformation towards BCC from softer FCC, increasing the hardness and reducing the ductility of the HEA [174], [180]. It may therefore be that workability of refractory metal HEAs will prove an issue in the development of this new family of alloys, though preliminary research does not agree on this point [181], [182].

2.5 Synchrotron Characterisation

The candidate structural materials presented exhibit favourable high temperature properties, but in order for critical design decisions to be made, it is crucial that a comprehensive understanding of material behaviour at high temperature be built up. While microstructural characterisation of materials after heat treatment/tensile testing produces helpful results as to the overall effect of high temperature testing, in-situ characterisation allows the evolution of microstructural features to be followed, developing greater understanding of material behaviour. Synchrotron X-ray diffraction (XRD) characterisation has long been used across a wide variety of materials to evaluate dynamic microstructural behaviours, such as phase transformation, lattice strain, and dislocation density evolution.

2.5.1 Synchrotron Radiation

One of the key benefits of synchrotron XRD is that the X-ray beam utilised is high energy, highly penetrating, and highly controllable. High penetration of hard (>50 keV) X-rays into test samples results in diffraction data averaged over large sampling volumes, meaning structural features revealed can be considered representative of bulk material properties [183].

Synchrotron sources produce high energy electron beams with a wide energy spectrum, and in order to produce properly distinct diffraction results, an input X-ray beam with a distinct tuned energy is desired. A tangential X-ray beam of desired energy is diverted from the synchrotron by use of either a) a bending magnet, or b) an insertion device. Bending magnets deflect a “radiation fan” of X-rays with varying energy and some spread of angular deflection. Meanwhile, insertion devices are arrays of magnets which induce oscillation in the path of the electron beam, in so doing removing path bending and producing a tangential X-ray beam. Insertion devices are classified as either “wiggler” or “undulator”; undulators producing a narrowed radiation cone with a sharp, high brightness X-ray spectrum, wigglers producing a large radiation cone and accompanying broad spectrum [184]–[186].

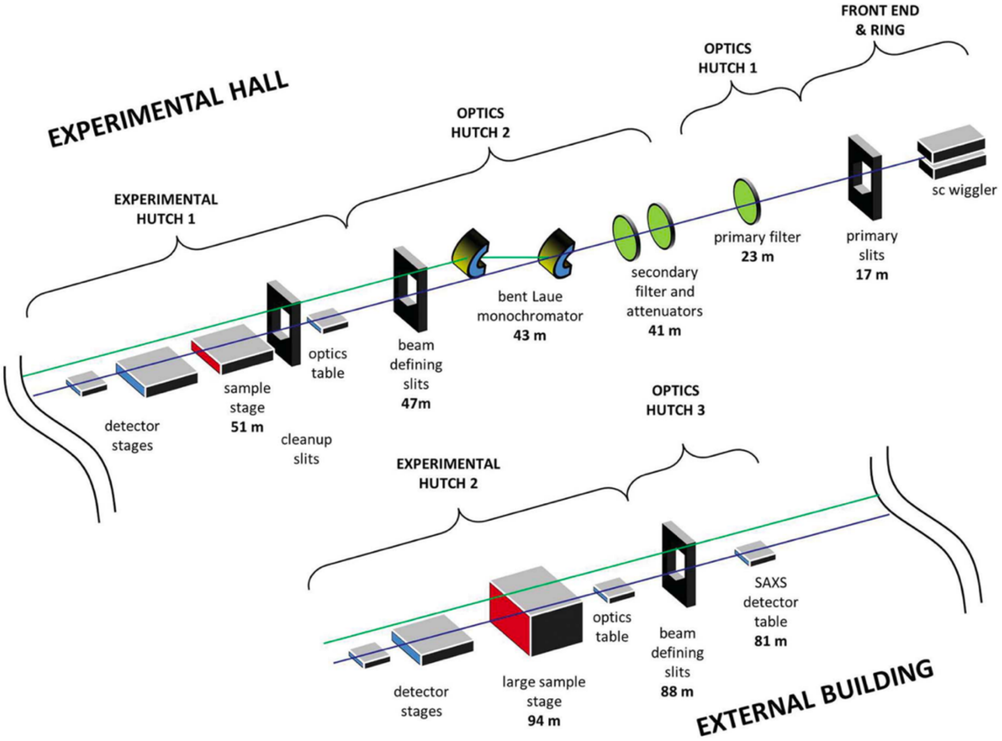

Figure 2.14 Schematic of Diamond Light Source UK’s I12 beamline demonstrating components required for beam refinement and filtering for experimental use. Recreated from [187]

The tangential X-ray beam must then be filtered and refined, requiring a series of slits, filters, and attenuators to strip out undesirable energies, and reduce the beam size. An example of the layout of such beamlines is shown in Figure 2.14, depicting a schematic of the I12 beamline at Diamond Light Source, UK [187].

2.5.2 High Energy X-Ray Diffraction

Synchrotron beamlines give access to a ready source of monochromatic, brilliant, highly penetrating X-rays. Synchrotron radiation offers the opportunity to provide diffraction data across the entire volume of an appropriately sized specimen, the variation of optimal beam energy with sample depth displayed in Figure 2.15. The data acquisition times of X-ray diffraction data is rapid (milliseconds to seconds), and so high energy X-ray diffraction can be used to monitor structural changes within test specimens in-situ. In-situ X-ray diffraction studies have been utilised across a broad range of materials classes, and have been used to evaluate phase changes, load partitioning, and fundamental mechanical properties.

It is well known that each Debye-Scherrer ring of a 2-D diffraction pattern corresponds to diffraction from the same grain family within a polycrystalline sample; the ring being the two dimensional projection of the diffraction cone produced by crystallites with the same orientation relative to the incident beam, but rotated relative to each other [188], [189]. Measuring intensity over specific azimuthal segments of the ring effectively records diffractograms related to specifically oriented grains within the sample, while taking intensity over the whole ring provides diffraction data across the whole polycrystal.

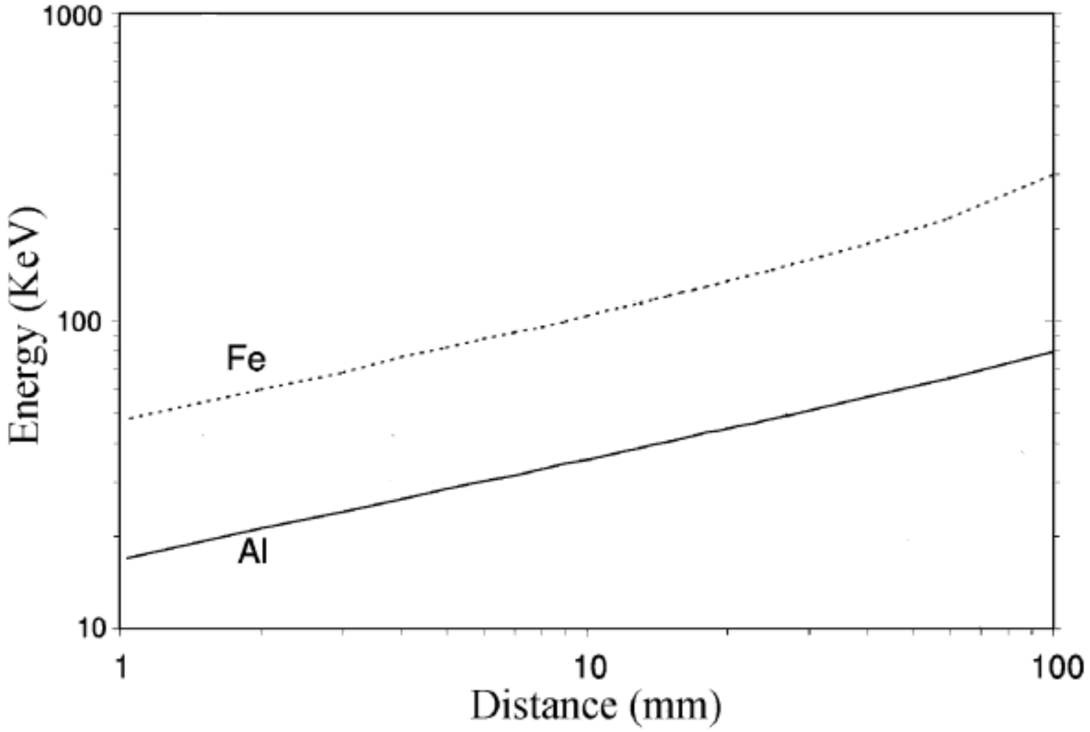

Figure 2.15 Variation of optimal energy with sample thickness for Al and Fe on ID31 synchrotron, assuming a flux independent of energy. Adapted from [190]

In-situ X-ray diffraction is not without its limitations: the requirement for sufficiently fine structure to allow sampling of many grains in polycrystalline materials, results reflecting a homogeneous bulk only with no insight as to inhomogeneity across the volume sampled, and – fundamentally – access to synchrotron facilities is limited. However, the ability to monitor real-time microstructural changes in samples is marks high energy X-ray diffraction as an important characterisation technique to bridge microscopic and macroscopic material response, without the need for extensive sample preparation or limited area of examination encountered during in-situ TEM.

2.5.3 Fundamental Mechanical Properties

The microstructural response to environment (ie temperature, applied load, etc) informs the macroscopic response of the material. Characterisation of microstructural evolution therefore captures, on a fundamental level, the properties that can be expected of the material. Elasticity is a fundamental property of crystalline materials; dictating such important materials considerations as crack propagation, workability, and toughness . The elastic response of a lattice to deformation can be expressed as a fourth rank tensor, which is simplified through symmetry to between 2 and 21 independent elements [191], [192], each component corresponding to orientational deformation experienced by the lattice based on differently oriented applied stresses. In the case of cubic crystals (such as ferrite, refractory metals, etc) the elastic tensor is symmetrically reduced to three components: C_{11}, C_{12}, and C_{44}.

Given their orientational dependencies, the single crystal elastic constants can be determined from the differing mechanical response of varyingly oriented grains in polycrystalline samples. The deformation behaviour of particularly oriented grains can be determined by analysis of specific sections of the Debye-Scherrer rings. Azimuthal segments parallel and perpendicular to the direction of macroscopic load are evaluated, and from the lattice strain-stress curves revealed, diffraction elastic constants are obtained. Several models have been suggested over the years relating diffraction elastic constant and grain family anisotropy parameter to the fundamental single crystal elastic constants [193]. Single crystal elastic constants are utilised in the calculation of bulk polycrystal elastic properties (bulk modulus, shear modulus, Poisson’s ratio) and the modelling of microstructural evolution under strain, phase change, etc [194]–[196].

In addition, XRD analysis allows measurement of the magnitude and character of dislocation density within polycrystalline samples. Broadening of diffracted peaks comes about as the result of crystallite size, systematic instrument broadening, and dislocation induced distortion [197], [198]. The dislocation contribution accounts for anisotropic peak broadening, and so by means of the peak width, details of the dislocation population can be estimated.

In-situ XRD therefore provides characterisation of materials properties fundamental to deformation behaviour. Temperature and stress induced changes in deformation behaviour must be appropriately considered in the extreme environment of a fusion reactor, and it is this information that in-situ XRD characterisation can provide.

2.6 Dislocation Moderated Plasticity

Dislocation population has important consequences for deformation, which is very sensitive to the ease of movement of dislocations through a material. Dislocation density evolution is therefore interesting behaviour to characterise, with important consequences as to material strength and ductility. Dislocation density character in BCC materials has recently been linked to the DBTT [199]–[201], dislocation density is commonly used in evaluating strengthening contributions within materials [202], [203], and microstructure induced changes in ease of deformation have been investigated through evaluation of the dislocation density [204]–[206]. This section presents the fundamental characteristics and mechanisms of dislocation, and how these properties are used to model plastic response through numerical modelling.

2.6.1 Characteristics and Movement of Dislocations

On their most fundamental level dislocations are characterised by two important parameters: Burgers vector and line direction, these describing the magnitude and direction of lattice distortion induced by a dislocation, and the bottom line of the half-plane introduced into the perfect lattice by the dislocation respectively. The Burgers vector is described by the Burgers circuit – the deviation from closure when a circuit which fully encircles the dislocation in the deformed crystal is applied to the ideal crystal. Fundamental dislocation types are illustrated in Figure 2.16, edge dislocations exhibit Burgers vector perpendicular to line direction, whilst screw dislocations exhibit Burgers vector parallel to line direction. In reality dislocations will generally present mixed character and largely do not exist as purely edge or screw.

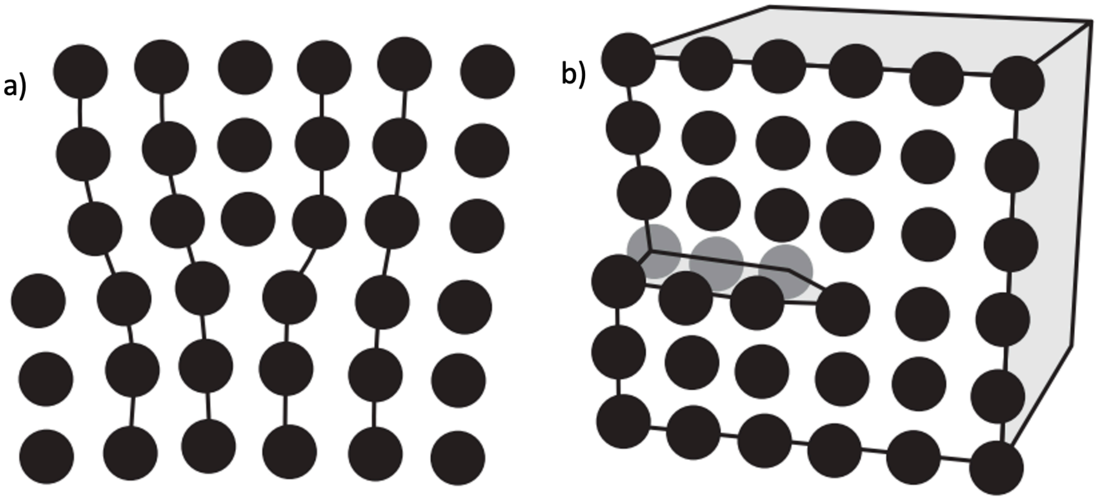

Figure 2.16 Schematic structure of dislocations of the a) edge type and b) screw type within a perfect lattice adapted from [207]

Dislocations may move by conservative (glide) or non-conservative (climb) motion – so called as glide does not produce a net change in volume (volume conserved), whilst climb progresses by incorporation of point defects and so does produce a change in volume (volume not conserved). Glide progresses across surfaces containing both Burgers vector and dislocation line direction; edge dislocation movement is therefore limited to slip planes (preferentially following close-packed planes to minimise slip step size), whilst screw dislocation slip is not constrained to a specific slip plane as the parallel characteristic vectors do not describe a unique plane. The less constrained nature of screw glide allows screw dislocations to switch glide planes by cross-slip. Climb progresses by migration of point defects to the dislocation line allowing movement outside slip planes, and is thus driven by thermal diffusion.

2.6.2 Dislocation Based Plasticity Modelling

Understanding dislocation behaviour on a mechanistic level allows change in dislocation population, and hence plastic deformation behaviour to be modelled. The kinematic basis of dislocation-based crystal plasticity modelling arises from a decomposition of the deformation gradient (*F*) into elastic (subscript *E*) and inelastic (subscript *P*) contributions [207]–[209] (demonstrated graphically in Figure 2.17), such that:

$$\boldsymbol{F} = \boldsymbol{F}_E \cdot \boldsymbol{F}_P \tag{2.6}$$

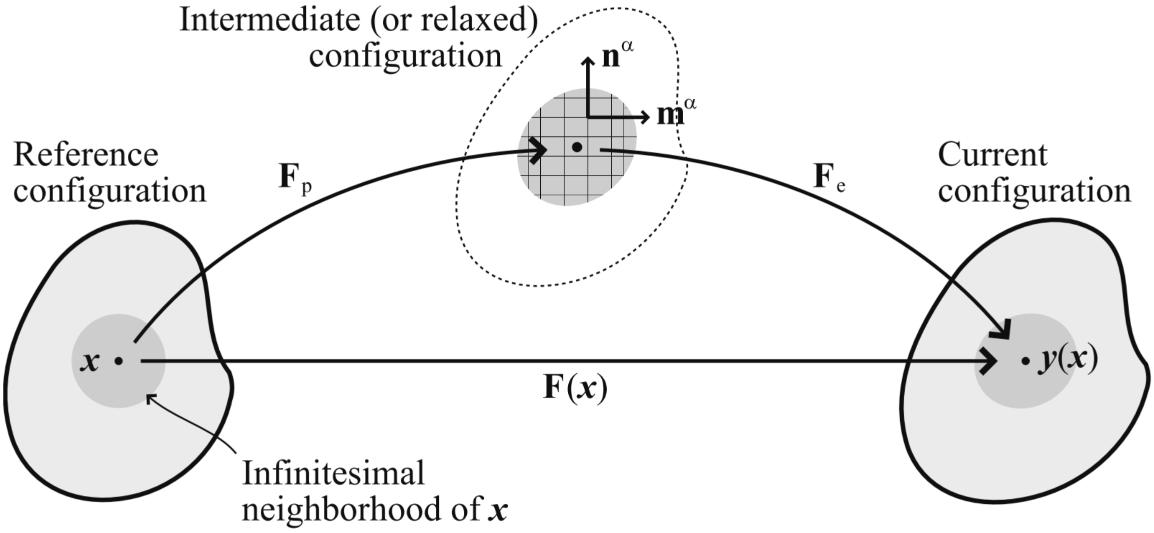

Figure 2.17 Decomposition of shape deformation into elastic reversible deformation and plastic irreversible deformation adapted from [208]

In order for models to consider evolving plastic deformation, an expression for rate of change of deformation through time must be formulated, expressed as

$$\dot{\boldsymbol{F}}_P = \boldsymbol{L}_P \boldsymbol{F}_{\boldsymbol{P}} \tag{2.7}$$

Where the L_P term is the plastic component of spatial gradient of total velocity. The simplest evaluation of this term assumes dislocation movement by slip only, considering the total velocity spatial gradient term as the sum of slip across all active slip planes. The L_P term is therefore formulated as

$$\boldsymbol{L}_P = \sum_{S} \dot{\gamma}_S \boldsymbol{m}_S \otimes \boldsymbol{n}_S \tag{2.8}$$

Where $\dot{\gamma}$ is the shear rate, *m* is a unit vector describing the slip direction, and *n* is a unit vector describing a normal to the slip plane, all for a given active slip plane, *S*.

In order for evolution of plastic deformation to be assessed, it is therefore necessary that an expression for shear rate be established. Approaches to evaluate the shear rate vary, common approaches being:

a) Phenomenological, based on power law relations, of the kind [209]:

$$\dot{\gamma}_S = \dot{\gamma}_0 \left|\frac{\tau_S}{g_S}\right|^n \operatorname{sign}(\tau_S) \tag{2.9}$$

where τ is the resolved shear stress on the system, *g* is the resistance to shear slip, $\dot{\gamma}_0$ and *n* are materials parameters controlling reference shear rate and rate sensitivity of slip respectively.

b) Physics-based, based on the Orowan equation [210]:

$$\dot{\gamma}_S = {\rho_S}^m b v_S \tag{2.10}$$

Where ρ^m is the mobile dislocation density, *b* is the Burgers vector, and *v* is the average dislocation velocity.

Phenomenological and physics-based crystal plasticity models are built up from the simple basis described above through equations which capture the complex competing microstructural relationships within deforming samples: hardening components (*g*) in the case of phenomenological models, and dislocation population characteristics (ρ and *v*) in the case of physics-based models. Focussing on physics-based models, a wide variety of formulae for dislocation velocity are utilised across literature, the dislocation velocity depending upon many variables: resolved shear stress, dislocation density, and temperature [210]. Formulas for dislocation velocity most often take a power law or hyperbolic function based formulation - when forest dislocation cutting is taken as the rate-determining process, the equation takes the form [208]:

$$v = v_0 \exp\left(-\frac{Q}{k_B T}\right) \sinh\left(\frac{\tau_{eff} V}{k_B T}\right) \operatorname{sign}(\tau) \tag{2.11}$$

Where v_0 is a velocity factor describing dislocation movement attempt frequency and distance, Q is the activation energy of dislocation movement, V is the activation volume, and τ_{eff} is the effective shear stress. The effective shear stress is zero below the passing stress (minimum stress which is capable of producing plastic deformation), reflecting the transition in shear strain rate dependency from the thermal activation to viscous glide regime. Mobile dislocation population should not be treated as a static figure, and dislocation density evolution is captured through combinations of rate equations. In order to incorporate the different mechanisms by which dislocations migrate and interact, these rate equations may include different terms for:

- contributions for edge and screw dislocations [211], [212]
- rates of nucleation, multiplication, and annihilation [213]
- rates of dislocation immobilisation and release [214]

In this way, sophisticated numerical models for plastic deformation of materials can be built up, validity of such models being dependent on availability of high quality microstructural data to define model parameters. The preceding relations concern slip plane specific shear strain, and as quoted in equation (2.8), plastic deformation requires summation of effects over all active slip planes. As a consequence of this, the orientation distribution of polycrystalline aggregates is a necessary model parameter; macroscopic yield predicted in polycrystalline samples arising after a sufficient proportion of grains have experienced micro-yield behaviour dependent upon their orientation relative to applied load.

Other insight into dislocation behaviour may be granted by modelling based upon relaxation behaviour. Even in the absence of external applied load, at high temperature dislocations move and annihilate in a process known as recovery. Recovery is an important process during thermo-mechanical treatments, producing anelastic strains during sample unloading which can threaten component precision during multi-pass working [215]. Modelling of dislocation recovery uses exponential or hyperbolic function based thermal activation rate equations, of the type suggested by Verdier [216] and Friedel [217]. These relationships are controlled by different factors dependent upon the mechanisms involved with dislocation movement – characterised not only by activation energies, but also activation volumes which described the volume of material associated with elementary recovery events. The modelled dislocation behaviour then communicates directly with material softening through the dislocation forest type hardening term included in constitutive consideration of flow stress described by:

$$\sigma = M\theta G(T)b\sqrt{\rho} \tag{2.12}$$

where $G(T)$ for a given test temperature M is the Taylor factor, θ is a constant parameter, b is the Burgers vector modulus, and ρ is dislocation density. Characterisation of fundamental microstructural parameters again allows for modelling of complex material response to deformation which could otherwise have unforeseen consequences for component design. Physically based modelling of static softening has been used in investigating microstructural behaviour for aluminium alloys during repeat loading/unloading [215], [218] and cold rolled iron and steel undergoing annealing (in a static state and under stress) [219]–[221], results being used to characterise the effect of factors including alloy composition and pre-strain on softening behaviours. Modelling of dislocation population evolution under loading/unloading using only recovery considerations is the least complex approach reported in literature [221], as loading/unloading also introduces more complex dislocation dynamics (the most notable of these being back-stress induced by piling of dislocations at grain boundaries) which may be captured in more sophisticated models.

Synchrotron high energy x-ray diffraction of tensile samples is extremely well suited to inform and validate crystal plasticity modelling results. As has been discussed in Section 2.5 Synchrotron Characterisation, in-situ synchrotron x-ray diffraction results provide means of experimentally observing strain partitioning between differently oriented grains during deformation, as well as dislocation population evolution, and fundamental elastic parameters. Combination of experimentally determined and crystal plasticity modelled microstructural plasticity provide improved insight into deformation mechanisms. Strong synergy between results of synchrotron diffraction experiments and crystal plasticity modelling is supported by Erinosho et al's 2016 work [222], in which the lattice strain-stress response captured for low carbon ferritic steel undergoing biaxial deformation is compared to the results of crystal plasticity modelling. The strong agreement between the reported results leads the authors to propose that experimental work might be used to validate and/or calibrate crystal plasticity parameters. This approach has been adopted in recent years: Chen et al's 2019 work

[223] uses comparison of single crystal elastic properties and lattice strain-stress response to assess modelled results, and Cheng et al's 2024 work [224] uses lattice strain-stress response to calibrate the hardening parameters which inform the resistance to shear slip term in Equation (2.9). This comparison allows deformation mechanisms to be characterised in the former work (compatibility of experimental results with and without back-stress is used to evaluate this mechanism's importance), and produces a model which is able to assess partitioning of stress about different phases and can more accurately predict textural evolution in the latter work. Stress distribution about alloy phases predicted by crystal plasticity modelling and supported by synchrotron diffraction experimentation has also been used to investigate the onset of cracking in duplex transformation induced plasticity steels [225], this leading to more detailed understanding of residual stress in differently drawn samples. Ultimately, marriage of detailed experimental results and physically sound modelling can be expected to produce good accuracy predictions of materials under complex loads, and such predictions are sorely needed in industry to support component design and implementation.

2.7 Summary

Nuclear fusion has become a focus of significant research and collaboration the world over, involving multiple projects to bring commercial fusion energy to reality. The challenging environment involved in a fusion reactor presents significant materials design challenges, particularly when considering the structural material used in breeder blanket design – a vital component to allow energy extraction. As fusion projects progress, several classes of candidate material have gained attention: reduced activation ferritic martensitic steels (notably EUROFER97), oxide dispersion strengthened RAFM steels (notably ODS EUROFER97), and refractory alloys (notably V-4Cr-4Ti). A complete understanding of material properties is desirable to inform future design choices, and in-situ XRD provides characterisation of fundamental elastic properties and microstructural characteristics which inform strengthening mechanisms. Further, whilst these materials all demonstrate high temperature strength to varying degrees, increasing candidate material's resistance to thermal creep will enable higher coolant operating temperatures, and hence higher efficiency. Microalloying of vanadium alloys with other low activity refractory metals is a field which is enjoying renewed interest and may yield alloys with extraordinary high temperature properties. Global effort to realise nuclear fusion's promise of clean renewable energy is at a crucial stage, and materials design and characterisation is needed in the path to optimise structural material high temperature properties.

CHAPTER 3 IN-SITU SYNCHROTRON INVESTIGATION OF THE ELASTIC AND TENSILE PROPERTIES OF OXIDE DISPERSION STRENGTHENED EUROFER97 STEEL

Tay Sparks[a], Michael Gorley[b], Jan Hoffmann[c], Yu-Lung Chiu[a], Thomas Connolley[d], Michael Rieth[c], Yiqiang Wang[b*], Biao Cai[a*]

[a]School of Metallurgy and Materials, University of Birmingham, Birmingham, UK

[b]UK Atomic Energy Authority, Culham Science Centre, Abingdon, Oxfordshire OX14 3DB, UK

[c]Institute for Applied Materials, Karlsruhe Institute of Technology, Karlsruhe, Germany

[d]Diamond Light Source Ltd, Harwell Science and Innovation Campus, Didcot, UK

Published at Acta Materialia, Volume 271, June 2024, 119876
https://doi.org/10.1016/j.actamat.2024.119876

(Revisions requested during review at Acta Materialia enacted after original thesis submission, which have not substantively altered results and discussion are not included)

Tay Sparks completed experimental work, analysed the data, and wrote and revised the manuscript. Biao Cai and Yiqiang Wang conceived and designed the experiment, assisted in experimental work, revising the manuscript and data analysis. Yu-Lung Chiu and Thomas Connolley assisted in experimental work and reviewing the manuscript. Jan Hoffmann and Michael Rieth provided materials for experimental work and assisted in reviewing the manuscript. Michael Gorley assisted in conceiving and designing the experiment and reviewing the manuscript.

3.1 Abstract

The augmentation of mechanical properties of reduced activation ferritic martensitic steels through the introduction of creep resistant nano-oxide particles produces a class of oxide dispersion strengthened steels, which have attracted significant interest as candidates for first wall supporting structural materials in future nuclear fusion reactors. In the present work, the effect of temperature on the elastic properties and micro-mechanics of 0.3 wt% Y_2O_3 oxide dispersion strengthened steel EUROFER97 is investigated using synchrotron high energy X-ray diffraction in-situ tensile testing at elevated temperatures, alongside the non-oxide strengthened base steel as a point of comparison. The single crystal elastic constants of both steels are experimentally determined through analysis of the diffraction peaks corresponding to specific grain families in the polycrystalline samples investigated. The effect of temperature on the evolving dislocation density and character in both materials is interrogated, providing insight into deformation mechanisms. Finally, a constitutive flow stress model is used to evaluate the factors affecting yield strength, allowing the strengthening contribution of the oxide particles to be assessed, and correlation between the thermally driven microstructural behaviour and macroscopic mechanical response to be determined.

Keywords: ODS ferritic steel; Elastic Properties; X-ray synchrotron radiation; Tensile testing; Mechanical properties (high-temperature deformation)

3.2 Introduction

Identifying and optimising suitable candidate structural materials for use in nuclear fusion reactors is a key area of study to help realise the promise of clean, reliable fusion energy in the years to come. EUROFER97 (E97) was developed within the EU as a candidate reduced activation ferritic martensitic (RAFM) steel with stable high temperature mechanical properties. The basis of EUROFER97's design is the addition of small percentages of refractory metals (V/Ta/W) to augment high temperature mechanical properties, addition of chromium to enhance corrosion resistance, and avoidance of undesirable microalloying contents (Nb/Co/etc) to maintain a low activation elemental composition [41], [226], [227]. As a result of these attractive characteristics, EUROFER97 was selected as the structural material for test blanket modules (TBMs) in ITER [228], and is extensively used as the structural material in DEMOnstration Fusion Power Reactor (DEMO) TBM concepts [31], [229]. The limitation facing the adoption of EUROFER97 in reactor structural designs is the limited operating temperature window over which the steel maintains robust mechanical integrity, the maximum application temperature of EUROFER97 being 550°C [230].

The operating temperature limit of EUROFER97 has been shown to be increased through control of precipitates distributed throughout the sample. These approaches have yielded two classes of advanced structural steels: castable nanostructured alloys (CNA's), and oxide dispersion strengthened (ODS) steels. The precipitates introduced in both CNA's and ODS steels are thermally stable [81], [231] particles which act as dislocation/grain pins and in so doing increase mechanical strength and reduce susceptibility to thermal creep [86], [231], [232]. Precipitates utilised in CNA's are V/Ta rich MX carbides/carbonitrides; these precipitates, present even within standard RAFMs, are distributed both at grain boundaries (alongside larger $M_{23}C_6$ carbides) but also within martensite laths [42]–[44]. Heat treatment can be employed to enhance CNA's MX precipitate distribution.

ODS steels, meanwhile, introduce a non-native precipitate – yttrium oxide nanoparticles – during fabrication most commonly by hot isostatic pressing of yttrium oxide and steel powders, producing alloys with diffuse populations of yttrium oxide nanoparticles, and small grain size [233]. The maximum application temperature of ODS EUROFER97 is at least 100°C higher than that of EUROFER97, reported as 650°C [35], [234]. Only small Y_2O_3 concentrations are required to achieve this augmentation; additions of 0.3 wt% and 0.5 wt% are commonly used [35], [235]–[237]. Both of these concentrations produce similar improvements in alloy tensile properties, although the increased strength with increasing yttria content is offset by degraded impact properties [237], and steels with higher ODS concentrations have reported significantly lower impact energy and strain to fracture at room temperature [238], [239]. Indeed, whilst the introduction of ODS particles strengthen the tensile properties of the alloy, their presence causes a rise in the ductile to brittle transition temperature [233], [240] and increased anisotropy in the alloy's mechanical response [241], [242]. Such properties have important consequences for structural design. Therefore, it is imperative to fully understand the effects of ODS particle strengthening on alloy mechanical response under representative operating conditions. This work is on-going.

High energy synchrotron X-ray diffraction (HE-XRD) has been widely used to interrogate microstructural properties such as phase information [243] and lattice parameters [244], and in-situ tensile testing can be utilised to evaluate the crystallographic response to mechanical load – characterising lattice strain, crystallographic anisotropy, and dislocation density. When used in conjunction with other characterisation techniques such as Electron Backscatter Diffraction (EBSD) and Scanning Electron Microscopy (SEM), in-situ HE-XRD tensile testing offers the ability to determine the effect of ODS on each component of the constitutive flow model. HE-XRD analysis of similar ODS RAFM steels was successfully employed to characterise elastic properties and dislocation behaviour [245]–[249], but to the best of our knowledge this important analysis has not been applied to EUROFER97. Similarly constitutive flow analysis was used to investigate the relative strengthening effects governing the ultimate strengthening power of ODS [75], [250]–[252], but such evaluation often relies extensively on existing literature data for elastic and dislocation properties. Together these points represent significant novelty – evaluation of the fundamental strength behaviour of a promising future structural material through in-depth characterisation of important structural properties.

In this work, HE-XRD is used in-situ to characterise the evolving microstructure of EUROFER97 and ODS EUROFER97 samples undergoing tensile testing at elevated temperature. The XRD results produced are used to characterise the single crystal elastic constants (SCECs), bulk elastic response, and elastic anisotropy of both alloys with increasing temperature. Further, differences in the evolution of dislocation density character during loading at varied temperatures are investigated by means of the modified Williamson-Hall relation. Finally, the properties investigated are used to evaluate the varying weight of individual strengthening contributions, considered through constitutive flow analysis. In this way, the work presents a comprehensive analysis of the effects of ODS particles on the EUROFER97 steel, which can inform future modelling and design decisions through determination of material elastic properties and dislocation behaviour.

3.3 Materials and methods

3.3.1. Materials and microstructure characterisation

The EUROFER97 and ODS EUROFER97 used in this research was provided by the Karlsruhe Institute of Technology in plate form. The elemental composition of each alloy is detailed in Table *3.1*, and a full description of the fabrication process conducted can be found for EUROFER97 in Wang et al's work [253], and for the ODS EUROFER97 in Renzetti et al's work [254].

The grain structure of both alloys was investigated using EBSD mapping applied over a 125µmx150µm area in undeformed samples at room temperature. The EBSD work employed an accelerating voltage of 20 kV, at a working distance of 15 mm, with step size 0.25 µm, and was performed using a TESCAN Mira3 Field Emission Gun Scanning Electron Microscope (SEM), with EBSD system controlled using the Oxford Instruments Aztec software. Subsequently, a second EBSD map of the undeformed ODS EUROFER97 sample was collected over a 250µmx100µm area using accelerating voltage 20keV, working distance 15 mm, and step size 0.4 µm, in order to evaluate coarser grains, inadequately sampled in the first map. Grain analysis of all EBSD data was performed using the MTEX software [255], [256], grain size was calculated using the Heyn Lineal Intercept Procedure presented in ASTM Designation E112-13 [257], and wider grain statistics were considered, weighted by contribution to total map area.

Table 3.1 *Elemental composition of supplied EUROFER97 and ODS EUROFER97 plates, provided as wt%*

Alloying element	EUROFER97	ODS EUROFER97
Cr	8.95	8.92
W	1.06	1.11
Mn	0.55	0.41
V	0.202	0.193
Ta	0.12	0.08
C	0.11	0.07
Si	0.03	0.11
Mo	0.005	0.037
Y_2O_3	-	0.3

3.3.2 In-situ synchrotron XRD experiments

Synchrotron two-dimensional X-ray diffraction was conducted in-situ at the I12 beamline of Diamond Light Source, Rutherford Appleton Laboratory (Oxfordshire, UK) [187] during mechanical testing of these samples in an Instron Electro-Thermal Mechanical Testing (ETMT) unit at room temperature (RT), 400°C, 550°C, and (in the case of ODS EUROFER97) 650°C. A schematic representation of experimental set-up is shown in Figure 3.1. Tensile dog-bone samples, gauge size 7.62×1.52×0.76 mm were cut via wire electron discharge machining from the supplied alloy plates, and ground to a fine surface finish using 1200 grit silicon carbide paper. All tests were performed in an inert atmosphere of argon, and temperature was monitored through a type R thermocouple, spot welded to the edge of each sample. Tensile tests were displacement controlled, with a strain rate of 0.0008 mm/s monitored using a linear variable differential transformer (LVDT). A strain gauge was not used over the experiments recorded, and so it must be noted that engineering strain quoted is a nominal value only, and may be subject to instrumental error through the effects of frame compliance, particularly at low loads. Strain rate is similarly subject to error, though over the course of the test it is expected actual strain rate should average to the reported value. Repeat load controlled tensile tests with a load rate of 1.5 N/s were conducted for selected samples: EUROFER97 at RT and 550°C, and ODS EUROFER97 at RT. Diffraction patterns were collected using a large-area (42 × 42 cm) 2D Thales Pixium RF4343 detector with 2880 × 2881 pixel (each pixel 148 × 148 µm), each pattern requiring a capture time of 1 s. The size of the monochromatic beam was 0.5 × 0.5 mm^2, with a beam of energy 80.03 keV (wavelength 0.015 nm). The beam energy, sample-detector distance and detector tilts required for diffraction pattern analysis were determined from patterns of a CeO_2 reference sample (NIST Standard Reference Material 674b). Calibration was performed in DAWN software [258]–[260].

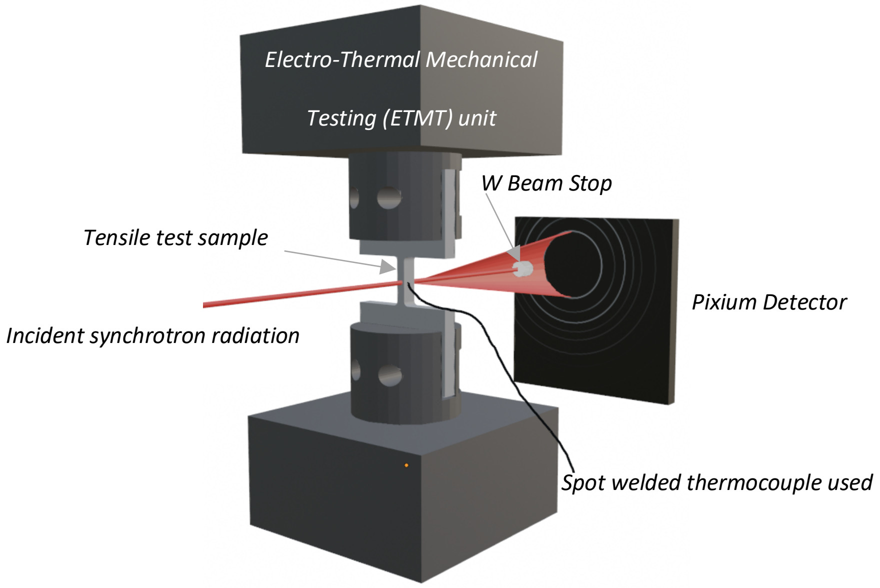

Figure 3.1 Schematic representation of in-situ synchrotron XRD experimental set-up

3.3.3 X-ray diffraction data processing

Data collected from these experiments were analysed using the DAWN Science visualisation and processing software [258]–[260] in conjunction with the MATLAB data analysis software for peak fitting, and the ANIZC software [261] for dislocation contrast factor determination.

3.3.3.1 Diffractogram peak fitting

Each 2D XRD pattern was converted to two diffractograms through integration of the pattern intensity in DAWN over two perpendicular 30° increments, one of which captured the diffracted beam in the direction of load, one the diffracted beam perpendicular to the loading direction.

Using MATLAB, a Pseudo-Voigt function was then employed to fit the diffraction peaks of each diffractogram recorded, allowing peak central position and full width half maximum to be recorded with varying macroscopic stress and strain. The Pseudo-Voigt function is a convolution of a Gaussian and Lorentzian function, and is of the form:

$$I(x) = I(0)\cdot\left[\mu_G\cdot e^{-\pi\frac{(x-x_0)^2}{\beta_G^2}} + \left(1-\mu_G\right)\cdot\frac{1}{\frac{\beta_C^2}{\pi^2}+(x-x_0)^2}\right] + h_0 \tag{3.1}$$

Where *I(x)* is the intensity, μ_G is the fraction of the convolution accounted for by the Gaussian model, x_0 is the peak centre, $\boxed{\beta_G}$ and $\boxed{\beta_C}$ are constants associated with the Gaussian and Lorentzian fits respectively, and h_0 is the background intensity.

3.3.3.2 Lattice strain evolution

Having established the peak central positions for each diffraction pattern capture, grain family lattice strain was determined through observation of the shift in diffractogram peak positions over the course of deformation. The grain family strain is calculated using the equation:

$$\varepsilon_{hkl} = \frac{q_{hkl}^0}{q_{hkl}} - 1 \tag{3.2}$$

Where ε_{hkl} is the lattice strain experienced by the {h,k,l} indexed grain family, q_{hkl} is the diffractogram peak position (in Å^{-1}) under strain, and q_{hkl}^0 the diffractogram peak position prior to load being applied. Analysis of the XRD pattern produced parallel to the load direction allowed the lattice strain of the sample under tension to be determined, whilst analysis of the pattern perpendicular to load determines the evolution of lattice strain under compression.

3.3.3.3 Single Crystal Elastic Constant (SCEC) calculation

The differing lattice strain-stress behaviour of individual grain families can subsequently be used to determine the material's single crystal elastic constants (SCECs). Several methods have been suggested to evaluate the SCECs in this way, but the model that most successfully accounts for orientation dependencies is the Kroner model [193], which is of the form:

$$G_{hkl}{}^{3} - \alpha G_{hkl}{}^{2} - \beta G_{hkl} - \gamma = 0 \tag{3.3}$$

Where $G_{h,k,l}$ is the diffraction modulus, and $\alpha, \beta,$ and γ are constants dependent upon the single crystal elastic constants, such that

$$\alpha = \frac{1}{5}(2\eta + 3\mu) - \frac{3}{8}(3K_M + 4(\mu + 3(\eta - \mu)A_{hkl}) \tag{3.4}$$

$$\beta = \frac{3}{40}(6K_M\eta + 9K_M\mu + 20\eta\mu) - \frac{3K_M}{4}(\mu + 3(\eta - \mu)A_{hkl}) \tag{3.5}$$

$$\gamma = \frac{3K_M\eta\mu}{4} \tag{3.6}$$

These equations being expressed in terms of the cubic shear moduli ($\mu \; and \; \eta$), the bulk modulus (K_M), and the elastic anisotropy factor (A_{hkl}) defined below:

$$K_M = \frac{1}{3}(c_{11} + 2c_{12}) \tag{3.7}$$

$$\eta = \frac{1}{2}(c_{11} - c_{12}) \tag{3.8}$$

$$\mu = c_{44} \tag{3.9}$$

$$A_{hkl} = \frac{h^2k^2 + k^2l^2 + h^2l^2}{(h^2 + k^2 + l^2)^2} \tag{3.10}$$

Where c_{11}, c_{12}, and c_{44} are the material's SCECs, and *h, k,* and *l* are the principle numbers indexing the grain families considered. In conjunction with the relation in Equation (*3.3*), the following Kroner model equations relating diffraction shear modulus to the experimentally determined diffraction elastic constants, E_{hkl}, and diffraction elastic ratios, ν_{hkl}, were used as a basis for data fitting.

$$\frac{1}{9K_M} - \frac{1}{6G_{hkl}} = -\frac{\nu_{hkl}}{E_{hkl}} \tag{3.11}$$

$$\frac{1}{G_{hkl}} = 2(\frac{1}{E_{hkl}} + \frac{\nu_{hkl}}{E_{hkl}}) \tag{3.12}$$

From these relations it was possible to evaluate the single crystal elastic constants, using MATLAB to fit the ${}^{\nu_{hkl}}/_{E_{hkl}}$- A_{hkl} and ${}^{1}/_{E_{hkl}}$- A_{hkl} relationships.

3.3.3.4 Dislocation density analysis

The dislocation density was correlated to the diffractogram peak broadening through the modified Williamson-Hall (mWH) relation [197], [198], which considers the full width half maximum (FWHM) of diffractogram peaks primarily as the product of strain broadening and size effects, as shown in the Equation (*3.13*):

$$(\Delta K)^2 \approx \left({}^{0.9}/_{D_0}\right)^2 + \frac{\pi m^2 b^2 K^2}{2} \cdot \rho C \pm O(K^4C^2) \tag{3.13}$$

Where ΔK is the peak FWHM, D_0 is the average domain size, m is the effective outer radius of dislocations, K is the peak position, ρ is the dislocation density, and C is the contrast factor of the grain family. The $O(K^4C^2)$ term refers to non-interpreted higher order terms which are considered weak relative to the size and strain terms. When modified by the contrast factor as per equation (3.13), the FWHM is therefore expected to vary linearly with peak position, with the y-intercept dependent upon particle size, and the gradient of the mWH curve directly proportional to the dislocation density. The parameter m was taken as 2, as has been successfully used in previous work [245], and the Burgers vector, b, was calculated from the lattice parameter of the alloy, further discussed in Section 3.3.

The contrast factor of dislocations with each grain family was calculated from the single crystal elastic constants previously determined, using the ANIZC software [261]. The contrast factor is dependent not only upon grain family diffraction vector, but also dislocation type, and for this reason the contrast factors relating to edge <111>{110} and screw <111> dislocations were calculated. The actual strain contribution should be the sum of the broadening effect of edge dislocations and screw dislocations, and so the contrast factor used should be a combination of the contrast factors calculated in proportion to their relative population, and, in fact, this allows for the dislocation character as well as total dislocation density to be approximated through the mWH plot.

3.4 Results and discussion

The results presented here encompass first the simple mechanical properties derived from the tensile testing of the ODS-EUROFER97/EUROFER97 samples, then the effects of temperature on the crystal lattice of the samples gathered from the diffraction data prior to load, followed by an evaluation of the elastic and microstructural changes induced by load at varying temperature, and finally examine the cumulative stress components which contribute to yield stress differences between the two materials at varying temperature.

3.4.1 Microstructure

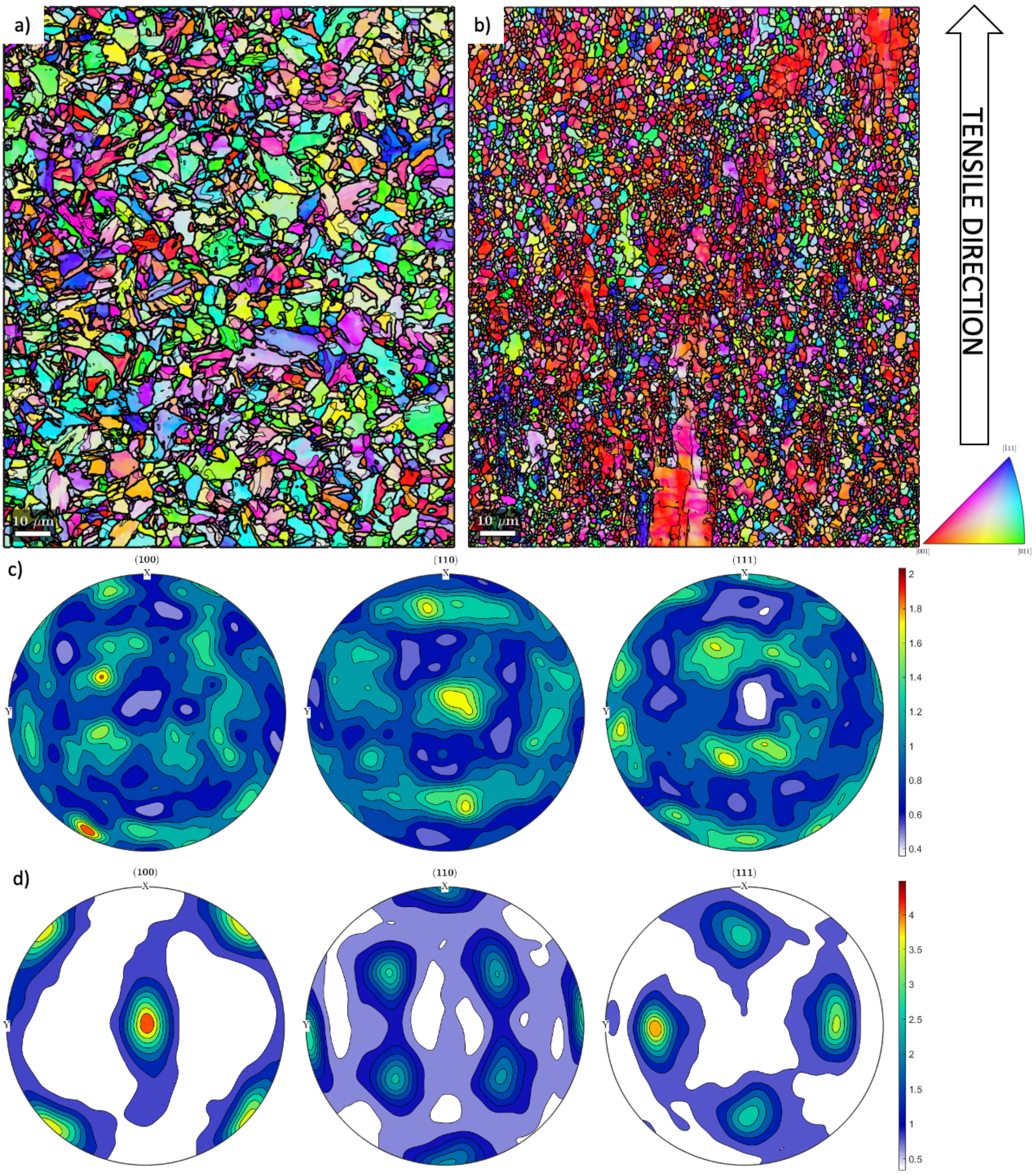

Figure 3.2 *EBSD map of a) EUROFER97 [and accompanying pole figure c)] and b) ODS EUROFER97 [and accompanying pole figure d)], step size 0.25um. High angle grain boundaries (>15º) shown in bold, low angle grain boundaries (<10º) outlined lightly.*

The results of EBSD mapping are collected in *Figure 3.2*. The baseline EUROFER97 alloy exhibits an essentially untextured grain structure (*Figure 3.2* c)) with an almost continuous distribution of grain sizes between 0.4-6 um, the grain size calculated via the

Heyn Lineal Intercept Procedure being 1.35 um. The ODS EUROFER97 alloy meanwhile demonstrates significantly different microstructure. The EBSD map produced for this samples indicates a highly textured grain structure (*Figure 3.2* d)), and a bimodal distribution of large and fine grains. The mapped area is dominated by fine grains with size 0.8-7.6 um, and the Heyn Lineal Intercept Procedure produces a grain size of 1.21 um. The coarse grains (EBSD mapped in the Appendices Figure 0.1) primarily varied in size 7.6-20 um, though individual grains as large as 36 um were observed, and a mean size of 18.32 um was found. The texture demonstrated in *Figure 3.2* b) and d) shows a rotated cube orientation: *Figure 3.2* d) presents the pole figure produced by {100}<100> oriented crystal, azimuthally rotated by 45° such that grains are oriented with the <110> plane along the rolling direction (parallel to the tensile direction indicated in the figure). This texture, known as α-fibre, has been previously reported in ODS high chromium steel, accompanying elongation of grains in the rolling direction, produced during deformation as part of fabrication [78], [242].

3.4.2 Tensile properties

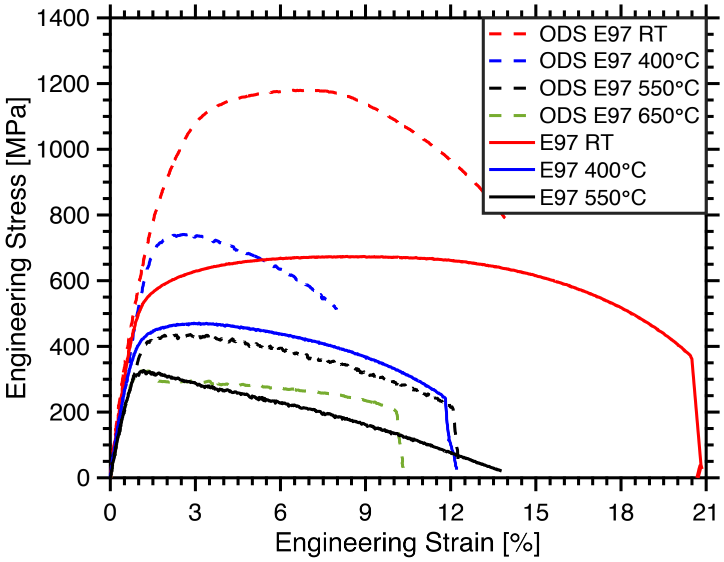

Figure 3.3 *Engineering stress-strain curve produced during the displacement controlled tensile testing of oxide dispersion strengthened EUROFER97 and EUROFER97 samples*

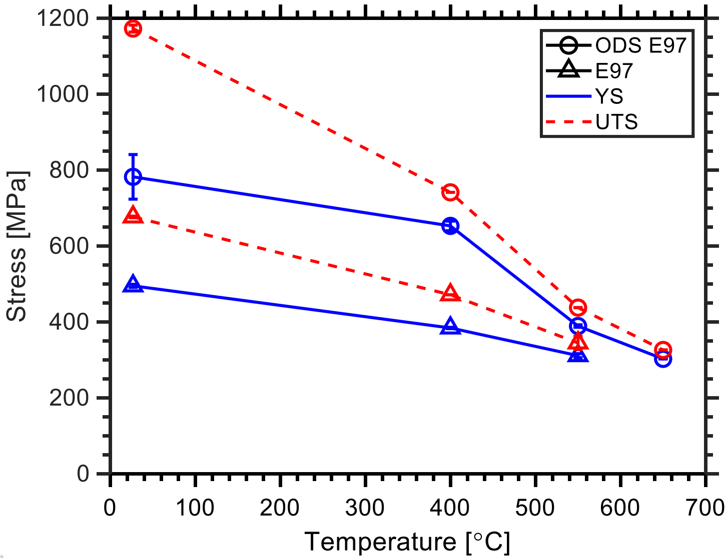

Figure 3.4 *Evolution of ultimate tensile stress and 0.2% yield stress with test temperature. Data presented for EUROFER97 at RT and 550℃, and ODS EUROFER97 at RT averaged over two tests (load controlled and strain controlled)*

The stress-strain curves produced during strain controlled tensile testing of the ODS-EUROFER97 and EUROFER97 samples at room temperature, 400°C, 550°C and 650°C are shown in Figure 3.3a). There is a noted difference in the mechanical response of the

Y_2O_3 strengthened material at all temperatures: the ultimate tensile stress attained is significantly increased, accompanied by a reduction in the total elongation attained before fracture. The effect of temperature on the ultimate tensile strength and yield strength (determined through the 0.2% offset method) is shown graphically in Figure *3.4*. It can be noted the strengthening effect of the oxide particles is present at all test temperatures, but as temperature increases the strengthening effect is degraded, in a manner that is consistent with existing literature [94], [251]. A breakdown in the effectiveness of ODS nanoparticles at elevated temperatures is also indicated by the total elongation recorded as test temperature was increased. Total elongation of ODS EUROFER97 samples increases as test temperature is increased from 400°C to 550°C, suggesting an increase in sample ductility. Furthermore, the strengthening imparted by the addition of ODS is significantly reduced at a test temperature of 550°C (ΔYS~70 MPa) than at 400°C (ΔYS~270 MPa). These changes can be attributed most simply to dislocations gaining energy in excess of the activation barrier corresponding to movement around such obstacles, but may also be linked to the movement agglomeration of oxide nanoparticles, into larger, less effective pinning particles. The increased total elongation observable in the 550°C EUROFER97 curve can be linked to the curves shape during plastic deformation. After yield, there is a much more limited window of strain hardening prior to the onset of necking, and hence the sample exhibits enhanced ductility in comparison with the test performed at 400°C.

3.4.3 Diffraction data analysis

Through the peak position and FWHM, XRD offers insight into microstructural deformation during macroscopic deformation. Using Bragg's law, the unloaded lattice constant of the alloy was determined from the relative position of indexed diffractogram peaks, determined at RT to be 0.28789 ± 0.0004 nm (EUROFER97) and 0.28790 ± 0.0006 nm (ODS EUROFER97). In addition to the diffraction patterns collected during tensile deformation, diffraction patterns were also collected during ramp up to target test temperature before any load was applied. As a result of this, the variation of lattice parameter with temperature, and grain family specific thermally induced lattice strain has also been recorded; associated curves can be found in the Appendices Figure 0.2. The low thermal expansion coefficient of EUROFER97 is recognised as one of the attractive properties of the material, low thermal expansion promoting an enhanced thermal stress parameter. The thermal stress parameter describes the ability of a material to withstand and alleviate thermal stress without fracture, larger parameter values suggesting more effective reduction in thermal stress [262], [263]. As thermal stress can be expected during heating and cooling, the ability of materials to effectively withstand thermal stress is an important performance indicator for reactor applications. Thermal stress resistance is not a purely material dependant issue – environment and specimen geometry/joining playing important roles [262] – but this parameter provides a useful point of comparison between candidate materials.

Through analysis of the curves produced for each alloy the thermal expansion coefficient at 400°C of each alloy was determined to be $13.9 \ \pm 0.2 \ \times 10^{-6}$$\text{K}^{-1}$ (EUROFER97) and $12.8 \pm 0.1 \ \times 10^{-6}$ K^{-1} (ODS EUROFER97). These results compare well to previously literature results of $12.7 \ \times 10^{-6}$ K^{-1} (EUROFER97 [264]) and $11.9 \ \times 10^{-6}$ K^{-1} (ODS EUROFER97 [265]). The lowered thermal expansion coefficient, increased yield strength, and slightly reduced high temperature elastic modulus (see Section 3.3.2) suggest the ODS EUROFER97 exhibits an increased resistance to thermal stress.

3.4.3.1 Lattice strain evolution

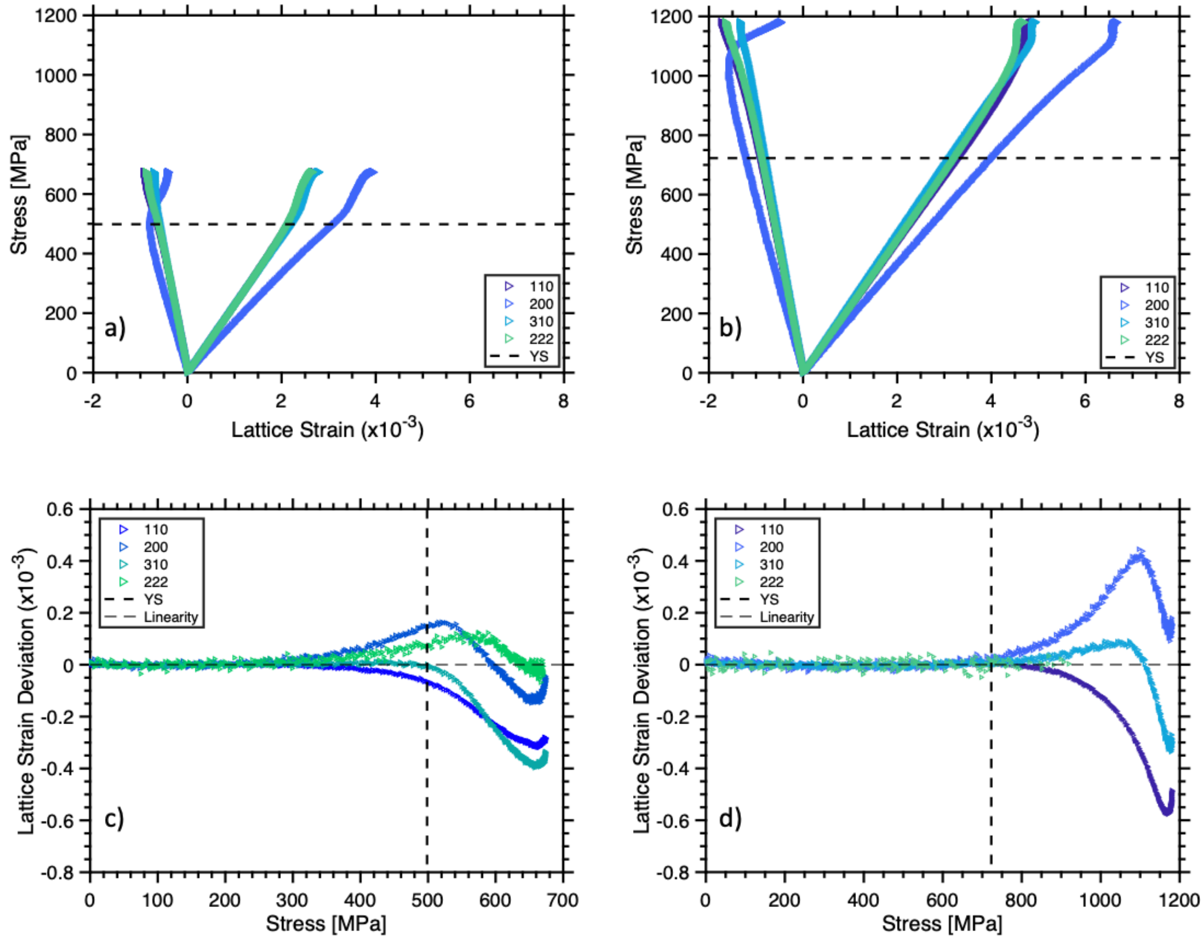

Figure 3.5Graphs demonstrating lattice strain evolution for a)/c) RT EUROFER97, and b)/d) RT ODS EUROFER97. Figures a) and b) depicting lattice strain-stress relation, figures c) and d) depicting the deviation of each grain family lattice strain-stress curve from linearity

Examples of the results produced by lattice strain analysis are shown in Figure 3.5 a) and in Figure 3.5b), for the EUROFER97 and ODS EUROFER97 samples respectively at room temperature, with the rest of the results at high temperatures collected in the Appendices Figure 0.3. From these figures, the diffraction elastic constant of each grain family (the gradient of the tensile lattice strain-stress curve prior to yield) and the diffraction elastic ratio of each grain family (the ratio between grain family curve gradients under tension and compression) can be measured. These results are collected in Table *3.2*.

Table 3.2 *Diffraction elastic constants and diffraction elastic ratio determined from lattice strain stress curves for EUROFER97 and ODS EUROFER97 samples*

Sample	Diffraction Elastic Constants [GPa]				Diffraction Elastic Ratio			
	{110}	{200}	{310}	{222}	{110}	{200}	{310}	{222}
E97 RT	228 ±2	167.0 ±0.9	191.9 ±0.8	251 ±1	0.299 ±0.001	0.283 ±0.002	0.298 ±0.002	0.249 ±0.002
E97 400°C	194 ±3	132.9 ±0.9	152.5 ±0.7	212 ±1	0.349 ±0.003	0.279 ±0.004	0.302 ±0.003	0.261 ±0.003
E97 550°C	176 ±3	106.6 ±0.9	126.1 ±0.8	184 ±2	0.350 ±0.005	0.307 ±0.004	0.327 ±0.003	0.244 ±0.004
ODS E97 RT	220 ±1	182.6 ±0.7	198.9 ±0.5	253.2 ±0.6	0.3010 ±0.0005	0.3093 ±0.0009	0.3143 ±0.0007	0.253 ±0.001
ODS E97 400°C	157 ±2	128.8 ±0.7	139.7 ±0.5	204 ±1	0.30 ±0.03	0.35 ±0.01	0.341 ±0.006	0.30 ±0.01
ODS E97 550°C	142 ±2	99.1 ±0.6	113.7 ±0.5	186 ±1	0.262 ±0.007	0.316 ±0.006	0.315 ±0.006	0.22 ±0.01
ODS E97 650°C	134 ±2	95.4 ±0.8	106.7 ±0.6	182 ±2	0.161 ±0.007	0.35 ±0.01	0.31 ±0.01	0.14 ±0.01

For both alloy compositions and across all temperatures, the {222} plane was the stiffest, whilst the {200} plane was the most compliant. This distinct variation of elastic compliance with grain family orientation reveals a notable anisotropy in the alloy's mechanical responses. This anisotropy causes load partitioning within the polycrystalline sample as the sample passes the limit of elasticity and grains begin to deform plastically as differently oriented grain family's undergo micro-yielding.

Figure 3.5c) and d) illustrate the deviation of each grain family's response from the initial linear elastic deformation to better demonstrate the differing points of yield between differing grain families, and Appendices Figure 0.4 illustrates the nonlinear relation between engineering strain and lattice strain above low engineering strains. The compliant {200} oriented grains yield first, and the stress is redistributed about the polycrystal, increasing load experienced by the non-yielded grains. It can be observed through the increasing difference between most and least compliant grain families at higher test temperatures (for the ODS EUROFER97 samples for example: $\Delta E_{200-222}^{RT} = 68.4$ GPa, $\Delta E_{200-222}^{650} = 86.8$ GPa), that mechanical anisotropy is accentuated at higher temperature.

3.4.3.2 Single Crystal Elastic Constant (SCEC)

The elasticity tensor describes the variation of a material's elastic response with orientation, information which has significant implications in mechanical modelling. Though the elasticity tensor has 36 components, cubic crystal symmetry allows the tensor to be reduced to only three unique components known as the single crystal elastic constants (SCECs). Despite the importance of the material information the SCECs represent, the characterisation of these properties is experimentally difficult. Historically, characterisation has been performed using ultrasonic pulsing, dependent upon the costly fabrication of large scale single crystal samples [266]–[268]. In this work, such difficulties are avoided - using the Kroner model fitting detailed in the method section and the plane dependant elastic properties collected in Table *3.2* allow the single crystal elastic constants of the alloy to be determined directly from the polycrystalline sample.

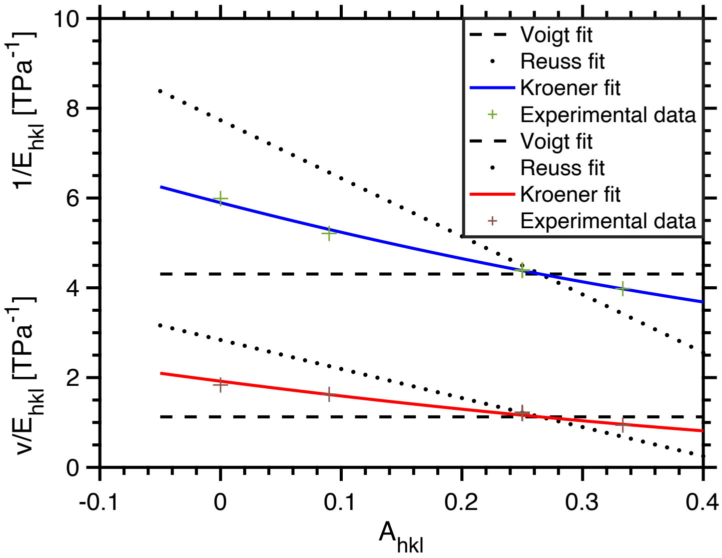

Figure 3.6 Example figure (data taken for RT EUROFER97) demonstrating variation of diffraction elastic constants and ratio as a function of anisotropy, and accompanying Kroner model fit, used to determine single crystal elastic constants.

An example of the Kroner model fits produced is shown in Figure *3.6* and the fits for each test are collected in the Appendices Figure 0.5, with the accompanying single crystal elastic constants collected in Table *3.3*. The error associated with these values was calculated by observing the deviation of each value when the fitting was performed over ten thousand arrays, for which the diffraction elastic constant (DEC) and diffraction elastic ratio were randomised within their respective error bars.

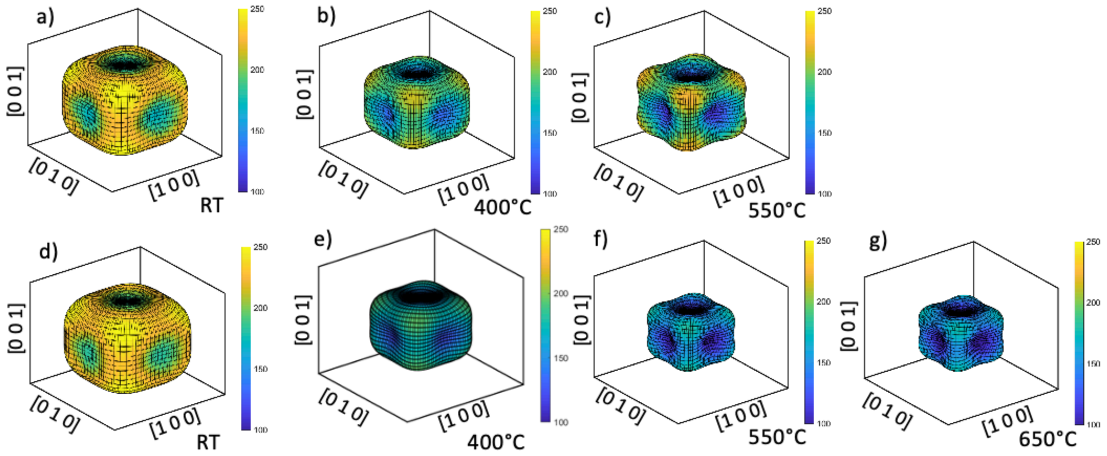

Figure 3.7 Three dimensional variation of polycrystalline elastic modulus for EUROFER97 (a)-c)) and ODS EUROFER97 (d)-g)) across test temperatures. Test temperature considered indicated on each subfigure.

Further, an approximation of the polycrystalline elastic properties was then determined from the single crystal elastic constants – taking a representative A_{hkl} value of 0.2 in the relations above. These results are presented alongside the single crystal elastic constants in Table *3.3*.

Table 3.3 Single crystal elastic constants and polycrystalline moduli determined from Kroner model fitting

Sample	C_{11} [GPa]	C_{12} [GPa]	C_{44} [GPa]	Zener Anisotropy	Elastic Modulus [GPa]	Shear Modulus [GPa]	Poisson's Ratio
E97 RT	230±10	130±10	119±1	2.5±0.3	213.6±0.8	83.2±0.8	0.28±0.02
E97 400°C	207±9	140±10	122±1	3.0±0.6	174.0±0.6	66.5±0.3	0.296±0.004
E97 550°C	170±10	120±10	109±3	4±1	161±1	62±1	0.30±0.01
ODS E97 RT	243±5	136±6	114.0±0.6	2.1±0.1	217.9±0.4	84.6±0.4	0.27±0.01
ODS E97 400°C	192±5	128±5	93.8±0.5	2.9±0.4	163.2±0.4	61.9±0.3	0.318±0.007
ODS E97 550°C	126±4	81±4	100±1	4.4±0.6	141.3±0.4	56.3±0.4	0.32±0.01
ODS E97 650°C	102±4	59±5	107±2	5.0±0.7	136.2±0.6	57.1±0.9	0.19±0.02

Whilst comparable experimental data is not currently available for the determination of EUROFER97 or ODS EUROFER97's SCECs, some comparison may be made with the results of experimental analysis of other similarly constituted RAFMs, and modelling based investigation. It is noted the SCEC produced for EUROFER97 at RT are appreciably similar to those experimentally determined for ferrite through ultrasonic pulse analysis of iron single crystals: C_{11}=226-233.1 GPa, C_{12}=132-140 GPa, C_{44}=115.9-117.8 GPa [268], [269]. In-situ synchrotron analysis to determine SCECs has previously been applied to nanostructured ferritic alloys with similar nominal compositions as ODS EUROFER97, the most similar alloy explored being 9YWTV [$Fe-9Cr-2W-0.4Ti-0.2V-0.05C-0.3Y_2O_3$ (wt%)]. Gan et al.'s elastic analysis of the 9YWTV alloy produced SCEC values C_{11}=213 GPa, C_{12}=109 GPa, and C_{44}=119 GPa at RT [248]. It may be expected that there should be only minor difference between these literature values and the results presented here, given the limited difference in elemental composition and similar lattice structure. The C_{11} values recorded differ by approximately 8%, whilst the C_{44} differ by less than 5%. While the C_{12} value difference is proportionally more significant, the tetragonal shear modulus ($C' = 0.5(C_{11} - C_{12})$) again differs by less than 10%.

Meanwhile, theoretical modelling can provide a baseline for comparison with the EUROFER97 SCEC values produced. In their 2018 work, Li et al. numerically evaluated the SCECs of EUROFER97 at 0K such that C_{11}=285.2 GPa, C_{12}=125.9 GPa, and C_{44}=120.3 GPa. These results are consistent with the values reported in Table *3.3*, the larger difference in C_{11} between modelled 0K and experimental RT than C_{12} and C_{44} consistent with the greater induced change in C_{11} with temperature (ie that $\frac{\partial C_{11}}{\partial T} > \frac{\partial C_{12/44}}{\partial T}$).

From a bulk perspective, the results presented are in good agreement with established literature, the elastic modulus of EUROFER97 having been previously reported between 187-200 GPa from fatigue testing at room temperature [270], and that of ODS EUROFER97 having been reported at 212 GPa at room temperature [265].Furthermore, characterisation of the alloys' SCECs and accompanying polycrystalline moduli, also allows for the anisotropy of the mechanical response to be evaluated, both through the Zener cubic anisotropy and by the construction of three dimensional surfaces of the elastic modulus. The Zener cubic anisotropy is calculated through the equation

$$Z = \frac{2C_{44}}{(C_{11} - C_{12})} \tag{3.14}$$

And the results of this analysis are found in Table *3.3*. The elastic modulus surfaces with varying temperature for both alloys are illustrated in Figure *3.7*. As was inferred from the increasing variance between diffraction elastic constants with increasing temperature, both alloys experience increased anisotropy at high temperature, demonstrated by the increasing Zener anisotropy, and sharpened contours of the elastic modulus surface. An increase in Zener anisotropy is expected as the temperature approaches the Curie temperature – as the tetragonal shear modulus rapidly decreases [271], while the trigonal shear modulus (C_{44}) remains relatively stable. The Curie temperature of EUROFER97 has been previously determined as 752-757°C [272], [273], while that of ODS EUROFER97 has been measured at 747°C [75]. The relation between tetragonal shear modulus and temperature has previously been described [246] through the fit

$$C' = a\sqrt{(1 - {}^{T}/_{T_C})} \tag{3.15}$$

Where a is a material dependent parameter, and T_C is the Curie temperature. From this relation T_c can be determined by plotting $(C')^2$ against temperature, and these plots for EUROFER97 and ODS EUROFER97 are shown in Appendices Figure 0.6. Analysis of these curves produced T_C values of 770°C and 730°C for EUROFER97 and ODS EUROFER97 respectively, which – whilst severely limited by the number of data points available for analysis – agrees with the literature values quoted, considering the error found (±100°C).

3.4.3.3 Dislocation density evolution

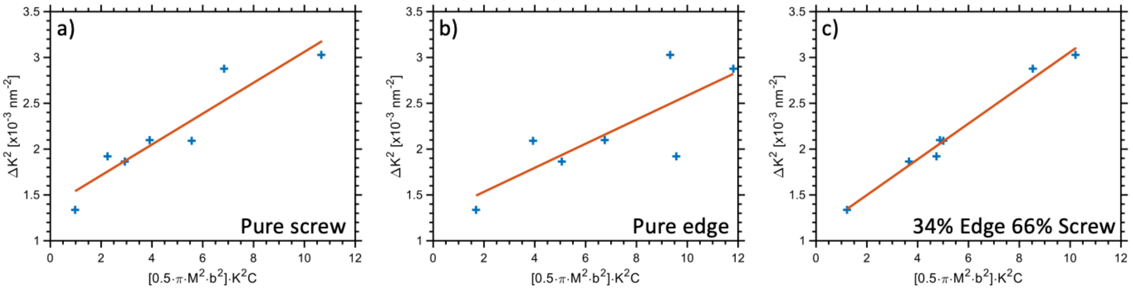

Figure 3.8 *Modified Williamson-Hall plots (data taken from unstrained RT ODS EUROFER97) using varying contrast factors, as dictated by the dislocation type considered, demonstrating the use of goodness of fit as a means of evaluating dislocation character. Whilst a) the pure screw case, and b) the pure edge case, produce poor linear fits, the mixed population selected in c) produces an R2 value of 0.99, an excellent linear fit.*

An example of the peak broadening seen over the course of tensile testing is shown in the Appendices Figure 0.10, which was used for dislocation characterisation as described in the Materials and Methods. Details of the contrast factors used in this analysis are collected in the Appendices, Table 0.1. Given the known expected linear relationship described in Equation (***(3.13***), we can use the goodness of fit parameter R^2 as an indicator of the correctness of edge/screw proportion used [274]. The closer R^2 becomes to one, the more accurate the edge/screw proportion used may be considered [275]. An example of this is illustrated in Figure *3.8*, in which the data for unstrained ODS EUROFER97 at RT is used. When either purely edge (Figure *3.8* a)) or purely screw (Figure *3.8*b)) dislocation populations were considered, the data did not produce a convincing linear fit. However, when a contrast factor produced by a dislocation population 34% Edge and 66% Screw was used (Figure *3.8*c)), the data produced a more convincing linear fit, with a high R^2 value (0.99).

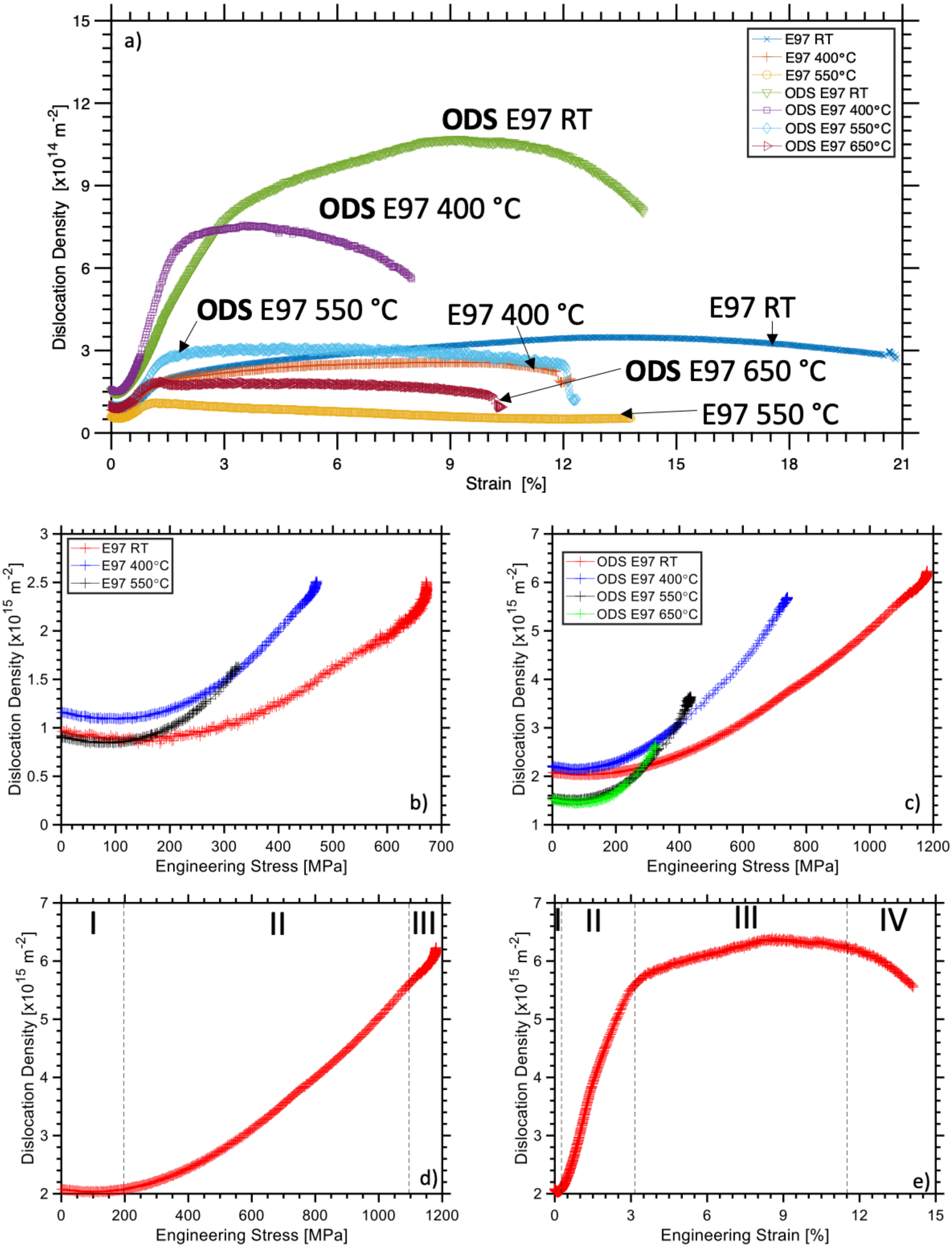

Figure 3.9 Dislocation density evolution during tensile testing of EUROFER97 and ODS EUROFER97 between room temperature and 650°C with a) engineering strain and b/c) engineering stress. Stages of dislocation density evolution are indicated on d/e) example data shown for room temperature deformation of ODS EUROFER97, transition points between stages marked by dashed lines

Table 3.4 *Tabulated dislocation density measurements determined through the Modified Williamson Hall Method, prior to load, at the limit of linearity, and at ultimate tensile stress*

Sample		Initial dislocation density [×10^{14} m^{-2}]			Dislocation density at limit of linearity [×10^{14} m^{-2}]			Dislocation density at UTS [×10^{14} m^{-2}]		
		Total	Edge	Screw	Total	Edge	Screw	Total	Edge	Screw
EUROFER97	RT	0.8 ±0.2	0.6 ±0.2	0.3 ±0.1	0.9 ±0.3	0.4 ±0.2	0.5 ±0.2	3.1 ±0.8	2.3 ±0.6	0.8 ±0.3
	400°C	0.9 ±0.3	0.5 ±0.2	0.4 ±0.2	1.0 ±0.3	0.5 ±0.2	0.2 ±0.4	2.5 ±0.6	1.2 ±0.2	1.3±0.2
	550°C	0.7±0.2	0.5±0.1	0.20±0.09	0.9±0.3	0.7±0.2	0.2±0.1	1.8±0.7	1.2±0.4	0.6±0.3
ODS EUROFER97	RT	2.0±0.7	0.8±0.3	1.2±0.5	1.9±0.2	0.7±0.1	1.3±0.1	10±3	8±2	2.0±0.9
	400°C	1.8±0.6	0.6±0.2	1.2±0.2	3.1±0.1	2.3±0.4	1.0±0.3	7±2	5.5±0.5	1.3±0.5
	550°C	1.4±0.5	1.0±0.4	0.4±0.2	1.7±0.6	1.2±0.5	0.4±0.2	4.3±0.1	1.9±0.3	2.4±0.3
	650°C	1.4±0.5	1.0±0.4	0.4±0.2	1.5±0.5	0.9±0.3	0.6±0.2	3.0±0.1	0.9±0.2	2.0±0.2

In this way, both the total dislocation density, and the dislocation density of edge and screw dislocations were estimated. The evolution of dislocation density and character with strain at varying temperature for both EUROFER97 and ODS EUROFER97 are collected in Figure *3.9*, Figure *3.10*, Appendices Figure 0.7-Figure 0.9, and tabulated in Table *3.4*. The dislocation density evolution in Figure *3.9* can be broadly divided into four distinct stages for each test as shown in Figure 3.9 d)/e).

- Stage I: Initial constant dislocation density, corresponding to the purely elastic region of deformation.
- Stage II: Sharp increase in dislocation density at the onset of plastic deformation.
- Stage III: Increase in net dislocation density slows and then plateaus.

- Stage IV: Dislocation density falls prior to sample failure at the onset of fracture.

It is immediately apparent comparing like temperature curves in Figure *3.9*) that the presence of strengthening oxide particles greatly increases the maximal dislocation density reached at each test temperature. The total dislocation density-strain curves can be seen in the Appendices Figure 0.7 and Figure 0.8, and from these curves the rate of dislocation density increase during Stage II was determined from the curve between the limit of linearity and the 0.2% offset yield stress. The rate of dislocation density produced by the ODS EUROFER97 sample was consistently greater than that of EUROFER97. This increased production of dislocations is attributed to the greater concentration of grain boundaries and material inclusions (i.e. the ODS nanoparticles) which are expected to act as dislocation sources. Neither sample presented significant temperature rate dependency.

Stage II commences prior to the macro-yield point, conventionally thought of as the transition point from elastic to plastic deformation in line with the micro-yielding behaviour observed in Figure 3.5. It is noted that the diffraction peaks started to broaden before macro-yielding (Appendices Figure 0.10). The only feasible reason for this is the multiplication of dislocations. There is a sharp increase of dislocation density across Stage II in the dislocation density verse strain curves (Figure 3.9a). This is mainly because that the stress level also increases rapidly as the strain is increased during this same period. The dislocation density was then plotted against stress up to the UTS (Figure 3.9), which shows that the rate of dislocation multiplication verse stress at Stage II started at a low rate then increases to be the same rate as that of the stage III.

The increase in dislocation density below macroscopic yield is the result of plastic deformation on the scale of individual grains. Dislocations are generated from grain boundaries because of orientation driven stress concentrations and move across grains to pile-up at grain boundaries: individual grains seeing plastic deformation dependent upon orientation, driving up the dislocation density. Such “micro-plastic” behaviour in polycrystalline samples has previously been observed using a variety of experimental techniques, including acoustic emission during tensile deformation [276], comparison of chemically etched deformed samples [277], in-situ TEM observation during tensile deformation [278] or loading/unloading in a sub-macro-yield regime [279], and in-situ high-energy XRD of other materials (aluminium [204], [205], nickel [206], etc).

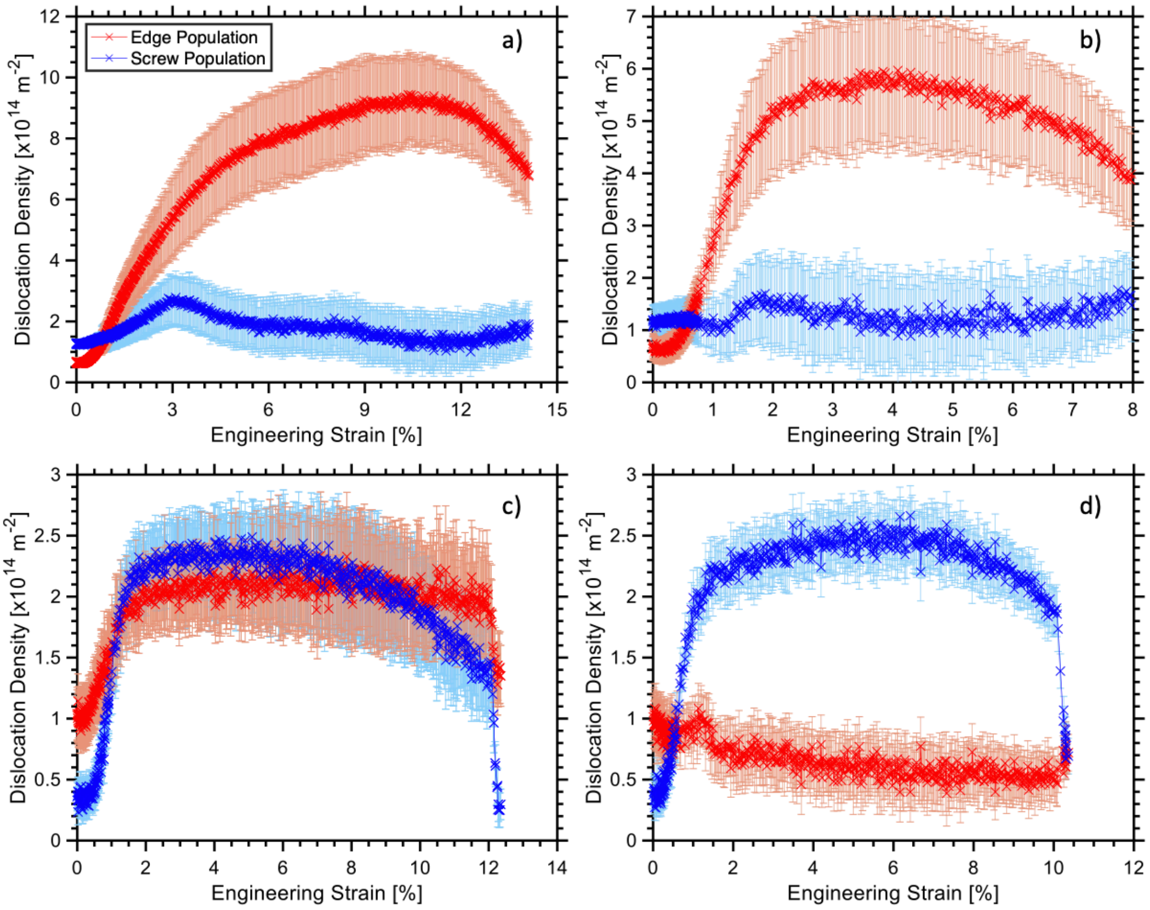

Figure 3.10 *Dislocation density evolution of screw (blue) and edge (red) type dislocations with strain during tensile testing of ODS EUROFER97 at RT (a), 400°C (b), 550°C (c), and 650°C (d), showing the increasing screw population proportion with increasing temperature.*

The evolving dislocation character (edge and screw) in the ODS EUROFER97 sample with strain across all test temperatures is depicted in Figure *3.10*. Dislocation density is dominated by edge type dislocations at room temperature and 400°C (Figure *3.10* a) and b)), moving through a mixed dislocation domain at 550°C (Figure *3.10* c)), to a screw dominated dislocation density at 650°C (Figure *3.10* d)). Other works reporting variable temperature tensile testing of high chromium steels have found the same dislocation character response as reported here – namely edge dominated deformation under room temperature [244], [274], [280], and screw dominance at >600°C [274], [275].

It is well known that BCC materials exhibit flow stress with a strong thermal dependency because of the thermally activated nature of screw dislocations. At low temperatures, the velocity of screw dislocations is significantly lower than that of edge dislocations, and so the movement of screw dislocations act as a rate determining step for the plastic deformation of BCC materials [281]. However, the temperature corresponding to thermal activation of screw dislocations is approximately 0.1 T_m, and has recently been compellingly linked to the DBTT [199]–[201]. All tests performed in this work were well above the DBTT of EUROFER97 and ODS EUROFER97, meaning screw dislocations should already be fully activated. Investigation of pure BCC metals around the DBTT has found that the velocity of edge and screw dislocations becomes approximately equal above the brittle to ductile transition [200], [201].

These results were determined for pure metals however, and it should be expected that alloying content will have a significant impact on dislocation behaviour. Study of BCC high entropy alloys has shown a transition from screw to edge governed plasticity as a result of the misfit between parent element and alloying content reducing the mobility of edge dislocations below that of screw dislocations [282]. This behaviour has been predicted in alloys with alloying content as low as 9.3 wt%, comparable to the total alloying content of the samples used in this work [283]. Also, to be considered is the presence of precipitates; MX/$M_{23}C_6$ carbides in EUROFER97 and Y_2O_3 nanoparticles for ODS EUROFER97. Edge dislocations in BCC metals are plane limited, whereas the ½<111> screw dislocation can glide across multiple slip planes [281], and molecular dynamics simulations have reported that precipitates within iron form stronger obstacles to edge dislocations than screw dislocations [284]. This again suggests a structure in which mobility of edge dislocations is lowered relative to that of screw dislocations, leaving the movement of edge dislocations a rate determining factor in overall plasticity. It should further be considered that the dislocation evaluation, presented in Figure 3.10 and Appendices Figure 0.9, plots how dislocation character changes, rather than actual populations of pure edge and screw dislocations. Bowing out of screw dislocations pinned at precipitates at moderate temperatures leads to highly curved dislocation segments which lowers overall screw dislocation character, as straight screw segments develop a non-screw character during curvature [285]. These factors suggest a dislocation structure at low temperature dominated by lowered mobility edge dislocations, pinned by precipitates and slowed by unusual stress valleys in the alloying content disrupted lattice.

The transition in dislocation character at elevated temperature reflects the thermally activated nature of the edge dislocation climb in body centred cubic materials [286]. At high temperature, edge dislocations gain sufficient energy to climb around precipitates, rather than bow around. Consequently, mobility of edge dislocations increases relative to that of screw dislocations, the equilibrium density of edge dislocations falls, and screw dislocations become dominant. This is borne out by the fact the equilibrium screw dislocation density remains roughly consistent across all test temperatures – ~$1x10^{14}$ m^{-2} in the case of EUROFER97, and ~$2x10^{14}$ m^{-2} in the case of ODS EUROFER97. Interestingly, the introduction of ODS has led to an increase in the edge dominated to screw dominated transition temperature – EUROFER97 showing a reduction in edge fraction at 400°C, whilst ODS EUROFER97 shows a reduction in edge fraction only at 550°C.

3.4.3.4 Constitutive flow analysis

Using the physical parameters established through the XRD analysis detailed above, it is possible to evaluate the yield stress of both materials at varying temperature by considering individual strengthening contributions. The yield stress is given in this way by the relation:

$$\sigma_y = \sigma_{SS} + \sigma_{HP} + \sigma_{CC} + \sigma_d \qquad \textbf{(3.16)}$$

Where σ_y is the calculated yield stress, σ_{SS} is the solid solution strengthening contribution, σ_{HP} is the Hall-Petch contribution [287], [288], σ_{CC} is the Coble creep contribution [289], and σ_d is the dislocation strengthening contribution. Of these, the solid solution strengthening contribution concerns the effect of alloying element content in disrupting the iron matrix, and is heavily dominated by the alloying elements Cr, W, Mn, and V. Meanwhile the Hall-Petch contribution concerns the effect of grain size on yield stress, and the Bailey-Hirsch strengthening component [290] relates dislocation density to stress. At elevated temperatures the Hall-Petch relation breaks down, and this term is replaced by the Coble creep contribution, in cases where $\sigma_{CC}<\sigma_{HP}$ [291]. Coble creep describes the diffusion driven flow of elements along grain boundaries, and is hence a thermally activated process, only becoming stress limiting at high temperature. The dislocation strengthening contribution is itself composed of two terms which describe the effects of dislocation-dislocation interactions and dislocation-particle interactions (where particles are present). The dislocation-particle interactions are accounted for by different mechanisms at low and elevated temperature. At low temperature, dislocation strengthening is given by

$$\sigma_d = \sqrt{\sigma_{BH}^2 + \sigma_K^2} \tag{3.17}$$

where σ_{BH} is the dislocation-dislocation Bailey-Hirsch contribution, and σ_K is the Orowan strengthening contribution [292], which relates to dislocation bowing caused by pinning obstacles. Meanwhile at elevated temperature

$$\sigma_d = \sqrt{\sigma_{BH}^2 + \sigma_{ARW}^2} \tag{3.18}$$

Where σ_{ARW} is the Arzt-Rosler-Wilkinson contribution [293], which considers dislocation climb around pinning obstacles. The use of the root mean squared analysis of dislocation strengthening is utilised here, as it has been shown to more accurately model experimental yield stress in ODS steels [203], [294]–[296].

Table 3.5 Solid solution strengthening coefficients relating to solid solution strengthening

Microalloying element	Strengthening coefficient, *k*
W	11000
Cr	1400
Mn	7000
V	4000

All the contributions discussed are evaluated using the following set of equations (Equations (3.19) (3.20) (3.22) [75], [202], [203], [251], [252], [294], [296], [297], Equation (3.21) [251], [291], [298], Equation (3.23) [75], [202], [203], [299], Equation (3.24) [251], [252]) such that:

$$\sigma_{SS} = 0.00689 \sum k{C_i}^n \tag{3.19}$$

$$\sigma_{HP} = \sigma_0 + \sigma_D = \sigma_0 + (\frac{G(T)}{G(RT)})^{0.5} \cdot \frac{K_H}{\sqrt{D}} \tag{3.20}$$

$$\sigma_{BH} = M\theta G(T) b\rho^{0.5} \tag{3.21}$$

$$\sigma_{CC} = \frac{k_b T D^3 \dot{\varepsilon}}{47\Omega \delta_B D_B} \exp\left({}^{Q_B}/_{RT}\right) \tag{3.22}$$

$$\sigma_K = \frac{0.81MG(T)b \ln(\frac{d\sqrt{{}^2/_3}}{|b|})}{2\pi(1-\nu)^{0.5} \cdot (L - d\sqrt{{}^2/_3})} \tag{3.23}$$

$$\sigma_{ARW} = 0.9M \frac{G(T)b{R_T}^{1.5}}{L(2\sqrt{2} + {R_T}^{1.5})} \tag{3.24}$$

In these equations, *k* is an alloying element specific constant (the values for which are reported in Table *3.5* [300]), C_i is the concentration in at. % of each alloying element, *n* is a constant, 0.75, σ_0 is the alloy's friction stress (taken as 53.9 MPa – that of single crystal Fe [295]), $G(T)$ and $G(RT)$ are the shear stress at test temperature and room temperature respectively, K_H is the Hall-Petch coefficient, D is the sample's grain size, $\dot{\varepsilon}$ is the experimental strain rate experienced by the sample, Ω is the atomic volume across the sample, δ_B is the pre-exponential factor of grain boundary diffusion, D_B is the grain boundary width, Q_B is the activation barrier energy to grain boundary diffusion, R is the gas constant (R=8.31 J/mol K), M is the Taylor factor for bcc metals, 3.06 [75], [202], [203], [250], [294], [298], θ is a constant parameter, 0.38 [75], [295], [299], [300],

b is the Burgers vector modulus, ρ is the sample's dislocation density prior to yield, d is the average oxide particle size, L average particle spacing, υ is the sample's Poisson ratio, and R_T is a constant, 0.77 [251], which accounts for the loss of line tension experienced by a dislocation segment whilst pinned. The pre-exponential term moderating grain boundary diffusion, $\delta_B D_B$, is taken as $1.1 \times 10^{-12}\ m^3 s^{-1}$ [251], [291]. The average oxide particle size was approximated as 12 nm, taken from previous TEM analysis of similarly processed ODS EUROFER97 steel [75], [77]. The interparticle spacing was estimated using the equation [75], [295], [301], [302]:

$$L = d\sqrt{\frac{2}{3}}(\sqrt{\frac{\pi}{4f}} - 1) \tag{3.25}$$

Where f is the volume fraction, estimated as 0.0047, given the percentage by weight and relative density of Y_2O_3 within the EUROFER97 alloy. In this work the Hall-Petch coefficient was estimated through the previously used relation [251]:

$$K_H = \frac{G(RT)\sqrt{b}}{5} \tag{3.26}$$

Substituting this estimate into the Equation (3.20) it was possible to evaluate the changing Hall-Petch contribution with temperature from the results of the XRD analysis.

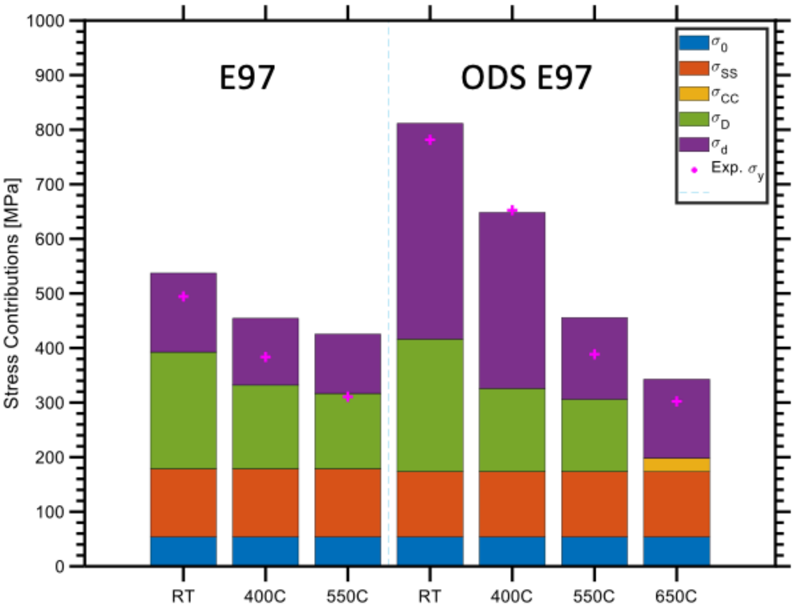

Figure 3.11 *Results of constitutive flow stress analysis for EUROFER97 and ODS EUROFER97 at the test temperatures considered, with the experimental yield stress recorded as a point of comparison.*

The results of the constitutive flow analysis are shown in Figure *3.11*, overlaid onto which are the yield stress values found through 0.2% offset analysis of the tensile stress-strain curves. The yield stress predicted by the constitutive flow method largely agrees well with the experimental values determined, the only major point of deviation being the EUROFER97 sample tested at room temperature. Looking at the relative weight of each contribution in each instance, it is immediately apparent that the means by which dislocations move past pinning obstacles has the greatest impact on the yield strength. At room temperature and 400°C, the dislocation strengthening dominates all other strengthening contributions but beyond 400°C, when the Orowan bowing contribution is replaced by the weaker thermally activated Arzt-Rosler-Wilkinson contribution, the expected sharp drop in yield stress is seen.

Table 3.6 Individual stress contributions to flow stress determined through Equations (19)-(24)

Sample	**EUROFER97**			**ODS EUROFER97**			
	RT	400°C	550°C	RT	400°C	550°C	650°C
σ_0 [MPa]	53.9	53.9	53.9	53.9	53.9	53.9	53.9
σ_{SS} [MPa]	124.9	124.9	124.9	119.7	119.7	119.7	119.7
σ_D [MPa]	213.8	153.2	138	242.9	152.4	132.3	-
σ_{CC} [MPa]	-	-	-	-	-	-	24.7
σ_d [MPa]	144.6	122.4	108.5	395.0	322.4	149.7	144.5
σ_{YS} [MPa]	422	390	373	871	757	497	472

This is borne out by the changing dislocation character, as observed in Figure *3.10*. At room temperature, dislocation density is dominated by edge type dislocations, but as the test temperature is increased the screw population accounts for more of the total dislocation density, eventually dominating at 650°C. Indeed, the transition to the screw dominated system only occurs above 400°C: the temperature at which the Arzt-Rosler-Wilkinson contribution overcomes the Orowan bowing term. In addition, there is a sharp drop in the dislocation density plateau reached in Figure *3.9* during tensile testing between 400°C and 550°C, from approximately 8.5×10^{14} m^{-2} to 4.4×10^{14} m^{-2}. This similarly suggests a sudden breakdown in the pinning efficiency of the ODS particles.

The Hall-Petch relation is only observed to breakdown at 650°C, the replacement of the Hall-Petch contribution with the lower Coble creep term accounting for the fall in yield stress observed experimentally, despite the lack of change in the dislocation density and shear moduli moving from 550°C to 650°C. Indeed, these results demonstrate that the drop in improved strength relative to EUROFER97 above 400°C is almost entirely correlated to a change in the processes of deformation to thermally activated mechanisms at elevated temperatures.

Whilst the results produced in this study exhibit generally good agreement with the constitutive flow analysis predictions, it must be noted the constitutive modelling used fails to accurately predict the experimentally determined yield stress of the 550°C EUROFER97 sample, and applying the same model to other high Cr ODS steels (Figure *3.12*) the accuracy of model prediction was not consistent. The results of this application are shown in Figure *3.12*b) – steels with Cr content between 5wt% and 20wt% were considered, with Y_2O_3 content between 0.2wt% and 0.5wt% [203], [236], [251], [294]–[296], [299], [301], [303]–[306]. In all but two cases, the constitutive flow analysis overestimated yield stress, and there are several considerations which could account for the common overestimation of yield stress seen in Figure *3.12*b). Firstly, the constitutive flow analysis has a high sensitivity to several factors which are significantly challenging to accurately evaluate – the interparticle spacing, particle size, and dislocation density. Such evaluation relies either on snapshots of material microstructure offered through TEM to calculate average values or larger interaction volume informed microstructural characterisation, as employed here, the first of which offers precise measurement which may represent local area rather than across sample properties, the second of which may produce more representative results at the expense of precision. Secondly, there is disagreement across existing literature as to appropriate values of utilised constants: the Taylor Factor, M, is reported between 2.5 [306] and 3.1 [291], [296] for bcc metals, the frictional stress, σ_0, is most commonly reported as 53.9MPa, but has been reported between 100 MPa [291] and 13 MPa [251],

[252], and the parameter θ is reported between 0.2 [296] and 0.5 [236], [307]. Beyond this, there are significant assumptions introduced in the evaluation of every term:

1. The use of a single, stable value for the matrix frictional stress, σ_0, independent of temperature
2. That all microalloying elemental content will contribute to solid solution strengthening, disregarding the proclivity of elements such as Cr and W to form precipitates within ODS steels.
3. Similarly, that the entire dislocation density population recorded will contribute to dislocation forest strengthening

Despite these limitations, the current work demonstrates that constitutive flow analysis can provide accurate assessment of material flow stress, and allows changes in flow stress to be described in microstructural terms. Assessment of microstructural contributions to flow stress in this work and the literature referenced informs future refinement of next generation fusion materials – identifying key parameters for the optimisation of oxide dispersion strengthening. Microstructural phenomena can be expected to fundamentally control macroscopic performance, and work directly connecting the two provides necessary insight into how fabrication and processing can be controlled to optimise performance criteria. The results presented here emphasize both the degree to which introduction and control of appropriate precipitates can positively augment material properties, and the increased importance of dislocation behaviour with the introduction of ODS; the temperature at which edge and screw dislocations become comparable corresponding to a significant decrease in yield stress.

Within the context of existing literature, these results help to build up a more complete picture of the ODS design space. The design and production of new structural materials, able to withstand higher operating temperature, will have important consequences for fusion reactor design; increased operating temperature allows for increased coolant cycle temperature, leading to increased efficiency of reactor energy production. Considering the proposed lifetime of currently considered nuclear fusion reactors, even small increases in efficiency can be expected to yield significant rewards, and optimisation of every aspect of reactor design is the best path to viable fusion energy.

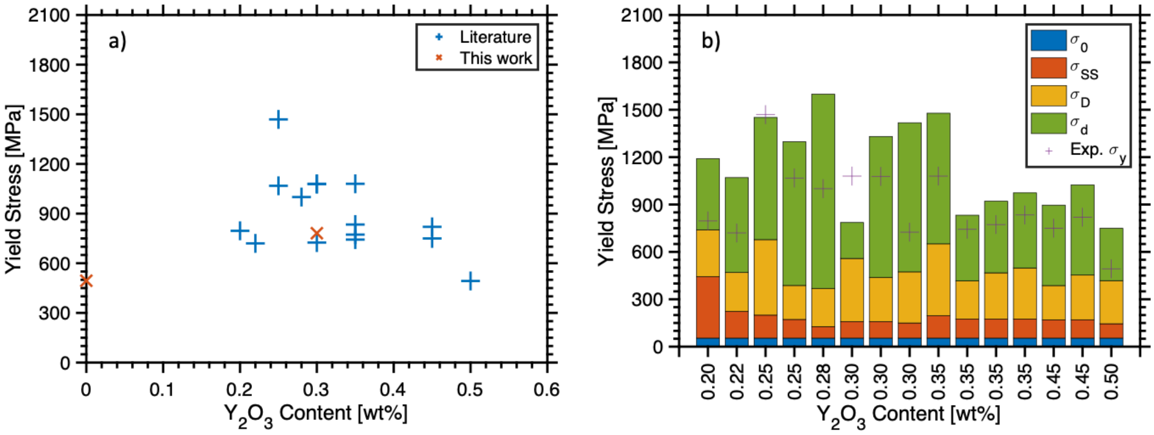

Figure 3.12 *a) Figure demonstrating effect of* Y_2O_3 *content on yield stress in high Cr ODS steels, b) comparative constitutive flow analysis of different wt%* Y_2O_3 *ODS steels demonstrating suitability and limitations of the constitutive flow model employed. The data presented is taken (left to right in subfigure b) from Zhao et al (2022), Chauhan et al. (2017), Kim et al. (2012), Shen et al. (2016), Cunningham et al. (2014), De Sanctis et al. (2018), Praud et al. (2013), Cao et al. (2021), Jarugula et al. (2021), Ren et al. (2018), Ren et al. (2018), Ren et al. (2018), Li et al. (2019), Li et al. (2019), and Wang et al. (2012).*

3.5 Conclusion

The elastic and mechanical properties of the promising reduced activation ferritic/martensitic steel EUROFER97, and an oxide-dispersion strengthened variant of this alloy were established using in-situ high energy X-ray diffraction during tensile testing. The strengthening effect of ODS particles was noted at room temperature, though this effect lessened with elevated temperatures, as oxide particles became less significant pinning obstacles. The single crystal elastic constants of EUROFER97 and ODS EUROFER97 at RT were determined in GPa as $C_{11} = 230 \pm 10$, $C_{12} = 130 \pm 10$, $C_{44} = 119 \pm 1$ and $C_{11} = 243 \pm 5$, $C_{12} = 136 \pm 6$, $C_{44} = 114.0 \pm 0.6$ respectively. Further the dislocation density of the test samples during deformation were evaluated through the modified Williamson-Hall method, and in addition to the increased annihilation imparted by elevated temperature, and the presence of ODS particles promoting dislocation formation, it was found that dislocation character became almost purely screw at elevated temperature. Using the material properties determined through XRD analysis, the yield strength of both materials at room temperature was approximated using constitutive flow modelling, revealing the relative influence of strengthening contribution in each case – Orowan bowing of dislocations around pinning obstacles in particular accounting for the ODS material's enhanced strength up to 400°C, and the advent of thermally activated dislocation climb and grain boundary diffusion producing the sharp declination in strength experienced above 400°C.

CHAPTER 4 HIGH ENERGY X-RAY SYNCHROTRON CHARACTERISATION OF EUROFER97-2 STEEL UNDER HIGH TEMPERATURE TENSILE AND RATCHETING TESTING

Tay Sparks[a], Michael Gorley[b], Yu-Lung Chiu[a], Thomas Connolley[d], Matthew Carrington[b], Oxana Magdysyuk[d], Michael Rieth[c], Yiqiang Wang[b]*, Biao Cai[a]*

[a]School of Metallurgy and Materials, University of Birmingham, Birmingham, UK

[b]UK Atomic Energy Authority, Culham Science Centre, Abingdon, Oxfordshire OX14 3DB, UK

[c]Institute for Applied Materials, Karlsruhe Institute of Technology, Karlsruhe, Germany

[d]Diamond Light Source Ltd, Harwell Science and Innovation Campus, Didcot, UK

In Preparation

Tay Sparks conceived, designed and conducted the experimental work, analysed the data, and wrote the manuscript. Biao Cai and Yiqiang Wang assisted in conceiving and designing the experiment, performing the experimental work, and writing the manuscript. Thomas Connolley and Matthew Carrington assisted in experimental work. Michael Gorley assisted in conceiving and designing the experiment and reviewing the manuscript. Oxana Magdysyuk assisted in experimental work and data analysis. Michael Rieth provided materials for experimental work.

4.1 Abstract

The reduced activation ferritic martensitic steel EUROFER97 fills an important role in many fusion reactor designs, as the structural material proposed for use in international fusion projects. In order to meet demand, large scale fabrication of EUROFER97 has proceeded in several batches, and characterisation across batches is required to ensure consistency of important mechanical properties throughout. In this work the mechanical properties, microstructure, and response to deformation of samples of EUROFER97-2 were tested across a range of operating reactor significant temperatures using in-situ high energy X-ray diffraction tensile testing, and X-ray computed tomography. Asymmetric cyclic testing at high temperature allowed stability of material properties to be assessed, and dislocation recovery dynamics were analytically evaluated using the Friedel and Verdier models. Results of recovery fitting indicated a significantly increased activation volume and activation energy for the recovery of screw dislocations over edge dislocations, the activation energy of screw dislocations consistent with the self-diffusion activation energy of chromium in ferrite, whilst the activation energy of edge dislocations were consistent with the dislocation core diffusion activation energy. These results confirmed consistent bulk elastic properties between different batch EUROFER97, and provided novel characterisation of dislocation dynamics and dislocation population evolution with tensile deformation.

4.2 Introduction

Choice of structural material to be used in nuclear fusion reactors is a critical issue in the design of future nuclear fusion reactors, the operating environment of a fusion reactor producing extremely harsh operating conditions including extremely high temperature and high energy neutron bombardment. Reduced activation ferritic martensitic (RAFM) steels are an important class of material in this arena, utilising the well documented high temperature strength of 9Cr steels whilst avoiding irradiation induced recycling concerns by the substitution of high activity microalloying content (Nb, Mo, etc) with low activity alternatives. EUROFER97 was developed in Europe to meet these requirements, and has been produced on a large scale in three batches, developed by Böhler Edelstahl GmbH, Austria and Saarschmiede, Germany [37].

Adoption of any material on an industrial scale requires a comprehensive understanding of material properties and behaviour, and it is therefore necessary that the deformation behaviour of each batch of EUROFER97 be fully characterised to ensure consistency of response across batches. Deformation behaviour in the elastic region is dictated by intrinsic material properties, characterised through single crystal elastic constants, and polycrystalline moduli, whilst in the plastic region generation and mobility of dislocations describe material response. In-situ X-ray diffraction of deformed samples has been used to extract fundamental material elastic properties from polycrystalline samples through characterisation of orientationally dependent elastic response, stress partitioning between differently oriented grains and phases, and quantification of dislocation density via the modified Williamson-Hall method.

X-ray computed tomography (XCT) allows detailed characterisation of morphology within in-situ samples. Difference in contrast in captured projections is utilised to discriminate between phases, precipitates, and voids in samples, and is commonly used to investigate solidification mechanisms, stress partitioning, and void coalescence.

Ratcheting of structural components at high temperature can be expected in fusion reactors during operation; reactor start-up/shut off and fluctuations in plasma density during operation produces thermomechanical fatigue. Cyclic testing of EUROFER97 has exclusively reported continuous cyclic softening at room and elevated temperature [308]–[312] with minor strain hardening restricted to the first one to five cycles at room temperature [312]. Previous low cycle fatigue characterisation of batch 1 EUROFER97 suggests softening rate is temperature independent up to 300°C, but annihilation of in grain dislocations and subgrain coarsening leads to a large increase in softening rate at 550°C [313]. EUROFER97's cyclic behaviour has been identified as a gap in materials data to support the International Thermonuclear Experimental Reactor's test blanket module design campaign [228], and modelling of ratcheting fatigue behaviour on the basis of experimental data remains an active concern [314], promoting need for further high temperature cyclic testing.

In this work, deformation behaviour of batch 2 EUROFER97 (hereafter EUROFER97-2) is investigated in the elastic and plastic region by in-situ synchrotron X-ray diffraction and computed tomography. Stability of elastic response and dislocation behaviour is investigated by means of asymmetric stress-controlled cyclic loading at elevated temperature. Fractographic analysis of failed samples is employed to comment on change in ductility with increasing test temperature,

4.3 Materials and Methods

Tensile samples of EUROFER97-2 provided as plates, manufactured by Saarschmiede and rolled by Böhler Bleche Austria, and cut by wire EDM were used in this work, nominal dimensions: gauge length 11 mm, thickness 1.5 mm, width 2 mm. Tensile load was applied using a DEBEN MT5000 tensile rig, and temperature was controlled by a DEBEN HC550 Temperature Controller. Temperature was applied via heating from the sample grips, monitored by use of a R-type thermocouple, welded to the centre of the sample gauge. Samples were deformed at a strain rate of 0.1 mm/min to fracture at room temperature, and target elevated temperatures 250°C, 350°C and 500°C. As the solder used to affix the monitoring thermocouple was expected to affect the mechanical response of the gauge, following temperature-monitored elevated temperature tensile testing, tests were repeated at the same target temperatures unmonitored, assuming the same heating of the gauge could be expected. In addition, a single sample (gauge dimensions: length 5.00 mm, thickness 1.48 mm, width 1.96 mm) was cyclically tested at target temperature 500°C – 97 cycles were performed, consisting of loading to a stress of 430 MPa, at which the sample was held for 4 seconds, before unloading to 5 MPa. The lack of a compressive stage produced a high stress ratio between maximum and minimum cyclic stress, which would be expected to return a low ratcheting effect, necessitating a high peak stress to ensure notable ratcheting effect despite high stress ratio.

A monochromatic beam, energy 90 keV was used in these tests, and diffraction data was collected continuously during testing, at a scan rate of 2.128 seconds per frame. Diffraction data was analysed using MATLAB and DAWN [258], [259] to yield lattice strain, diffraction elastic constants, and dislocation density.

X-ray computed tomography characterisation of a room temperature tensile sample was also performed. A 90 keV monochromatic beam was used to collect projections through the sample using the I12 high resolution imaging camera, optical modules M3 and M4 (resolution 3.24x3.24 um per pixel and 1.3x1.3 um per pixel respectively). Tomographs were taken at regular intervals during plastic deformation, reconstructed at Diamond Light Source, and were processed in MATLAB to evaluate the onset of necking, and formation of microvoids within deformed samples. During projection collection deformation was paused, and the drop in stress corresponding to this hold time is indicated in Figure 4.5.

Fractographs of failed samples at all test temperatures were collected on a TESCAN MIRA3 scanning electron microscope at 20kV, working distance indicated on images. EBSD characterisation of the EUROFER97 sample in the undeformed state and in the deformation region of failed room temperature tensile samples was also performed. The MTEX toolbox [255], [256] was used to analyse grain structure in MATLAB from these images, and change in texture as a result of deformation was evaluated.

An extensometer was not used in this work, and sample extension was measured from the displacement between sample grips, leading to an initially non-linear extension-load relation, which came about as the result of frame compliance. In order to ensure accuracy of recorded results, the expected linear behaviour observed was extrapolated back (from data at the points surrounding half ultimate tensile stress), replacing displacement measurements that deviated from the projected displacement by more than 2.5x the displacement resolution. Quoted strain must therefore be viewed as a nominal value only, allowing comparison only between samples within this study, and not applicable on a broader level.

4.3.2 Dislocation Density Analysis

The dislocation density during loading of tensile and cyclic samples was evaluated by way of the full width half maximum (FWHM) of diffractogram peaks. Diffractogram peak broadening (β_T) is attributed to domain size, instrument broadening (β_i), and dislocation populations. The effects of instrumental broadening are removed by way of a CeO_2 standard – the instrument induced broadening subtracted on the basis of the Pseudo-Voigt function's Gaussian/Lorentzian fraction between $\beta_S = \beta_T - \beta_i$ in the purely Lorentzian case, and ${\beta_S}^2 = {\beta_T}^2 - {\beta_i}^2$ to isolate the sample induced broadening (β_S).

Of the two principal sample induced broadening contributions, domain size is constant, whilst dislocation density is anisotropic, the equation describing X-ray peak FWHM being the modified Williamson-Hall (mWH) equation, as below:

$$(\Delta K)^2 \approx \left({}^{0.9}/_{D_0}\right)^2 + \frac{\pi m^2 b^2}{2} \cdot \rho K^2 C \pm O(K^4 C^2) \tag{4.1}$$

Where ΔK is the peak FWHM, D_0 is the domain size, b is the Burgers vector, m is the effective outer radius of dislocations, K is the peak position, ρ is the dislocation density, and C is the contrast factor of the grain family. Higher order terms are considered negligible relative to dislocation and domain size contributions and are disregarded (denoted by the $O(K^4C^2)$ term). The dislocation density is then evaluated by way of the gradient of the linear relationship between peak FWHM and the K^2C term. The peak contrast factor is controlled by the character of dislocation affecting the broadening – the contrast factors of edge <110> and screw <111> dislocations were estimated on the basis of the EUROFER97 contrast factors determined in our previous work (Chapter 3), using the quasi-linear temperature dependency summarised in the Appendices Table 0.1.

The presumed edge fraction of dislocation density was varied between 0 and 1 in 0.01 increments, effective contrast factor utilised in mWH fitting taken as a linear combination of edge and screw contrast factors weighted by relevant fraction. Given the predicted linear relationship between the K and KC terms, maximised R^2 factor was used as a fitness parameter, meaning dislocation density and edge/screw fraction were estimated during deformation.

4.3.3 Lattice Strain Analysis During Cyclic Testing

2D diffraction patterns collected in-situ were azimuthally integrated over 30° segments centred around those directions parallel and perpendicular to applied load. The resulting diffractograms were peak fitted using a Pseudo-Voigt function used to evaluate shifting peak position with load. Changing peak centroid position provides a measure for lattice strain (ε) of individual grain families:

$$\varepsilon_{hkl} = \frac{{q_{hkl}}^0}{q_{hkl}} - 1 \tag{4.2}$$

Where q_{hkl}^0 is the unstrained peak centroid position and q_{hkl} is the loaded peak centroid position. The diffraction elastic constant relates lattice strain to stress (σ) by the equation:

$$\sigma = \varepsilon_{hkl} E_{hkl} \tag{4.3}$$

In order to avoid possible error in determination of q_{hkl}^0 introduced in the initially non-linear sample loading, equation (4.2) was substituted into equation (4.3), and diffraction elastic constants were evaluated from the intercept of linearly fitted stress-1/q_{hkl} data.

4.4 Results & Discussion

4.4.1 Microstructure

The grain structure of the EUROFER97-2 utilised in this work is demonstrated in Figure 4.1, characterised by EBSD mapping of the undeformed sample. Rolling employed during sample fabrication has produced very limited effect on sample microstructure: the sample presents a homogeneous distribution of equiaxed grains with limited texture, exhibiting only weak evidence of combined α-fibre and γ-fibre consistent with previous texture analysis of rolled bcc metals [315]. The grain size determined from area weighted averaging of EBSD determined grain equivalent radius as 3±2 um, with mode grain size 1.6-2 um and the unweighted mean being 1.7 um. The Heyn lineal intercept method meanwhile returned a grain size of 1.56 um.

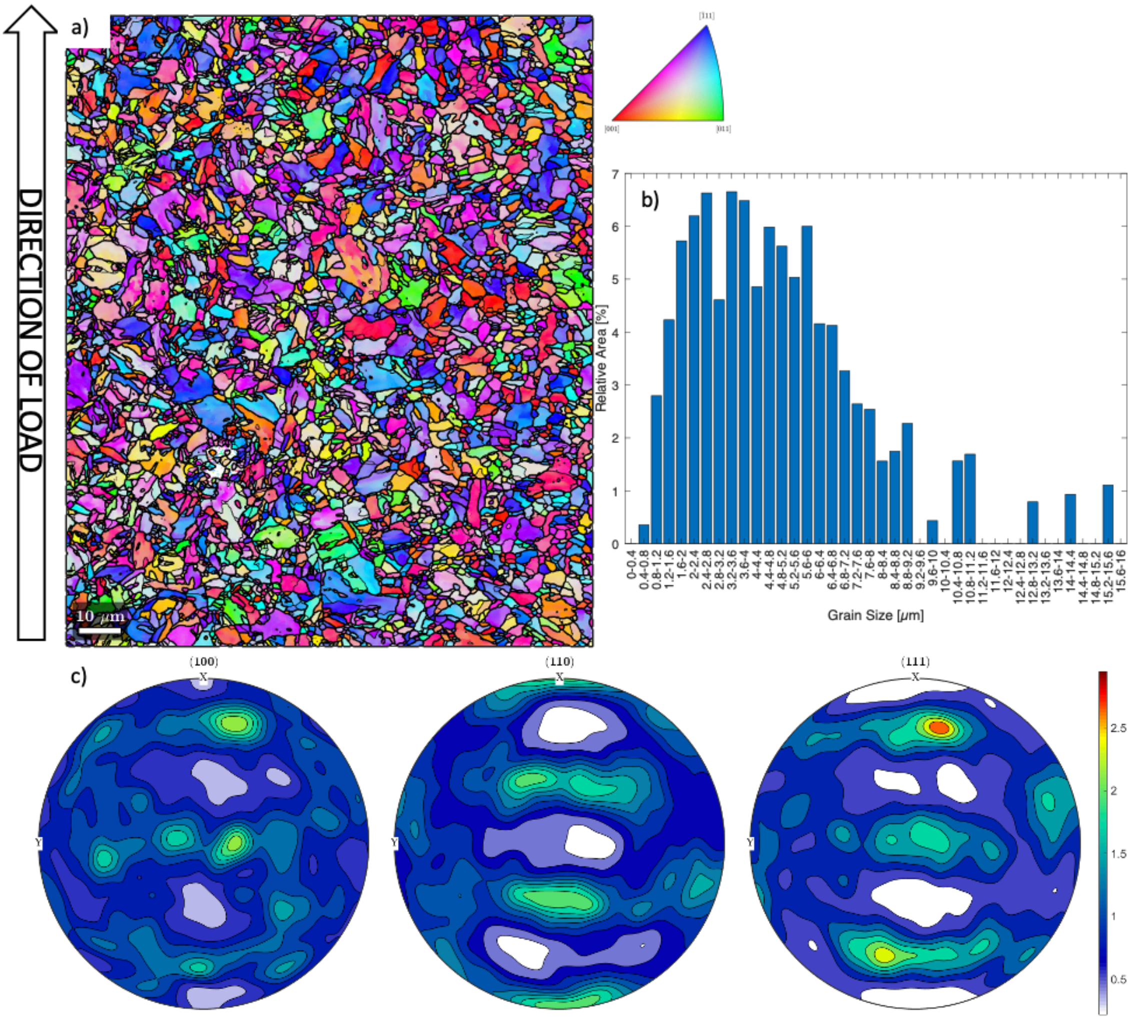

Figure 4.1 a) EBSD map of EUROFER97 high angle grain boundaries (>15^o) shown in bold, low angle grain boundaries (<10^o) outlined lightly, b) grain statistics histogram weighted by relative area, and c) pole figures produced during EBSD mapping.

4.4.2 Tensile Testing

The macroscopic results of tensile testing are collected in Figure 4.2, corrected tensile data presented. Yield stress was evaluated as the 0.2% offset stress, recorded in Table 4.1, in addition to ultimate tensile stress and total elongation. Also presented in the percentage area reduction, determined from the fractographs of the post-test sample surfaces are collected in Figure 4.3. Orientational effects with respect to loading direction are not discussed, given the weak texture observed in Figure 4.1, and the lack of strong orientational influence previously reported when comparing yield properties of batch 1 and 2 EUROFER97 [36].

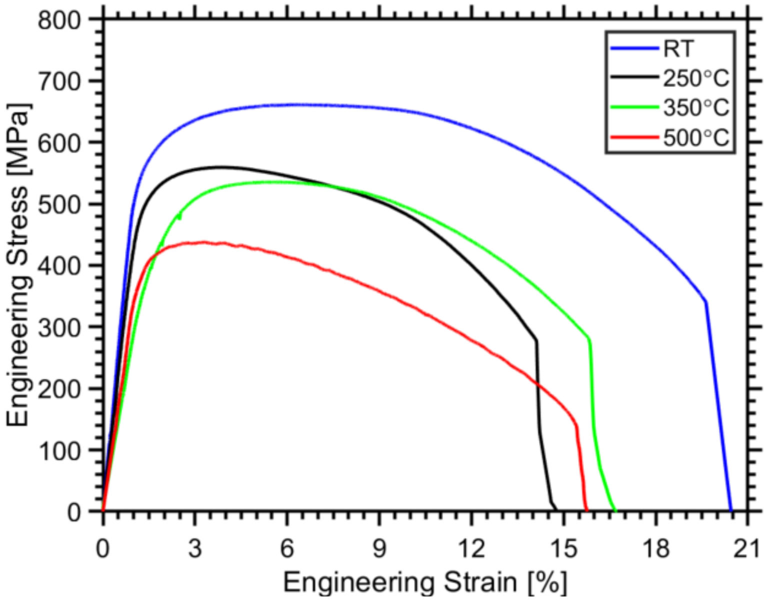

Figure 4.2 Stress strain curve of EUROFER97 tensile sample deformed at varied nominal temperature. Data plotted for sample without thermocouple monitored temperature, corrected to remove initial non-linearity by projecting linear behaviour back to axis intercept.

Considered on a macroscopic level, the results of tensile testing show limited degradation of strength across the temperature range considered, and a fall in total elongation at intermediate temperatures giving way to increased total elongation at high temperature. The collected results are in agreement with previously reported data for EUROFER97-1 and EUROFER97-2 products [36], [42], [50], though total elongation can be compared in trend only, given the nominal engineering strain reported.

The fractographs collected in Figure 4.3 all demonstrate heavily dimpled surfaces of the cup and cone type, indicative of ductile fracture under the tensile mode, transitioning to shear lips towards the edges of the sample – particularly the shorter cross section edges. The room temperature surface exhibits a greater degree of shearing, two sheared valleys formed at the edges of this sample. The high temperature fracture surfaces (350 and 500°C) also exhibit tear mode fracture evidenced by the formation of channels between microvoids as depicted in Figure 4.4b), presumed to be as a result of larger microvoid formation with increased temperature. The dimples formed are largely equiaxed and suggest even, tensile mode ductile fracture at all temperatures.

High magnification imaging of the cup sites (Figure 4.4a) indicated the presence of micron-scale inclusions at the base of dimples, expected to be carbides $M_{23}C_6$, MX, etc. Increased test temperature led to a rapid increase in dimple cup size, the failed RT sample exhibiting dimples less than 5 um in diameter, while the 500°C sample exhibited dimples of diameter 10-20 um. The low density and size of microvoids in the room temperature sample support the lack of microvoid formation observed using tomography – the inclusions which nucleate microvoids are too small to be observed given the resolution used, and only the largest dimples correlate to microvoids that could be reliably imaged. The results of fractography suggest future tomographic study of tensile samples at around 300°C may be of more utility in identifying the onset of tearing mode fracture between larger microvoids to better understand the processes of fracture in EUROFER97.

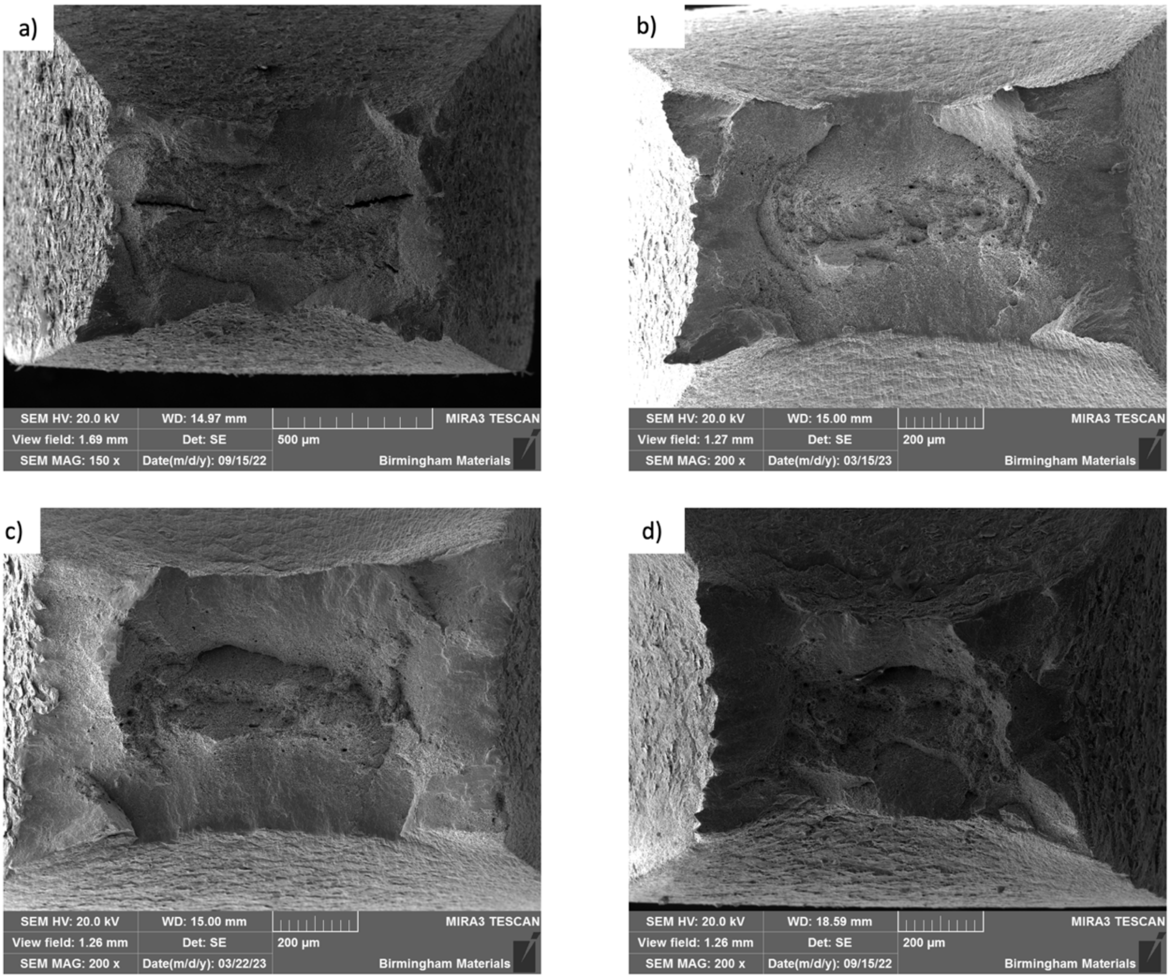

Figure 4.3 Fractographs taken from failed EUROFER97 samples at a) room temperature, b) 250℃, c)350℃ and d) 500℃, imaging parameters shown in ribbon

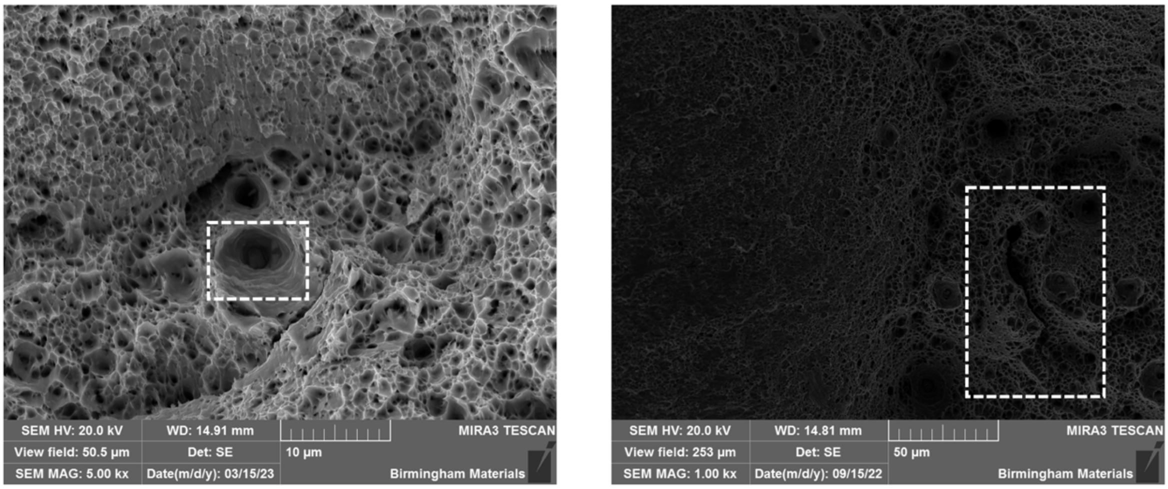

Figure 4.4 Details from fractographs taken from failed EUROFER97 samples at a) 250℃ demonstrating presence of inclusions at dimple base, and b) 500℃ demonstrating tearing between microvoids. Imaging parameters shown in ribbon.

Table 4.1 Macroscopic tensile testing data results derived from stress-strain curves and fractographs. Thermocouple measured temperature is shown in [] alongside nominal temperature.

Test temperature [^{o}C]	Yield Strength [MPa]	Ultimate Tensile Strength [MPa]	Total Elongation [%]	Reduction in Area [%]
25	561	677	19.7	76.4
250 [250]	503	573	14.2	77.1
350 [333]	408	540	15.9	74.1
500 [460]	407	452	15.5	82.7

Reconstructed tomographs of EUROFER97-2 during room temperature deformation are collected in Figure 4.5. Figure 4.5 collects minimum sample cross-section with increasing strain, showing progression of necking through the plastic region – cross section area indicated on figure. Pores were identified through contrast thresholding of reconstructed projections, as shown in Figure 4.6 – pores verifiably reported only at strains above 30%, size limited by pixel resolution to those over ~50 um^2 (5 pixels).

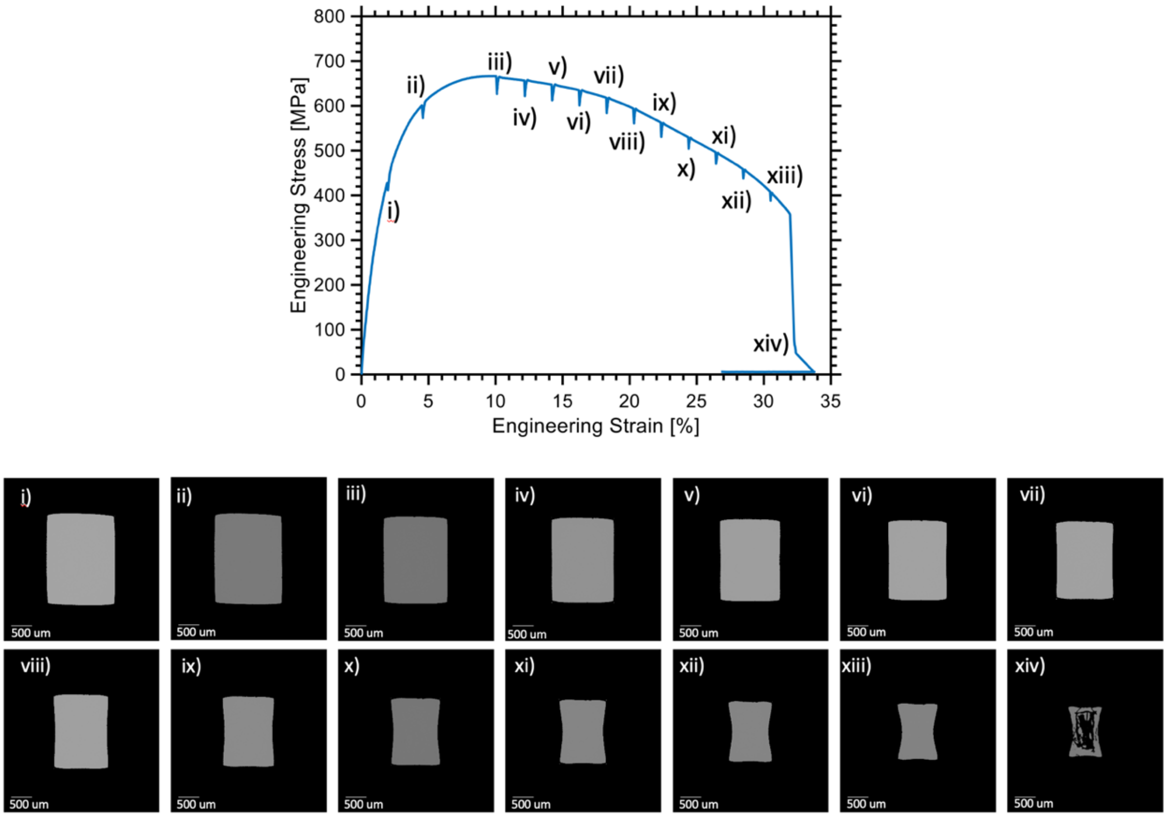

Figure 4.5 Stress strain curve of EUROFER97 tensile sample deformaed at room temperature, paused for X-ray computed tomography. Below: minimum cross sectional area of sample at the point of scan.

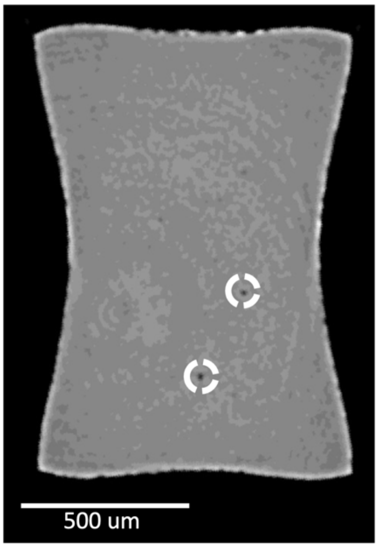

Figure 4.6 Cross section of EUROFER97 sample held at 30.5% engineering strain, contrast enhanced to demonstrate microvoids prior to fracture (circled)

4.4.3 Dislocation Density Evolution During Tensile Testing

The dislocation density evolution observed during tensile deformation is shown in Figure 4.7 and Figure 4.8, including both total dislocation density and edge/screw dislocation densities. The total dislocation behaviour seen across all samples can be divided into four stages: during Stage I dislocation density is essentially constant as the sample undergoes purely elastic deformation, this gives way to a sharp increase in dislocation density during Stage II corresponding to the onset of plastic deformation as grains begin to undergo microyielding as dictated by their relative orientation, before a dislocation density capable of perpetuating plastic deformation is established in Stage III, and finally there is a sharp drop in dislocation density with unloading and fracture in Stage IV. The transition from Stage I to Stage II can be more plainly seen from the dislocation-stress relation is presented in Figure 4.7b), wherein initial constant stress values transition to a linear $\sqrt{\rho}$-stress relationship, as per dislocation forest strengthening, until the stress approaches ultimate tensile stress and sample necking.

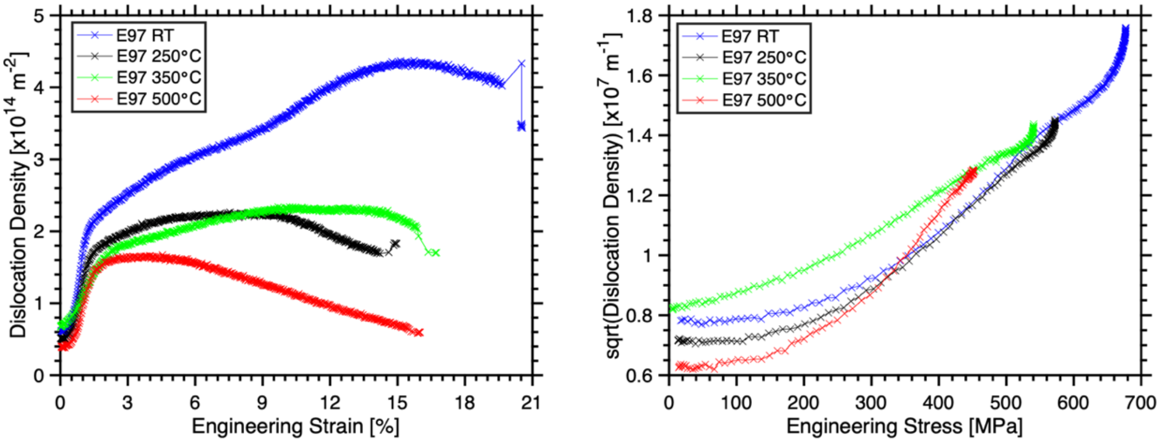

Figure 4.7 Total dislocation density evolution for EUROFER-97 samples at varied temperature with a) increasing engineering strain, and b) increasing engineering stress to UTS

Considering the changing character of recorded dislocation density, tests at room temperature, 250°C, and 350°C all presented similar dislocation behaviour: Stage I consisted of an initially near exclusive edge dislocation population, with increase of screw dislocation population in Stage II leading to a peak in screw fraction around macroscopic yield (peak screw fraction around 0.25), beyond which the screw dislocation fell slightly before reaching a stable level in Stage III, and falling away to nothing at the onset of Stage IV. Edge dislocation population continued to grow at the expense of the screw dislocation population during Stage III deformation of the room temperature and 350°C samples, though this behaviour was not observed in the 250°C sample. The 500°C sample presents significantly different dislocation behaviour – dislocation density initially presents with notable screw character during Stage I, transitioning to an almost 1:1 edge:screw ratio beyond Stage II.

Across the test temperatures investigated, increased temperature resulted in suppressed total dislocation during plastic deformation. This is the result of increased recovery with increased test temperature, as per the Arrhenius type recovery temperature relation, lowering the equilibrium total dislocation density attainable at higher test temperatures.

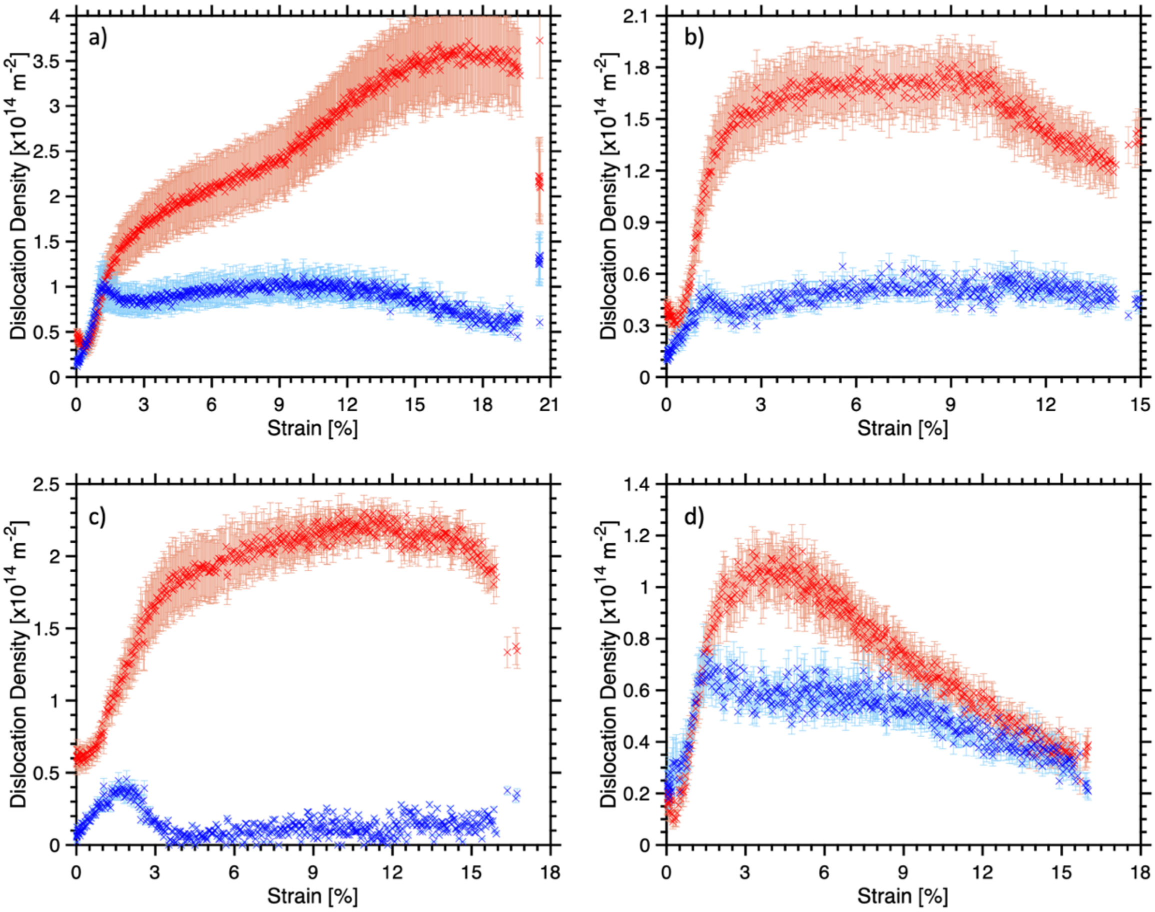

Figure 4.8 Evolution of edge/screw dislocation density character with for EUROFER-97 samples at a) room temperature, b) 250℃, c) 350℃, and d) 500℃. Edge dislocation density indicated in red, screw dislocation density indicated in blue.

The increased screw dislocation character observed comparing results between room temperature and 500°C test specimens is correlated to a change in dislocation mechanism with test temperature. The dominant edge character prior to plastic load at room temperature, 250°C, and 350°C suggests inhibited mobility of edge dislocations in the base alloy – screw dislocations introduced during fabrication are sufficiently mobile to cross-slip and annihilate in the absence of plastic stress.

Such observations are consistent with existing literature: transition from edge to screw dominated dislocation density evolution was previously seen in our previous work concerning EUROFER97 (Chapter 3). The transition point was not well determined in previous work, but the results presented here narrow the range of edge climb activation to 350°C to 500°C. Indeed, considering the work conducted presented in Chapter 3 concerning batch 3 EUROFER97, the range of activation can be further refined to 350-400°C, provided dislocation behaviour is consistent between sample batches. This assumption appears reasonable given the consistency of elastic response, grain size, and total dislocation density between batches.

The change in edge/screw dislocation mobility may also be further supported by an interesting feature of the dislocation density-strain plots: a peak in screw character at the onset of Region III, immediately followed by a fall-off in screw character to a stable value just below the peak. As discussed, at the onset of Region III increase in total dislocation density is blunted as a population of dislocations sufficient to propagate plastic deformation is established. Whilst total dislocation density is maintained at this level, dislocation populations are not static, and the edge and screw populations change to reach an equilibrium on the basis of relative annihilation rates, dislocation generation being limited by the plastic deformation applied. The result of this is a peak of dislocation density when formation is unconstrained, leading into a steady decline of one population in favour of the other as the total dislocation density ceiling is reached. This may explain the behaviour seen in these curves: the enhanced mobility of screw dislocations relative to edge promoting an enhanced screw annihilation rate, resulting in a situation where annihilated screw dislocations start to be replaced with edge dislocations when the plastic deformation imposed dislocation limit is reached.

4.4.4 In-Situ X-ray Diffraction Cyclic Testing

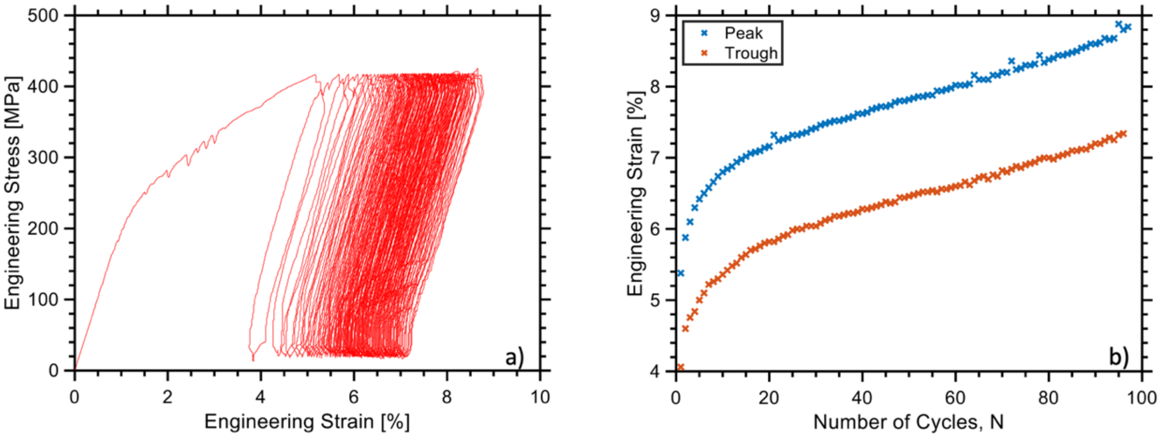

Figure 4.9 Asymmetric cycling loading of EUROFER97 sample at 500℃, load controlled at 430 MPa over 97 cycles showing a) stress-strain evolution and b) extreme engineering strain during cycling

The engineering stress-strain behaviour during cyclic loading is presented in Figure 4.9. The cycling presented in this work is asymmetric, lacking compression of equivalent amplitude to the tension applied, and hence leads to rapid accumulation of plastic stress in the test sample. The width of the asymmetric loops produced can be used as a means of qualitatively measuring cyclic hardening/softening – wider loops for the same stress amplitude indicating a softer material response. The tests conducted in this work found the hysteresis loop narrowed rapidly within the first 10 cycles, loop width becoming more stable beyond the 20th cycle. The hardening behaviour is also seen in the peak engineering strain and lattice strain measurements, though the presence or otherwise of lattice strain hysteresis loops of varied width cannot be verified: any apparent hysteresis loops formed in the grain families investigated so narrow as to fall within the bounds of experimental error. During the first 10 cycles the peak engineering strain increases rapidly from 5.4% to 7%, the rate of increase becoming constant between 10 and 20 cycles. Such cyclic hardening suggests the action of dynamic strain ageing, a state in which strain rate and test temperature are such that solutes in the matrix are able to diffuse to and pin the movement of dislocations, followed by so-called "jerky flow" when dislocations break free. This is borne out by the sawtooth serrations in the stress-strain curve (Figure 4.9a)), which correspond to intermittent movement of dislocations breaking free of solute atoms. This phenomenon has been observed during cyclic testing of other high chromium ferritic-martensitic steels in the range 250-450°C, but has not yet been investigated for EUROFER97.

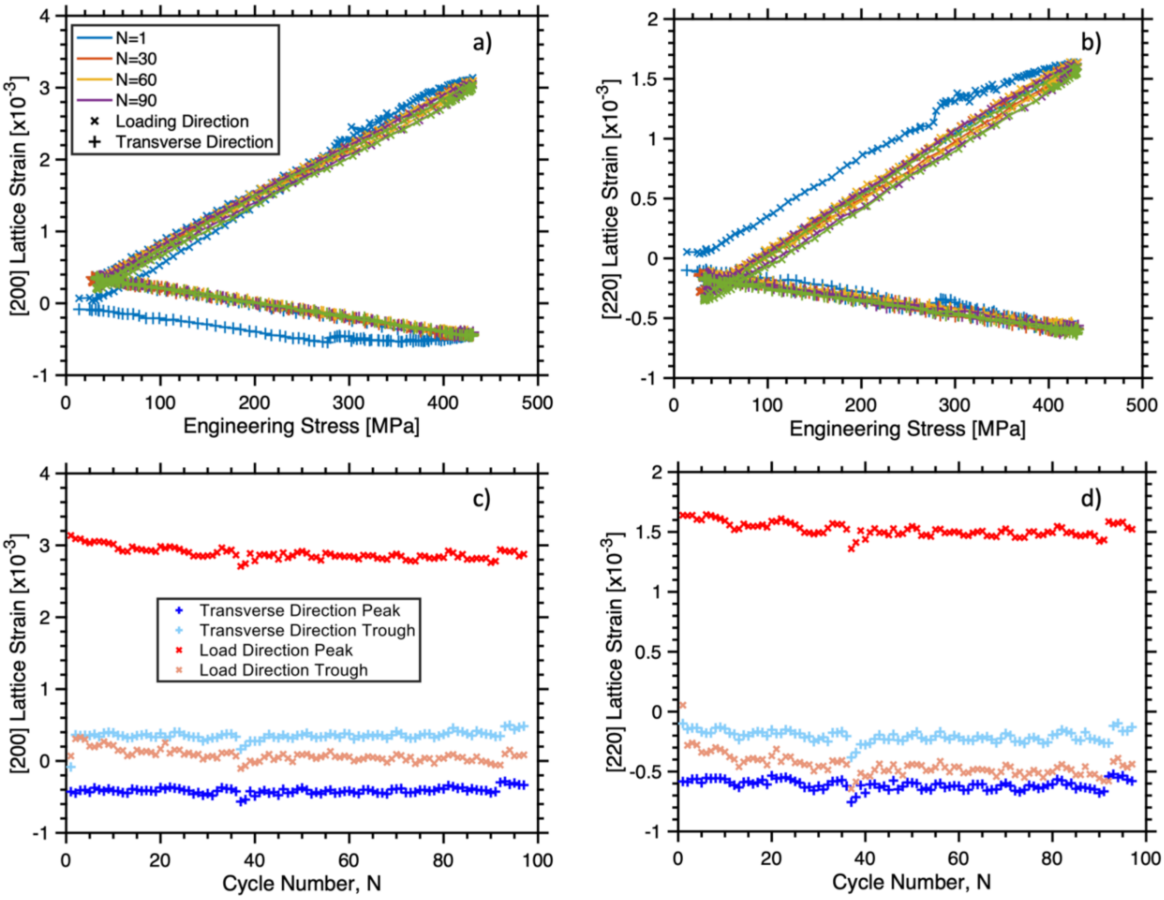

Figure 4.10 a)/b) Lattice strain evolution during asymmetric cycling, and c)/d) extreme lattice strain during cycling of the a)/c) compliant {200} grain family and the b)/d) stiff {220} grain family

The most notable feature of the lattice strain evolution is the progression of minimum load lattice strain. Beyond the first cycle each grain family develops a non-zero residual lattice strain that rapidly stabilises – the sign and magnitude of this offset differing between grain family orientations. The plastically compliant {200} plane exhibits a residual tension of $(0.36 \pm 0.05) \times 10^{-3}$ and $(0.05 \pm 0.05) \times 10^{-3}$ in the transverse and loading directions respectively, while the plastically stiff {110}/{220} plane exhibits a residual compression of $(0.21 \pm 0.04) \times 10^{-3}$ and $(0.34 \pm 0.06) \times 10^{-3}$ in the transverse and loading directions respectively. This reflects a redistribution of stress about the sample upon unloading; plastic deformation induced initially in compliant grains produces residual tension in these grains, and accompanying change in grain distribution imposes compression upon non-plastically deformed stiff grains. This phenomenon also provides explanation for the difference in lattice strain hysteresis loops developed during cyclic loading: previous work which has examined lattice strain evolution during cyclic testing using in-situ synchrotron XRD and neutron diffraction has demonstrated that lattice strain hysteresis loops demonstrate different widths dictated by their orientation and hence the level of plastic deformation they accommodate [316], [317]. It has also been observed in previous works which include tension/compression cycling of steel samples that residual lattice strain following unloading from tension rapidly levels off within the first 10 tension/compression cycles [316], [318], and the residual/peak lattice strains recorded in Figure 4.10 show a similar flattened response to increasing cycle number, in contrast to the steadily accumulation of macroscale engineering strain observed. Lattice strain redistribution as a result of tensile loading/unloading is an important consideration in textural evolution and modelling of polycrystalline samples under load.

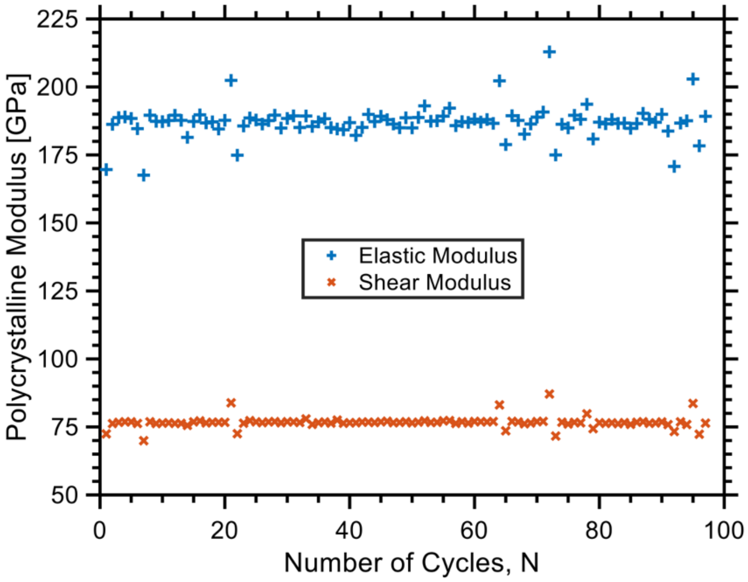

Figure 4.11 Change in polycrystalline elastic moduli with increasing cycle number

Whilst accumulation of plastic strain influences the residual strain recorded in Figure 4.9 and Figure 4.10, the elastic loading/unloading behaviour is consistent across the whole test cycle. The results presented in Figure 4.11 demonstrate little variation in elastic properties with cyclic loading – the elastic modulus remaining approximately constant at 185 GPa over the cycling considered, indicative of the stable composition of the EUROFER97 alloy. The value produced from evaluation of synchrotron samples in this way corresponds very well to values previously reported for the EUROFER97-2 alloy: a Young's modulus has previously been reported as 186.7 GPa at 450°C and 165.8 GPa at 550°C [314]. The multiple elastic characterisation of 500°C cyclic testing provides a useful means of tensile elastic analysis – averaging of the elastic constants reported during cyclic testing returns the following values: $C_{11}=160\pm10$ GPa, $C_{12}=83\pm9$ GPa, and $C_{44}=118\pm6$ GPa.

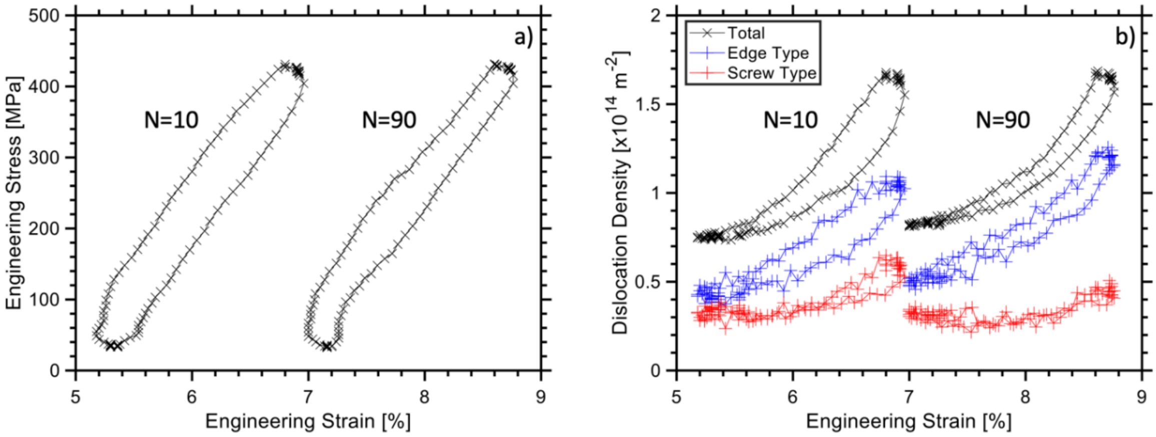

Figure 4.12 Hysteresis loops formed during asymmetric cyclic loading, in terms of a) engineering stress-strain, b) dislocation density-strain

Dislocation populations meanwhile are moderated by plastic deformation and therefore show more pronounced variation with cycle number, presented in Figure 4.13. The peak dislocation density falls off with increasing cycle number between 1 and 20 cycles, and a rapid decrease in dislocation generation rate during loading is also seen over this range. Outside this range peak dislocation density stabilises at $1.85\text{x}10^{14}$ m^{-2}, minimum dislocation density increases slowly, and the rate of dislocation generation during loading continues to fall, though the rate of decline is reduced. This corresponds to the hardening behaviour qualitatively observed with regard to hysteresis loop width:

increasing initial dislocation density increases the flow stress as movement of dislocations is inhibited by increased dislocation-dislocation interaction.

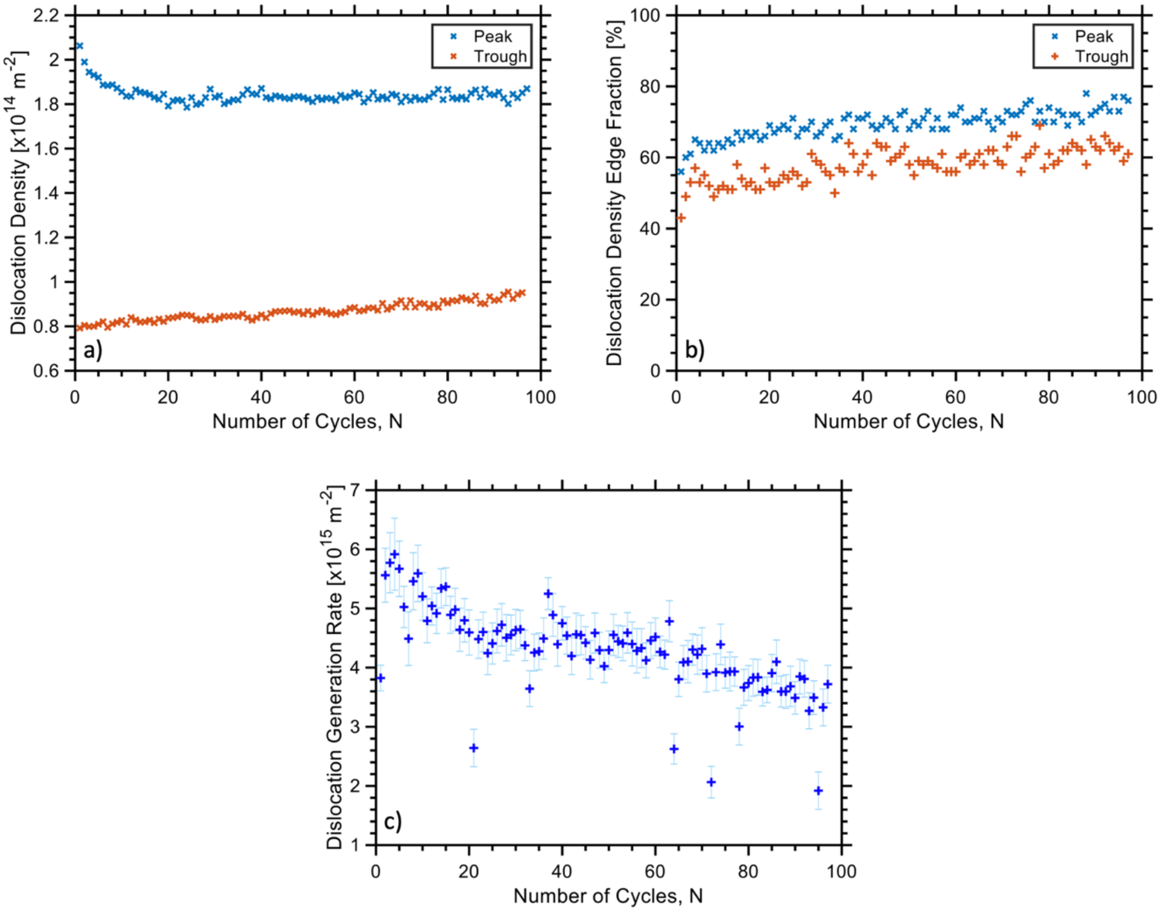

Figure 4.13 Change in dislocation behaviour with increasing cycle number, relating to a) extreme dislocation density population, b) dislocation density character denoted by dislocation density edge fraction, and c) dislocation generation rate with engineering strain, determined from linear fitting of load portion of the hysteresis loop

During elastic unloading dislocation density rapidly falls off as the result of thermally driven dislocation recovery. Thermally activated dislocation mobility is controlled by one of four competing mechanisms: edge dislocation climb, screw dislocation cross-slip, jogged screw dislocation glide, and solute drag.

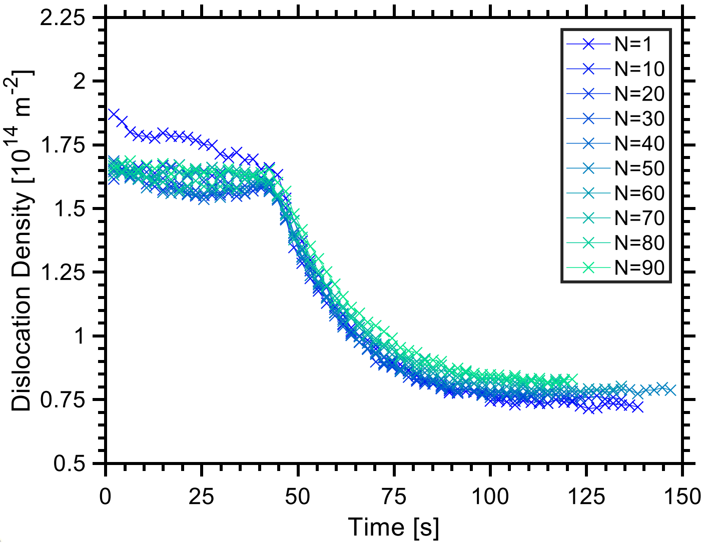

Figure 4.14 Recovery behaviour of dislocation density after reaching peak load with increasing cycle number

Several recent studies have attempted modelling of dislocation density in iron with limited success – application of the climb moderated Friedel model to annealing of ferritic steel showed poor fitting beyond the initially sharp decline [219], similarly poor fit reported in the fitting of cross-slip moderated recovery of ferritic steel [319]. The current work improves over previous research in terms of statistical significance, and considers dislocation character in the fitting of both Friedel and Verdier models.

Recovery behaviour with increasing cycle number is shown in Figure 4.14. Dislocation density can be expected to fall during elastic unloading as a result of thermally driven recovery, for which several models have been proposed. The original relaxation model proposed in this arena is that of Friedel [217] which considers dislocation annihilation by means of thermally induced cross-slip:

$$\boldsymbol{\frac{d\sigma_d}{dt}_S = -C_S \exp\left(\frac{-(Q_{0,S} - V_S\sigma_d)}{RT}\right)} \tag{4.4}$$

Or thermally induced climb:

$$\frac{d\sigma_d}{dt}_C = -C_C \frac{{\sigma_d}^3}{k_B T} \exp\left(\frac{-\left(Q_{0,C} - V_C \sigma_d\right)}{RT}\right) \tag{4.5}$$

In these models, σ_d is the stress due to dislocations, *t* is time after load release, C_S/C_C are scaling factors, $Q_{0,S}$/$Q_{0,C}$ are the activation energy for recovery processes, V_C/V_s are the activation volumes, R is the gas constant, and T is test temperature. The dislocation induced stress is calculated from the equation below:

$$\sigma_d = M\theta G b \sqrt{\rho} \tag{4.6}$$

Where M is the Taylor factor (taken as 3.06 for bcc materials), θ is a constant parameter 0.38, G is the shear modulus, b is the Burgers vector, and ρ is the dislocation density. Within this framework, total dislocation annihilation can be described as a linear combination of annihilation by cross-slip and climb. Substituting equation (4.6) into equation (4.5)/(4.4), numerically assessed gradient of the dislocation density-time curves during recovery were also fitted by the resulting equation:

$$\frac{d\rho}{dt} = -A_F {\rho_E}^2 \exp\left(B_F \sqrt{\rho_E}\right) - C_F \sqrt{\rho_S} \exp\left(D_F \sqrt{\rho_S}\right) \tag{4.7}$$

$$A_F = C_C \frac{2(M\theta b G)^2}{k_B T} \exp\left(\frac{-Q_{0,C}}{RT}\right) \tag{4.8}$$

$$B_F = \frac{M\theta b G V_C}{k_B T} \tag{4.9}$$

$$C_F = C_S \frac{2}{M\theta b G} \exp\left(\frac{-Q_{0,S}}{RT}\right) \tag{4.10}$$

$$D_F = \frac{M\theta b G V_S}{k_B T} \tag{4.11}$$

Where ρ_E and ρ_S refer to the dislocation density of edge and screw type dislocations respectively.

An alternate model proposed by Verider et al. (1999) [216] is also considered, the basis of this model is the consideration of relaxation as inverse load, and therefore derives its expression for stress relaxation from plastic relaxation strain such that

$$\frac{d\sigma_d}{dt} = -E\dot{\varepsilon_p} = -E\frac{\rho b^2 v_D}{M} \exp\left(\frac{-Q_0}{RT}\right) \sinh\left(\frac{\sigma_d V}{k_B T}\right) \tag{4.12}$$

Where v_D is the Debye frequency and $\dot{\varepsilon_p}$ is the plastic relaxation strain rate. Substituting equation (4.6) into equation (4.12), numerically assessed gradient of the dislocation density-time curves during recovery was also fitted by the resulting equation:

$$\frac{d\rho}{dt} = -A_V\, {\rho_E}^{3/2} \sinh\left(B_V\sqrt{\rho_E}\right) - C_V\, {\rho_S}^{3/2} \sinh\left(D_V\sqrt{\rho_S}\right) \tag{4.13}$$

$$A_V = \frac{2Ebv_D}{M^2\theta G} \exp\left(\frac{-Q_{0,E}}{RT}\right) \tag{4.14}$$

$$B_V = \frac{M\theta GbV_E}{k_B T} \tag{4.15}$$

$$C_V = \frac{2Ebv_D}{M^2\theta G} \exp\left(\frac{-Q_{0,S}}{RT}\right) \tag{4.16}$$

$$D_V = \frac{M\theta GbV_S}{k_B T} \tag{4.17}$$

Using A_V, B_V, C_V, and D_V as fitting parameters.

The results of recovery curve fitting are demonstrated in Figure 4.15– the fitting parameters recorded in Figure 4.16. The Verdier model fitting parameters can be easily converted to activation volume and activation energy as per equations (4.15)/(4.17) and (4.14)/(4.16) respectively, and the Friedel model activation volume of edge climb and screw cross-slip were determined from fitting parameters B_F and D_F as per equation (4.9) and (4.11). The climb and cross-slip activation energies cannot be easily deconvoluted from the pre-exponential scaling factors (C_C and C_S). In order to estimate activation energies previously reported values for the scaling factors in deformed ferrite were used: $C_C=2.3 \times 10^{-34}$ J Pa^{-2} s^{-1} and $C_S=10^{13}$ Pa s^{-1} [219], [319].

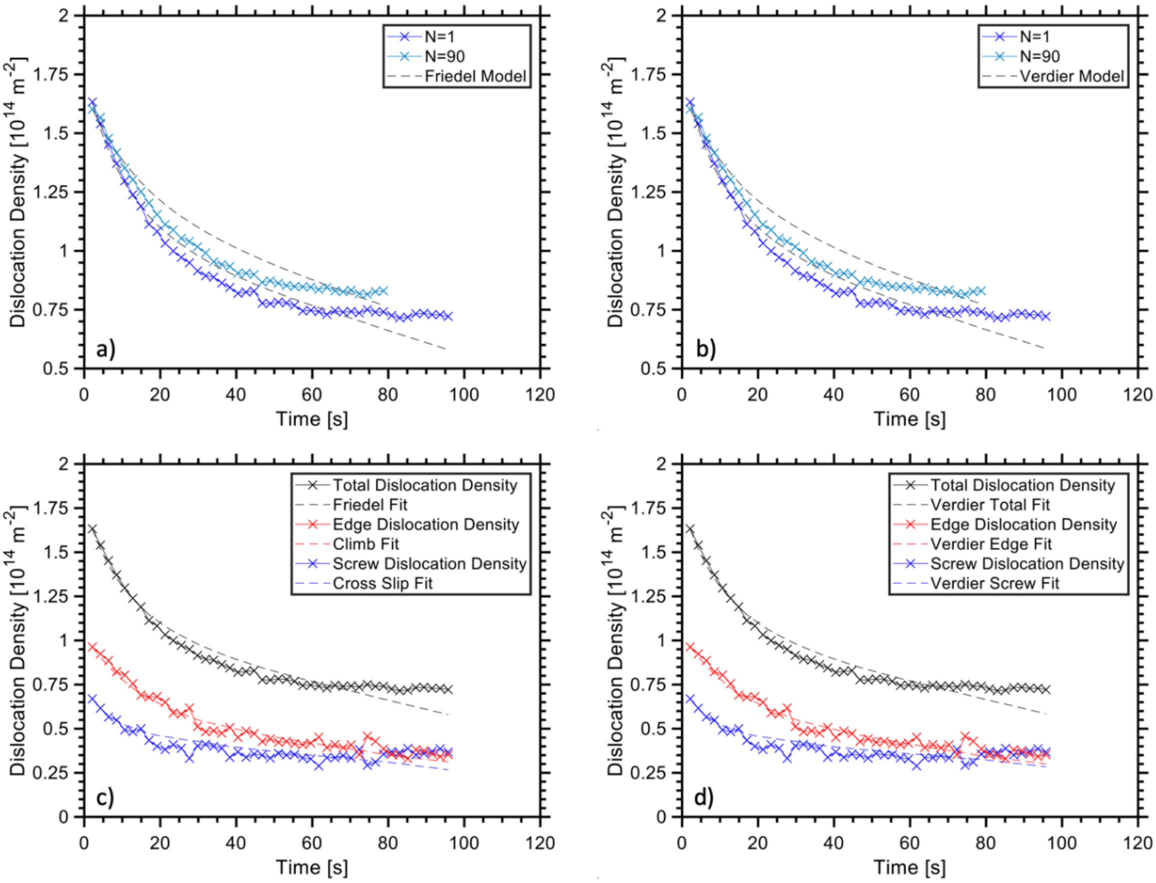

Figure 4.15 Fitting of dislocation recovery from peak load using the a/c) Friedel model, and b/d) verdier model. a/b) Total fitting shown at beginning (N=1) and nearing end (N=90) of cyclic testing. c/d) Fittings shown on the basis of dislocation type for N=1 recovery.

Modelling of the dislocation density recovery with the Friedel model returned an edge dislocation climb activation volume of 80±40 Å^3 (5 b^3) and a screw dislocation cross slip activation volume of 500±200 Å^3 (30 b^3), whilst the Verdier model produced an edge recovery activation volume value of 110±50 Å^3 (7 b^3) and a screw recovery activation volume of 500±200 Å^3 (30 b^3). Further, the Friedel model produced an estimation of climb activation energy of 79±5 kJ mol^{-1} and a cross-slip activation energy estimate of 140±10 kJ mol^{-1}, whilst the Verdier activation energy of edge dislocation recovery was determined as 180±10 kJ mol^{-1}, and the screw activation energy was determined as 220±20 kJ mol^{-1}. Fit parameters between both models showed only random variation with cycle number, and the values recorded are the average of all recovery fittings, error provided as statistical deviation.

The activation energy produced from the Verdier fitting of the screw dislocation density corresponds well to the self-diffusion activation energy of chromium in ferrite, 267±4 kJ mol^{-1} [320], suggesting the rate controlling step of screw dislocation movement is as a result of solute-dislocation drag, rather than cross-slip, which may go some way to account for the poor fit between the Friedel model applied and experimental data. Also to be considered is the assumption inherent in the approach used that thermally driven recovery is dominant over other mechanisms promoting dislocation movement – such as reverse slip driven by back-stress formed during loading. This assumption is based on the findings of previous work concerning loading/unloading of martensitic steels, which has shown the influence of back-stress diminishes relative to other recovery mechanisms with increasing temperature [321]. The models employed and results produced would likely be improved by the further inclusion of a term describing the contribution of back-stress to dislocation movement during unloading at the cost of greater complexity.

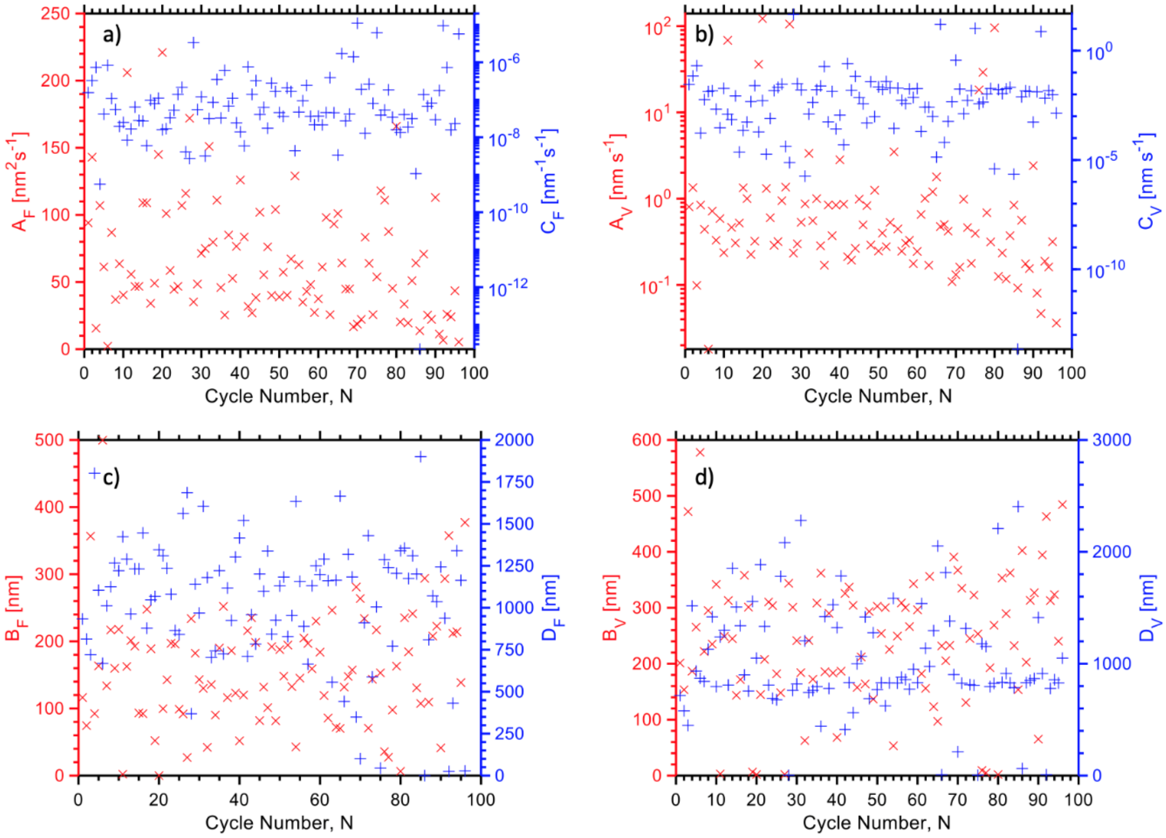

*Figure 4.16 Cyclic variation of fitting parameters of dislocation recovery from peak load using the a/c) Friedel model [Equation (**4.4**)/(**4.5**)], and b/d) Verdier model [Equation (**4.12**)]*

4.5 Conclusions

In this work, the deformation behaviour of batch-2 EUROFER97 was investigated over a range of test temperatures using in-situ synchrotron X-ray diffraction and X-ray computed tomography of tensile test specimens, and post-test characterisation of failed sample by fractography. Asymmetric cyclic loading allowed high temperature elastic properties to be determined with high accuracy, and dislocation density recovery activation energy and volume was determined for edge and screw dislocations. Tomography characterisation of room temperature EUROFER97-2 found very little evidence of microvoid formation before fracture, suggesting voids formed were beyond the resolution of the camera used, <1.3x1.3 um.

CHAPTER 5 MECHANICAL CHARACTERISATION OF V-4CR-4TI ALLOY: TENSILE TESTS UNDER HIGH ENERGY SYNCHROTRON DIFFRACTION

Tay Sparks[a], Duc Nguyen-Manh[b], Pengfei Zheng[c], Jan S. Wróbel[d], Damian Sobieraj[d], Michael Gorley[b], Thomas Connolley[e], Christina Reinhard[e], Yiqiang Wang[b*], Biao Cai[a*]
[a]School of Metallurgy and Materials, University of Birmingham, Birmingham, UK

[b]UK Atomic Energy Authority, Culham Science Centre, Abingdon, Oxfordshire OX14 3DB, UK

[c]Center for Fusion Science of Southwestern Institute of Physics, Chengdu, 610041, China

[d]Faculty of Materials Science and Engineering, Warsaw University of Technology, ul. Wołoska 141, 02-507 Warsaw, Poland.

[e]Diamond Light Source Ltd, Harwell Science and Innovation Campus, Didcot, UK

Published at the Journal of Nuclear Materials, Volume 569, October 2022, 153911
https://doi.org/10.1016/j.jnucmat.2022.153911

Tay Sparks completed the experimental work, analysed the data, and wrote and revised the manuscript. Biao Cai and Yiqiang Wang conceived and designed the experiment, and assisted in experimental work, revising the manuscript and data analysis. Duc Nguyen-Manh completed experimental modelling, wrote up and revised the density functional theory calculation. Pengfei Zheng provided materials for experimental work, and assisted in reviewing the manuscript. Jan Wrobel and Damian Sobieraj assisted in completing density functional theory calculation and reviewing the manuscript. Thomas Connolley and Christina Reinhard assisted in performing experimental work and reviewing the manuscript. Michael Gorley assisted in conceiving and designing the experiment and reviewing the manuscript.

5.1.Abstract

Vanadium base alloys represent potentially promising candidate structural materials for use in nuclear fusion reactors due to vanadium's low activity, high thermal strength, and good swelling resistance. In this work, the mechanical properties of the current frontrunner vanadium base alloy, V-4Cr-4Ti, have been interrogated using in-situ high energy X-ray diffraction (XRD) tensile testing at varying temperatures. The single crystal elastic constants of the samples were determined from the in-situ XRD data and used to evaluate results from density functional theory calculations. Polycrystalline elastic properties and Zener anisotropy were calculated from the single crystal elastic constants produced, revealing the effect of elevated temperature on the alloy’s elastic properties. These results characterise important thermomechanical properties, valuable in mechanical modelling, that will allow further and improved analysis of the structural suitability of V-4Cr-4Ti ahead of alloy adoption in the mainstream.

5.2.Introduction

In recent decades vanadium alloys have become a focus of attention in realising nuclear fusion, exhibiting more favourable activation properties, higher elevated temperature strength and lower swelling rate than reduced activation ferritic martensitic steels [322], [323]. These properties mark vanadium alloys as well suited for use as new structural materials in nuclear fusion reactors, which are required to be able to withstand high thermal fluxes, thermal cycling, and irradiation over a long lifetime without suffering structural degradation. Such application would see vanadium employed as a structural support for the self-cooled liquid Li breeder blanket array; attractive as this design is estimated to have a high power efficiency [323], and does not require the use of beryllium as a multiplier – removing the handling difficulties associated with beryllium [118][324].

The vanadium alloy V-4Cr-4Ti weight percent (V44 hereafter) represents a very promising candidate structural material for nuclear fusion reactors; the addition of chromium providing attractive solid solution strengthening, and the addition of titanium suppressing irradiation swelling and impurity embrittlement through the gettering of interstitial impurities into strengthening titanium precipitates (Ti(C,O,N)) [122], [127], [325]. Significant research has been conducted over recent years to fully establish the thermomechanical properties of this composition. V44 has been found to exhibit high yield strength to temperatures in excess of 700°C [117], [141], maintain its ductility significantly below room temperature [124], and has a viably low thermal expansion coefficient [322] – with these factors cumulatively describing an alloy with highly suitable thermomechanical properties.

In situ diffraction characterisation of tensile samples provides important information as to the lattice dependent physical parameters, in addition to typical mechanical properties. Both X-ray diffraction (XRD) and neutron diffraction are commonly employed to interrogate microstructural properties in this way, but it is notable that neutron diffraction cannot be effectively employed in the characterisation of vanadium-based alloys. This is the result of vanadium's very small coherent scattering cross section, which severely limits results producible from neutron diffraction. Synchrotron high energy XRD, however, can be used to effectively characterise vanadium based alloys, and provides useful information, representative of the bulk sample [326]. Substantial progress has been made over recent decades in the interrogation of such data, allowing for greater insight into the evolution and character of microstructural defects during mechanical testing [274], [327], [328]. As a highly accurate non-destructive characterisation technique, it is unsurprising there is already a well-established body of literature utilising *in situ* XRD to characterise crystallographic and thermomechanical properties of varied alloys. *In situ* XRD analysis at varying temperature has been used to establish evolving crystal phase and lattice parameters [243], [244], lattice strain (and hence the distribution of stress about crystal systems) [329]–[332], single crystal elastic constants (SCECs) [181], [333], [334], and the nature and density of dislocations generated during deformation [244], [335]–[337]. To the best of our knowledge, high energy in-situ XRD tensile testing has not been used to characterise the mechanical response of V-based alloys.

Mechanical properties can be concisely evaluated in the form of SCECs , the unique components of the material's elastic tensor from which the whole of a material's elastic response may be evaluated [338]. The single crystal elastic constants of pure vanadium at room temperatures have been experimentally studied using ultra-sonic pulse echoing on specially grown large single crystal samples [267], [339], [340]. More common is the theoretical investigation of SCECs using density functional theory (DFT) approaches, which has previously been applied to V-(0-50)Cr-(0-47)Ti alloys [341], [342]. It is well known that DFT calculations allow material properties to be determined from the fundamental electronic structure and energy of an atomic structure, giving unique insight into atomic interaction and chemically driven elemental segregation[343]–[345]. Such results have long been used to supplement experimental data in materials discovery[346], [347]. However, DFT results have been found to be substantially improved when used in concert with experimental results [342]. To develop robust systems which are able to accurately calculate material properties, it is necessary to first ensure an experimental basis of results which may be used to augment modelled results exists. Despite the fact DFT based analysis of the elastic properties of V-Cr-Ti alloys already exists, to the best of our knowledge, experimentally determined values for the single crystal elastic constants of the V44 alloy at room and high temperatures have yet to be reported.

In this work, *in situ* real-time XRD characterisation is performed during tensile testing of a V44 alloy at room and elevated temperature (550 °C and 700°C), with results being analysed to determine thermomechanical properties, lattice strain evolution and single crystal elastic constants. The results presented in this work serve as a confirmation for the favourable thermomechanical properties of the V44 alloy. Furthermore, these results may be used as a basis from which more complete characterisation of the thermomechanical properties of V-based alloys. The single crystal elastic constants produced can be used to inform future theoretical modelling. DFT results produced using the Vienna Ab initio Simulation (VASP) package are then presented as a point of comparison for experimentally derived SCECs, and as a means of demonstrating the enhancement of DFT results through experimental correction.

5.3.Materials and Methods

5.3.1. Materials

The V44 SWIP-30 alloy analysed in this work was supplied by the Southwestern Institute of Physics (SWIP) [141]. A brief summary of the fabrication process first detailed in Fu et al.'s paper [141] is presented here. Over the course of fabrication, a 30kg ingot of SWIP-30 was prepared from >99.95% pure V/Cr/Ti powders, through a process of repeated re-melting, canning, and forming at high vacuum. This process resulted in plates of ~6 mm thickness, which were finally annealed at 1273-1293 K, producing homogeneous plates of high purity. The elemental composition of the alloys ultimately produced are collected in Table 5.1.

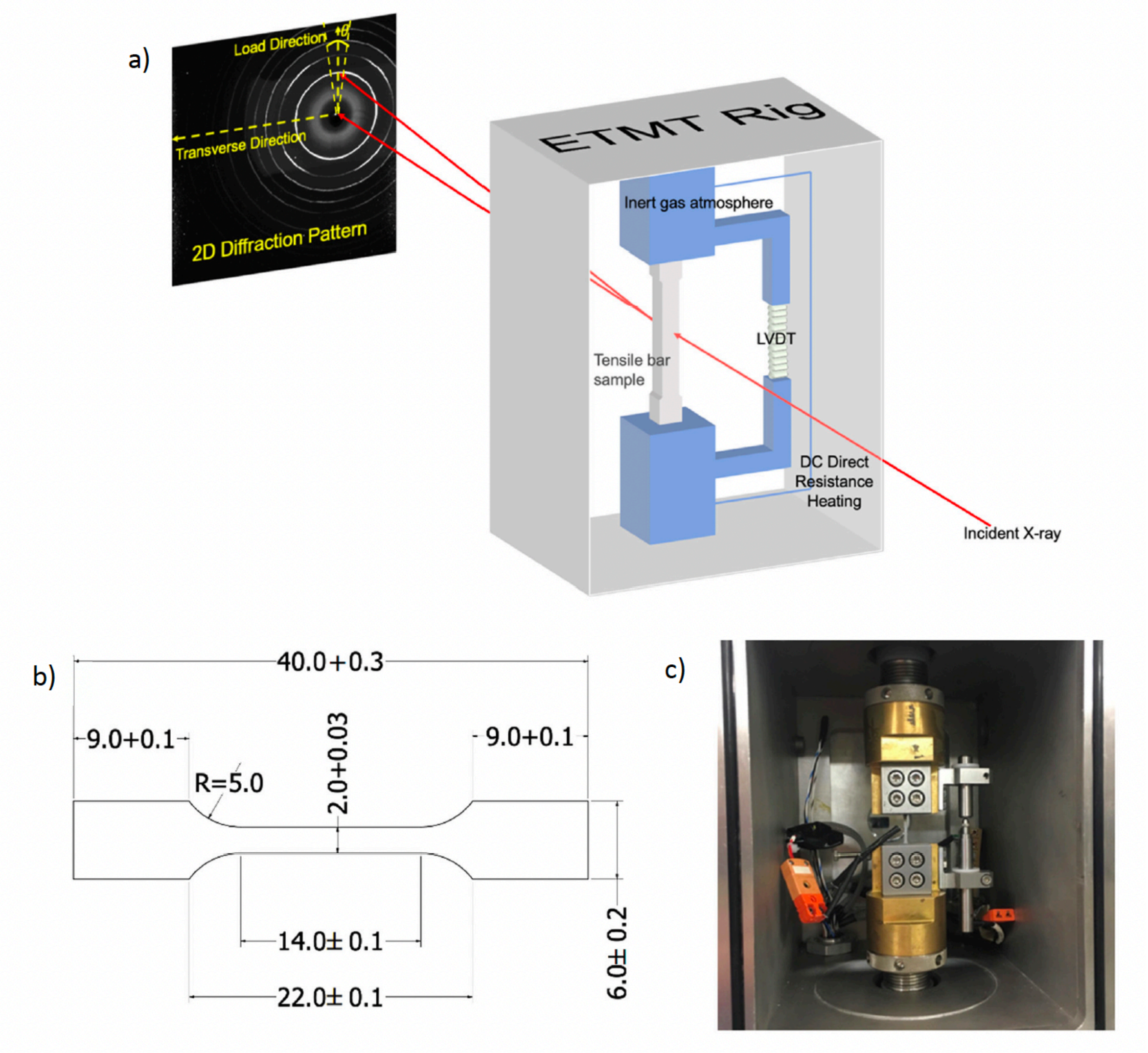

Figure 5.1 a) Schematic illustrating the experimental set-up of the in-situ ETMT tensile rig, photographed in c) (labelled angle $\theta = 30^{\circ}$). Subfigure (b) provides dimensions in mm for the dogbone tensile (sample thickness 1.0±0.05 mm) samples machined from V44 for in-situ tensile XRD characterisation

Table 5.1 Chemical composition of the SWIP-30 V44 plates [141]

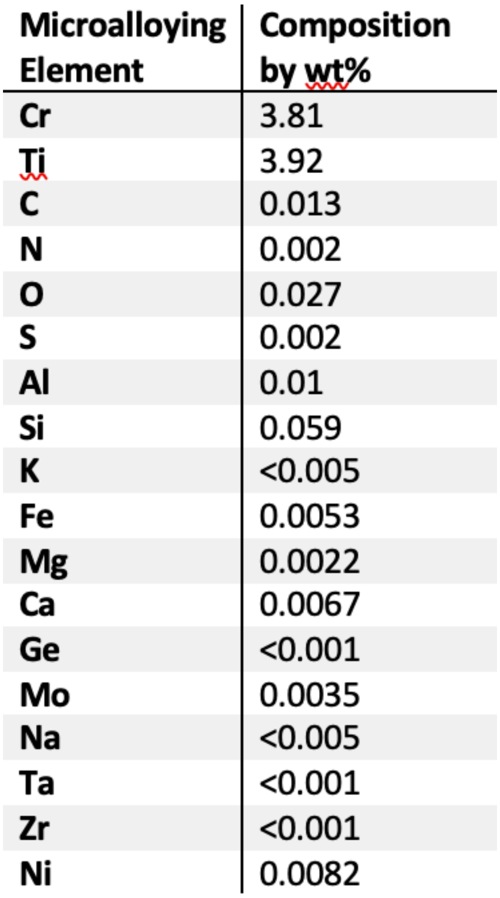

Microalloying Element	Composition by wt%
Cr	3.81
Ti	3.92
C	0.013
N	0.002
O	0.027
S	0.002
Al	0.01
Si	0.059
K	<0.005
Fe	0.0053
Mg	0.0022
Ca	0.0067
Ge	<0.001
Mo	0.0035
Na	<0.005
Ta	<0.001
Zr	<0.001
Ni	0.0082

5.3.2.Synchrotron Experiments

Synchrotron two-dimensional X-ray diffraction of the V44 SWIP-30 alloy was performed *in situ* during tensile testing at room temperature (RT), 550°C, and 700°C at the Joint Engineering, Environmental and Processing (I12-JEEP) beamline, Diamond Light Source Ltd (UK) [348]. A schematic example of the experimental set-up can be seen in Figure 5.1a). Flat dog-bone samples for tensile testing (Figure 5.1b) were machined from the as-received V44 alloy using electrical discharge machining, and then ground with 1200 grit SiC paper. Tensile tests were conducted in an Instron electro-thermal mechanical testing (ETMT) rig, with an applied displacement rate of 0.0003 mm s^{-1} prior to yielding, and 0.0013 mm s^{-1} after yield, measured by a linear variable differential transformer (LVDT). It should be noted that no strain gauge was attached to the sample, and so the strain shown was determined from the displacement measured by the LVDT. This means the strain recorded may be subject to inaccuracy due to displacement caused by extension in the loading array, unrelated to strain in the dogbone gauge length, particularly during initial loading. Temperature was applied through direct resistance heating across the samples. Tensile testing at 700°C failed during plastic deformation, and so analysis of this test is limited to elastic deformation and only the initial onset of plastic deformation. Test temperature was monitored through a type R thermocouple, spot welded to the edge of the dogbone samples at the middle of the gauge length. Diffraction patterns were collected using a large-area (42 × 42 cm) 2D Thales Pixium RF4343 detector with 2880 × 2881 pixel (each pixel 148 × 148 µm), each scan requiring a capture time of 1 s. The size of the monochromatic beam was 0.5 × 0.5 mm^2, with a beam of energy 80.03 keV (wavelength 0.015 nm). A CeO_2 reference sample (NIST Standard Reference Material 674b) was measured for calibration. Data collected from these experiments was analysed using the DAWN Science visualisation and processing software [258] in conjunction with the MATLAB data analysis software for peak fitting. Following tensile testing, fractographs of the tensile sample surfaces were collected using a JEOL JSM-6060 LV Scanning Electron Microscope, operated at 20 keV.

5.3.3. X-ray Data Analysis

Appropriate analysis of the XRD data collected during synchrotron experimentation can yield important baseline information as to the crystallographic structure of V44. The DAWN software allowed the intensity of the diffracted pattern to be integrated over two perpendicular 30° increments, producing diffractograms correlating to the diffracted beam parallel and perpendicular to the direction of load.

The diffraction peaks were fitted in MATLAB using a Pseudo-Voigt function to accurately record the centroid position, and full width half maxima (FWHM). The Pseudo-Voigt function is a convolution of a Gaussian and Lorentzian function, and is of the form:

$$I(x) = I(x_0) \cdot \left[\mu_G \cdot e^{-\pi \frac{(x-x_0)^2}{\beta_G^2}} + (1-\mu_G) \cdot \frac{1}{\frac{\beta_C^2}{\pi^2} + (x-x_0)^2} \right] + h_0 \tag{5.1}$$

Where *I(x)* is the intensity, μ_G is the fraction of the convolution accounted for by the Gaussian model, x_0 is the peak centre, β_G and β_C are constants associated with the Gaussian and Lorentzian fits respectively, and h_0 is the background intensity.

Further mechanical properties can also be determined from the response of the diffractogram peak positioning to stress. The lattice strain associated with each plane can be determined from the equation,

$$\varepsilon_{hkl} = \frac{d_{hkl} - d_0}{d_o} = \frac{q_0}{q_{hkl}} - 1 \tag{5.2}$$

where d_0 and q_0 are the initial *d* spacing of the plane and q-value of the peak centre prior to stress being applied respectively, and $\mathrm{d}_{\mathrm{hkl}}$ and q_{hkl} are the *d* spacing and peak centre q-value for a given stress. The diffractograms collected parallel to load exhibit the axial tension experienced by the sample, whilst the diffractograms collected perpendicular to load exhibit the radial compression.

5.3.4. Elastic Constant Calculation Using Density Functional Theory

The density functional theory (DFT) calculations were conducted using the VASP package [349], [350], with the projector augmented wave (PAW) method and the Perdew-Burke-Enzerhof (PBE) generalized gradient functional [351]. The PAW pseudoptentials were used with semi-core electron contribution with 10, 11 and 12 electrons treated as valence for Ti, V and Cr, respectively. The plane wave cut-off energy applied in the calculations was 500 eV. Total energies were computed using a Γ-centered Monkhorst-Pack mesh [352] of k-points in the Brillouin zone, with k-mesh spacing of 0.15 $Å^{-1}$, which corresponds to 4×4×4 Gamma-centred k-point meshes for a 4x4x4 supercell of BCC conventional unit cell containing 128 atoms. The representative structures of V-4Cr-4Ti alloy were obtained using Monte Carlo simulations using the cluster expansion model developed for the Cr-Ta-Ti-V-W system [343]. The disordered and short-range ordered structures were generated at 2000 K and 300 K, respectively. Both structures were optimized allowing the full relaxation of volume, ionic positions and cell shape with forces converged to 0.01 eV/Å. The convergence criterion for total energy was set to 10^{-5} eV/cell. To investigate the effect of the value of lattice parameter on the elastic properties of V-4Cr-4Ti alloy, the disordered structure was additionally optimized with a fixed volume corresponding to the experimentally determined lattice parameter at the room temperature. The elastic constants were calculated by deforming the optimized structure and analysing the corresponding variation of total energy as a function of components of strain[353], [354]

5.4 Results and Discussion

The results produced in this paper are collected below; with results gathered from crystallographic interrogation prior to load presented first. Lattice strain evolution as a function of stress is presented afterwards and used to calculate single crystal elastic constants (SCECs). These results, in conjunction with SCECs determined through DFT calculations, were used to evaluate the effect of short-range ordering in the alloy and the value of lattice parameter on the elastic properties of the alloy.

5.4.1. Synchrotron Testing

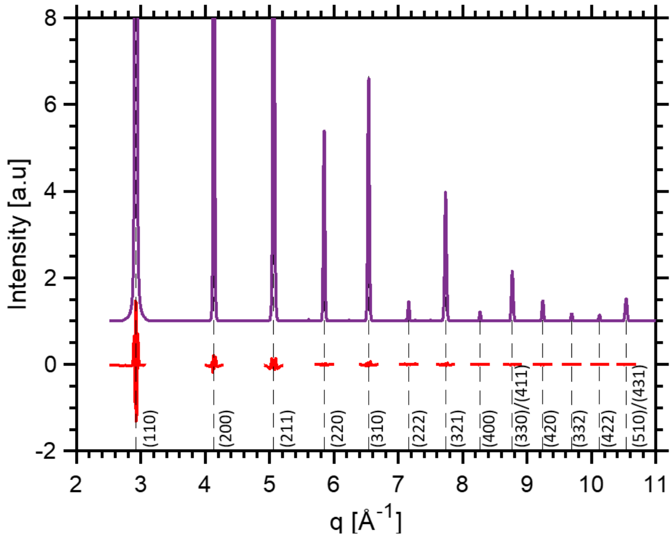

Figure 5.2 *Example figure showing single diffractogram with the residual after pseudo-voigt fitting is plotted below each peak. Diffraction pattern of the sample tested at room temperature analysed over a 30 degree increment centred on the direction of load.*

Figure 5.2 is an example diffractogram of the kind collected with evolving strain. The matrix phase was confirmed to be body-centred cubic, and this did not transform during heating up to 700 °C, or during deformation. The lattice parameter of the room temperature V44 sample was found to be 3.0396 ± 0.0006 Å prior to load, and this result agrees well with previously recorded experimental and theoretical values for this alloy (~2.994-3.03 Å [355] and 3.000 Å [341]). Error in the peak centre recorded was assessed by considering the effect of pixel size on fit results. Pixel binning limits imposed an error of ±0.002 Å^{-1} on the x-values recorded, and in order to evaluate the influence of this error on the peak position recorded, peak fitting was performed over one thousand iterations with each x-value randomised within its error bounds. The standard deviation of the histogram yielded from this iterative fitting was used as the error in peak position – this producing a result of approximately ±0.0006 Å^{-1}, consistent for all peaks.

5.4.1.1. Thermal Expansion

Diffraction data was also recorded during the ramp up from room temperature to test temperature (700 °C), during which time no load was applied. Thus, it has been possible to record the lattice parameter-temperature relationship exhibited by the V44 alloy, and in so doing evaluate its thermal expansion coefficient. The thermal expansion coefficient of the alloy was calculated as $10.26 \times 10^{-6} \pm 0.08 \times 10^{-6}$ K^{-1} at 500°C. This compares well to the literature value 10.3×10^{-6} K^{-1} [322], and confirms the favourably low thermal expansion of vanadium alloys when compared to other structural materials under consideration: 18×10^{-6} K^{-1} for 316 stainless steel [322] and 11.9×10^{-6} K^{-1} for oxide dispersion strengthened Eurofer 97 [265].

5.4.1.2. Tensile Testing

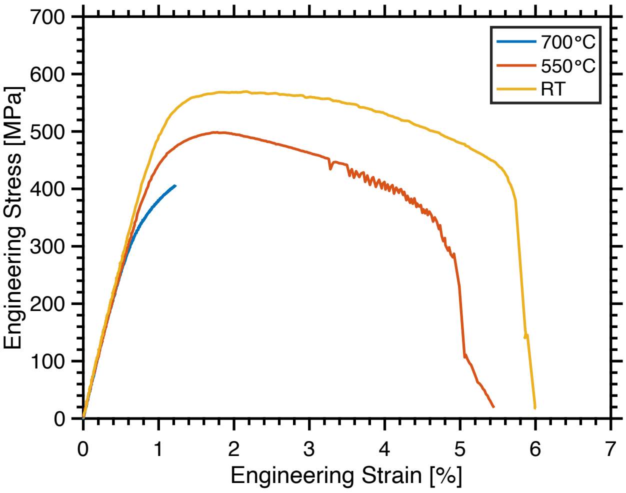

Figure 5.3 *Engineering stress-strain curve produced during the tensile testing of electron beam melted V44 at varying test temperatures*

The engineering stress-strain relations observed during tensile testing are illustrated in Figure 5.3. Using the 0.2% offset method, yield strength was calculated as $\boxed{420 \pm 10}$ MPa, $\boxed{466 \pm 6}$ MPa and 359 ± 1 MPa for measurements at room temperature, 550°C, and 700°C respectively whilst the engineering stress corresponding to ultimate tensile strength was found to be 570 MPa at room temperature, and 500 MPa at 550°C. When tested at 550°C, serrations are observed during plastic deformation beyond the ultimate tensile strength; this is likely the result of strain-ageing, by which dislocations move in 'jerky flow' governed by their capture and release by mobile impurities. The presence of this behaviour at elevated temperature may indicate increased dissolution of impurity from precipitates and increased solute impurity mobility. Serrated flow has previously been observed at intermediate temperatures (300-600°C [105], [122], [123], [162], [356], [357]), and is considered an undesirable effect due to the associated reduction in ductility – upheld here.

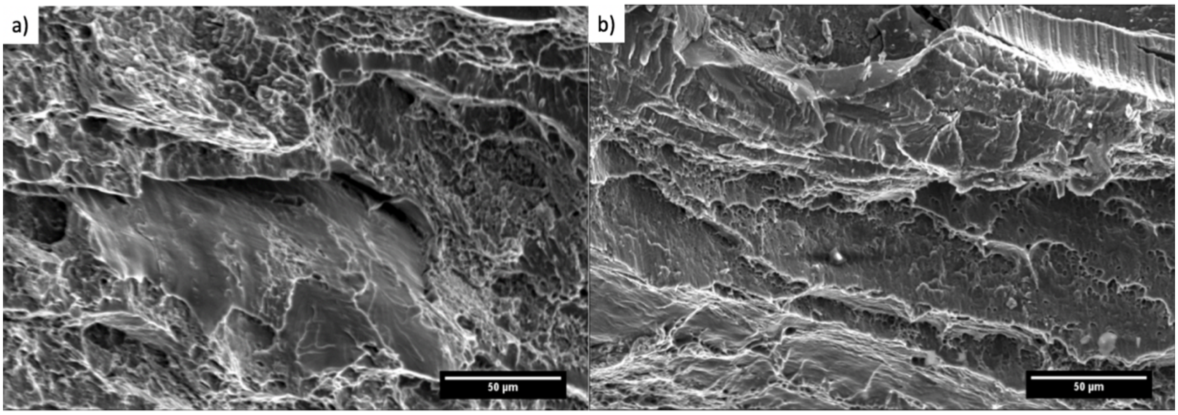

Figure 5.4 Fractographs collected from V44 tensile samples tested at a) room temperature and b) 550°C. Both samples demonstrate semi-ductile fracture given the presence, in addition to ductile dimples, of in a) cleavage and in b) striations.

Fractographs of the tensile sample surface after fracture at both temperatures are shown in Figure 5.4. These figures further demonstrate the character of sample fracture: when tested both at room temperature and 550°C the fracture surfaces exhibited ductile dimples to a degree, indicating semi-ductile fracture. However, the smooth shelf observed in Figure 5.4a) indicate a cleavage element to the fracture at room temperature. Similarly, Figure 5.4b) exhibits some deviation away from a purely ductile system in the sample tested at 550°C, with the presence of some striations across the sample surface. These striations may be taken as evidence of load cycling, further supporting the presence of strain ageing.

5.4.1.3. Lattice Strain Evolution During Load-Up

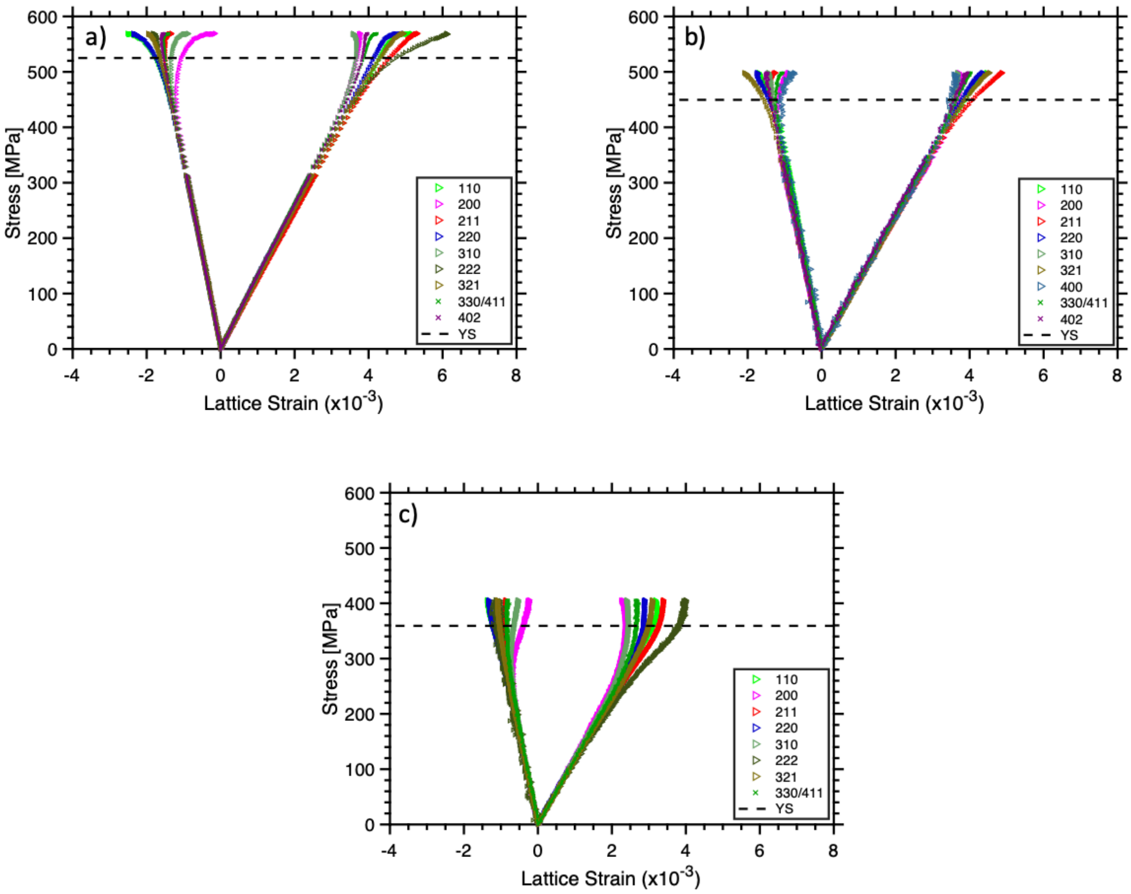

Figure 5.5 *Figures illustrating the compressive and tensile lattice strain experienced by the sample under stress when tested at a) room temperature, b) 550°C, and c) 700°C, with bulk yield stress (calculated from Figure 5.4 by the 0.2% offset method) overlaid.*

The lattice strain-stress relations for each indexed peak are shown graphically in Figure 5.5, from which the effect of grain orientation can be interpretated. Prior to yielding, up to stresses approaching 450 MPa in Figure 5.5a) 400 MPa in Figure 5.5b), and 200 MPa in Figure 5.5c), all grain families exhibit a linear response to applied stress corresponding to elastic deformation. From the gradients of this elastic response the diffraction elastic constant of each sample can be determined. Further, by comparing the positive tensile gradient and negative compressive gradient of the regions of linear extension in these plots, the diffraction elastic ratio can be calculated using the equation below:

$$\upsilon_{hkl} = {}^{E_{\parallel hkl}}/_{E_{\perp hkl}} \qquad \textbf{(5.3)}$$

where υ is the diffraction elastic ratio, $\mathrm{E}_{\parallel \mathrm{hkl}}$ and $E_{\perp hkl}$ are the elastic moduli of the lattice plane parallel and perpendicular to the direction of load, respectively. The results of this analysis, including diffraction elastic constants and diffraction elastic ratio, are collected in Table 5.2. Observing both the change in grain family stiffness (measured through diffraction elastic constant), and the onset and degree of non-linearity exhibited by each grain family at elevated temperature, the directional dependency of elastic response can be commented upon.

Table 5.2 *Crystal plane specific tensile Young's Modulus Poisson's Ratio at each test temperature, error included calculated from the error in gradient provided by MATLAB. Blank entries correspond to cases where the diffraction peaks produced were too weak to be accurately recorded.*

Lattice Plane	**Diffraction Elastic Constant (RT) / GPa**	**Diffraction Elastic Constant (550°C) / GPa**	**Diffraction Elastic Constant (700°C) / GPa**	**Diffraction Elastic Ratio (RT)**	**Diffraction Elastic Ratio (550°C)**	**Diffraction Elastic Ratio (700°C)**
{110}	125±2	121±2	114±1	0.37±0.03	0.33±0.03	0.35±0.03
{200}	130±1	121±1	125±1	0.38±0.02	0.40±0.01	0.37±0.02
{211}	123.2±0.8	119.3±0.8	114.4±0.6	0.35±0.01	0.37±0.01	0.35±0.01
{220}	130.4±0.8	122.6±0.7	117.1±0.6	0.391±0.009	0.349±0.008	0.377±0.008
{310}	131.1±0.7	120.1±0.6	120.5±0.5	0.378±0.008	0.357±0.007	0.345±0.007
{222}	129.1±0.6		107.7±0.4	0.373±0.007		0.354±0.005
{321}	128.3±0.5	118.6±0.5	113.7±0.4	0.383±0.006	0.372±0.005	0.355±0.005
{420}	131.4±0.5	125.8±0.5		0.387±0.005	0.407±0.004	

At room temperature the {222}, {110}, and {211} grain families appeared most elastically compliant, whilst the {200} grain family was elastically stiffest. Approaching bulk yield, it can be seen the planes begin to diverge from linearity; the stiff {200}, {310}, and {330/411} grain families move into plastic deformation at 400 MPa. This yielding causes a redistribution of accumulated stress among the grains, the pre-yield grains experiencing increased stress, and hence increased elastic strain – producing an accompanying non-linear response in the more compliant grain families. There is some variation in lattice plane dependent elastic response with test temperature. At 550°C, all grain families maintain a strongly linear response almost to the point of yield, and even during plastic deformation the deviation in grain family response is only slight. Indeed the diffraction elastic constants produced by the stiffest and most compliant grains only differ by ~6.5 GPa at this temperature. However, at 700°C the relative stiffness of each grain family is more distinct, and the linear response of each grain family breaks down at noticeably different stresses, suggesting a more directionally dependent elastic response at this temperature.

It is important to note there is some notable disagreement between the {110} and {220} curves recorded at room temperature: the diffraction elastic constants recorded being 125 ± 2 GPa and 130.4 ± 0.8 GPa respectively. This disagreement is unphysical as the diffracting planes contributing to both curves are the same, and so the diffraction elastic constants recorded are expected to agree with each other. Whilst the two values only differ by ~5.4 GPa, and so are still in reasonably good objective agreement, they fall significantly outside three standard deviations of one another. This points to an incomplete consideration of error sources within this analysis; the cumulative effects of detector sensitivity, software processing, and material inhomogeneity [358], [359] not exhaustively considered, though it must be noted these subtle sources of error are difficult to account for.

5.4.1.4. Single Crystal Elastic Constants

The polycrystalline elastic diffraction constants associated with each crystallographic plane can be used to evaluate the elastic modulus and single crystal elastic constants of the V44 alloy, using the Kroner model [193]. In this model, the diffraction shear modulus, G_{hkl}, follows the relation:

$$G_{hkl}{}^{3} - \alpha G_{hkl}{}^{2} - \beta G_{hkl} - \gamma = 0 \qquad \textbf{(5.4)}$$

Where α, β, and γ are constants ultimately derived from the single crystal elastic constants such that

$$\alpha = \frac{1}{5}(2\eta + 3\mu) - \frac{3}{8}(3K_M + 4(\mu + 3(\eta - \mu)A_{hkl}) \qquad \textbf{(5.5)}$$

$$\beta = \frac{3}{40}(6K_M\eta + 9K_M\mu + 20\eta\mu) - \frac{3K_M}{4}(\mu + 3(\eta - \mu)A_{hkl}) \qquad \textbf{(5.6)}$$

$$\gamma = \frac{3K_M\eta\mu}{4} \qquad \textbf{(5.7)}$$

These equations being expressed in terms of the cubic shear moduli ($\mu \; and \; \eta$), the bulk modulus (K_M), and the elastic anisotropy factor (A_{hkl}) defined below:

$$K_M = \frac{1}{3}(c_{11} + 2c_{12}) \qquad \textbf{(5.8)}$$

$$\mu = \frac{1}{2}(c_{11} - c_{12}) \qquad \textbf{(5.9)}$$

$$\eta = c_{44} \qquad \textbf{(5.10)}$$

In conjunction with the relation in Equation (5.4), the following Kroner model equations relating diffraction shear modulus to the experimentally determined diffraction elastic constants, E_{hkl}, and diffraction elastic ratios, ν_{hkl}, were used as a basis for data fitting.

$$\frac{1}{9K_M} - \frac{1}{6G_{hkl}} = -\frac{\nu_{hkl}}{E_{hkl}} \tag{5.11}$$

$$\frac{1}{G_{hkl}} = 2(\frac{1}{E_{hkl}} + \frac{\nu_{hkl}}{E_{hkl}}) \tag{5.12}$$

MATLAB was then used to identify appropriate values for the single crystal elastic constants (and hence α, β, and γ) so as to provide an optimised fit of the experimental data provided, whilst also satisfying the relations given in Equation (***5.4***), Equation (***5.11***), and Equation (***5.12***). The fit generated at the three temperatures by the Kroner model is demonstrated graphically in Figure 5.6a), Figure 5.6d), and Figure 5.6g). The single crystal elastic constants corresponding to this fit were then used in the Reuss and Voigt models [193], and the fit produced from these models is overlaid so as to compare the suitability of these models in describing the elastic anisotropy of the sample. It can be observed the Kroner model provides a better fit than the Reuss or Voigt plots, but the variation in the diffraction elastic properties is only slight at room temperature and 550°C– the elastic diffraction constant remains approximately constant over all lattice plane orientations, indicating largely isotropic elasticity, represented graphically in Figure 5.6b), c), e), and f).

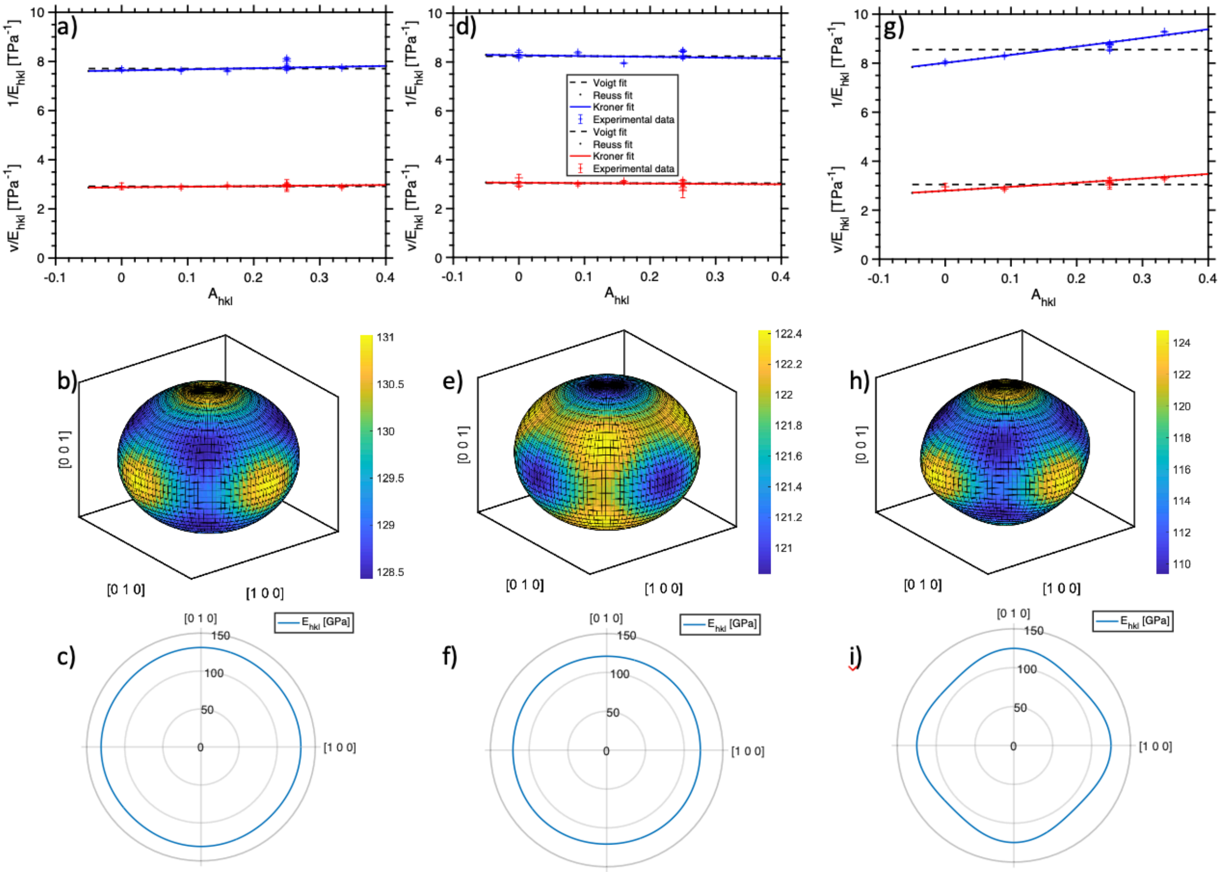

Figure 5.6 *Figures demonstrating the directional variation of V44's elastic properties: a), b), and c) at room temperature, d), e), and f) at 550°C, g), h), and i) at 700°C. Figures a), d), and g) demonstrate the dependency of the plane specific elastic constants on elastic anisotropy including the fit provided by the Voigt, Reuss, and Kroner models used to determine the single crystal elastic constants. The legend provided in Figure 6d) applies to a), d), and g). Figures b), e) and h) show the three dimensional variation of elastic modulus with direction, and figures c), f) and i) are a projection of this modulus-direction dependency onto the XY plane.*

Table 5.3 *Comparison of non-zero elastic tensor components and related elastic properties of the V44 alloy determined through experimentation and calculation. All elastic properties and tensor components given in GPa*

		C_{11} [GPa]	C_{12} [GPa]	C_{44} [GPa]	Z	υ	Polycrystalline Moduli		
							B [GPa]	*G* [GPa]	*E* [GPa]
Calculation	Short-range ordered 300K (a=2.9825 Å)	276.5 ±0.2	139.4 ±0.1	10.4 ±0.2	0.152	0.45 ±0.03	185.0	24.6	70.3
	Disordered 2000K (*a*=2.9825 Å)	285.1 ±0.8	136.2 ±0.9	16.5 ±0.3	0.222	0.43 ±0.03	185.9	31.9	90.1
	Disordered 2000K (*a*=3.0396 Å)	259 ±2	136 ±3	15 ±2	0.24	0.44 ±0.03	177.0	27.5	78.3
Experimental	In situ XRD at 298K	240 ±10	150 ±10	46.0 ±0.2	1.0 ±0.2	0.379 ±0.008	181 ±7	46.9 ±0.2	129.5 ±0.4
	In situ XRD at 823K	212 ±8	125 ±9	45.1 ±0.2	1.0 ±0.1	0.368 ±0.007	154 ±6	44.5 ±0.2	121.8 ±0.3
	In situ XRD at 973K	205 ±8	103 ±8	37.3 ±0.2	0.73 ±0.08	0.360 ±0.008	137 ±6	42.4 ±0.2	115.3 ±0.3

The single crystal elastic constants produced from this fitting are recorded in Table 5.3. The error associated with these values was calculated by observing the deviation of each value when the fitting was performed over ten thousand arrays, for which the diffraction elastic constant and diffraction elastic ratio were randomised within their respective error bars. The result at room temperature agrees well with theoretical values previously calculated for V-Cr-Ti alloys (and corrected from existing experimental data); C_{11} previously having been reported on the order $\sim 240 - 280$ GPa, C_{12} $\sim 110 - 130$ GPa, C_{44} $\sim 36.2 - 60$ GPa [341], [342].

Moreover, the difference in elastic diffraction coefficient between grain orientations provides some indication of Zener anisotropy ratio, when one considers the effect of elastic anisotropy, A_{hkl} – an indexing parameter reliant upon the plane orientations such that:

$$A_{hkl} = \frac{h^2k^2 + k^2l^2 + h^2l^2}{(h^2 + k^2 + l^2)^2} \tag{5.13}$$

Whereas the cubic Zener anisotropy ratio, Z, is dependent upon the single crystal elastic constants (C_{11}, C_{12}, C_{44}), defined by the relation:

$$Z = \frac{2c_{44}}{c_{11} - c_{12}} \tag{5.14}$$

In the case where Z>1 the diffraction elastic coefficient increases as A_{hkl} decreases, whereas when Z<1 the diffraction elastic coefficient increases with A_{hkl}, whilst Z=1 indicates a purely isotropic structure. As can be seen in Table 5.3 the Z value is 1.0 at both room temperature and 550 °C, indicating a very isotropic structure.

The elastic modulus recorded at room temperature is determined as 129.5 ± 0.4 GPa, consistent with the literature values of 121-140 GPa produced from previous analysis of variously fabricated V44 samples [322], [360]–[362]. The change in elastic modulus with increased temperature, is in fairly good agreement with the values suggested by the Young's modulus-temperature dependency previously observed [100], [360], [361]. In addition to this, whilst the temperature dependency of the Poisson's ratio of V44 has not been investigated, the value produced for Poisson's ratio at room temperature, 0.379 ± 0.008, agrees fairly well with the literature value of 0.36 [322]. The good agreement between these results and previously recorded physical properties provides a source of validation for the data fitting performed on the diffraction data.

5.4.2 Density functional theory calculations

The full components of the elastic tensor, calculated in Monte Carlo simulations detailed above, are collected in the Appendices, Table 0.3. As expected, the C_{ij} components calculated at room temperature for $i = 1 - 6, j = 4 - 6, i \neq j$ were very close to zero, and the variation between the sets of components C_{11}, C_{22}, and C_{33}, and C_{44}, C_{55}, and C_{66} was very slight – these being features common to cubic symmetry systems. As a result of this, the full tensor components have been condensed to C_{11}, C_{12}, and C_{44}. The single crystal elastic constants and associated elastic properties generated in this way are collected in Table 5.3. The values for C_{11}, C_{12}, and C_{44} presented in Table 5.3 are averaged from calculated values of equivalent components: C_{11} from C_{11}, C_{22}, and C_{33}, C_{12} from C_{12}, C_{13}, and C_{23}, and C_{44} from C_{44}, C_{55}, and C_{66}. The polycrystalline shear moduli presented are calculated via the Voigt-Reuss-Hill method such that:

$$G_{VRH} = 0.5 \times (G_{Voigt} + G_{Reuss}) \quad \textbf{(5.15)}$$

where

$$G_{Voigt} = \left({}^{1}\!/_{5}\right) \times (C_{11} - C_{12} + 3C_{44}) \quad \textbf{(5.16)}$$

$$G_{Reuss} = \frac{5}{4(S_{11} - S_{12}) + 3S_{44}} \quad \textbf{(5.17)}$$

Sij being components of the compliance tensor, defined by $[S]=[C]^{-1}$. The polycrystalline bulk moduli and elastic moduli are then calculated in the same way as reported in Tang et al.’s recent work [363].

5.4.2.1. Atomic Short Range Ordering

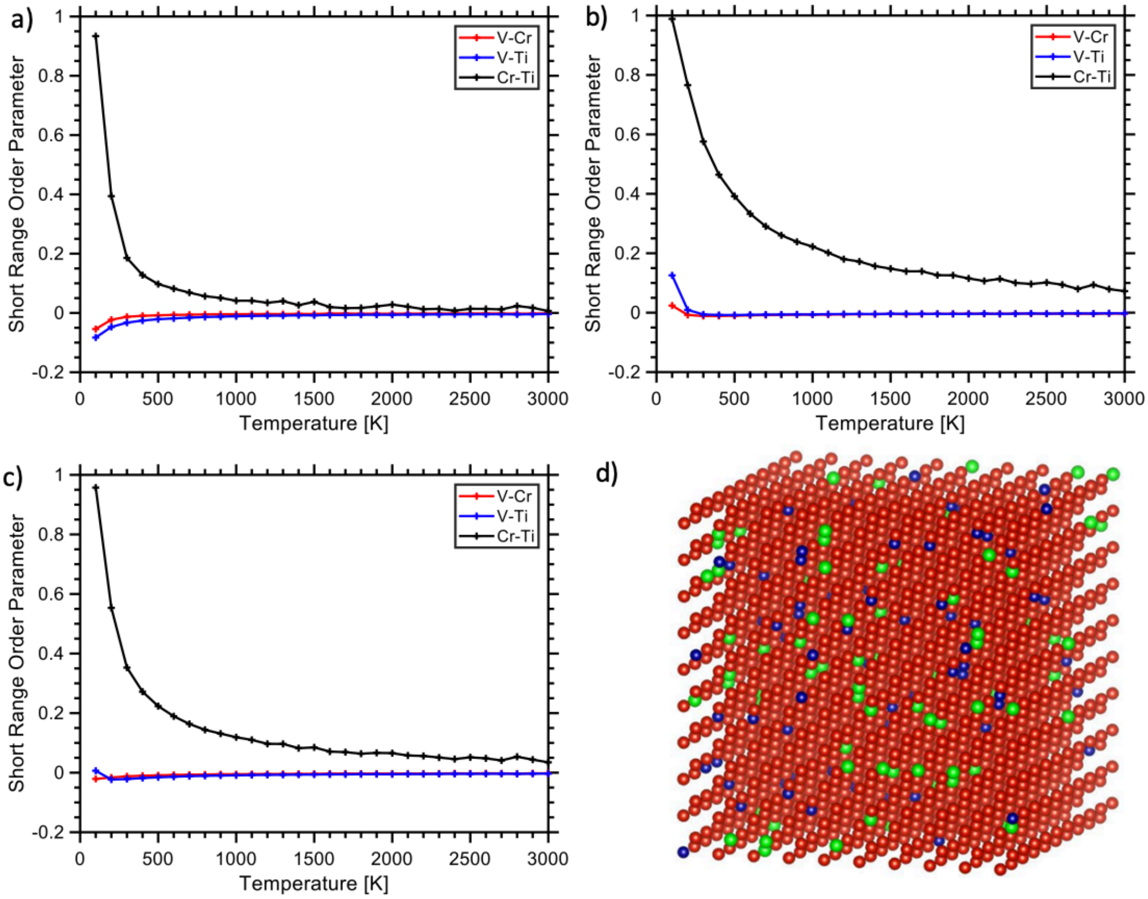

Figure 5.7 *Figures depicting the influence of temperature on the short range order parameter corresponding to a) the first shell, b) the second shell, and c) the average of the two shells, and d) the atomic cell structure generated from Monte Carlo simulation using the DFT energy model (red – V, blue – Cr, green – Ti)*

DFT modelling over a range of states, from ordered to disordered, allows the chemical affinity of alloy elements for one another to be evaluated. The configuration of the modelled supercell is recorded through the short-range order (SRO) parameter – this parameter describes the probability of finding pairs of elements within proximity of each other, ie the probability of finding a particular element, *a*, within a set volume around another element, *b*. The SRO parameter is therefore important in determining how the presence of alloying elements influences the lattice structure of the parent element, and predicting elemental segregation within the alloy. This in turn allows a fuller understanding of factors informing alloy mechanical properties to be developed relating underlying atomic structure to changing mechanical response.

SRO parameters were evaluated between pairs of atoms in V-4Cr-4Ti using the combination of Monte Carlo simulations with DFT-based energy model as a function of temperature. This evaluation was performed over the first shell (Figure 5.7a), the second shell (Figure 5.7 The dependency of these parameters on temperature demonstrated that Cr and Ti have a different behaviour within the V host at the low temperature region (Figure 5.7). While the SRO parameter behaviour between Cr and Ti is strongly positive, the SRO between V and Cr, and V and Ti become negative. This demonstrates that both Ti and Cr atoms exhibit strong chemical bonding with V, but tend to segregate away from one another. The atomistic structure of V-4Cr-4Ti alloys simulated at 300K by our Monte Carlo simulation is also shown in Figure 5.7d. It can be clearly seen in this figure that Ti atoms (in green) and Cr atoms (in blue) are present in segregated clusters throughout the V atoms (in red), with little contact between these clusters.

5.4.2.2. DFT Calculation of Elastic Constants

Our detailed elastic constant calculations (Table 5.3) showed only a slight increase of C_{11} and C_{44} for the configuration generated at 300K in a comparison with those at 2000K. This indicates that atomic ordering in the V-4Cr-4Ti alloy does not have a significant influence on its elastic properties and the investigated alloy should maintain similar elastic properties even after long annealing/aging times. As has been previously reported for DFT assessed V and V-rich alloys [338], [341], the average elastic constants computed for the fully relaxed structure are quite far from the values measured experimentally. Most notably, the average C_{11} value is strongly overestimated and the average C_{44} value is noticeably underestimated in comparison with the experimental results measured at RT, and this discrepancy can be explained in several ways. Firstly, one important consideration is the impact of distortive sample working experienced by tensile samples, which can be expected to increase disagreement between experimental and DFT predicted microstructure. Whilst a short ranged ordered structure is utilised in DFT modelling at RT, residual mechanical stresses may mean the structure of the non-ideal test sample may be more disordered. Discrepancy between experimental and modelled results therefore comes about simply because the model and experimental sample are not consistent.

Another explanation of such a disagreement is the underestimation of the lattice parameter, which is equal to 2.98 Å for the disordered structure optimized using PBE functional and is almost 0.06 Å smaller than the experimental value at RT. As given in Table 5.3, the elastic constants computed for the structure with the experimental lattice parameter are noticeably closer to the experimental values. In particular, the C_{11} value is almost 25 GPa less overestimated when the DFT calculations are performed for the experimental lattice parameter instead of the fully relaxed structure. These results show that the elastic constants are strongly related with the value of lattice parameter.

In fact, a significant decrease of C_{11}, and a decrease of C_{12} with increasing lattice parameter is in qualitative agreement with the experimental observations showing the same trends for the sample with increased volume measured at 550°C. The unfortunately high uncertainty in the C_{44} value produced using the experimental lattice parameter makes comparison between these two conditions less clearly defined, but the apparently slight variation in C_{44} produced by the increased lattice parameter is as expected.

In addition to the effect of lattice constant, it should be noted an important feature of the V44 alloy is the presence of Ti(C,O,N) precipitates, which increase the strength of this alloy. The model presented does not include the presence of impurities, and so does not consider the formation or dispersity of such precipitates, leading to an atomic structure which is not an accurate representation of the alloy as tested. When considering the model relative to the experimental data, the titanium content is augmented, and the impurity content is reduced. The lack of significant change in calculated elastic properties over such a large temperature may be related to this lack of precipitation. At 2000K all Ti-precipitates present at 300K would be expected to have long since dissolved, inducing a significant change in elastic properties, not seen in these results. Furthermore, the ductility predicted by the calculated data (read through the Poisson's ratio such that a high Poisson's ratio correlates to high ductility [364]) is significantly enhanced relative to that measured through in-situ tensile testing. It must also be considered that the addition of even small concentrations of oxygen to pure vanadium has been shown to marginally increase measured single crystal elastic constants, elastic modulus, and Poisson's ratio [267]. Previous DFT calculation of the elastic properties of V/Ti(C,O,N) heterostructures has indicated the introduction of small volumetric percentages of TiC only weakly increases the elastic modulus, whereas the introduction of many V-TiC interfaces markedly increases the elastic modulus [365]. Whilst the significant difference in atomic structures considered between the current results and the referenced work limits the extent to which quantitative comparisons can be applied, qualitatively both results point to the importance of Ti(C,O,N) type precipitates when considering elastic properties. The presence of oxygen in the vanadium alloy, then, has significant effects on the elastic properties, and some disparity between experimental results and any model which cannot account for this is to be expected.

Previous work has also reported a discrepancy between experimental and theoretically determined elastic properties of vanadium [366]–[369] – specifically underestimation of vanadium's trigonal shear elastic constant (C_{44}) and hence misestimation of its polycrystalline elastic properties. This underestimation has been linked to the complex electronic structure of vanadium, including an electronic topological transition in the metal's Fermi surface with a significantly weakening effect on shear elastic properties under ambient pressure [370], [371], and thermally induced broadening of the Fermi surface which produces anomalous shear behaviour [372], [373]. Whilst the underestimation of C_{44} reported here is more severe than in other DFT calculation works concerning vanadium [341], [369], the methodology applied in this work (higher cut-off wave energy and more accurate exchange-correlation functional) should return a more accurate model. Indeed, a similarly severe C_{44} underestimation was seen in other work using high cut-off wave energies for a variety of functionals [366], [367], and in the Materials Project[338], [374]. This suggests the poor agreement between the theoretical and experimental results presented here is attributable, not to inaccuracy in the model applied, but rather to the challenging structure of vanadium.

Such considerations emphasize the importance of experimental characterisation of such values – both as a means to circumvent complex modelling issues, and to inform and assess future models. Whilst current DFT results have allowed for the fundamental effects of solute addition to be better understood through the SRO effects, the inclusion of impurities and the use of experimentally determined parameters to fine tune modelling must be explored to produce more accurate DFT modelled results. Future work therefore requires further experimental determination of material properties, and the construction of more comprehensive theoretical models.

5.5.Conclusions

The mechanical properties of electron beam melted V44 were investigated using synchrotron XRD analysis of *in situ* tensile testing, at room and high temperature. These test temperatures allowed the confirmation of V44's suitable thermomechanical properties, including a measured linear thermal expansion coefficient of 10.3×10^{-6} K^{-1}. The effective elastic properties of V44 determined from experiment at room temperature were consistent with existing literature, including a Poisson's ratio value of 0.378, and an elastic modulus of 127.8 GPa. The key point of interest can be said to be the determination of the single crystal elastic constants, C_{11}, C_{12}, and C_{44}, which are commonly used in the mechanical modelling of materials. At room temperature these were found to be 240 GPa, 150 GPa, and 46.0 GPa respectively, whilst at 550°C these were determined as 212 GPa, 125 GPa, and 45.0 GPa, and at 700°C 205 GPa, 103 GPa, and 37.3 GPa. The decrease in single crystal elastic constants with increasing temperature produced a fall in bulk moduli properties that was consistent with existing literature concerning the V44 alloy. The elastic properties calculated through DFT-

Monte Carlo simulation were found to be in poor agreement with the experimental results presented: the calculated polycrystalline elastic modulus at room temperature, 70.3 GPa, differing significantly from the experimentally determined value of 129.5 GPa. This disagreement was proposed as the result of the base element's complex electronic structure, paired with lattice parameter mis-estimation, and precipitation behaviour currently unaccounted for. Results produced demonstrated the effectiveness of DFT modelling in elucidating fundamental atomic interactions, and the need for experimental qualification when applying these principles to macroscopic properties.

5.6 Consequences of Elastic Characterisation

Detailed characterisation of microstructural and mechanical properties is of use, not only in broadening materials databases, but also allows forms the basis of figures of merit for comparison of structural material applicability to high temperature performance. One such figure of merit is the thermal stress fracture resistance parameter, presented in Figure 5.8, which quantifies the maximum allowable temperature difference a material can experience without fracture measured in K [262]. This parameter, R_S, is assessed such that:

$$R_S = \frac{\sigma_U \cdot (1 - \nu)}{\alpha_T E} \tag{5.18}$$

Where σ_U is the ultimate strength, ν is the Poisson's ratio, α_T is the thermal expansion coefficient, and E is the elastic modulus. Using these parameters, determined in Chapter 3 and Chapter 5, the R_S figure of merit was assessed for EUROFER97, ODS EUROFER97, and V-4Cr-4Ti. Figure 5.8 demonstrates the increase in thermal stress resistance exhibited in next generation structural materials, and particularly the excellent high temperature capability of refractory based materials. Such assessment provides realistic estimates for high temperature performance, with consequences for reactor design, and this is only possible through collection and curation of technically sound, high temperature materials data, as presented in this work.

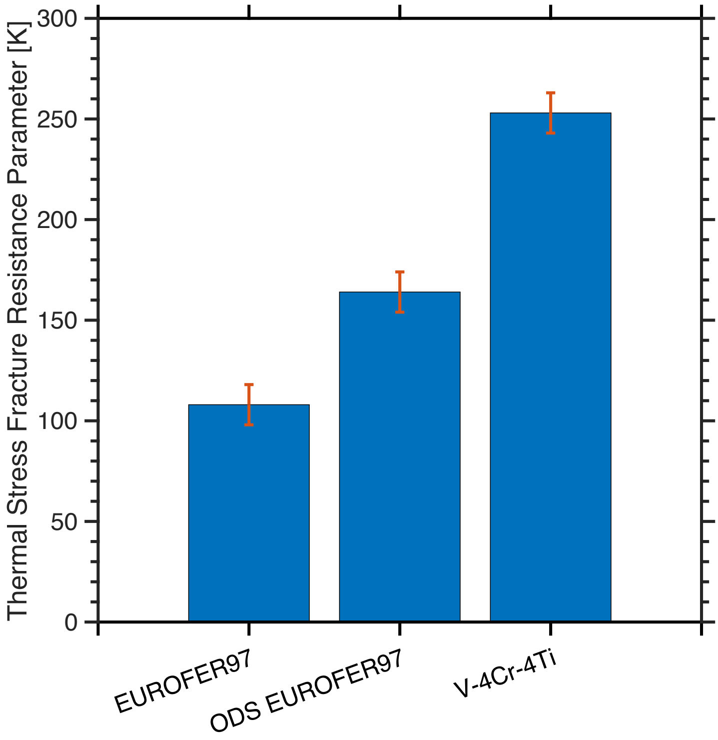

Figure 5.8 Thermal stress fracture resistance parameter of considered structural materials assessed at 550 ℃ from mechanical and elastic properties determined in Chapter 3 and 5.

CHAPTER 6 PREPARATION AND HARDNESS TESTING OF LABORATORY SCALE VANADIUM-BASED TANTALUM ALLOYS

Tay Sparks[a], Pengfei Zheng[c], Michael Gorley[b], Yiqiang Wang[b*], Biao Cai[a*]
[a]School of Metallurgy and Materials, University of Birmingham, Birmingham, UK

[b]UK Atomic Energy Authority, Culham Science Centre, Abingdon, Oxfordshire OX14 3DB, UK

[c]Center for Fusion Science of Southwestern Institute of Physics, Chengdu, 610041, China

In Preparation

Tay Sparks conceived and designed the experiment, completed the experimental work, analysed the data, and wrote the manuscript. Biao Cai and Yiqiang Wang assisted in conceiving and designing the experiment and data analysis. Pengfei Zheng provided materials for the experimental work. Michael Gorley assisted in conceiving and designing the experiment.

6.1 Abstract

The effect of low tantalum content on V-Ti and V-Ti-Cr alloys was investigated over a laboratory scale batch of arc melted and annealed alloys, with tantalum content ≤10wt%. Indentation testing on a micro- and macro- scale revealed inconsistent elastic response: initial results suggest tantalum acts as a suitable replacement for chromium in terms of solid solution strengthening ability – little significant deviation in hardness between V-Ti-Cr-Ta and V-Ti-Ta alloys with like tantalum content.

6.2 Introduction

Vanadium alloys are recognised as an attractive candidate first wall material in nuclear fusion reactor design: as a refractory metal, vanadium presents excellent high temperature strength, low activation, and suitable ductile to brittle transition temperature (DBTT) [375], [376]. The V-4Cr-4Ti alloy is a particularly favoured candidate; the addition of a small percentage of chromium increasing strength through solid solution strengthening whilst maintaining low DBTT , and the addition of titanium increasing resistance to irradiation swelling and gettering embrittling interstitials into Ti(C,O,N) precipitates [116], [119], [322].

V-4Cr-4Ti presents excellent high temperature strength up to around 700°C, but – though it maintains strength well at very high temperatures – its strength is considerably lower than other candidate structural materials (EUROFER97, F82H, PM2000, SiC) at moderate temperatures (room temperature – 400°C). In addition, the alloy exhibits significant irradiation induced embrittlement at 350-400°C irradiation temperatures

[123]. Current research aims to widen the operating temperature of vanadium alloys and improve general mechanical properties by micro-alloying.

Tantalum is another of the refractory metals, exhibits excellent high temperature mechanical properties, low thermal expansion, and low activation [23] – these properties mark tantalum as a suitable alloying element for the augmentation of fusion structural materials. Recent work by Jain et al. and Miyazawa et al. has led to renewed interest in the use of tantalum as a microalloying element: V-Ti-Ta alloys with tantalum content 1-7 wt% exhibiting superior wear resistance to unalloyed vanadium [377], and V-Ti-Cr-Ta alloys (tantalum content 4-35 wt%) exhibiting significantly increased strength, maintained to very high temperature (800°C) [171].

Indentation testing is a viable means of mechanically characterising small-scale samples, able to yield important information such as the indentation modulus – which relates back to material's fundamental elastic properties. The indentation modulus is dependent upon isotropy of test material, but for homogeneous and isotropic samples the indentation modulus will approach the Young's modulus of the material. Meanwhile hardness measurements stand as a useful indicator towards material strength and wear resistance – whilst not a substitute for these measurements, as a first characterisation hardness testing does provide a point of comparison between like samples.

In this work a pilot scheme of small scale V-Ti-(Cr,Ta) alloy samples fabricated by arc melting are microstructurally examined using basic composition confirming techniques, and then tested using macro and micro indentation techniques to characterise basic mechanical response. The results presented will help to establish the effects of varying content of tantalum on vanadium-based alloys, and select promising candidate compositions for testing and fabrication beyond the laboratory scale.

6.3 Materials and Methods

Test compositions were selected to cover a broad compositional space whilst avoiding the increase in DBTT expected with a total microalloying content greater than 10-20 wt% [124]. Test specimens were fabricated by vacuum arc melting of elemental components 99.7% purity or better. In order to ensure the best vacuum possible, the melting chamber was flushed with argon and re-evacuated several times prior to melting, and a titanium getter was used to capture lingering gaseous impurities prior to melting of the samples. Samples were flipped and remelted three times during melting in order to encourage homogeneous melting of sample components, before being left under vacuum to solidify and cool to room temperature on the water-cooled crucible.

Example samples for testing were cut from the as-cast buttons using a Struers Accutom 5 cutting machine, equipped with an aluminium oxide cutting wheel lubricated with a water jet. The buttons then underwent heat treatment in a TAV high vacuum furnace in order to recrystallise the grain structure away from the temperature gradient dictated grain structure expected from arc melted samples. Heat treatment followed standard annealing procedure employed for V-base alloys [141], consisting of heating at 1000°C for two hours, heating rate of 20°C/min, followed by gas quenching to room temperature. In order to prevent uptake of impurity present in the furnace during heating, V-alloys were wrapped in high purity (99.9997%) titanium foil, to act as a getter.

Following heat treatment, buttons were unwrapped, and samples were again sectioned from the buttons using the Accutom cutting machine.

Samples of the test V-alloys (both as-cast and heat treated) were then mounted in bakelite using an Opal 460 mounting press, and ground and polished to a mirror finish. The nominal test compositions used are collected in Table 6.1, alongside the post melting test compositions – measured during EDS mapping of the samples conducted on a TESCAN Mira3 Field Emission Gun SEM. In order to facilitate phase identification and lattice parameter determination, glancing XRD analysis of the heat treated samples was performed using a Bruker D8 Advanced X-ray Diffractometer, Cu (1.5418 Å) wavelength, collected over 2θ range 35-110.

Microhardness testing was performed on a Struers Duracsan Microhardness Indentation tester using a micro-Vickers diamond head indenter. Indentations were performed using a load of 200gf, and Vickers hardness value was calculated from the diagonal of the resulting indent, as per the standard equation:

$$HV = \frac{0.1891F}{d^2} \tag{6.1}$$

Where HV is the Vickers hardness in MPa, F is the load force (200gf or 1.96 N), d is the average length of the diameter in mm, and 0.1891 is a scaling factor accounting for the indenter geometry and area-diagonal relation.

Indentation testing was performed using a Deben CT5000 compression stage, 5 kN loadcell, with a spherical tungsten carbide indenter, diameter 3.12 mm. Two peak loads were selected for investigation, 30kgf and 50kgf, and during loading/unloading a displacement rate of 0.1 mm/min was used. Upon reaching peak load, the load was held for 2 seconds before unloading. A schematic of the macro-indentation Deben CT5000 compression stage is provided in Figure 6.1.

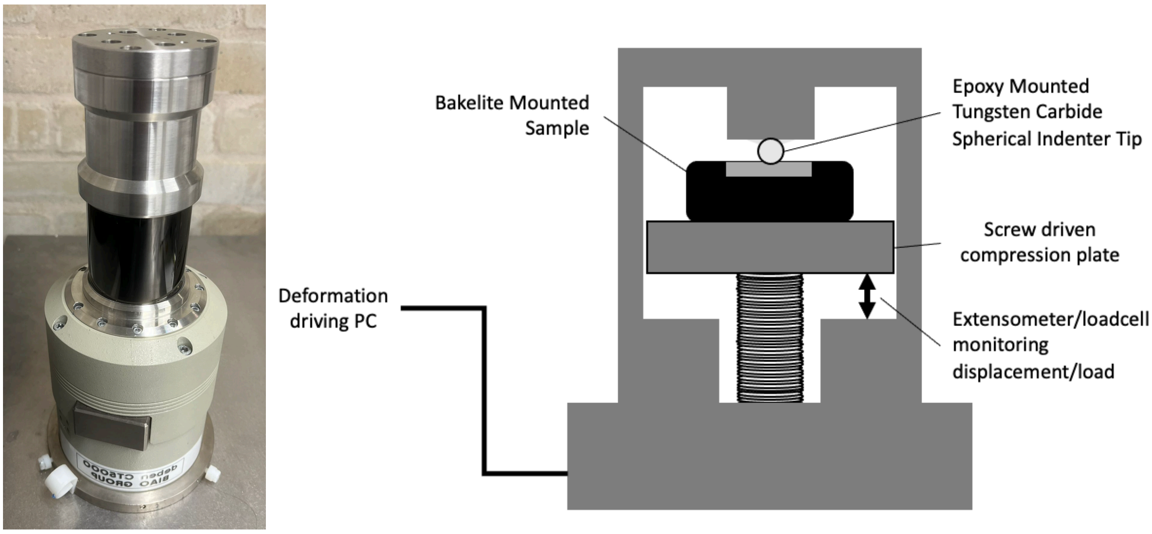

Figure 6.1 a) Photograph and b) schematic of Deben CT5000 compression used for macro-indentation testing

The macro-indentation data was evaluated as per the seminal work of Oliver-Pharr [378], the basis of which is the load-displacement relation:

$$P = Ah^m \tag{6.2}$$

Where P is the indentation load, h is the indenter depth, and A and m are test condition constants. The load-displacement curves recorded for the experimental set-up described exhibited an initial non-standard relation, indicative of systematic error which required correction.

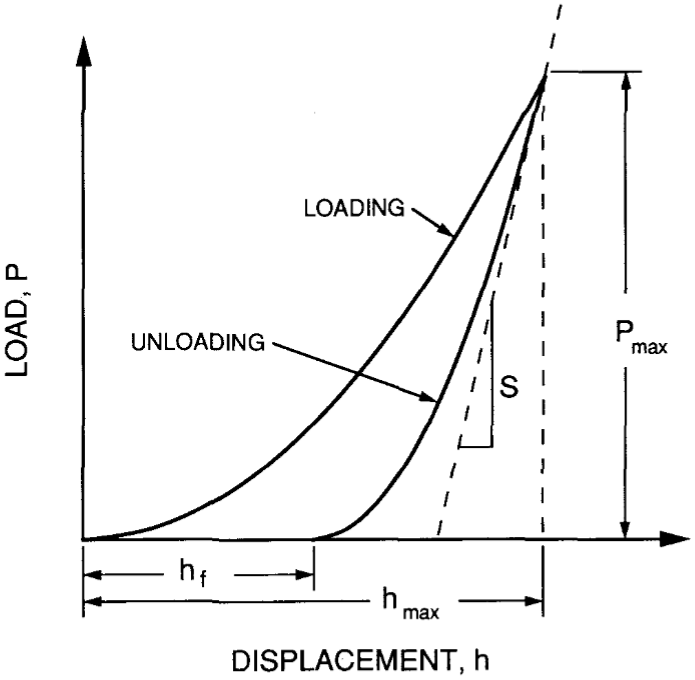

Figure 6.2Indentation Load-Displacement curves generated during macro-indentation, curve parameters indicated on figure, recreated from Oliver-Pharr (1992) [378]

As per the established standard, indentation load/unload curves were evaluated to determine indentation hardness, indentation modulus, and elastic/plastic proportion of indentation work [379]. Determination of these material parameters required the calculation of indenter contact depth (h_c) and the contact stiffness (S_C); these values indicated in the example loading/unloading curve shown in Figure 6.2, and calculated via the equations:

$$h_c = h_{max} - \varepsilon_g \cdot (h_{max} - h_T) \tag{6.3}$$

$$S_C = (\frac{dP}{dh})_{max} \tag{6.4}$$

Where h_{max} is the depth at maximum load, h_T is the tangent depth, indicated in Figure 6.2, and ε_g is an indenter geometry dependent parameter (taken as 0.75 for spherical indenters [379]). The measured contact stiffness is accounted for, not only by the sample response to indentation, but also by stiffness of the indentation rig during deformation. Sample stiffness (S_S) is therefore related to contact stiffness and frame stiffness (S_f) through the equation:

$$\frac{1}{S_C} = \frac{1}{S_f} + \frac{1}{S_s} \tag{6.5}$$

The sample stiffness response is itself dictated by the elastic properties at the indenter/surface interface, known as the reduced modulus, E_r. The reduced modulus of indentation is calculated as:

$$\frac{1}{E_r} = \frac{2\sqrt{A_p}}{S_S\sqrt{\pi}} = \frac{1-\nu^2}{E_{IT}} + \frac{1-{\nu_i}^2}{E_i} \tag{6.6}$$

Where A_p is the projected area of contact at h_c, E_{IT} is the sample indentation modulus, ν is the sample Poisson's ratio, ν_i is the indenter Poisson's ratio, E_i is the indenter modulus, and E_r is the reduced modulus of indentation contact. The indentation modulus is intrinsically linked to material elastic response, and direct comparison between indentation modulus and elastic modulus has previously been reported. Therefore, in order to evaluate the S_f term in equation (6.5), indentation testing was performed on a sample with a known elastic modulus. In order to avoid any material dependency of the S_f term, a V-4Cr-4Ti provided by the South-Western Institute of Physics [141] was used for this purpose, elastic modulus 129.5 Gpa.

Indentation hardness was calculated from the equation below:

$$H_{IT,0} = \frac{F}{A_p} \tag{6.7}$$

Where $H_{IT,0}$ is the indentation hardness, F is the maximum applied force, and A_p is the projected area of contact at h_c. The indentation modulus of the sample (E_{IT}) is found by removing the influence of indenter elastic response on loading/unloading behaviour observed, calculated by:

$$E_{IT} = \frac{1 - {\nu_s}^2}{\frac{1}{E_r} - \frac{1 - {\nu_i}^2}{E_i}} \tag{6.8}$$

Where E_{IT} is the sample indentation modulus, ν_s is the sample Poisson's ratio, ν_i is the indenter Poisson's ratio, E_i is the indenter modulus, and E_r is the reduced modulus of indentation contact.

The elastic fraction of work (η_{el}) is also of interest, and is determined simply as

$$\eta_{el} = \frac{W_{el}}{W_T} \tag{6.9}$$

Where W_{el} is the work done by elastic deformation, and W_T is the total work done during deformation. Work done was estimated from trapezium-rule approximation of the area under the curve a) up to h_{max} (total work done), and b) between h_{max} and full unloading (elastic work done), performed in MATLAB.

6.4 Results & Discussion

6.4.1 Microstructural Characterisation

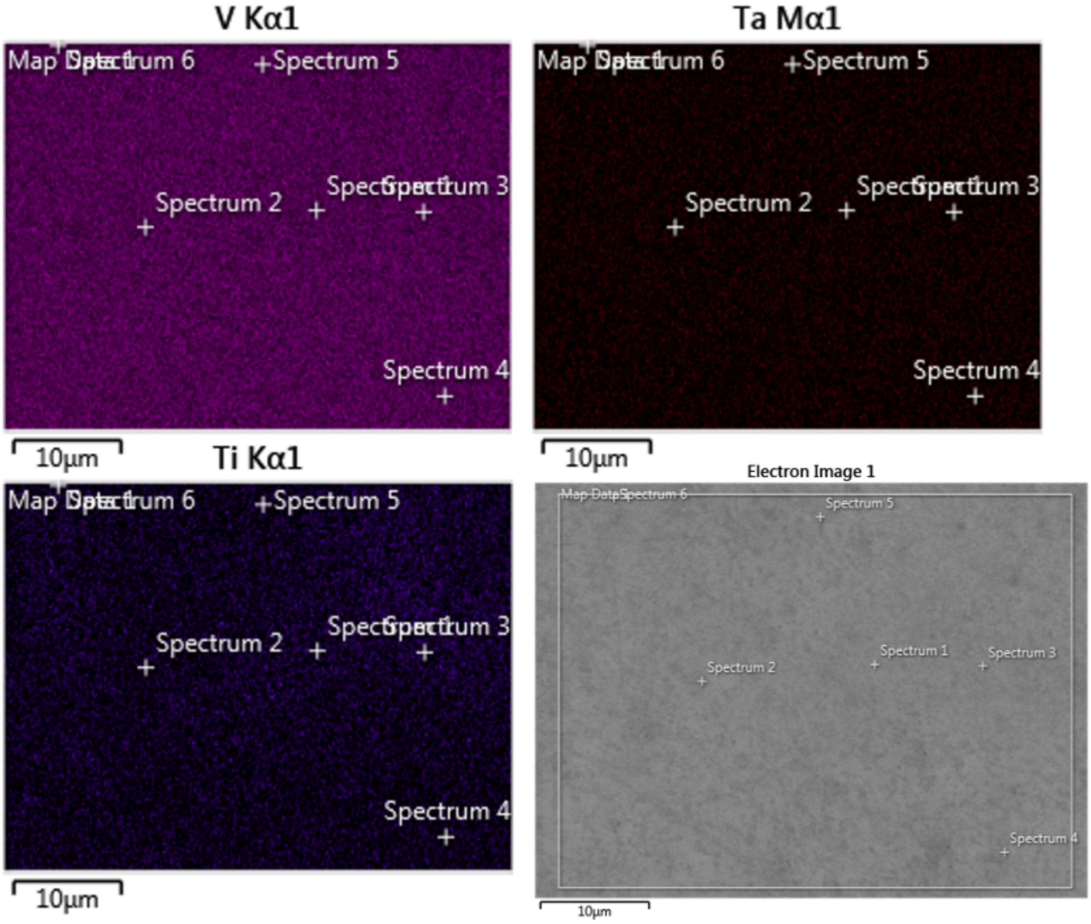

Figure 6.3 Example of EDS mapping, demonstrating homogeneous elemental distribution – example shown for V-4Ti-1Ta

Table 6.1Elemental composition of fabricated V-based alloys by weight percent measured by EDS, V balance.

Nominal Composition	**Cr (wt%)**	**Ti (wt%)**	**Ta (wt%)**
V-4Cr-4Ti	3.1±0.1	3.8±0.1	-
V-4Ti-1Ta	-	3.6±0.1	1.2±0.1
V-4Ti-4Ta	-	4.6±0.1	4.1±0.1
V-4Ti-8Ta	-	3.8±0.1	8.7±0.1
V-4Ti-10Ta	-	4.0±0.1	10.6±0.1
V-4Cr-4Ti-0.1Ta	3.6±0.6	4.4±0.3	0.3±0.2
V-4Cr-4Ti-1Ta	2.8±0.1	3.8±0.1	1.6±0.1
V-4Cr-4Ti-8Ta	3.8±0.1	4.1±0.1	8.4±0.1
V-4Cr-4Ta	3.9±0.1	-	4.1±0.1

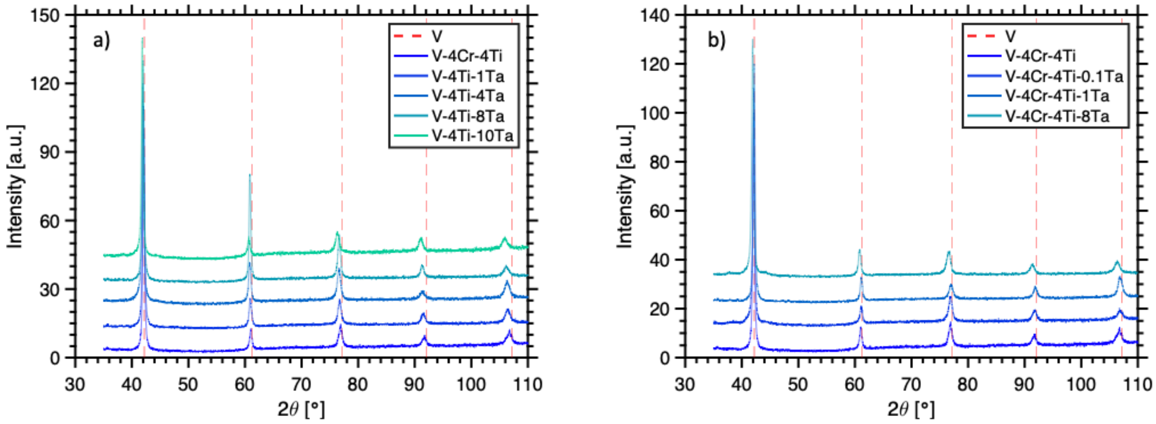

Figure 6.4X-ray diffraction profile of a) V-4Ti-xTa alloys, and b) V-4Ti-4Cr-xTa alloys over the range $35^{\circ}<2\theta<110^{\circ}$*, copper source, wavelength 1.5418 A, position of pure V diffraction peaks overlaid. Profiles offset for ease of comparison*

Basic alloy characterisation is presented in Table 6.1 (EDS alloy composition), and Figure 6.4 (results of XRD testing). EDS mapping of heat treated samples did not reveal areas of significant enrichment/depletion of any constituent element, elemental composition appearing homogeneous across considered samples as demonstrated in Figure 6.3. X-ray diffractograms showed limited peak shift with alloying content, the positions of peaks expected for unalloyed vanadium are superimposed on these images to better demonstrate peak shift. The only peaks observed corresponded to the bcc structure expected of the vanadium matrix, slight shifts in peak position anticipated as a result of alloying content dissolution into the matrix. Peaks were fitted using a Pseudo-Voigt function, and lattice parameter was evaluated from diffractogram peak positions – indicated in Table 6.2.

Table 6.2 Lattice parameter of fabricated V-based alloys determined via glancing angle X-ray diffraction

Nominal Composition	**Lattice Parameter (Å)**
V-4Cr-4Ti	3.034±0.002
V-4Ti-1Ta	3.033±0.003
V-4Ti-4Ta	3.046±0.003
V-4Ti-8Ta	3.037±0.002
V-4Ti-10Ta	3.053±0.003
V-4Cr-4Ti-0.1Ta	3.033±0.005
V-4Cr-4Ti-1Ta	3.026±0.002
V-4Cr-4Ti-8Ta	3.049±0.004
V-4Cr-4Ta	3.026±0.002

The combined evidence of apparently uniform Ta distribution across sample surface and the bcc patterned XRD diffractograms produced, strongly indicate a single-phase matrix has been produced in each case. The Ta-Ti-V system reported by Enomoto supports this observation, reporting high vanadium V-Ti-Ta alloys as single phase above 90 %atm V. Repeated remelting during fabrication and subsequent heat treatment can be expected to promote a homogeneous elemental distribution across the samples, limiting the possibility of unmelted tantalum inclusions within cast samples. SEM imaging of sample surfaces revealed uniform surface morphology with little evidence of residual elemental phase inclusions or precipitate formation, though pores were observed in the surface even following heat treatment. Controlled variation of the brightness/contrast at low working distances (<10 mm) and low accelerating voltages (10 kV) allowed the grain structure of certain samples to be observed through electron contrast channelling of back scattered electrons. The grain structure of the V-4Ti-4Ta sample was clearly revealed using electron channelling contrast imaging, as shown in Figure 6.5, but grains were found to exhibit much weaker contrast in other imaged samples, meaning grain analysis could not be broadly applied using this technique. Figure 6.5 shows a grain structure dominated by large, irregularly shaped grains >100 um in diameter, with little evidence of columnar grain structure produced by thermal gradients during cooling.

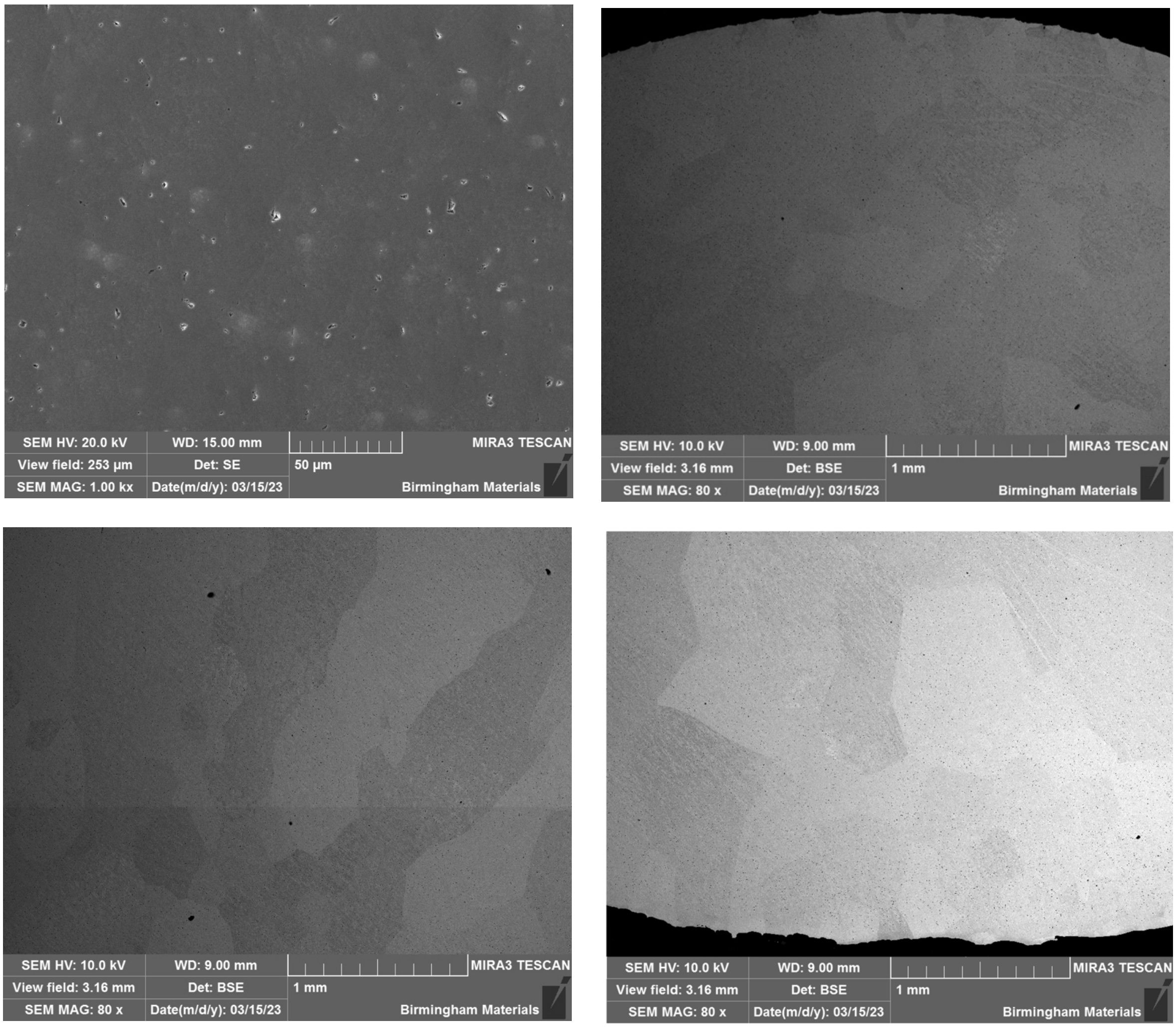

Figure 6.5 SEM imaging of V-4Ti-4Ta sample surface in a) secondary electron imaging mode revealing fabrication induced micropores, and b)/c)/d) backscattered electron imaging revealing grain structure through electron channelling contrast from a) the top of the button cross-section, b) the centre of the button cross-section, and c) the base of the button cross-section. Imaging parameters shown in ribbon

6.4.2 Indentation Testing

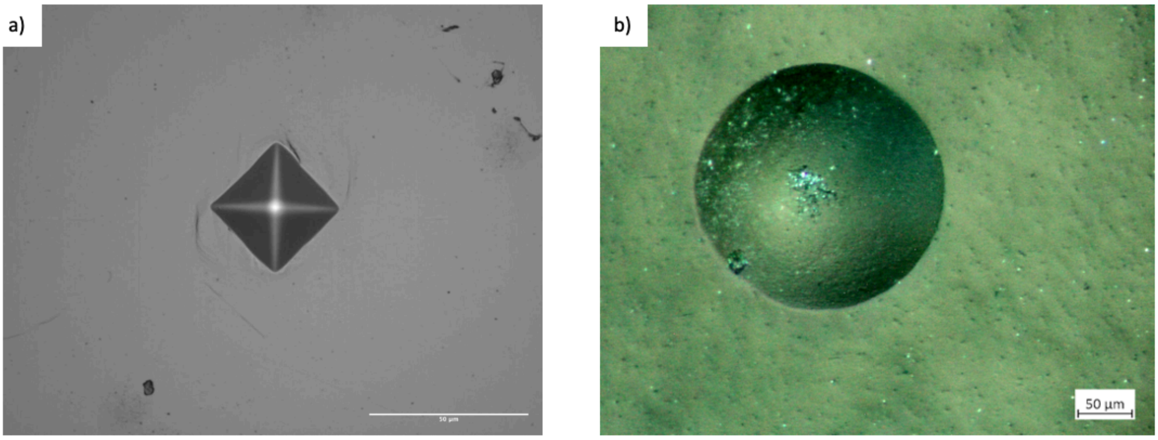

Figure 6.6 Example of indentations left following a) Vicker's micro-indentation, and b) spherical head macroscopic indentation loading.

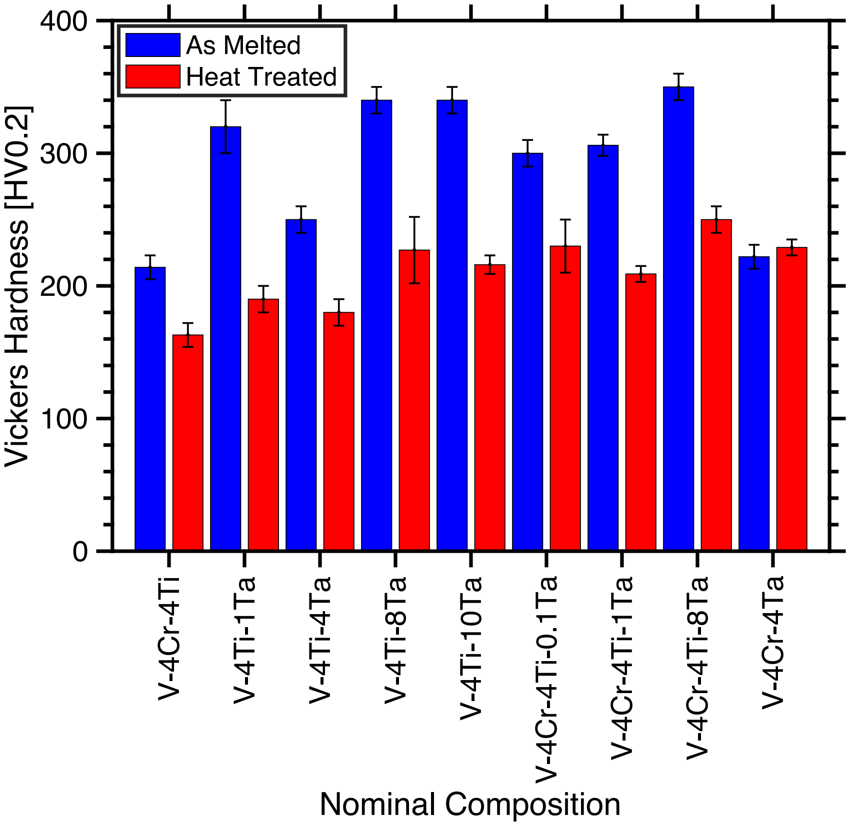

Figure 6.7Vicker's hardness of as melted and heat treated laboratory scale V-Cr-Ti-Ta alloys

Hardness results produced by Vickers hardness testing are collected in Figure 6.7, and an example of the indentations produced is shown in Figure 6.6, captured using an optical microscope. Error quoted in Figure 6.7 is taken as statistical standard deviation across all measurements.

An example of the raw load-displacement curves is shown in Figure 6.8a), and it may be noted that low load zones, on both the loading and unloading curves are dominated by a linear region, the linear region showing behaviour expected of spring-like systems. Indeed, gradient of these regions is consistent between the loading and unloading curves, and for this reason it is anticipated that this behaviour is the result of instrumental compression rather than indentation.

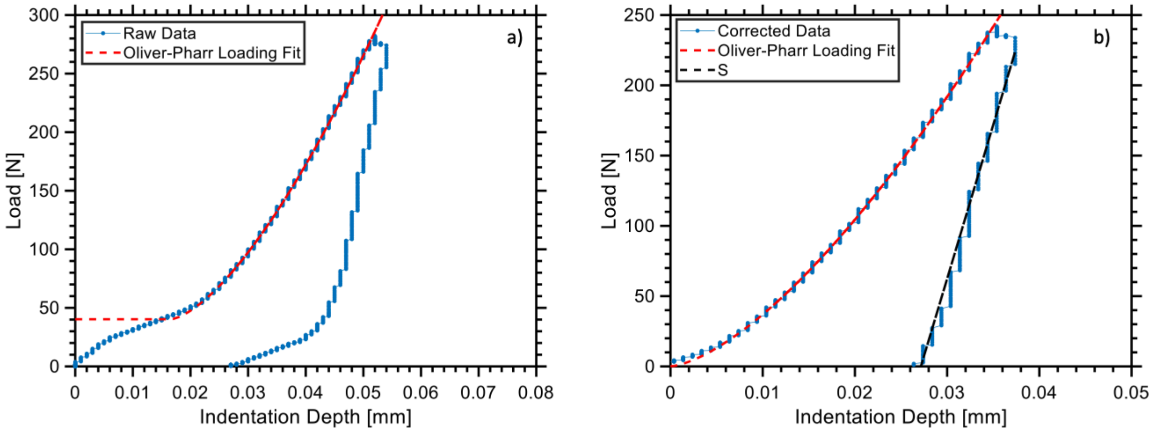

Figure 6.8Example indentation Load-Displacement curves generated during macro-indentation a) in the raw state, high load curve fitted with Oliver-Pharr loading relation (equation (2)), and b) corrected data, offset on the basis of loading fitting. Data displayed generated during indentation of arc melted V-4Cr-4Ti

In order to evaluate the point at which load-displacement behaviour was accounted for by sample deformation rather than instrumental compression, the higher load region was extrapolated as per Equation (6.2) to determine an appropriate offset to load and displacement. It is assumed that deformation in this region is dominated by indenter-sample interaction, any other deformation effects being negligible. This allowed the load-displacement curves to be reduced to the area of interest (ie sample deformation behaviour only), as shown in Figure 6.8.

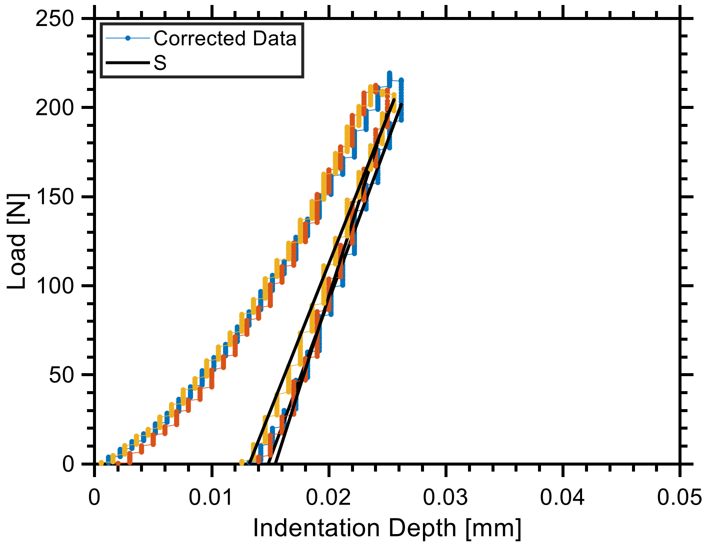

Figure 6.9Indentation load-displacement curves collected during macro-indentation of SWIP V-4Cr-4Ti

Table 6.3 Parameters used in determination of frame stiffness from indentation loading-unloading of SWIP V-4Cr-4Ti

Parameter	**Value**
E [GPa]	129.5±0.4
v	0.379±0.008
E_i [GPa]	700
v_i	0.31
E_r [Nmm^{-1}]	127±3
A [mm^2]	0.18±0.01
S_S	61000±1000
S_c [Nmm^{-1}]	21000±1000
S_f [Nmm^{-1}]	33000±2000

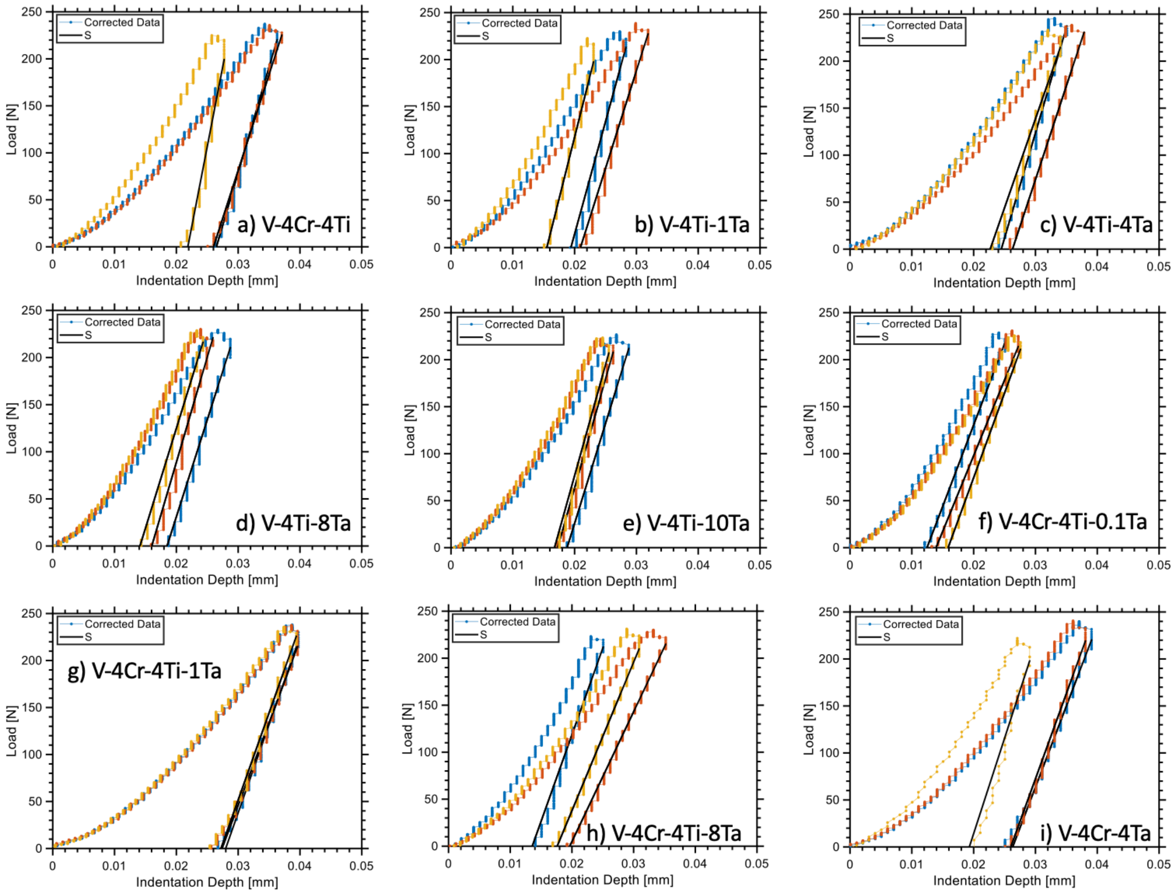

Figure 6.10Indentation load-displacement curves collected during macro-indentation of heat treated arc melted V-Ti-Ta-Cr alloys, composition indicated on figure.

The corrected loading-unloading curves gathered during macro-indentation are collected in Figure 6.9 and Figure 6.10, and an example of the resulting indent is shown in Figure 6.6b. The indentation loading/unloading curves are smooth, showing no evidence of pop-ins coupled to sample porosity. The frame compliance term evaluated with the known elastic modulus value is reported in Table 6.3, and the indentation modulus, indentation hardness values, and elastic fraction of work are recorded in Figure 6.11, Figure 6.12 and Table 6.4, shown with varying tantalum content.

The indentation hardness results – both in the micro and macro range – show very little significant variation with tantalum content. However, some consistent variation in hardness is observed: similar or improved hardness was observed considering tantalum either as a replacement for chromium or alongside chromium. The V-4Ti-1Ta alloy reported a micro-indentation hardness of 190±10 HV0.2, compared to 163±9 HV0.2 of V-4Cr-4Ti, suggesting that lower tantalum content can produce a comparable strengthening effect. The most consistent strengthening was seen for the V-4Ti-4Cr-8Ta alloy, which displayed a hardening relative to V-4Cr-4Ti of 90±10 HV0.2 under micro-indentation and 150±30 MPa under macro-indentation after heat treatment. Notably, significant strengthening was observed, even for the V-4Ti-4Cr-0.1Ta alloy, which displayed an increase in hardness relative to V-4Cr-4Ti of 70±20 HV0.2 under micro-indentation and 230±80 MPa under macro-indentation after heat treatment.

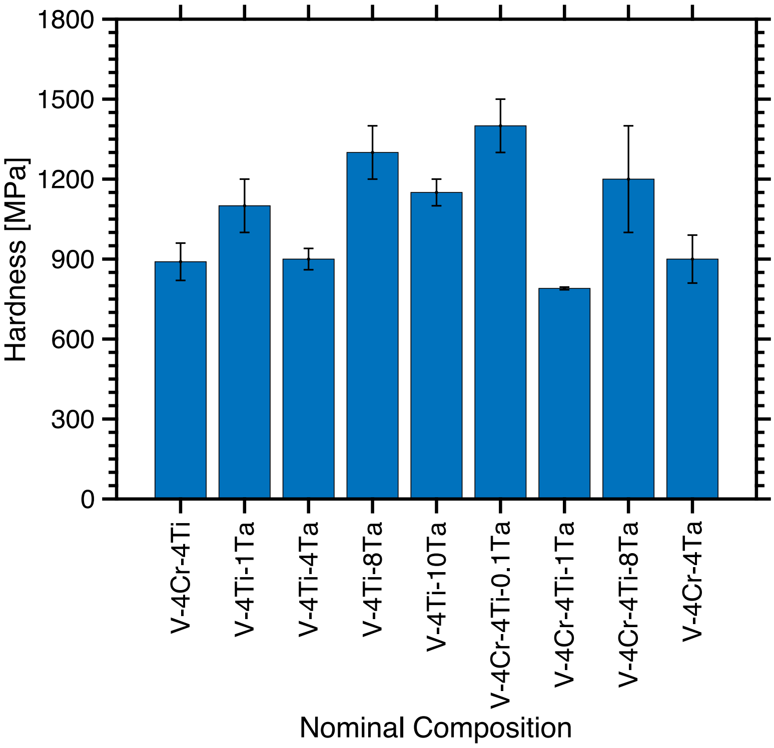

Figure 6.11Hardness of heat treated laboratory scale V-Cr-Ti-Ta alloys loaded to 30KGF

The V-4Ta-4Cr demonstrates improved hardness relative to V-4Ti-4Cr on the micro-scale, but reduced hardness relative to V-4Ti-4Cr on the macro-scale. This could potentially be attributed to incomplete recrystallisation in this alloy: the microhardness measurements prior to and following the 1273K annealing are practically unchanged for this alloy (222±9 HV0.2 and 229±6 HV0.2 respectively), whilst all other alloys demonstrate a fall in hardness of at least 50HV following heat treatment. A fall in hardness following heat treatment is caused by recrystallisation and recovery within the treated sample, a reduction in Vickers hardness on the order of 100 HV from the cold rolled state commonly reported for V-Ti-Cr alloys following equivalent heat treatments [380]–[382]. That the Vickers hardness of V-4Ta-4Cr is unaffected by the heat treatment employed therefore suggests the regime employed has been insufficient to induce recrystallisation. To the best of our knowledge there does not exist a comprehensive phase diagram for the V-Cr-Ta system at 1000°C, however experimentally determined isothermal section of the V-Cr-Ta system at 1200°C suggests V-based solid solution remains the only thermodynamically favourable phase provided a V concentration of >80 at% [383]. Also to be considered is that the V-4Cr-4Ti-7Ta alloy (an alloy with similar at% Cr and Ta content) considered did exhibit the expected fall in Vickers hardness. Macroscale hardness testing is not sensitive to factors such as grain size and dislocation density in the same way as microscale testing, and as a result of this, the results yielded from 30kgf indentation testing may tentatively be taken as more directly comparable to other test alloys.

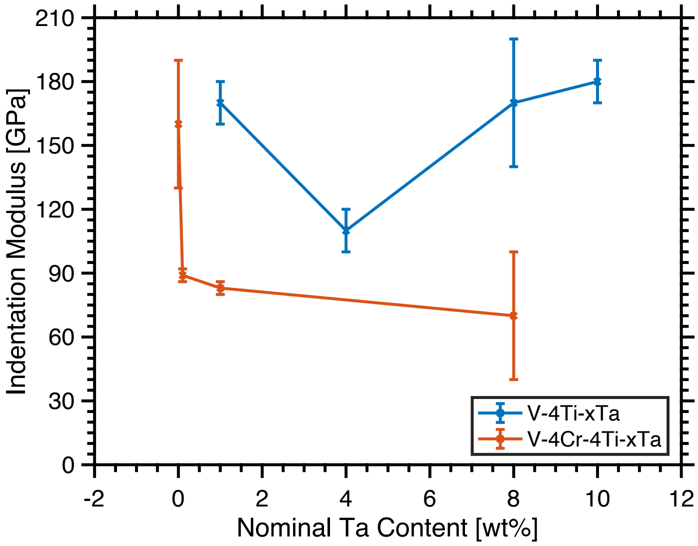

Figure 6.12 Indentation modulus of V-Cr-Ti-Ta alloys with changing tantalum content

Interpretation of the variation in indentation modulus is severely limited by the precision of displacement measurement during unloading and accompanying error in measurement. Indentation modulus values produced had an unfortunately high corresponding error, and limited data comprising unloading curves produced several unfeasibly high (>400 Gpa) values for indentation modulus which were discarded. Despite these shortcomings, it does appear that V-Ti-Ta alloys consistently exhibited a higher indentation modulus and lower fraction elastic work than equivalent Ta content V-Ti-Cr-Ta alloys. Taking indentation modulus as analogous to elastic modulus, the level of variation seen is inconsistent with the anticipated behaviour: addition of chromium to vanadium is expected to increase elastic moduli [384], whilst the indentation modulus reported for V-Ti-Ta-Cr alloys is consistently lower than that of equivalent Ta content V-Ti-Ta alloys. This speaks to the instrumental limitations in the methodology employed, and may be taken as an indication the variation in indentation modulus seen in Figure 6.12 is most probably the result of instrumentally induced noise.

Table 6.4 Parameters characterising indentation response of heat treated V-Cr-Ti-Ta alloys

Alloy Composition	**h_c [mm]**	**H_{IT} [MPa]**	**W_{el} [%]**	**S_c [Nmm^{-1}]**	**E_{IT} [GPa]**
V-4Ti-4Cr	0.0299 ±0.0001	890 ±70	10.5 ±0.6	25000 ±1000	160 ±30
V-4Ti-1Ta	0.025 ±0.001	1100 ±100	13 ±1	24700 ±500	170 ±10
V-4Ti-4Ta	0.028 ±0.002	900 ±40	13.1 ±0.2	22500 ±500	110 ±10
V-4Ti-8Ta	0.020 ±0.002	1300 ±100	15 ±1	23900 ±700	170 ±30
V-4Ti-10Ta	0.0222 ±0.001	1150 ±50	13 ±1	25000 ±500	180 ±10
V-4Cr-4Ti-0.1Ta	0.018 ±0.001	1400 ±100	22 ±2	19200 ±500	89 ±3
V-4Cr-4Ti-1Ta	0.0314 ±0.0002	790 ±5	13.6 ±0.6	21100 ±300	83 ±3
V-4Cr-4Ti-8Ta	0.021 ±0.003	1200 ±200	20.6 ±0.8	18000 ±2000	70 ±30
V-4Cr-4Ta	0.0182 ±0.0005	900 ±90	14.7 ±0.9	20000 ±1000	80 ±10

Though these results do not show a significant effect imparted by the addition of low Ta content, the experiments conducted exhibit several limitations. The most fundamental of these concerns the composition of the alloys themselves: whilst nominal composition was confirmed by the EDS results already discussed, this did not allow for usable quantification of impurity content. Impurity (oxygen, carbon, nitrogen) content has a significant impact on the mechanical properties of vanadium alloys, both through solid solution strengthening and precipitate strengthening. Whilst impurity content has been attempted to be suppressed during fabrication, even contents <1000 wppm have a notable hardening effect in vanadium metal, and a reducing total impurity content within this region lead to a reduction in hardness of approximately 30-50% [385]. The presence of impurity gettering titanium and tantalum in all alloys is expected to supress this hardening effect, but variation in impurity content between test samples may go some way to explaining the somewhat random indentation results recorded.

Also to be considered are limitations associated with the methodology employed. As has been discussed, the frame compliance was corrected for by indentation measurement at multiple test loads, however frame compliance is a particularly important issue at large depths [386], and potential unaccounted for inaccuracy in the compliance correction applied may have a larger impact on indentation modulus calculations than intended. Further, the precision of displacement measurements recorded is low relative to the magnitude of measurements taken (0.001 mm in maximum displacements ~0.03 mm), which limits the precision of sharp gradient measurements required for determination of sample stiffness.

Two key assumptions have been made regarding the parameters considered in the calculation of indentation modulus and indentation hardness – specifically relating to the sample Poisson's ratio, and the projected indenter area. The sample Poisson ratio was taken as 0.36 across all compositions; this being the value quoted for both pure vanadium, and V-Cr-Ti alloys [322]. Whilst variation in alloy composition can be expected to produce some effect upon Poisson's ratio, the fact the addition of tantalum has not seen the formation of new phases, the consistency in Poisson's ratio between unalloyed vanadium and V-Cr-Ti alloys, and the small theoretically predicted variation of Poisson's ratio (>0.01) with Cr/Ti alloying content up to 20 wt% [341] suggests this assumption is broadly good. The projected area utilised works on the assumption of a uniform indenter head geometry: a perfect sphere. Variation in indenter head geometry away from uniformity can have a significant impact on calculated properties at small length scales – micro-indentation testing being particularly susceptible to such effects. However, the depth scales considered in this work are significantly larger than the length scales associated with indenter head size variation, and so the effects of misestimated projected area are likely to be small when compared to error of measurements.

Ultimately the macro-indentation results provided are limited by instrumental error, arising as the result of low precision depth measurement, high frame stiffness, and instrumental compression during initial loading. Despite these shortcomings, the results presented have allowed for some qualitative analysis of the effect of tantalum content on vanadium-based alloy response to deformation. The low precision of macro-indentation results reported could be somewhat mitigated in future by increased quantity of data across sample surfaces in a defined pattern – such work would increase the accuracy of averaged results, and help to definitively exclude sample inhomogeneity as a source of variation in response.

Future work should aim to confirm the qualitative findings produced here, utilising load-displacement monitored nano- or micro-indentation testing to avoid the unfortunately high frame stiffness encountered in macro-indentation testing.

6.5 Conclusions

In this work, a series of vanadium-based V-Ti-Ta-Cr alloys were fabricated. Macro-indentation testing of fabricated alloys did not reveal any significant correlation between tantalum content and mechanical properties – characterised as indentation modulus and hardness. Whilst the difficulty of frame compliance correction and projected area analysis limited the extent to which meaningful comparison can be made between considered compositions, the use of tantalum in addition to titanium is confirmed to lead to hardening of the alloy, expected to correspond to an217ncreasee in strength. These results may only be taken as an initial confirmation of the favourable strengthening behaviour of Ta, but also highlight areas for future research – namely, the addition of very low Ta content V-4Cr-4Ti alloys, and the effect of Ta on V-based alloy elastic response.

CHAPTER 7 CONCLUSIONS

7.1 Future Work

Concerning the existing structural materials discussed in this work (EUROFER97, ODS EUROFER97, V-4Cr-4Ti), the elastic properties determined in Chapters 3-5 open the door to accurate component modelling across a range of temperatures relevant to reactor operation. The difficulty in DFT determination of V44 elastic properties in particular highlights the merit of such experimental characterisation as a supplement and support for modelled results. As a fundamental material property the results of elastic characterisation can be broadly applied; that is to say processed microstructure and component geometry should not be expected to influence these parameters.

The mechanical data collected concerning the structural materials considered is of interest and importance in strengthening the wealth of high temperature property data available at fusion relevant temperatures. Furthermore, the comparison of constitutively determined stress between EUROFER97 and ODS EUROFER97 in Chapter 3 could find greater interest with the additional characterisation and quantification of other ODS fraction variants. Examination of the effect of ODS particle size and distribution on the flow stress of EUROFER97 on the constitutive level would help to identify optimal ODS fraction addition and fabrication requirements.

Investigation into the dislocation density behaviour of EUROFER97 during high temperature ratcheting in Chapter 4 is an area which bears further scrutiny. On the most fundamental level, instrumental limitations excluded the possibility of a compressive portion to the cyclic testing performed: as stress ratio between cyclic extremes is known to strongly control ratcheting rate. A more comprehensive study including varying stress ratios and samples driven to ultimate fracture would therefore represent useful future work, allowing easier comparison with existing examination of ratcheting behaviour, and identification of changing dislocation behaviour during the transition to tertiary stage ratcheting deformation and fracture. The cyclical multiplication and annihilation of dislocations, ease of dislocation motion, and formation of dislocation networks, moderate the cyclical hardening/softening of steels during high temperature ratcheting and as such full understanding of this behaviour can be expected to provide crucial information informing long-term structural viability of candidate materials. To this end, in-situ TEM characterisation of dislocation behaviour during cyclic deformation is necessary to support the dislocation character analysis during cycling, which – without validation – can only be viewed as an estimation. Further, as the recovery behaviour examined is by its nature thermally driven, additional work including a wider range of test temperatures which fusion structural components can realistically be expected would do much to widen understanding of this behaviour and increase its applicability to fusion.

Additionally, further work may look to employ the characterisation of dislocation populations presented here in dislocation-based crystal plasticity modelling. As has been discussed, experimentally informed microstructural parameters could contribute significantly to the effectiveness of crystal plasticity modelling as a tool for predicting deformation behaviour of reactor components. Furthermore, working conditions of a fusion reactor must be anticipated to produce complex dislocation behaviour over life. Phenomena including cyclic loading induced dislocation population growth, high temperature thermal recovery, and irradiation induced phenomena (such as the formation of dislocation loops which subsequently as dislocation obstacles) must be considered. Future work must therefore look to employ the microstructural parameters investigated here to support increased complexity of numerical modelling employed to be able to account for conditions more aligned with the working conditions of a fusion reactor. Indeed, if nuanced analysis of dislocation population is able to be developed which can produce estimations of dislocation loop density from peak broadening analysis, in-situ XRD tensile testing of irradiated samples could provide a direct route to the microstructural properties needed to inform numerical modelling of materials under high temperature, high irradiation conditions.

Concerning the proposed next generation vanadium-based alloys proposed in Chapter 6, progression from conception to adoption in a broad industrial setting is complex, and the use of tantalum in improved vanadium-based alloys is still very much in its infancy in this regard. Strength-weakness-opportunity-threat (SWOT) assessment of the prospects of Ta microalloyed V-based alloys are presented in Table 7.1. The results presented in Chapter 6 of this work concern a pilot scheme of laboratory scale specimens, and deal with only a limited compositional window with respect to tantalum content. In order for the suitability of V-Ta alloy application to fusion design to be adequately addressed, there are two essential challenges to be faced: detailed characterisation of candidate alloys on the laboratory scale, and consistent production of candidate alloys on a larger scale.

Table 7.1 SWOT analysis of Ta addition to V-based alloys prospects

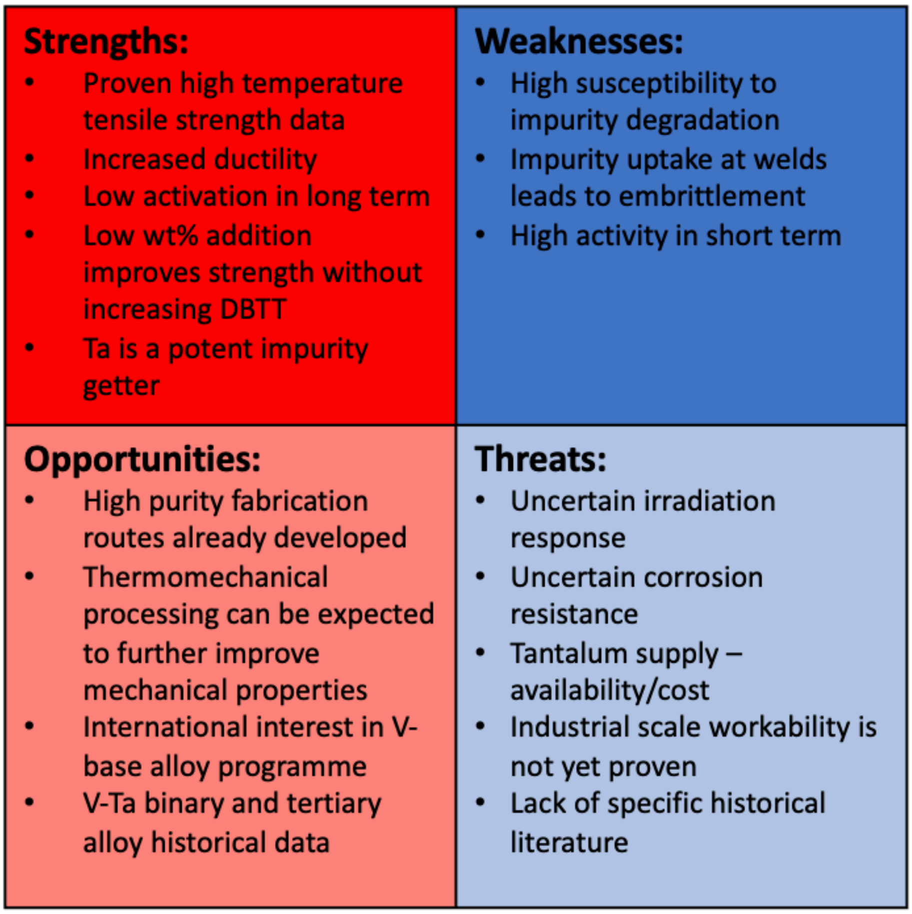

Strengths: • Proven high temperature tensile strength data • Increased ductility • Low activation in long term • Low wt% addition improves strength without increasing DBTT • Ta is a potent impurity getter	**Weaknesses:** • High susceptibility to impurity degradation • Impurity uptake at welds leads to embrittlement • High activity in short term
Opportunities: • High purity fabrication routes already developed • Thermomechanical processing can be expected to further improve mechanical properties • International interest in V-base alloy programme • V-Ta binary and tertiary alloy historical data	**Threats:** • Uncertain irradiation response • Uncertain corrosion resistance • Tantalum supply – availability/cost • Industrial scale workability is not yet proven • Lack of specific historical literature

Immediate future work in this arena must focus on the first of these challenges: the mechanical characterisation performed in Chapter 6 faces severe limitations (as discussed), and more comprehensive understanding of mechanical properties at room and elevated temperatures is clearly necessary to supplement this work. On the laboratory scale this may be limited to the production of tensile test specimens for mechanical testing at room temperature, and elevated temperature up to 700°C, in order to directly establish more widely comparable metrics for comparison between the new alloy compositions suggested and existing structural materials. There is a clear need for precipitate characterisation in order to assess the relative impurity gettering ability of Ta impurity uptake, and the effect of Ta and Cr content on the size and distribution of such precipitates, atom probe tomography and TEM analysis suggested techniques to achieve this. Further research into differing heat treatments should also be considered – grain size control through cold rolling prior to annealing may result in more consistent mechanical response between samples, and this may also be expected to have an effect on precipitate size and distribution.

Once the promise or otherwise of the proposed alloys has been established, production of industrial scale should be demonstrated by the fabrication of plates on the 1-10 kg scale, and the mechanical and microstructural properties of such batches must be confirm those found from further laboratory scale experimentation. In success several batches from different manufacturers would be produced, so as to ensure the scalability of the proposed alloys. Ultimately, the furthering of alloy design is reliant on strong systems of support between laboratory scale research and industrial manufacture; just as the fusion project as a whole is reliant on strong systems of support between research, industry, and government.

7.2 Conclusions

Energy demand is higher than ever, and current energy sources are either insufficient to meet this demand or otherwise carry with them the burden of increased carbon emission, and contribution to climate crisis. Nuclear fusion is an attractive solution to the energy crisis, but still faces substantial challenges despite international collaboration towards this goal. Not the least of these challenges is the materials challenge the irradiation heavy and high temperature environment of an operating fusion reactor present for structural components. Such considerations necessitate the development and detailed characterisation of low activity, radiation resistant materials, with stable mechanical properties at extremely high temperatures. In particular, the deformation properties of candidate structural materials are key performance indicators – the onset of plasticity, susceptibility to brittle fracture, and resistance to deformation of obvious importance when considering the thermal stresses involved in reactor operation on/off cycling.

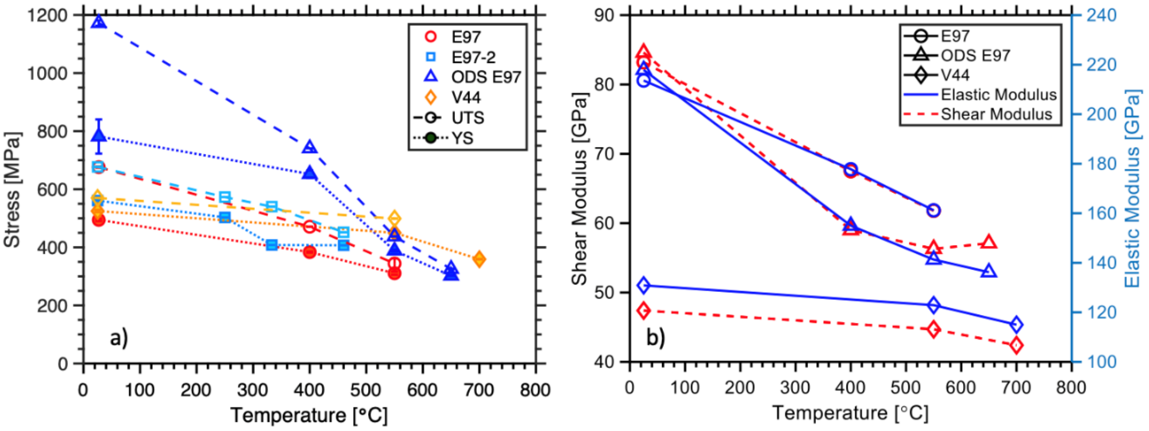

Figure 7.1 Variation of a) yield and ultimate tensile strength, and b) polycrystalline moduli with temperature for tested structural materials

In this work, the elastic properties of three of the front-runner structural materials (EUROFER97 steel, oxide dispersion strengthened EUROFER97 steel, and the refractory alloy V-4Cr-4Ti) were characterised at room and elevated temperature through in-situ synchrotron X-ray diffraction tensile testing. These fundamental materials properties (summarised in Figure 7.1) broaden understanding of deformation of these structural materials, provide data supporting figures of merit for easy comparison between structural materials, and are expected to inform future reactor component modelling.

In addition, evolution of microstructural properties which dictate deformation were also investigated, in the form of dislocation density character evolution (via the modified Williamson-Hall method) and microvoid formation and coalescence (via results of fractographic analysis and computed X-ray tomography). Finally, the next generation of structural materials were considered: the effects of tantalum addition to vanadium-based alloys investigated through a test scheme of V-Ti-Cr-Ta alloys fabricated through arc melting. Mechanical characterisation of the fabricated alloys through micro- and macro- indentation testing confirmed the room temperature strengthening effect of tantalum content in V-based alloys, but results were compromised by unknown impurity content, and difficulty of frame compliance calculation.

The results presented in this work pull together a range of characterisation techniques, providing information on relevant structural properties for baseline, advanced, and next generation nuclear fusion structural materials, which can be expected to inform fusion reactor design decisions going into the future.

BIBLIOGRAPHY

[1] BP, “BP Statistical Review of World Energy 2022,(71st edition),” *Bp*, pp. 1–60, 2022.

[2] ZeroTracker, “Net Zero Tracker,” 2023. [Online]. Available: https://zerotracker.net/. [Accessed: 08-Sep-2023].

[3] International Energy Agency, “Net Zero by 2050: A Roadmap for the Global Energy Sector,” *Int. Energy Agency*, p. 224, 2021.

[4] K. Kim *et al.*, “Design concept of K-DEMO for near-term implementation,” *Nucl. Fusion*, vol. 55, no. 5, 2015.

[5] N. Asakura *et al.*, “Power exhaust concepts and divertor designs for Japanese and European DEMO fusion reactors,” *Nucl. Fusion*, vol. 61, no. 12, 2021.

[6] S. Entler, J. Horacek, T. Dlouhy, and V. Dostal, “Approximation of the economy of fusion energy,” *Energy*, vol. 152, pp. 489–497, 2018.

[7] D. Armstrong *et al.*, “UK Fusion Materials Roadmap 2021-2040,” 2021.

[8] J. Clark and G. MacKerron, “Great expectations. A review of nuclear fusion research,” *Energy Policy*, vol. 17, no. 1, pp. 49–56, 1989.

[9] A. Lépine-Szily and P. Descouvemont, “Nuclear astrophysics: Nucleosynthesis in the Universe,” *Int. J. Astrobiol.*, vol. 11, no. 4, pp. 243–250, 2012.

[10] S. Atzeni and J. Meyer-ter-vehn, “3 Inertial confinement by spherical implosion,” in *The Physics of Inertial Fusion: Beam Plasma Interaction, Hydrodynamics, Hot Dense Matter*, 2004, pp. 47–74.

[11] DOE, “DOE National Laboratory Makes History by Achieving Fusion Ignition [Press Release],” 2022. [Online]. Available: https://www.energy.gov/articles/doe-national-laboratory-makes-history-achieving-fusion-ignition. [Accessed: 10-Sep-2023].

[12] Y. Xu, “A general comparison between tokamak and stellarator plasmas,” *Matter Radiat. Extrem.*, vol. 1, no. 4, pp. 192–200, 2016.

[13] R. Jorge, A. Goodman, M. Landreman, J. Rodrigues, and F. Wechsung, “Single-stage stellarator optimization: combining coils with fixed boundary equilibria,” *Plasma Phys. Control. Fusion*, vol. 65, no. 7, pp. 1–23, 2023.

[14] G. McCracken and P. Stott, “4 - Man-Made Fusion,” in *Fusion: The Energy of the Universe*, 2005, pp. 33–46.

[15] B. Biagini and A. Sagar, “Nongovernmental Organizations (NGOs) and Energy,” *Encycl. Energy*, vol. 4, pp. 301–314, 2004.

[16] G. Arfken, D. Griffing, D. Kelly, and J. Priest, “43 - Nuclear Structure and Nuclear Technology,” in *University Physics*, Academic Press, 1984, pp. 842–869.

[17] W. R. Meier, “Tritium Breeding Blanket for a Commercial Fusion Power Plant-A System Engineering Assessment,” 2014.

[18] G. Federici, L. Boccaccini, F. Cismondi, M. Gasparotto, Y. Poitevin, and I. Ricapito, “An

overview of the EU breeding blanket design strategy as an integral part of the DEMO design effort," *Fusion Eng. Des.*, vol. 141, no. January, pp. 30–42, 2019.

[19] G. Federici *et al.*, "Overview of the DEMO staged design approach in Europe," *Nucl. Fusion*, vol. 59, no. 6, pp. 2012–2021, 2019.

[20] D. J. Campbell *et al.*, "Innovations in Technology and Science R&D for ITER," *J. Fusion Energy*, vol. 38, no. 1, pp. 11–71, 2019.

[21] S.-H. Hong, "A review of DEMO reactor concepts: open questions and issues," *AAPPS Bull.*, vol. 32, no. 1, 2022.

[22] UKAEA, "Fusion energy record demonstrates powerplant future [Press Release]," 2022. [Online]. Available: https://www.gov.uk/government/news/fusion-energy-record-demonstrates-powerplant-future. [Accessed: 23-Jun-2023].

[23] D. J. Mazey and C. A. English, "Role of refractory metal alloys in fusion reactor applications," *J. Less-Common Met.*, vol. 100, no. C, pp. 385–427, 1984.

[24] R. Wenninger *et al.*, "The DEMO wall load challenge," *Nucl. Fusion*, vol. 57, no. 4, 2017.

[25] I. R. Maemunah, Z. Su'ud, A. Waris, and D. Irwanto, "Tritium Breeding Performance Analysis of HCLL Blanket Fusion Reactor Employing Vanadium Alloy (V-5Cr-5Ti) as First Wall Material," *Sci. Technol. Nucl. Install.*, vol. 2022, 2022.

[26] S. Malang and M. S. Tillack, "Development of Self-Cooled Liquid Metal Breeder Blanktes-FZKA5581," no. November 1995, p. 236, 1995.

[27] L. M. Giancarli *et al.*, "Overview of the ITER TBM Program," *Fusion Eng. Des.*, vol. 87, no. 5–6, pp. 395–402, 2012.

[28] G. Federici *et al.*, "DEMO design activity in Europe: Progress and updates," *Fusion Eng. Des.*, vol. 136, no. April, pp. 729–741, 2018.

[29] S. Malang, M. Tillack, C. P. C. Wong, N. Morley, and S. Smolentsev, "Development of the Lead Lithium (DCLL) Blanket Concept," *Fusion Sci. Technol.*, vol. 60, no. 1, pp. 249–256, 2011.

[30] R. Boullon, J. C. Jaboulay, and J. Aubert, "Molten salt breeding blanket: Investigations and proposals of pre-conceptual design options for testing in DEMO," *Fusion Eng. Des.*, vol. 171, no. June, 2021.

[31] L. V. Boccaccini *et al.*, "Objectives and status of EUROfusion DEMO blanket studies," *Fusion Eng. Des.*, vol. 109–111, pp. 1199–1206, 2016.

[32] S. J. Zinkle and J. T. Busby, "Structural materials for fission & fusion energy," *Mater. Today*, vol. 12, no. 11, pp. 12–19, 2009.

[33] F. Abe, "Precipitate design for creep strengthening of 9% Cr tempered martensitic steel for ultra-supercritical power plants," *Sci. Technol. Adv. Mater.*, vol. 9, no. 1, 2008.

[34] E. E. Bloom *et al.*, "Low activation materials for fusion applications," *J. Nucl. Mater.*, vol. 122, no. 1–3, pp. 17–26, 1984.

[35] R. Lindau *et al.*, "Present development status of EUROFER and ODS-EUROFER for application in blanket concepts," *Fusion Eng. Des.*, vol. 75–79, no. SUPPL., pp. 989–996,

2005.

[36] E. Gaganidze, F. Gillemot, I. Szenthe, M. Gorley, M. Rieth, and E. Diegele, “Development of EUROFER97 database and material property handbook,” *Fusion Eng. Des.*, vol. 135, no. February, pp. 9–14, 2018.

[37] M. Rieth *et al.*, “Technological processes for steel applications in nuclear fusion,” *Appl. Sci.*, vol. 11, no. 24, 2021.

[38] K. D. Zilnyk, V. B. Oliveira, H. R. Z. Sandim, A. Möslang, and D. Raabe, “Martensitic transformation in Eurofer-97 and ODS-Eurofer steels: A comparative study,” *J. Nucl. Mater.*, vol. 462, pp. 360–367, 2015.

[39] E. Gaganidze, H. C. Schneider, B. Dafferner, and J. Aktaa, “High-dose neutron irradiation embrittlement of RAFM steels,” *J. Nucl. Mater.*, vol. 355, no. 1–3, pp. 83–88, 2006.

[40] B. Yan *et al.*, “The effect of precipitate evolution on austenite grain growth in RAFM steel,” *Materials (Basel).*, vol. 10, no. 9, pp. 1–11, 2017.

[41] A. Möslang *et al.*, “Towards reduced activation structural materials data for fusion DEMO reactors,” *Nucl. Fusion*, vol. 45, no. 7, pp. 649–655, 2005.

[42] P. Fernandez, A. M. Lancha, J. Lapena, D. Gomez-Briceno, M. Serrano, and M. Hernandez-Mayoral, “Reduced Activation Ferritic/Martensitic Steel Eurofer’97 as Possible Structural Material for Fusion Devices. Metallurgical Characterization on As-Received Condition and After Simulated Service Conditions.,” *Inf. Técnicos Ciemat*, p. 73, 2004.

[43] M. Klimenkov, R. Lindau, E. Materna-Morris, and A. Möslang, “TEM characterization of precipitates in EUROFER 97,” *Prog. Nucl. Energy*, vol. 57, pp. 8–13, 2012.

[44] P. Fernández, A. M. Lancha, J. Lapeña, and M. Hernández-Mayoral, “Metallurgical characterization of the reduced activation ferritic/martensitic steel Eurofer’97 on as-received condition,” *Fusion Eng. Des.*, vol. 58–59, pp. 787–792, 2001.

[45] M. Rieth *et al.*, “EUROFER 97 Tensile, Charpy, Creep and Structural tests,” 2003.

[46] R. Lindau and M. Schirra, “First results on the characterisation of the reduced-activation-ferritic-martensitic steel EUROFER,” *Fusion Eng. Des.*, vol. 58–59, pp. 781–785, 2001.

[47] J. Rensman, E. Lucon, J. Boskeljon, J. Van Hoepen, R. Den Boef, and P. Ten Pierick, “Irradiation resistance of Eurofer97 at 300 °C up to 10 dpa,” *J. Nucl. Mater.*, vol. 329–333, no. 1-3 PART B, pp. 1113–1116, 2004.

[48] E. Gaganidze and J. Aktaa, “Assessment of neutron irradiation effects on RAFM steels,” *Fusion Eng. Des.*, vol. 88, no. 3, pp. 118–128, 2013.

[49] E. Lucon, R. Chaouadi, and M. Decréton, “Mechanical properties of the European reference RAFM steel (EUROFER97) before and after irradiation at 300 °C,” *J. Nucl. Mater.*, vol. 329–333, no. 1-3 PART B, pp. 1078–1082, 2004.

[50] C. Petersen, A. Povstyanko, V. Prokhorov, A. Fedoseev, O. Makarov, and M. Walter, “Tensile and low cycle fatigue properties of different ferritic/martensitic steels after the fast reactor irradiation ‘ARBOR 1,’” *J. Nucl. Mater.*, vol. 386–388, no. C, pp. 299–302, 2009.

[51] A. Bhattacharya *et al.*, “Irradiation hardening and ductility loss of Eurofer97 steel variants after neutron irradiation to ITER-TBM relevant conditions,” *Fusion Eng. Des.*, vol. 173, no. November, p. 112935, 2021.

[52] E. Materna-Morris, H. C. Schneider, and A. Möslang, “Tensile behavior of RAFM alloys after neutron irradiation of up to 16.3 dpa between 250 and 450 °c,” *J. Nucl. Mater.*, vol. 455, no. 1–3, pp. 728–734, 2014.

[53] M. Klimenkov, U. Jäntsch, M. Rieth, and A. Möslang, “Correlation of microstructural and mechanical properties of neutron irradiated EUROFER97 steel,” *J. Nucl. Mater.*, vol. 538, 2020.

[54] E. Gaganidze *et al.*, “Mechanical properties and TEM examination of RAFM steels irradiated up to 70 dpa in BOR-60,” *J. Nucl. Mater.*, vol. 417, no. 1–3, pp. 93–98, 2011.

[55] B. van der Schaaf, C. Petersen, Y. De Carlan, J. W. Rensman, E. Gaganidze, and X. Averty, “High dose, up to 80 dpa, mechanical properties of Eurofer 97,” *J. Nucl. Mater.*, vol. 386–388, no. C, pp. 236–240, 2009.

[56] G. R. Odette, M. J. Alinger, and B. D. Wirth, “Recent developments in irradiation-resistant steels,” *Annu. Rev. Mater. Res.*, vol. 38, pp. 471–503, 2008.

[57] F. A. Garner, M. B. Toloczko, and B. H. Sencer, “Comparison of swelling and irradiation creep behavior of fcc-austenitic and bcc-ferritic/martensitic alloys at high neutron exposure,” *J. Nucl. Mater.*, vol. 276, no. 1, pp. 123–142, 2000.

[58] P. Fernández, M. García-Mazarío, A. M. Lancha, and J. Lapeña, “Grain boundary microchemistry and metallurgical characterization of Eurofer’97 after simulated service conditions,” *J. Nucl. Mater.*, vol. 329–333, no. 1-3 PART A, pp. 273–277, 2004.

[59] B. Van der Schaaf *et al.*, “The development of EUROFER reduced activation steel,” *Fusion Eng. Des.*, vol. 69, no. 1-4 SPEC, pp. 197–203, 2003.

[60] H. Hadraba and I. Dlouhy, “Effect of thermal ageing on the impact fracture behaviour of Eurofer’97 steel,” *J. Nucl. Mater.*, vol. 386–388, no. C, pp. 564–568, 2009.

[61] J. Li, C. Zhang, B. Jiang, L. Zhou, and Y. Liu, “Effect of large-size M23C6-type carbides on the low-temperature toughness of martensitic heat-resistant steels,” *J. Alloys Compd.*, vol. 685, pp. 248–257, 2016.

[62] M. Klimenkov, U. Jäntsch, M. Rieth, and A. Möslang, “Evolution of the EUROFER97 microstructure during thermal treatment up to 122,000 h,” *Nucl. Mater. Energy*, vol. 35, no. February, 2023.

[63] W. Wang, S. Liu, G. Xu, B. Zhang, and Q. Huang, “Effect of Thermal Aging on Microstructure and Mechanical Properties of China Low-Activation Martensitic Steel at 550 °C,” *Nucl. Eng. Technol.*, vol. 48, no. 2, pp. 518–524, 2016.

[64] Q. Min, Q. Guo-xing, C. Ming-chong, D. Qing, C. Lei, and W. Hong-yan, “Microstructure Stability and Mechanical Properties of Reduced Activated Ferritic Martensitic Steel during Thermal Aging at 550 °C for 5000 h,” *J. Mater. Eng. Perform.*, 2022.

[65] K. Shiba, H. Tanigawa, T. Hirose, H. Sakasegawa, and S. Jitsukawa, “Long-term properties of reduced activation ferritic/martensitic steels for fusion reactor blanket system,” *Fusion Eng. Des.*, vol. 86, no. 12, pp. 2895–2899, 2011.

[66] A. F. Armas, C. Petersen, R. Schmitt, M. Avalos, and I. Alvarez, “Cyclic instability of martensite laths in reduced activation ferritic/martensitic steels,” *J. Nucl. Mater.*, vol. 329–333, no. 1-3 PART A, pp. 252–256, 2004.

[67] R. Lindau, A. Möslang, M. Schirra, P. Schlossmacher, and M. Klimenkov, “Mechanical and microstructural properties of a hipped RAFM ODS-steel,” *J. Nucl. Mater.*, vol. 307–311, no. 1 SUPPL., pp. 769–772, 2002.

[68] R. Schaeublin, T. Leguey, P. Spätig, N. Baluc, and M. Victoria, “Microstructure and mechanical properties of two ODS ferritic/martensitic steels,” *J. Nucl. Mater.*, vol. 307–311, no. 1 SUPPL., pp. 778–782, 2002.

[69] E. Lucon, A. Leenaers, and W. Vandermeulen, “Post Irradiation Examination of a Thermo-Mechanically Improved Version of EUROFER ODS,” p. 35, 2006.

[70] M. Klimiankou, R. Lindau, and A. Möslang, “Direct correlation between morphology of (Fe,Cr)23C6 precipitates and impact behavior of ODS steels,” *J. Nucl. Mater.*, vol. 367-370 A, no. SPEC. ISS., pp. 173–178, 2007.

[71] A. Das *et al.*, “Microstructure and fracture toughness characterization of three 9Cr ODS EUROFER steels with different thermo-mechanical treatments,” *J. Nucl. Mater.*, vol. 542, p. 152464, 2020.

[72] E. Lucon, “Tensile and Fracture Toughness Properties of EUROFER ODS (‘EU Batch’ - 6 mm Plate) in the Unirradiated Condition EFDA Long Term Programme Task TW5-TTMS-006 Deliverable D08,” 2006.

[73] Y. Zhou, S. Yin, Y. Jiang, Q. Zhou, J. Peng, and Y. Yan, “Wire and arc additive manufacturing fabrication of ODS-RAFM steels and preliminary evaluation on microstructures and mechanical properties,” *J. Nucl. Mater.*, vol. 572, p. 154068, 2022.

[74] G. Spartacus *et al.*, “Characterization of the nature and morphology of coarse precipitation in various oxide dispersion strengthened steels,” *Materialia*, vol. 17, no. January, p. 101117, 2021.

[75] J. Fu, J. C. Brouwer, R. W. A. Hendrikx, I. M. Richardson, and M. J. M. Hermans, “Microstructure characterisation and mechanical properties of ODS Eurofer steel subject to designed heat treatments,” *Mater. Sci. Eng. A*, vol. 770, 2020.

[76] M. Klimenkov, R. Lindau, U. Jäntsch, and A. Möslang, “Effect of irradiation temperature on microstructure of ferritic-martensitic ODS steel,” *J. Nucl. Mater.*, vol. 493, pp. 426–435, 2017.

[77] M. Klimiankou, R. Lindau, and A. Möslang, “HRTEM study of yttrium oxide particles in ODS steels for fusion reactor application,” *J. Cryst. Growth*, vol. 249, no. 1–2, pp. 381–387, 2003.

[78] K. D. Zilnyk *et al.*, “Long-term microstructural stability of oxide-dispersion strengthened Eurofer steel annealed at 800 °c,” *J. Nucl. Mater.*, vol. 448, no. 1–3, pp. 33–42, 2014.

[79] R. Mateus *et al.*, “Microstructural characterization of the ODS Eurofer 97 EU-batch,” *Fusion Eng. Des.*, vol. 86, no. 9–11, pp. 2386–2389, 2011.

[80] V. S. M. Pereira, H. Schut, and J. Sietsma, “A study of the microstructural stability and defect evolution in an ODS Eurofer steel by means of Electron Microscopy and Positron

Annihilation Spectroscopy," *J. Nucl. Mater.*, vol. 540, p. 152398, 2020.

[81] K. D. Zilnyk, K. G. Pradeep, P. Choi, H. R. Z. Sandim, and D. Raabe, "Long-term thermal stability of nanoclusters in ODS-Eurofer steel: An atom probe tomography study," *J. Nucl. Mater.*, vol. 492, pp. 142–147, 2017.

[82] C. Heintze *et al.*, "Microstructure of oxide dispersion strengthened Eurofer and iron-chromium alloys investigated by means of small-angle neutron scattering and transmission electron microscopy," *J. Nucl. Mater.*, vol. 416, no. 1–2, pp. 35–39, 2011.

[83] J. Fu, T. P. Davis, A. Kumar, I. M. Richardson, and M. J. M. Hermans, "Characterisation of the influence of vanadium and tantalum on yttrium-based nano-oxides in ODS Eurofer steel," *Mater. Charact.*, vol. 175, no. January, 2021.

[84] A. Das, P. Chekhonin, E. Altstadt, F. Bergner, C. Heintze, and R. Lindau, "Microstructural characterization of inhomogeneity in 9Cr ODS EUROFER steel," *J. Nucl. Mater.*, vol. 533, p. 152083, 2020.

[85] D. Brimbal *et al.*, "Microstructural characterization of Eurofer-97 and Eurofer-ODS steels before and after multi-beam ion irradiations at JANNUS Saclay facility," *J. Nucl. Mater.*, vol. 465, pp. 236–244, 2015.

[86] G. Yu, N. Nita, and N. Baluc, "Thermal creep behaviour of the EUROFER 97 RAFM steel and two European ODS EUROFER 97 steels," *Fusion Eng. Des.*, vol. 75–79, no. SUPPL., pp. 1037–1041, 2005.

[87] H. Oka, T. Tanno, Y. Yano, S. Ohtsuka, T. Kaito, and Y. Tachi, "Microstructural stability of ODS steel after very long-term creep test," *J. Nucl. Mater.*, vol. 547, p. 152833, 2021.

[88] P. Zheng *et al.*, "On the thermal stability of a 9Cr-ODS steel aged at 700 °C up to 10000 h - Mechanical properties and microstructure," *Mater. Sci. Eng. A*, vol. 783, no. February, p. 139292, 2020.

[89] R. Schäublin *et al.*, "Microstructural development under irradiation in European ODS ferritic/martensitic steels," *J. Nucl. Mater.*, vol. 351, no. 1–3, pp. 247–260, 2006.

[90] N. V. Luzginova *et al.*, "Irradiation response of ODS Eurofer97 steel," *J. Nucl. Mater.*, vol. 428, no. 1–3, pp. 192–196, 2012.

[91] E. Materna-Morris, R. Lindau, H. C. Schneider, and A. Möslang, "Tensile behavior of EUROFER ODS steel after neutron irradiation up to 16.3 dpa between 250 and 450 °c," *Fusion Eng. Des.*, vol. 98–99, pp. 2038–2041, 2015.

[92] M. Kolluri, P. D. Edmondson, N. V. Luzginova, and F. A. V. D. Berg, "Influence of irradiation temperature on microstructure of EU batch of ODS Eurofer97 steel irradiated with neutrons," *Energy Mater. Mater. Sci. Eng. Energy Syst.*, vol. 9, no. 3, pp. 1697–1703, 2014.

[93] E. Lucon, A. Leenaers, and W. Vandermeulen, "Mechanical response of oxide dispersion strengthened (ODS) EUROFER97 after neutron irradiation at 300 °C," *Fusion Eng. Des.*, vol. 82, no. 15–24, pp. 2438–2443, 2007.

[94] D. A. McClintock, M. A. Sokolov, D. T. Hoelzer, and R. K. Nanstad, "Mechanical properties of irradiated ODS-EUROFER and nanocluster strengthened 14YWT," *J. Nucl. Mater.*, vol. 392, no. 2, pp. 353–359, 2009.

[95] M. Kolluri, P. D. Edmondson, N. V. Luzginova, and F. A. V. D. Berg, “A structure-property correlation study of neutron irradiation induced damage in EU batch of ODS Eurofer97 steel,” *Mater. Sci. Eng. A*, vol. 597, pp. 111–116, 2014.

[96] J. Ribis, E. Bordas, P. Trocellier, Y. Serruys, Y. De Carlan, and A. Legris, “Comparison of the neutron and ion irradiation response of nano-oxides in oxide dispersion strengthened materials,” *J. Mater. Res.*, vol. 30, no. 14, pp. 2210–2221, 2015.

[97] S. Yamashita, N. Akasaka, S. Ukai, and S. Ohnuki, “Microstructural development of a heavily neutron-irradiated ODS ferritic steel (MA957) at elevated temperature,” *J. Nucl. Mater.*, vol. 367-370 A, no. SPEC. ISS., pp. 202–207, 2007.

[98] A. Bhattacharya *et al.*, “Irradiation damage concurrent challenges with RAFM and ODS steels for fusion reactor first-wall/blanket: A review,” *JPhys Energy*, vol. 4, no. 3, 2022.

[99] “Encyclopedia Britannica.” [Online]. Available: https://www.britannica.com/science/periodic-table. [Accessed: 20-Apr-2023].

[100] D. Hancock, D. Homfray, M. Porton, I. Todd, and B. Wynne, “Refractory metals as structural materials for fusion high heat flux components,” *J. Nucl. Mater.*, vol. 512, pp. 169–183, 2018.

[101] T. Muroga, *Refractory metals as core materials for Generation IV nuclear reactors*. Elsevier Ltd, 2016.

[102] S. Boeriu, P. O. Box, S. Barbara, and U. S. A. Ca, “Impact of hafnium content on nuclear performance of breeder and multiplier materials containing zirconium in fusion assemblies,” pp. 8–11, 1993.

[103] T. Noda, F. Abe, Y. Hiroka, H. Araki, T. Fujii, and M. Okada, “Low Activation First Wall Materials for Fusion Reactors,” *Fusion Eng. Des.*, vol. 10, pp. 463–467, 1989.

[104] M. R. Gilbert, J.-C. Sublet, and R. A. Forrest, “Handbook of activation, transmutation and radiation damage properties of the elements simulated using FISPACT-II and TENDL-2014,” 2015.

[105] L. L. Snead, D. T. Hoelzer, M. Rieth, and A. A. N. Nemith, *Refractory Alloys: Vanadium, Niobium, Molybdenum, Tungsten*. Elsevier Inc., 2019.

[106] I. V. Gorynin *et al.*, “Effects of neutron irradiation on properties of refractory metals,” *J. Nucl. Mater.*, vol. 191–194, pp. 421–425, 1992.

[107] S. Nogami *et al.*, “Tungsten–tantalum alloys for fusion reactor applications,” *J. Nucl. Mater.*, vol. 566, p. 153740, 2022.

[108] F. . Campbell, “Refractory Metals,” in *Elements of Metallurgy and Engineering Alloys*, ASM International, 2008, pp. 583–596.

[109] E. M. Savitskii and G. S. Burkhanov, “Interatomic Bond, Crystal Structure, and Principal Physical Properties of Refractory Metals,” in *Physical Metallurgy of Refractory Metals and Alloys*, 1995.

[110] R. E. Gold and D. L. Harrod, “Refractory metal alloys for fusion reactor applications,” *J. Nucl. Mater.*, vol. 85–86, no. PART 2, pp. 805–815, 1979.

[111] F. W. Wiffen, “The Microstructure and Swelling of Neutron Irradiated Tantalum,” *J.*

Nucl. Mater., vol. 67, pp. 119–130, 1977.

[112] K. J. Leonard, J. T. Busby, and S. J. Zinkle, "Microstructural and mechanical property changes in the Ta-base T-111 alloy following thermal aging," *J. Nucl. Mater.*, vol. 366, no. 3, pp. 353–368, 2007.

[113] J. R. DiStefano and H. E. McCoy, "Mechanical properties of T-111 at low to intermediate temperatures," *Int. J. Refract. Met. Hard Mater.*, vol. 20, no. 5–6, pp. 381–387, 2002.

[114] K. . Leonard, "Radiation effectis in Refractory Metals and Alloys," in *Comprehensive Nuclear Materials*, 2012, pp. 190–193.

[115] F. W. Wiffen, "Effects of Irradiation on Properties of Refractory Alloys with Emphasis on SPace Power Reactor Applications," in *Proceedings of Symposium on Refractory Alloy Technology for Space Nuclear Power Applications*, 1984, vol. 8308130, pp. 252-.

[116] R. J. Kurtz *et al.*, "Recent progress on development of vanadium alloys for fusion," *J. Nucl. Mater.*, vol. 329–333, no. 1-3 PART A, pp. 47–55, 2004.

[117] J. M. Chen, V. M. Chernov, R. J. Kurtz, and T. Muroga, "Overview of the vanadium alloy researches for fusion reactors," *J. Nucl. Mater.*, vol. 417, no. 1–3, pp. 289–294, 2011.

[118] T. Muroga, J. M. Chen, V. M. Chernov, R. J. Kurtz, and M. Le Flem, "Present status of vanadium alloys for fusion applications," *J. Nucl. Mater.*, vol. 455, no. 1–3, pp. 263–268, 2014.

[119] B. A. Loomis, D. L. Smith, and F. A. Garner, "Swelling of neutron-irradiated vanadium alloys," *J. Nucl. Mater.*, vol. 179–181, no. PART 1, pp. 771–774, 1991.

[120] A. O. Boev, K. P. Zolnikov, I. V. Nelasov, and A. G. Lipnitskii, "Effect of titanium on the primary radiation damage answelling of vanadium-titanium alloys," *Lett. Mater.*, vol. 8, no. 3, pp. 263–267, 2018.

[121] J. Shen, T. Nagasaka, M. Tokitani, T. Muroga, R. Kasada, and S. Sakurai, "Effects of titanium concentration on microstructure and mechanical properties of high-purity vanadium alloys," *Mater. Des.*, vol. 224, p. 111390, 2022.

[122] B. A. Loomis, R. H. Lee, D. L. Smith, and J. R. Peterson, "Strength, ductility, and ductile-brittle transition temperature for MFR candidate vanadium alloys," *J. Nucl. Mater.*, vol. 155–157, no. PART 2, pp. 631–638, 1988.

[123] S. J. Zinkle *et al.*, "Research and development on vanadium alloys for fusion applications," *J. Nucl. Mater.*, vol. 258–263, no. PART 1 A, pp. 205–214, 1998.

[124] K. Sakai, M. Satou, M. Fujiwara, K. Takanashi, A. Hasegawa, and K. Abe, "Mechanical properties and microstructures of high-chromium V-Cr-Ti type alloys," *J. Nucl. Mater.*, vol. 329–333, no. 1-3 PART A, pp. 457–461, 2004.

[125] H. M. Chung, B. A. Loomis, and D. L. Smith, "Development and testing of vanadium alloys for fusion applications," *J. Nucl. Mater.*, vol. 239, no. 1–3, pp. 139–156, 1996.

[126] M. M. Potapenko *et al.*, "Manufacture of semifinished items of alloys V-4Ti-4Cr and V-10Ti-5Cr for use as a structural material in fusion applications," *J. Nucl. Mater.*, vol. 233–237, no. PART 1, pp. 438–441, 1996.

[127] D. R. Diercks and B. A. Loomis, "Alloying and Impurity Effects in Vanadium-Base Alloys,"

J. Nucl. Mater., vol. 143, pp. 1117–1124, 1986.

[128] J. Chen, S. Qiu, L. Yang, Z. Xu, Y. Deng, and Y. Xu, “Effects of oxygen, hydrogen and neutron irradiation on the mechanical properties of several vanadium alloys,” *J. Nucl. Mater.*, vol. 302, no. 2–3, pp. 135–142, 2002.

[129] T. Muroga, T. Nagasaka, A. Iiyoshi, A. Kawabata, S. Sakurai, and M. Sakata, “NIFS program for large ingot production of a V-Cr-Ti alloy,” *J. Nucl. Mater.*, vol. 283–287, pp. 711–715, 2000.

[130] T. Nagasaka, T. Muroga, K. I. Fukumoto, H. Watanabe, M. L. Grossbeck, and J. Chen, “Development of fabrication technology for low activation vanadium alloys as fusion blanket structural materials,” *Nucl. Fusion*, vol. 46, no. 5, pp. 618–625, 2006.

[131] T. Nagasaka, J. F. King, M. L. Grossbeck, and T. Muroga, “Comparison of impact property of Japanese and US reference heats of V-4Cr-4Ti after gas-tungsten-arc welding,” *Fusion Technol.*, vol. 39, no. 2, pp. 664–668, 2001.

[132] T. Nagasaka *et al.*, “High-temperature creep properties of NIFS-HEAT-2 high-purity low-activation vanadium alloy,” *Nucl. Fusion*, vol. 59, no. 9, p. 096046, 2019.

[133] N. J. Heo, T. Nagasaka, T. Muroga, and H. Matsui, “Effect of impurity levels on precipitation behavior in the low-activation V-4Cr-4Ti alloys,” *J. Nucl. Mater.*, vol. 307–311, no. 1 SUPPL., pp. 620–624, 2002.

[134] A. Impagnatiello, T. Toyama, and E. Jimenez-Melero, “Ti-rich precipitate evolution in vanadium-based alloys during annealing above 400 °C,” *J. Nucl. Mater.*, vol. 485, pp. 122–128, 2017.

[135] B. Zhu, S. Yang, M. Zhang, J. Ding, Y. Long, and F. Wan, “Formation and evolution of platelet-like Ti-rich precipitates in the V-4Cr-4Ti alloy,” *Mater. Charact.*, vol. 111, pp. 60–66, 2016.

[136] N. I. Budilkin *et al.*, “Comparison of mechanical properties and structure of vanadium alloys relevant to DEMO conditions of the first wall and blanket,” *J. Nucl. Mater.*, vol. 233–237, no. PART 1, pp. 431–437, 1996.

[137] J. M. Chen, T. Nagasaka, T. Muroga, S. Y. Qiu, C. Li, and N. Nita, “Mechanical properties of V-4Cr-4Ti strengthened by precipitation and cold rolling,” *J. Nucl. Mater.*, vol. 374, no. 1–2, pp. 298–303, 2008.

[138] A. F. Rowcliffe, S. J. Zinkle, and D. T. Hoelzer, “Effect of strain rate on the tensile properties of unirradiated and irradiated V-4Cr-4Ti,” *J. Nucl. Mater.*, vol. 283–287, no. PART I, pp. 508–512, 2000.

[139] M. C. Billone, H. M. Chung, and D. L. Smith, “Revision of the tensile database for V-Ti and V-Cr-Ti alloys tested at ANL,” *J. Nucl. Mater.*, vol. 258–263, no. PART 2 B, pp. 1523–1527, 1998.

[140] M. Li and S. J. Zinkle, “Deformation mechanism maps of unirradiated and irradiated V-4Cr-4Ti,” *ASTM Spec. Tech. Publ.*, vol. 1475 STP, no. 10, pp. 328–344, 2006.

[141] H. Y. Fu *et al.*, “Fabrication using electron beam melting of a V-4Cr-4Ti alloy and its thermo-mechanical strengthening study,” *J. Nucl. Mater.*, vol. 442, no. 1-3 SUPPL.1, p. S336, 2013.

[142] T. Muroga, T. Nagasaka, P. F. Zheng, Y. F. Li, and H. Watanabe, “Dislocation evolution during thermal creep deformation in V-4Cr-4Ti with various thermal and mechanical treatments,” *J. Nucl. Mater.*, vol. 442, no. 1-3 SUPPL.1, pp. 354–359, 2013.

[143] P. F. Zheng, T. Nagasaka, T. Muroga, J. M. Chen, and Y. F. Li, “Creep properties of V-4Cr-4Ti strengthened by cold working and aging,” *Fusion Eng. Des.*, vol. 86, no. 9–11, pp. 2561–2564, 2011.

[144] T. Muroga, T. Nagasaka, J. M. Chen, Y. F. Li, and H. Watanabe, “Microstructure of creep-deformed V-4Cr-4Ti strengthened by precipitation and cold rolling,” *J. Nucl. Mater.*, vol. 386–388, no. C, pp. 606–609, 2009.

[145] L. L. Snead, S. J. Zinkle, D. J. Alexander, A. F. Rowcliffe, J. . Robertson, and W. . Eatherly, “Summary of the Investigation of Low Temperature, Low Dose Radiation Effects on the V-4Cr-4Ti Alloy,” *Fusion Mater.*, vol. DOE/ER-031, p. 81, 1997.

[146] S. J. Zinkle, “Thermophysical and Mechanical Properties of V-(4-5)%Cr-(4-5)%Ti Alloys,” 1998.

[147] D. S. Gelles, P. . Rice, S. . Zinkle, and H. . Chung, “Microstructural examination of irradiated V-(4-5 %)Cr-(4-5%)Ti,” *Fusion Mater. Semiannu. Prog. Rep. period End. December 31, 1997*, pp. 1380–1385, 1998.

[148] K. I. Fukumoto *et al.*, “Radiation-induced precipitation in V-(Cr, Fe)-Ti alloys irradiated at low temperature with low dose during neutron or ion irradiation,” *J. Nucl. Mater.*, vol. 283–287, pp. 535–539, 2000.

[149] K. ichi Fukumoto, H. Matsui, H. Ohkubo, Z. Tang, Y. Nagai, and M. Hasegawa, “Identification of ultra-fine Ti-rich precipitates in V-Cr-Ti alloys irradiated below 300 °C by using positron CDB technique,” *J. Nucl. Mater.*, vol. 373, no. 1–3, pp. 289–294, 2008.

[150] K. Fukumoto, K. Tone, T. Onitsuka, and T. Ishigami, “Effect of Ti addition on microstructural evolution of V–Cr–Ti alloys to balance irradiation hardening with swelling suppression,” *Nucl. Mater. Energy*, vol. 15, no. February, pp. 122–127, 2018.

[151] M. Satou, T. Chuto, and K. Abe, “Improvement in post-irradiation ductility of neutron irradiated V-Ti-Cr-Si-Al-Y alloy and the role of interstitial impurities,” *J. Nucl. Mater.*, vol. 283–287, no. PART I, pp. 367–371, 2000.

[152] L. Peng, C. Jiang, X. Li, P. Zhou, Y. Li, and X. Lai, “The formation of precipitates and its effect on grain structure in V-4Cr-4Ti alloys with yttrium addition,” *J. Alloys Compd.*, vol. 694, pp. 1165–1174, 2017.

[153] T. Furuno *et al.*, “Effects of grain size on high temperature creep of fine grained, solution and dispersion hardened V-1.6Y-8W-0.8TiC,” *J. Nucl. Mater.*, vol. 417, no. 1–3, pp. 299–302, 2011.

[154] T. Chuto, M. Satou, A. Hasegawa, K. Abe, T. Muroga, and N. Yamamoto, “Effects of small amount of additional elements on control of interstitial impurities and mechanical properties of V-4Cr-4Ti-Si-Al-Y alloys,” *J. Nucl. Mater.*, vol. 326, no. 1, pp. 1–8, 2004.

[155] T. Miyazawa *et al.*, “Effect of Yttrium Addition on Mechanical Properties for V-4Cr-4Ti Alloy Contaminated with Oxygen and Nitrogen Impurities,” *Plasma Fusion Res.*, vol. 8, no. 1405166, pp. 1–6, 2013.

[156] J. Chen, T. Muroga, T. Nagasaka, Y. Xu, and S. Qiu, “The recovery and recrystallization of cold rolled V-W-Ti alloys,” *J. Nucl. Mater.*, vol. 322, no. 1, pp. 73–79, 2003.

[157] J. M. Chen *et al.*, “The development of advanced vanadium alloys for fusion applications,” *J. Nucl. Mater.*, vol. 329–333, no. 1-3 PART A, pp. 401–405, 2004.

[158] J. M. Chen *et al.*, “The mechanical properties of V-4Cr-4Ti in various thermo-mechanical states,” *Fusion Eng. Des.*, vol. 81, no. 23–24, pp. 2899–2905, 2006.

[159] V. M. Chernov *et al.*, “Microstructure and mechanical properties of V-Me(Cr,W)-Zr alloys as a function of their chemical-thermal treatment modes,” *Nucl. Mater. Energy*, vol. 3–4, pp. 17–21, 2015.

[160] A. N. Tyumentsev *et al.*, “The effect of thermomechanical treatment regimes on microstructure and mechanical properties of V–Me(Cr, W)–Zr–C alloys,” *Phys. At. Nucl.*, vol. 78, no. 10, pp. 1092–1099, 2015.

[161] B. R. Rajala and R. J. V. A. N. Thyne, “The Development of Improved Vanadium-Base Alloys for Use at Temperatures Up to 1800F,” *J. Less Common Met.*, vol. 3, pp. 489–500, 1961.

[162] D. L. Harrod and R. E. Gold, “Mechanical properties of vanadium and vanadium-base alloys,” *Int. Met. Rev.*, vol. 25, no. 1, pp. 163–211, 1980.

[163] T. Kainuma, N. Iwao, T. Suzuki, and R. Watanabe, “Creep and creep rupture properties of unalloyed vanadium and solid-solution-strengthened vanadium-base alloys,” *J. Less-Common Met.*, vol. 86, no. C, pp. 263–277, 1982.

[164] N. Iwao, T. Kainuma, T. Suzuki, and R. Watanabe, “Mechanical properties of vanadium-base binary alloys,” *J. Less-Common Met.*, vol. 83, no. 2, pp. 205–217, 1982.

[165] V. V. Shyrokov, C. B. Vasyliv, and O. V. Shyrokov, “Ways of improving the high-temperature work service of vanadium and some alloys used in reactors,” *J. Nucl. Mater.*, vol. 394, no. 1, pp. 114–122, 2009.

[166] N. Iwao, T. Kainuma, R. Watanabe, and T. Shimomura, “Mechanical Properties of Vanadium-Tantalum Alloys,” *Trans. JIM*, vol. 20, pp. 172–180, 1979.

[167] N. Iwao, T. Kainuma, T. Suzuki, and R. Watanabe, “Mechanical properties of high strength vanadium-base ternary alloys,” *J. Less-Common Met.*, vol. 83, no. 2, pp. 219–225, 1982.

[168] U. Jain, J. Sonber, and R. Tewari, “High temperature oxidation behaviour of V-Ti-Ta alloys,” *Fusion Eng. Des.*, vol. 144, no. March, pp. 125–132, 2019.

[169] U. Jain, A. Mukherjee, and G. K. Dey, “Thermodynamic properties of Ti in V-Ti-Ta alloys: Effect of Ta addition,” *J. Alloys Compd.*, vol. 686, pp. 946–950, 2016.

[170] U. Jain *et al.*, “Recrystallization and structure-property correlation in V-Ti-Ta alloys,” *Mater. Sci. Eng. A*, vol. 803, no. March 2020, p. 140648, 2020.

[171] T. Miyazawa, Y. Hishinuma, T. Nagasaka, and T. Muroga, “Effect of tantalum addition on the tensile properties of V-Ta-4Cr-4Ti quaternary alloys,” *Fusion Eng. Des.*, vol. 165, no. December 2020, p. 112191, 2021.

[172] T. Miyazawa *et al.*, “Effect on impact properties of adding tantalum to V-4Cr-4Ti ternary

vanadium alloy," *Nucl. Mater. Energy*, vol. 31, no. April, p. 101198, 2022.

[173] P. J. Barron, A. W. Carruthers, J. W. Fellowes, N. G. Jones, H. Dawson, and E. J. Pickering, "Towards V-based high-entropy alloys for nuclear fusion applications," *Scr. Mater.*, vol. 176, pp. 12–16, 2020.

[174] M. H. Tsai and J. W. Yeh, "High-entropy alloys: A critical review," *Mater. Res. Lett.*, vol. 2, no. 3, pp. 107–123, 2014.

[175] J. W. Yeh, "Alloy design strategies and future trends in high-entropy alloys," *JOM*, vol. 65, no. 12, pp. 1759–1771, 2013.

[176] O. El-Atwani *et al.*, "Outstanding radiation resistance of tungsten-based high-entropy alloys," *Sci. Adv.*, vol. 5, no. 3, pp. 1–10, 2019.

[177] X. Xian *et al.*, "A high-entropy V35Ti35Fe15Cr10Zr5 alloy with excellent high-temperature strength," *Mater. Des.*, vol. 121, pp. 229–236, 2017.

[178] S. Praveen and H. S. Kim, "High-Entropy Alloys: Potential Candidates for High-Temperature Applications – An Overview," *Adv. Eng. Mater.*, vol. 20, no. 1, pp. 1–22, 2018.

[179] X. Zhang *et al.*, "Investigation of the interstitial oxygen behaviors in vanadium alloy: A first-principles study," *Curr. Appl. Phys.*, vol. 18, no. 2, pp. 183–190, 2018.

[180] Z. Lyu, C. Lee, S. Y. Wang, X. Fan, J. W. Yeh, and P. K. Liaw, "Effects of Constituent Elements and Fabrication Methods on Mechanical Behavior of High-Entropy Alloys: A Review," *Metall. Mater. Trans. A Phys. Metall. Mater. Sci.*, vol. 50, no. 1, pp. 1–28, 2019.

[181] C. Lee *et al.*, "Lattice distortion in a strong and ductile refractory high-entropy alloy," *Acta Mater.*, vol. 160, pp. 158–172, 2018.

[182] S. J. Zinkle, "Advanced irradiation-resistant materials for Generation IV nuclear reactors," in *Structural Materials for Generation IV Nuclear Reactors*, Elsevier Ltd, 2016, pp. 569–594.

[183] H. G. Brokmeier, E. Maawad, R. E. Bolmaro, Z. Y. Zhong, and N. Schell, "Combined materials characterization by area detector investigations using hard X-rays," *IOP Conf. Ser. Mater. Sci. Eng.*, vol. 82, no. 1, 2015.

[184] K. Wille, "Introduction to Insertion Devices," *Cern Accel. Sch.*, pp. 61–75, 1996.

[185] R. P. Walker, "New lamps for old: Synchrotron radiation and free-electron laser x-ray sources," *AIP Conf. Proc.*, vol. 389, pp. 21–42, 1997.

[186] W. . Bassett and G. . Brown, "Synchrotron radiation: Applications in the Earth Sciences," *Annu. Rev. Earth Planet. Sci.*, no. 18, pp. 387–447, 1990.

[187] M. Drakopoulos *et al.*, "I12: The Joint Engineering, Environment and Processing (JEEP) beamline at Diamond Light Source," *J. Synchrotron Radiat.*, vol. 22, no. 2015, pp. 828–838, 2015.

[188] B. B. He, "Introduction," in *Two Dimensional X-ray Diffraction*, John Wiley & Sons, 2009, pp. 1–28.

[189] C. Hammond, “X-ray diffraction of polycrystalline materials,” *Basics Crystallogr. Diffr.*, pp. 252–282, 2015.

[190] P. J. Withers, “Depth capabilities of neutron and synchrotron diffraction strain measurement instruments. II. Practical implications,” *J. Appl. Crystallogr.*, vol. 37, no. 4, pp. 607–612, 2004.

[191] A. P. Sutton, “Hooke’s Law and Elastic Constants,” in *Physics of Elasticity and Crystal Defects*, 2020, pp. 29–53.

[192] J. B. Ketterson, “Elastic Behavior of Solids,” in *The Physics of Solids*, 2016, pp. 3–20.

[193] R. De Wit, “Diffraction elastic constants of a cubic polycrystal,” *J. Appl. Crystallogr.*, vol. 30, no. 4, pp. 510–511, 1997.

[194] L. Q. Chen, “Phase-field models for microstructure evolution,” *Annu. Rev. Mater. Sci.*, vol. 32, pp. 113–140, 2002.

[195] S. E. Esfahani, I. Ghamarian, V. I. Levitas, and P. C. Collins, “Microscale phase field modeling of the martensitic transformation during cyclic loading of NiTi single crystal,” *Int. J. Solids Struct.*, vol. 146, pp. 80–96, 2018.

[196] D. Tourret, H. Liu, and J. LLorca, “Phase-field modeling of microstructure evolution: Recent applications, perspectives and challenges,” *Prog. Mater. Sci.*, vol. 123, no. March 2021, p. 100810, 2022.

[197] T. Ungár and A. Borbély, “The effect of dislocation contrast on x-ray line broadening: A new approach to line profile analysis,” *Appl. Phys. Lett.*, vol. 69, no. 21, pp. 3173–3175, 1996.

[198] T. Ungár, I. Dragomir, Á. Révész, and A. Borbély, “The contrast factors of dislocations in cubic crystals: The dislocation model of strain anisotropy in practice,” *J. Appl. Crystallogr.*, vol. 32, no. 5, pp. 992–1002, 1999.

[199] Y. H. Zhang and W. Z. Han, “Mechanism of brittle-to-ductile transition in tungsten under small-punch testing,” *Acta Mater.*, vol. 220, p. 117332, 2021.

[200] Y. Lu, Y. H. Zhang, E. Ma, and W. Z. Han, “Relative mobility of screw versus edge dislocations controls the ductile-to-brittle transition in metals,” *Proc. Natl. Acad. Sci. U. S. A.*, vol. 118, no. 37, pp. 1–6, 2021.

[201] Y. H. Zhang, E. Ma, J. Sun, and W. Z. Han, “A unified model for ductile-to-brittle transition in body-centered cubic metals,” *J. Mater. Sci. Technol.*, vol. 141, pp. 193–198, 2023.

[202] S. Xu, Z. Zhou, H. Jia, and Z. Yao, “Microstructure Characterization and Mechanical Properties of Al Alloyed 9Cr ODS Steels with Different Al Contents,” *Steel Res. Int.*, vol. 90, no. 7, pp. 1–11, 2019.

[203] R. Jarugula, S. Channagiri, S. G. S. Raman, and G. Sundararajan, “Strengthening Mechanisms in Nano Oxide Dispersion-Strengthened Fe-18Cr Ferritic Steel at Different Temperatures,” *Metall. Mater. Trans. A Phys. Metall. Mater. Sci.*, vol. 52, no. 5, pp. 1901–1912, 2021.

[204] H. Adachi, H. Mizowaki, M. Hirata, D. Okai, and H. Nakanishi, “Measurement of dislocation density change during tensile deformation in coarse-grained aluminum by

in-situ XRD technique with tester oscillation+1," *Mater. Trans.*, vol. 62, no. 1, pp. 62–68, 2021.

[205] H. Adachi, Y. Miyajima, M. Sato, and N. Tsuji, "Evaluation of dislocation density for 1100 aluminum with different grain size during tensile deformation by using In-situ X-ray diffraction technique," *Keikinzoku/Journal Japan Inst. Light Met.*, vol. 64, no. 10, pp. 463–469, 2014.

[206] H. Adachi, Y. Karamatsu, S. Nakayama, T. Miyazawa, M. Sato, and T. Yamasaki, "Elastic and plastic deformation behavior studied by in-situ synchrotron x-ray diffraction in nanocrystalline nickel," *Mater. Trans.*, vol. 57, no. 9, pp. 1447–1453, 2016.

[207] Z. Zhuang, Z. Liu, and Y. Cui, "Dislocation-Based Single-Crystal Plasticity Model," *Dislocation Mech. Cryst. Plast.*, pp. 91–119, 2019.

[208] F. Roters, P. Eisenlohr, L. Hantcherli, D. D. Tjahjanto, T. R. Bieler, and D. Raabe, "Overview of constitutive laws, kinematics, homogenization and multiscale methods in crystal plasticity finite-element modeling: Theory, experiments, applications," *Acta Mater.*, vol. 58, no. 4, pp. 1152–1211, 2010.

[209] G. Z. Voyiadjis and M. Yaghoobi, "Chapter 3 - Nonlocal crystal plasticity," in *Size Effects in Plasticity*, 2019, pp. 191–232.

[210] A. Ma, F. Roters, and D. Raabe, "A dislocation density based constitutive model for crystal plasticity FEM including geometrically necessary dislocations," *Acta Mater.*, vol. 54, no. 8, pp. 2169–2179, 2006.

[211] R. Juan, W. Liu, X. G. Inza, X. D. Ureta, J. M. Olaeta, and J. Lian, "Crystal Plasticity Modeling of Al Alloy under Linear and Non-Linear Loading," *Key Eng. Mater.*, vol. 926 KEM, pp. 2099–2108, 2022.

[212] A. Arsenlis and D. M. Parks, "Modeling the evolution of crystallographic dislocation density in crystal plasticity," *J. Mech. Phys. Solids*, vol. 50, no. 9, pp. 1979–2009, 2002.

[213] Y. C. Ye, F. Y. Zhao, C. M. Huang, S. X. Bai, and Q. Chen, "Multiscale simulation and experimental measurements of the elastic response for constructional steel," *Sci. Rep.*, vol. 12, no. 1, pp. 1–11, 2022.

[214] S. A. Pitts, W. Jiang, D. Pizzocri, E. I. Barker, and H. M. Zbib, "A Continuum Dislocation Dynamics Crystal Plasticity Approach to Irradiated Body-Centered Cubic α-Iron," *J. Eng. Mater. Technol. Trans. ASME*, vol. 144, no. 1, 2022.

[215] H. Hou, G. Zhao, J. Yu, and D. Wei, "Nonlinear unloading-reloading behavior and macro/micro models during multi-pass cyclic hot compression of aluminum alloys," *Mater. Sci. Eng. A*, vol. 882, no. July, p. 145447, 2023.

[216] M. Verdier, Y. Brechet, and P. Guyot, "Recovery of A1Mg alloys: Flow stress and strain-hardening properties," *Acta Mater.*, vol. 47, no. 1, pp. 127–134, 1998.

[217] J. Friedel, "Chapter X: Annealing, Polygonization, Recrystallization, Grain Boundaries," in *Dislocations*, Elsevier Science & Technology, 1964, pp. 277–278.

[218] J. Tang *et al.*, "Integrated physically based modeling for the multiple static softening mechanisms following multi-stage hot deformation in Al-Zn-Mg-Cu alloys," *Int. J. Plast.*, vol. 134, no. May, p. 102809, 2020.

[219] C. Couchet *et al.*, “Recovery of severely deformed ferrite studied by in situ high energy X-ray diffraction,” *Mater. Charact.*, vol. 179, no. March, 2021.

[220] S. Sugiyama, T. Ogawa, L. He, Z. Wang, and Y. Adachi, “Quantitative analysis of the recovery process in pure iron using X-ray diffraction line profile analysis,” *Materials (Basel).*, vol. 14, no. 4, pp. 1–13, 2021.

[221] A. Smith, H. Luo, D. N. Hanlon, J. Sietsma, and S. Van Der Zwaag, “Recovery processes in the ferrite phase in C-Mn steel,” *ISIJ Int.*, vol. 44, no. 7, pp. 1188–1194, 2004.

[222] T. O. Erinosho, D. M. Collins, A. J. Wilkinson, R. I. Todd, and F. P. E. Dunne, “Assessment of X-ray diffraction and crystal plasticity lattice strain evolutions under biaxial loading,” *Int. J. Plast.*, vol. 83, pp. 1–18, 2016.

[223] W. Chen *et al.*, “Microscale residual stresses in additively manufactured stainless steel,” *Nat. Commun.*, vol. 10, no. 1, pp. 1–12, 2019.

[224] J. Cheng, B. K. Lin, N. S. Pottore, S. Sadagopan, H. Zhu, and X. Hu, “A mesoscale crystal plasticity model to predict room-temperature deformation and martensitic transformation of high-strength Quenching and Partitioning (Q&P) Steels and validation with synchrotron X-ray diffraction,” *Int. J. Plast.*, vol. 172, no. 103833, 2024.

[225] P. Hou *et al.*, “Synchrotron x-ray diffraction and crystal plasticity modeling study of martensitic transformation, texture development, and stress partitioning in deep-drawn TRIP steels,” *Materialia*, vol. 18, no. June, p. 101162, 2021.

[226] A. A. F. Tavassoli, E. Diegele, R. Lindau, N. Luzginova, and H. Tanigawa, “Current status and recent research achievements in ferritic/martensitic steels,” *J. Nucl. Mater.*, vol. 455, no. 1–3, pp. 269–276, 2014.

[227] H. Tanigawa, K. Shiba, H. Sakasegawa, T. Hirose, and S. Jitsukawa, “Technical issues related to the development of reduced-activation ferritic/martensitic steels as structural materials for a fusion blanket system,” *Fusion Eng. Des.*, vol. 86, no. 9–11, pp. 2549–2552, 2011.

[228] M. Zmitko *et al.*, “The European ITER Test Blanket Modules: EUROFER97 material and TBM’s fabrication technologies development and qualification,” *Fusion Eng. Des.*, vol. 124, pp. 767–773, 2017.

[229] L. Forest *et al.*, “Status of the EU DEMO breeding blanket manufacturing R&D activities,” *Fusion Eng. Des.*, vol. 152, no. October 2018, p. 111420, 2020.

[230] F. Tavassoli, “Eurofer steel, development to full code qualification,” *Procedia Eng.*, vol. 55, pp. 300–308, 2013.

[231] L. Tan, L. L. Snead, and Y. Katoh, “Development of new generation reduced activation ferritic-martensitic steels for advanced fusion reactors,” *J. Nucl. Mater.*, vol. 478, pp. 42–49, 2016.

[232] L. Tan, Y. Katoh, and L. L. Snead, “Development of castable nanostructured alloys as a new generation RAFM steels,” *J. Nucl. Mater.*, vol. 511, pp. 598–604, 2018.

[233] S. J. Zinkle *et al.*, “Development of next generation tempered and ODS reduced activation ferritic/martensitic steels for fusion energy applications,” *Nucl. Fusion*, vol. 57, no. 9, 2017.

[234] R. Andreani and M. Gasparotto, “Overview of fusion nuclear technology in Europe,” *Fusion Eng. Des.*, vol. 61–62, no. 2002, pp. 27–36, 2002.

[235] A. Wasilkowska, M. Bartsch, U. Messerschmidt, R. Herzog, and A. Czyrska-Filemonowicz, “Creep mechanisms of ferritic oxide dispersion strengthened alloys,” *J. Mater. Process. Technol.*, vol. 133, no. 1–2, pp. 218–224, 2003.

[236] J. Wang, W. Yuan, R. S. Mishra, and I. Charit, “Microstructure and mechanical properties of friction stir welded oxide dispersion strengthened alloy,” *J. Nucl. Mater.*, vol. 432, no. 1–3, pp. 274–280, 2013.

[237] P. Olier, A. Bougault, A. Alamo, and Y. de Carlan, “Effects of the forming processes and Y2O3 content on ODS-Eurofer mechanical properties,” *J. Nucl. Mater.*, vol. 386–388, no. C, pp. 561–563, 2009.

[238] Y. de Carlan *et al.*, “CEA developments of new ferritic ODS alloys for nuclear applications,” *J. Nucl. Mater.*, vol. 386–388, no. C, pp. 430–432, 2009.

[239] D. Kumar, U. Prakash, V. V. Dabhade, K. Laha, and T. Sakthivel, “High yttria ferritic ODS steels through powder forging,” *J. Nucl. Mater.*, vol. 488, pp. 75–82, 2017.

[240] Z. Lu, R. G. Faulkner, N. Riddle, F. D. Martino, and K. Yang, “Effect of heat treatment on microstructure and hardness of Eurofer 97, Eurofer ODS and T92 steels,” *J. Nucl. Mater.*, vol. 386–388, no. C, pp. 445–448, 2009.

[241] A. Alamo, H. Regle, G. Pons, and J. L. Béchade, “Microstructure and Textures of Ods Ferritic Alloys Obtained by Mechanical Alloying,” *Mater. Sci. Forum*, vol. 88–90, no. January, pp. 183–190, 1992.

[242] J. Shen *et al.*, “Study on anisotropy in microstructure and tensile properties of the 12Cr oxide dispersion strengthened (ODS) steel,” *Fusion Eng. Des.*, vol. 146, no. February, pp. 1082–1085, 2019.

[243] R. Blondé *et al.*, “High-energy X-ray diffraction study on the temperature-dependent mechanical stability of retained austenite in low-alloyed TRIP steels,” *Acta Mater.*, vol. 60, no. 2, pp. 565–577, 2012.

[244] X. Zhang *et al.*, “In situ high-energy X-ray diffraction study of tensile deformation of neutron-irradiated polycrystalline Fe-9%Cr alloy,” *Acta Mater.*, vol. 126, pp. 67–76, 2017.

[245] R. A. Renzetti, H. R. Z. Sandim, R. E. Bolmaro, P. A. Suzuki, and A. Möslang, “X-ray evaluation of dislocation density in ODS-Eurofer steel,” *Mater. Sci. Eng. A*, vol. 534, pp. 142–146, 2012.

[246] G. M. Stoica, A. D. Stoica, M. K. Miller, and D. Ma, “Temperature-dependent elastic anisotropy and mesoscale deformation in a nanostructured ferritic alloy,” *Nat. Commun.*, vol. 5, pp. 1–8, 2014.

[247] J. L. Lin *et al.*, “In situ synchrotron tensile investigations on 14YWT, MA957, and 9-Cr ODS alloys,” *J. Nucl. Mater.*, vol. 471, pp. 289–298, 2016.

[248] Y. Gan *et al.*, “Temperature effect of elastic anisotropy and internal strain development in advanced nanostructured alloys: An in-situ synchrotron X-ray investigation,” *Mater. Sci. Eng. A*, vol. 692, no. March, pp. 53–61, 2017.

[249] K. Mo *et al.*, “Synchrotron study on load partitioning between ferrite/martensite and nanoparticles of a 9Cr ODS steel,” *J. Nucl. Mater.*, vol. 455, no. 1–3, pp. 376–381, 2014.

[250] R. Husák, H. Hadraba, Z. Chlup, M. Heczko, T. Kruml, and V. Puchý, “ODS EUROFER steel strengthened by y-(Ce, hf, la, sc, and zr) complex oxides,” *Metals (Basel).*, vol. 9, no. 11, pp. 1–14, 2019.

[251] M. De Sanctis *et al.*, “Temperature dependent mechanical behavior of ods steels,” *Mater. Sci. Forum*, vol. 941 MSF, pp. 257–262, 2018.

[252] M. De Sanctis *et al.*, “Mechanical characterization of a nano-ODS steel prepared by low-energy mechanical alloying,” *Metals (Basel).*, vol. 7, no. 8, pp. 1–12, 2017.

[253] Y. Q. Wang, M. Gorley, S. Kabra, and E. Surrey, “Influence of a 1.5 T magnetic field on the tensile properties of Eurofer-97 steel,” *Fusion Eng. Des.*, vol. 141, no. January, pp. 68–72, 2019.

[254] R. A. Renzetti, H. R. Z. Sandim, A. F. Padilha, D. Raabe, R. Lindau, and A. Möslang, “Annealing effects on the microstructure of ferritic-martensitic ODS-Eurofer steel,” *Fusion Sci. Technol.*, vol. 60, no. 1 T, pp. 22–26, 2011.

[255] F. Bachmann, R. Hielscher, and H. Schaeben, “Grain detection from 2d and 3d EBSD data-Specification of the MTEX algorithm,” *Ultramicroscopy*, vol. 111, no. 12, pp. 1720–1733, 2011.

[256] F. Bachmann, R. Hielscher, and H. Schaeben, “Texture analysis with MTEX- Free and open source software toolbox,” *Solid State Phenom.*, vol. 160, pp. 63–68, 2010.

[257] ASTM, “Standard Test Methods for Determining Average Grain Size,” 2021.

[258] J. Filik *et al.*, “Processing two-dimensional X-ray diffraction and small-angle scattering data in DAWN 2,” *J. Appl. Crystallogr.*, vol. 50, no. 3, pp. 959–966, 2017.

[259] M. Basham *et al.*, “Data Analysis WorkbeNch (DAWN),” *J. Synchrotron Radiat.*, vol. 22, pp. 853–858, 2015.

[260] M. L. Hart, M. Drakopoulos, C. Reinhard, and T. Connolley, “Complete elliptical ring geometry provides energy and instrument calibration for synchrotron-based two-dimensional X-ray diffraction,” *J. Appl. Crystallogr.*, vol. 46, no. 5, pp. 1249–1260, 2013.

[261] A. Borbély, J. Dragomir-Cernatescu, G. Ribárik, and T. Ungár, “Computer program ANIZC for the calculation of diffraction contrast factors of dislocations in elastically anisotropic cubic, hexagonal and trigonal crystals,” *J. Appl. Crystallogr.*, vol. 36, no. 1, pp. 160–162, 2003.

[262] E. Brochen, J. Pötschke, and C. G. Aneziris, “Improved thermal stress resistance parameters considering temperature gradients for bricks in refractory linings,” *Int. J. Appl. Ceram. Technol.*, vol. 11, no. 2, pp. 371–383, 2014.

[263] R. W. Conn, “First wall and divertor plate material selection in fusion reactors,” *J. Nucl. Mater.*, vol. 76–77, no. C, pp. 103–111, 1978.

[264] A. Paúl, A. Beirante, N. Franco, E. Alves, and J. A. Odriozola, “Phase transformation and structural studies of EUROFER RAFM alloy,” *Mater. Sci. Forum*, vol. 514–516, no. PART 1, pp. 500–504, 2006.

[265] P. Norajitra, “3 - Detailed Design of a Helium cooled Divertor for a Fusion Power Plant,” in *Divertor Development for a Future Fusion Power Plant*, KIT Scientific Publishing, 2011, pp. 29–104.

[266] K. W. Katahara, M. H. Manghnani, and E. S. Fisher, “Pressure derivatives of the elastic moduli of BCC Ti-V-Cr, Nb-Mo and Ta-W alloys,” *J. Phys. F Met. Phys.*, vol. 9, no. 5, pp. 773–790, 1979.

[267] J. D. Greiner, O. N. Carlson, and J. F. Smith, “Single-crystal elastic constants of vanadium and vanadium with oxygen additions,” *J. Appl. Phys.*, vol. 50, no. 6, pp. 4394–4398, 1979.

[268] J. A. Rayne and B. S. Chandrasekhar, “Elastic constants of iron from 4.2 to 300°K,” *Phys. Rev.*, vol. 122, no. 6, pp. 1714–1716, 1961.

[269] S. A. Kim and W. L. Johnson, “Elastic constants and internal friction of martensitic steel, ferritic-pearlitic steel, and α-iron,” *Mater. Sci. Eng. A*, vol. 452–453, pp. 633–639, 2007.

[270] P. Magaud and F. Le Vagueres, “Annual Report of the Annual Report of the Association CEA / EURATOM,” *Fusion Technol.*, 1996.

[271] V. I. Razumovskiy, A. V. Ruban, and P. A. Korzhavyi, “Effect of temperature on the elastic anisotropy of pure Fe and Fe 0.9Cr0.1 random alloy,” *Phys. Rev. Lett.*, vol. 107, no. 20, pp. 1–5, 2011.

[272] F. Tavassoli, “Fusion Demo Interim Structural Design Criteria (DISDC) Appendix A Material Design Limit Data,” 2004.

[273] K. Mergia and N. Boukos, “Structural, thermal, electrical and magnetic properties of Eurofer 97 steel,” *J. Nucl. Mater.*, vol. 373, no. 1–3, pp. 1–8, 2008.

[274] G. Zhang *et al.*, “The evolution of internal stress and dislocation during tensile deformation in a 9Cr ferritic/martensitic (F/M) ODS steel investigated by high-energy X-rays,” *J. Nucl. Mater.*, vol. 467, pp. 50–57, 2015.

[275] M. Li, L. Wang, and J. D. Almer, “Dislocation evolution during tensile deformation in ferritic-martensitic steels revealed by high-energy X-rays,” *Acta Mater.*, vol. 76, pp. 381–393, 2014.

[276] Q. Tian *et al.*, “Study of micro-plastic deformation in pure iron before macro-yielding using acoustic emission, electron backscattered diffraction and transmission electron microscopy,” *Mater. Sci. Eng. A*, vol. 771, no. July 2019, p. 138645, 2020.

[277] W. D. Brentnall and W. Rostoker, “Some observations on microyielding,” *Acta Metall.*, vol. 13, no. 3, pp. 187–198, 1965.

[278] S. Takaki, D. Akama, N. Nakada, and T. Tsuchiyama, “Effect of grain boundary segregation of interstitial elements on hallpetch coefficient in steels,” *Mater. Trans.*, vol. 55, no. 1, pp. 28–34, 2014.

[279] F. Mompiou, M. Legros, D. Caillard, and H. Mughrabi, “In situ TEM observations of reverse dislocation motion upon unloading of tensile-deformed UFG aluminium,” *J. Phys. Conf. Ser.*, vol. 240, 2010.

[280] S. Takaki, T. Masumura, and T. Tsuchiyama, “Dislocation characterization by the direct-fitting/modified Williamson–Hall (DF/mWH) method in cold worked ferritic steel,” *ISIJ*

Int., vol. 59, no. 3, pp. 567–572, 2019.

[281] D. Hull and D. J. Bacon, “Movement of Dislocations,” in *Introduction to Dislocations*, Elsevier Ltd, 2011, pp. 43–62.

[282] C. Lee *et al.*, “Strength can be controlled by edge dislocations in refractory high-entropy alloys,” *Nat. Commun.*, vol. 12, no. 1, pp. 6–13, 2021.

[283] C. Baruffi, F. Maresca, and W. A. Curtin, “Screw vs. edge dislocation strengthening in body-centered-cubic high entropy alloys and implications for guided alloy design,” *MRS Commun.*, vol. 12, no. 6, pp. 1111–1118, 2022.

[284] G. Bonny, D. Terentyev, and L. Malerba, “Interaction of screw and edge dislocations with chromium precipitates in ferritic iron: An atomistic study,” *J. Nucl. Mater.*, vol. 416, no. 1–2, pp. 70–74, 2011.

[285] G. Monnet, S. Naamane, and B. Devincre, “Orowan strengthening at low temperatures in bcc materials studied by dislocation dynamics simulations,” *Acta Mater.*, vol. 59, no. 2, pp. 451–461, 2011.

[286] R. Lesar, “Simulations of dislocation structure and response,” *Annu. Rev. Condens. Matter Phys.*, vol. 5, no. 1, pp. 375–407, 2014.

[287] E. O. Hall, “The deformation and ageing of mild steel: III Discussion of results,” *Proc. Phys. Soc. Sect. B*, vol. 64, no. 9, pp. 747–753, 1951.

[288] A. Cracknell and N. J. Petch, “Frictional forces on dislocation arrays at the lower yield point in iron,” *Acta Metall.*, vol. 3, no. 2, pp. 186–189, 1955.

[289] R. L. Coble, “A Model for Boundary Diffusion Controlled Creep in Polycrystalline Materials,” *J. Appl. Phys.*, vol. 34, no. 6, pp. 1679–1682, 1963.

[290] J. E. Bailey and P. B. Hirsch, “The dislocation distribution, flow stress, and stored energy in cold-worked polycrystalline silver,” *Philos. Mag.*, vol. 5, no. 53, pp. 485–497, 1960.

[291] S. Seils, A. Kauffmann, F. Hinrichs, D. Schliephake, T. Boll, and M. Heilmaier, “Temperature dependent strengthening contributions in austenitic and ferritic ODS steels,” *Mater. Sci. Eng. A*, vol. 786, no. January, p. 139452, 2020.

[292] E. Orowan, *Symposium on Internal Stresses in Metals and Alloys*. London: Institute of Metal, 1948.

[293] J. Rösler and E. Arzt, “A new model-based creep equation for dispersion strengthened materials,” *Acta Metall. Mater.*, vol. 38, no. 4, pp. 671–683, 1990.

[294] A. Chauhan *et al.*, “Microstructure characterization and strengthening mechanisms of oxide dispersion strengthened (ODS) Fe-9%Cr and Fe-14%Cr extruded bars,” *J. Nucl. Mater.*, vol. 495, pp. 6–19, 2017.

[295] J. Shen *et al.*, “Microstructural characterization and strengthening mechanisms of a 12Cr-ODS steel,” *Mater. Sci. Eng. A*, vol. 673, pp. 624–632, 2016.

[296] R. Zhao, H. Jia, S. Cao, Z. Tong, and Z. Zhou, “Effect of the addition of Y and Y2O3 on microstructure and mechanical properties of 15Cr-15Ni ODS steel,” *Nucl. Mater. Energy*, vol. 31, no. May, p. 101196, 2022.

[297] Y. Li, L. Zhang, D. Long, L. Yu, and H. Li, “The precipitated particle refinement in high-cr ods steels by microalloying element addition,” *Materials (Basel).*, vol. 14, no. 24, pp. 1–12, 2021.

[298] J. H. Schneibel and M. Heilmaier, “Hall-petch breakdown at elevated temperatures,” *Mater. Trans.*, vol. 55, no. 1, pp. 44–51, 2015.

[299] J. H. Kim, T. S. Byun, D. T. Hoelzer, C. H. Park, J. T. Yeom, and J. K. Hong, “Temperature dependence of strengthening mechanisms in the nanostructured ferritic alloy 14YWT: Part II-Mechanistic models and predictions,” *Mater. Sci. Eng. A*, vol. 559, pp. 111–118, 2013.

[300] Q. Li, “Modeling the microstructure-mechanical property relationship for a 12Cr-2W-V-Mo-Ni power plant steel,” *Mater. Sci. Eng. A*, vol. 361, no. 1–2, pp. 385–391, 2003.

[301] S. Cao and Z. Zhou, “Microstructure and mechanical properties of an ODS ferritic steel with very low Cr content,” *J. Nucl. Mater.*, vol. 551, p. 152971, 2021.

[302] B. Kombaiah and K. L. Murty, “Coble, Orowan Strengthening, and Dislocation Climb Mechanisms in a Nb-Modified Zircaloy Cladding,” *Metall. Mater. Trans. A Phys. Metall. Mater. Sci.*, vol. 46, no. 10, pp. 4646–4660, 2015.

[303] J. Ren, L. Yu, Y. Liu, C. Liu, H. Li, and J. Wu, “Effects of Zr addition on strengthening mechanisms of al-alloyed high-Cr ODS steels,” *Materials (Basel).*, vol. 11, no. 1, pp. 1–13, 2018.

[304] W. Li, H. Xu, X. Sha, J. Meng, and Z. Wang, “Microstructure and Mechanical Properties of 14Cr-ODS Steels with Zr Addition,” *High Temp. Mater. Process.*, vol. 38, no. 2019, pp. 404–410, 2019.

[305] N. Cunningham, Y. Wu, D. Klingensmith, and G. R. Odette, “On the remarkable thermal stability of nanostructured ferritic alloys,” *Mater. Sci. Eng. A*, vol. 613, pp. 296–305, 2014.

[306] M. Praud *et al.*, “Study of the deformation mechanisms in a Fe-14% Cr ODS alloy,” *J. Nucl. Mater.*, vol. 428, no. 1–3, pp. 90–97, 2012.

[307] A. Steckmeyer *et al.*, “Tensile properties and deformation mechanisms of a 14Cr ODS ferritic steel,” *J. Nucl. Mater.*, vol. 405, no. 2, pp. 95–100, 2010.

[308] M. F. Giordana, I. Alvarez-Armas, M. Sauzay, and A. F. Armas, “Mechanical behaviour and microstructure evolution of eurofer97 during low-cycle fatigue at room temperature and 550°C,” *Key Eng. Mater.*, vol. 465, pp. 358–361, 2011.

[309] K. Zhang, M. Walter, and J. Aktaa, “Ratcheting and fatigue behavior of Eurofer97 at high temperature, part 1: Experiment,” *Fusion Eng. Des.*, vol. 150, no. May 2019, p. 111407, 2020.

[310] K. Zhang and J. Aktaa, “Ratcheting behavior of Eurofer97 at 550 °C,” *Nucl. Mater. Energy*, vol. 15, no. December 2017, pp. 97–102, 2018.

[311] M. F. Giordana, I. Alvarez-Armas, and A. Armas, “Microstructural characterization of EUROFER 97 during low-cycle fatigue,” *J. Nucl. Mater.*, vol. 424, no. 1–3, pp. 247–251, 2012.

[312] M. Roldán, E. Leon-Gutierrez, P. Fernández, and A. Gómez-Herrero, “Deformation

behaviour and microstructural evolution of EUROFER97-2 under low cycle fatigue conditions," *Mater. Charact.*, vol. 158, no. May 2018, p. 109943, 2019.

[313] P. Marmy and T. Kruml, "Low cycle fatigue of Eurofer 97," *J. Nucl. Mater.*, vol. 377, no. 1, pp. 52–58, 2008.

[314] K. Zhang and J. Aktaa, "Ratcheting and fatigue behavior of Eurofer97 at high temperature, part 2: modeling," *Fusion Eng. Des.*, vol. 152, no. December 2019, p. 111426, 2020.

[315] M. Hölscher, D. Raabe, and K. Lücke, "Rolling and recrystallization textures of bcc steels," *Materials Technology Steel Research*, vol. 62. pp. 567–575, 1991.

[316] A. A. Saleh, E. V. Pereloma, B. Clausen, D. W. Brown, C. N. Tomé, and A. A. Gazder, "On the evolution and modelling of lattice strains during the cyclic loading of TWIP steel," *Acta Mater.*, vol. 61, no. 14, pp. 5247–5262, 2013.

[317] J. A. Wollmershauser, B. Clausen, and S. R. Agnew, "A slip system-based kinematic hardening model application to in situ neutron diffraction of cyclic deformation of austenitic stainless steel," *Int. J. Fatigue*, vol. 36, no. 1, pp. 181–193, 2012.

[318] M. W. Zhu, N. Jia, F. Shi, and B. Clausen, "Neutron diffraction study of low-cycle fatigue behavior in an austenitic-ferritic stainless steel," *Acta Metall. Sin. (English Lett.*, vol. 28, no. 10, pp. 1247–1256, 2015.

[319] M. Moreno, "Mécanismes métallurgiques et leurs interactions au recuit d'aciers ferrito-perlitiques laminés: Caractérisation et modélisation," 2019.

[320] C.-G. Lee, Y. Ijima, T. Hiratani, and K.-I. Hirano, "Diffusion of Chromium in a-Iron," *Mater. Trans. JIM*, vol. 31, no. 4, pp. 255–261, 1990.

[321] C. Keller, M. M. Margulies, Z. Hadjem-Hamouche, and I. Guillot, "Influence of the temperature on the tensile behaviour of a modified 9Cr-1Mo T91 martensitic steel," *Mater. Sci. Eng. A*, vol. 527, no. 24–25, pp. 6758–6764, 2010.

[322] D. L. Smith, H. M. Chung, B. A. Loomis, H. Matsui, S. Votinov, and W. Van Witzenburg, "Development of vanadium-base alloys for fusion first-wall-blanket applications," *Fusion Eng. Des.*, vol. 29, no. C, pp. 399–410, 1995.

[323] D. L. Smith, M. C. Billone, S. Majumdar, R. F. Mattas, and D. K. Sze, "Materials integration issues for high performance fusion power systems," *J. Nucl. Mater.*, vol. 258–263, no. PART 1 A, pp. 65–73, 1998.

[324] T. Muroga, "Vanadium alloys for fusion blanket applications," *Mater. Trans.*, vol. 46, no. 3, pp. 405–411, 2005.

[325] H. M. Chung, B. A. Loomis, and D. L. Smith, "Properties of V4Cr4Ti for application as fusion reactor structural components," *Fusion Eng. Des.*, vol. 29, no. C, pp. 455–464, 1995.

[326] F. Laliberte, M. Li, J. Almer, and L. Liu, "In-situ synchrotron X-ray study of microstructural evolution during creep deformation in Grade 91 steel," *Mater. Sci. Eng. A*, vol. 737, no. September, pp. 115–123, 2018.

[327] B. Sun and T. Shen, "Probing the deformation mechanisms of nanocrystalline silver by in-situ tension and synchrotron x-ray diffraction," *Metals (Basel).*, vol. 10, no. 12, pp. 1–

14, 2020.

[328] A. Bénéteau, P. Weisbecker, G. Geandier, E. Aeby-Gautier, and B. Appolaire, “Austenitization and precipitate dissolution in high nitrogen steels: An in situ high temperature X-ray synchrotron diffraction analysis using the Rietveld method,” *Mater. Sci. Eng. A*, vol. 393, no. 1–2, pp. 63–70, 2005.

[329] Y. Miao *et al.*, “Load-partitioning in an oxide dispersion-strengthened 310 steel at elevated temperatures,” *Mater. Des.*, vol. 111, pp. 622–630, 2016.

[330] B. Clausen, T. Lorentzen, M. A. M. Bourke, and M. R. Daymond, “Lattice strain evolution during uniaxial tensile loading of stainless steel,” *Mater. Sci. Eng. A*, vol. 259, no. 1, pp. 17–24, 1999.

[331] B. Clausen, “Characterisation of Polycrystal Deformation by Numerical Modelling and Neutron Diffraction Measurements,” *Riso Natl. Lab. Roskilde ISBN*, vol. 985, p. 1, 1997.

[332] D. Kiefer, J. Gibmeier, and A. Stark, “Determination of temperature-dependent elastic constants of steel AISI 4140 by use of in situ x-ray dilatometry experiments,” *Materials (Basel).*, vol. 13, no. 10, 2020.

[333] Z. Wang, A. D. Stoica, D. Ma, and A. M. Beese, “Diffraction and single-crystal elastic constants of Inconel 625 at room and elevated temperatures determined by neutron diffraction,” *Mater. Sci. Eng. A*, vol. 674, pp. 406–412, 2016.

[334] Y. Wu *et al.*, “Phase Stability and Deformation Behavior of TiZrHfNbO High-Entropy Alloys,” *Front. Mater.*, vol. 7, no. November, pp. 1–7, 2020.

[335] Z. Fan, B. Jóni, G. Ribárik, É. Ódor, Z. Fogarassy, and T. Ungár, “The Microstructure and strength of a V–5Cr–5Ti alloy processed by high pressure torsion,” *Mater. Sci. Eng. A*, vol. 758, no. March, pp. 139–146, 2019.

[336] X. Zhang *et al.*, “High-energy synchrotron x-ray study of deformation-induced martensitic transformation in a neutron-irradiated Type 316 stainless steel,” *Acta Mater.*, vol. 200, pp. 315–327, 2020.

[337] C. Xu *et al.*, “In-situ high-energy X-ray characterization of neutron irradiated HT-UPS stainless steel under tensile deformation,” *Acta Mater.*, vol. 156, pp. 330–341, 2018.

[338] M. De Jong *et al.*, “Charting the complete elastic properties of inorganic crystalline compounds,” *Sci. Data*, vol. 2, pp. 1–13, 2015.

[339] G. A. Alers, “Elastic Moduli of Vanadium,” *Network*, vol. 119, no. 5, pp. 1532–1535, 1960.

[340] D. I. Bolef, R. E. Smith, and J. G. Miller, “Elastic properties of vanadium. I. Temperature dependence of the elastic constants and the thermal expansion,” *Phys. Rev. B*, vol. 3, no. 12, pp. 4100–4108, 1971.

[341] X. Li *et al.*, “Elastic properties of vanadium-based alloys from first-principles theory,” *Phys. Rev. B - Condens. Matter Mater. Phys.*, vol. 86, no. 1, 2012.

[342] J. Fu, X. Li, B. Johansson, and J. Zhao, “Improved Finnis-Sinclair potential for vanadium-rich V–Ti–Cr ternary alloys,” *J. Alloys Compd.*, vol. 705, pp. 369–375, 2017.

[343] D. Sobieraj *et al.*, “Chemical short-range order in derivative Cr-Ta-Ti-V-W high entropy

alloys from the first-principles thermodynamic study," *Phys. Chem. Chem. Phys.*, vol. 22, no. 41, pp. 23929–23951, 2020.

[344] Y. Ikeda, B. Grabowski, and F. Körmann, "Ab initio phase stabilities and mechanical properties of multicomponent alloys: A comprehensive review for high entropy alloys and compositionally complex alloys," *Mater. Charact.*, vol. 147, no. June 2018, pp. 464–511, 2019.

[345] E. Kiely, R. Zwane, R. Fox, A. M. Reilly, and S. Guerin, "Density functional theory predictions of the mechanical properties of crystalline materials," *CrystEngComm*, vol. 23, no. 34, pp. 5697–5710, 2021.

[346] K. Alberi *et al.*, "The 2019 materials by design roadmap," *J. Phys. D. Appl. Phys.*, vol. 52, 2019.

[347] Y. Liu, T. Zhao, W. Ju, S. Shi, S. Shi, and S. Shi, "Materials discovery and design using machine learning," *J. Mater.*, vol. 3, no. 3, pp. 159–177, 2017.

[348] T. Connolley, C. M. Beavers, and P. Chater, "High-Energy Adventures at Diamond Light Source," *Synchrotron Radiat. News*, vol. 33, no. 6, pp. 31–36, 2020.

[349] G. Kresse and J. Furthmuller, "Effecient iterative schemes for ab initio total energy calculations using a plane-wave basis set," *Phys. Rev. B*, vol. 54, no. 16, pp. 11169–11183, 1996.

[350] G. Kresse and J. Furthmüller, "Efficiency of ab-initio total energy calculations for metals and semiconductors using a plane-wave basis set," *Comput. Mater. Sci.*, vol. 6, no. 1, pp. 15–50, 1996.

[351] J. P. Perdew, K. Burke, and M. Ernzerhof, "Generalized gradient approximation made simple," *Phys. Rev. Lett.*, vol. 77, no. 18, pp. 3865–3868, 1996.

[352] H. Monkhorst and J. Pack, "Special points for Brillouin-zone integrations," *Phys. Rev. B*, vol. 13, no. 12, pp. 5188–5192, 1976.

[353] J. S. Wróbel *et al.*, "Elastic dipole tensors and relaxation volumes of point defects in concentrated random magnetic Fe-Cr alloys," *Comput. Mater. Sci.*, vol. 194, 2021.

[354] J. F. Nye, *Physical Properties of Crystals - Their Representation Tensors and Matrices*. 1986.

[355] Z. D. Li, Q. Li, Y. Li, and T. D. Ma, "Microstructure and properties of V–5Cr–5Ti alloy after hot forging," *Fusion Eng. Des.*, vol. 127, no. 2, pp. 83–90, 2018.

[356] M. Satou, K. Abe, and H. Kayano, "High-temperature deformation of modified V-Ti-Cr-Si type alloys," *J. Nucl. Mater.*, vol. 179–181, no. PART 1, pp. 757–761, 1991.

[357] T. Miyazawa *et al.*, "Effect of yttrium on dynamic strain aging of vanadium alloys," *J. Nucl. Mater.*, vol. 442, no. 1-3 SUPPL.1, pp. S341–S345, 2013.

[358] E. T. C. Filho, J. T. N. Medeiros, L. G. Martinez, and V. C. Pinto, "Study of Error Analysis and Sources of Uncertainty in the Measurement of Residual Stresses by the X-Ray Diffraction," *Residual Stress. 2018*, vol. 6, pp. 75–80, 2018.

[359] C. Simpson, D. Knowles, and M. Mostafavi, "Influence of Microstructure on Synchrotron X-ray Diffraction Lattice Strain Measurement Uncertainty," *Metals (Basel).*, vol. 11, no.

774, 2021.

[360] B. K. Kardashev and V. M. Chernov, “Internal friction, plastic properties, and impact toughness of V-Ti-Cr alloys,” *Phys. Solid State*, vol. 50, no. 5, pp. 854–859, 2008.

[361] B. K. Kardashev, V. M. Chernov, O. A. Plaskin, V. A. Stepanov, and L. P. Zavialski, “Internal friction and Young’s modulus of V-Ti-Cr alloy before, during and after proton irradiation,” *J. Alloys Compd.*, vol. 310, no. 1–2, pp. 102–106, 2000.

[362] H. Luo *et al.*, “The effect of yttrium addition on the microstructure and irradiation hardening in V-4Cr-4Ti alloy under self-ion irradiation,” *Metals (Basel).*, vol. 11, no. 7, 2021.

[363] L. Tang *et al.*, “Deformation mechanisms of FeCrNi medium entropy alloy at 293 and 15 K,” *Acta Mater.*, 2022.

[364] G. N. Greaves, A. L. Greer, R. S. Lakes, and T. Rouxel, “Poisson’s ratio and modern materials,” *Nat. Mater.*, vol. 10, no. 11, pp. 823–837, 2011.

[365] X. Zhang *et al.*, “Precipitate/vanadium interface and its strengthening on the vanadium alloys: A first-principles study,” *J. Nucl. Mater.*, vol. 527, p. 151821, 2019.

[366] Y. X. Wang, H. Y. Geng, Q. Wu, and X. R. Chen, “Orbital localization error of density functional theory in shear properties of vanadium and niobium,” *J. Chem. Phys.*, vol. 152, no. 2, 2020.

[367] N. Nagasako, M. Jahnátek, R. Asahi, and J. Hafner, “Anomalies in the response of V, Nb, and Ta to tensile and shear loading: Ab initio density functional theory calculations,” *Phys. Rev. B - Condens. Matter Mater. Phys.*, vol. 81, no. 9, pp. 1–13, 2010.

[368] P. Söderlind, O. Eriksson, J. M. Wills, and A. M. Boring, “Theory of elastic constants of cubic transition metals and alloys,” *Phys. Rev. B*, vol. 48, no. 9, pp. 5844–5851, 1993.

[369] Y. L. Liu, H. B. Zhou, and Y. Zhang, “Ideal mechanical properties of vanadium by a first-principles computational tensile test,” *J. Nucl. Mater.*, vol. 416, no. 3, pp. 345–349, 2011.

[370] L. Koči, Y. Ma, A. R. Oganov, P. Souvatzis, and R. Ahuja, “Elasticity of the superconducting metals V, Nb, Ta, Mo, and W at high pressure,” *Phys. Rev. B - Condens. Matter Mater. Phys.*, vol. 77, no. 21, pp. 1–5, 2008.

[371] A. Landa *et al.*, “Fermi surface nesting and pre-martensitic softening in v and Nb at high pressures,” *J. Phys. Condens. Matter*, vol. 18, no. 22, pp. 5079–5085, 2006.

[372] F. C. Yang, O. Hellman, and B. Fultz, “Temperature dependence of electron-phonon interactions in vanadium,” *Phys. Rev. B*, vol. 101, no. 9, 2020.

[373] E. Walker, “Anomalous Temperature Behaviour of the Shear Elastic Constant C44 in Vanadium,” *Solid State Commun.*, vol. 28, pp. 587–589, 1978.

[374] A. Jain *et al.*, “Commentary: The materials project: A materials genome approach to accelerating materials innovation,” *APL Mater.*, vol. 1, no. 1, 2013.

[375] D. L. Smith, M. C. Billone, and K. Natesan, “Vanadium-base alloys for fusion first-wall / blanket applications,” *Int. J. Refract. Metals Hard Mater.*, vol. 213–224, no. 18, 2000.

[376] T. Muroga *et al.*, “Vanadium alloys - Overview and recent results,” *J. Nucl. Mater.*, vol. 307–311, no. 1 SUPPL., pp. 547–554, 2002.

[377] U. Jain, K. Sairam, K. Singh, and R. Tewari, “Wear Behavior of Vanadium and V-Ti-Ta Alloys under Reciprocating Sliding Conditions,” *J. Mater. Eng. Perform.*, vol. 28, no. 6, pp. 3372–3380, 2019.

[378] W. C. Oliver and G. M. Pharr, “An improved technique for determining hardness and elastic modulus using load and displacement sensing indentation experiments W.,” no. 1, 1992.

[379] BSI, “BS EN ISO 14577-1:2015 Metallic materials - Instrumented indentation test of hardness and materials parameters. Part 1: Test Method,” 2015.

[380] N. J. Heo, T. Nagasaka, and T. Muroga, “Recrystallization and precipitation behavior of low-activation V-Cr-Ti alloys after cold rolling,” *J. Nucl. Mater.*, vol. 325, no. 1, pp. 53–60, 2004.

[381] A. Nishimura, A. Iwahori, N. J. Heo, T. Nagasaka, T. Muroga, and S. I. Tanaka, “Effect of precipitation and solution behavior of impurities on mechanical properties of low activation vanadium alloy,” *J. Nucl. Mater.*, vol. 329–333, no. 1-3 PART A, pp. 438–441, 2004.

[382] J. Shen, K. Saito, M. Tokitani, and T. Muroga, “Effects of annealing temperature on microstructure and hardness of cold rolled high-purity V-4Cr-xTi alloys,” *Fusion Eng. Des.*, vol. 194, no. May, p. 113905, 2023.

[383] X. J. Liu *et al.*, “Experimental Investigations of Phase Equilibria in the Ta-V-Cr Ternary System,” *J. Phase Equilibria Diffus.*, vol. 41, no. 6, pp. 891–899, 2020.

[384] J. T. Lenkkeri and E. E. Lahteenkorva, “An investigation of elastic moduli of vanadium-chromium alloys,” *J. Phys. F Met. Phys.*, vol. 8, no. 8, pp. 1643–1651, 1978.

[385] T. Muroga and T. Nagasaka, “Reduction of impurity levels of vanadium and its alloys for fusion application,” *Int. J. Refract. Met. Hard Mater.*, vol. 18, no. 4–5, pp. 225–230, 2000.

[386] W. C. Oliver and G. M. Pharr, “Measurement of hardness and elastic modulus by instrumented indentation: Advances in understanding and refinements to methodology,” *J. Mater. Res.*, vol. 19, no. 1, pp. 3–20, 2004.

APPENDICES

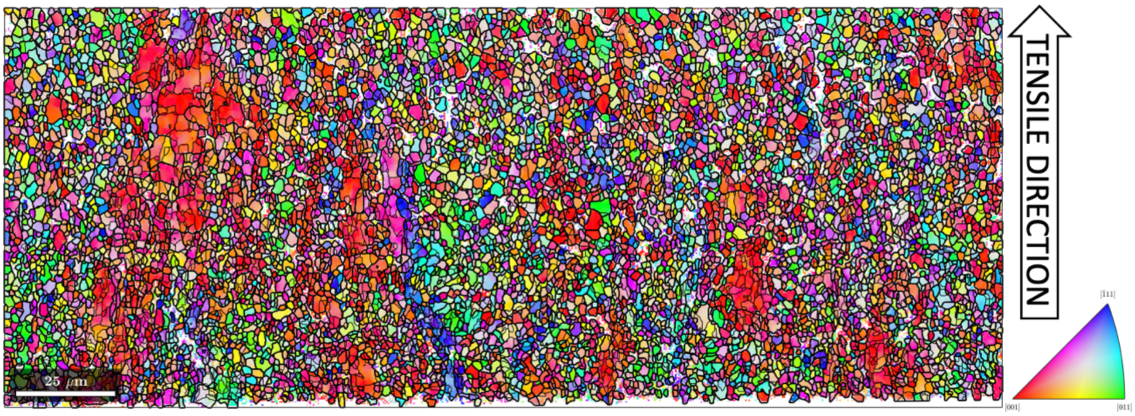

Figure 0.1 EBSD map of ODS EUROFER97, step size 0.4um. High angle grain boundaries (>15º) shown in bold, low angle grain boundaries (<10º) outlined lightly.

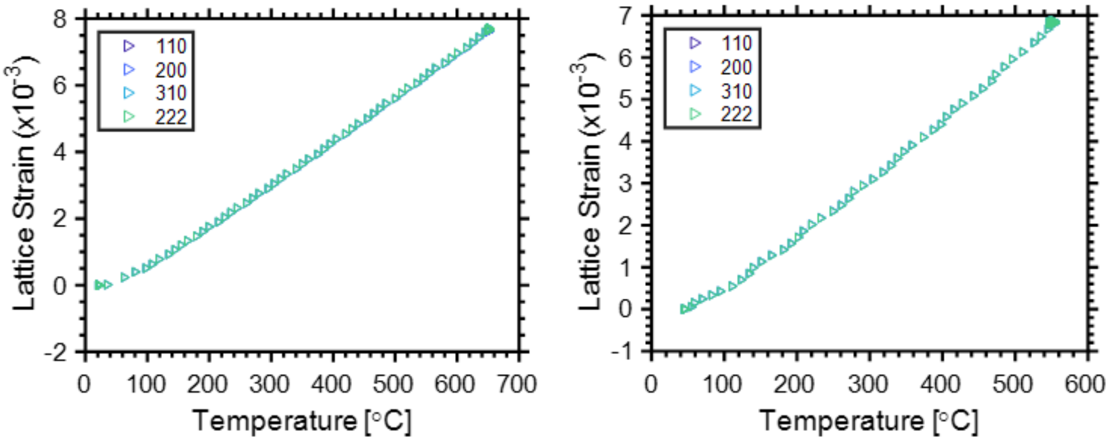

Figure 0.2 Graphs demonstrating thermally induced lattice strain evolution for a) EUROFER97, and b) ODS EUROFER97 during ramp up to elevated temperature

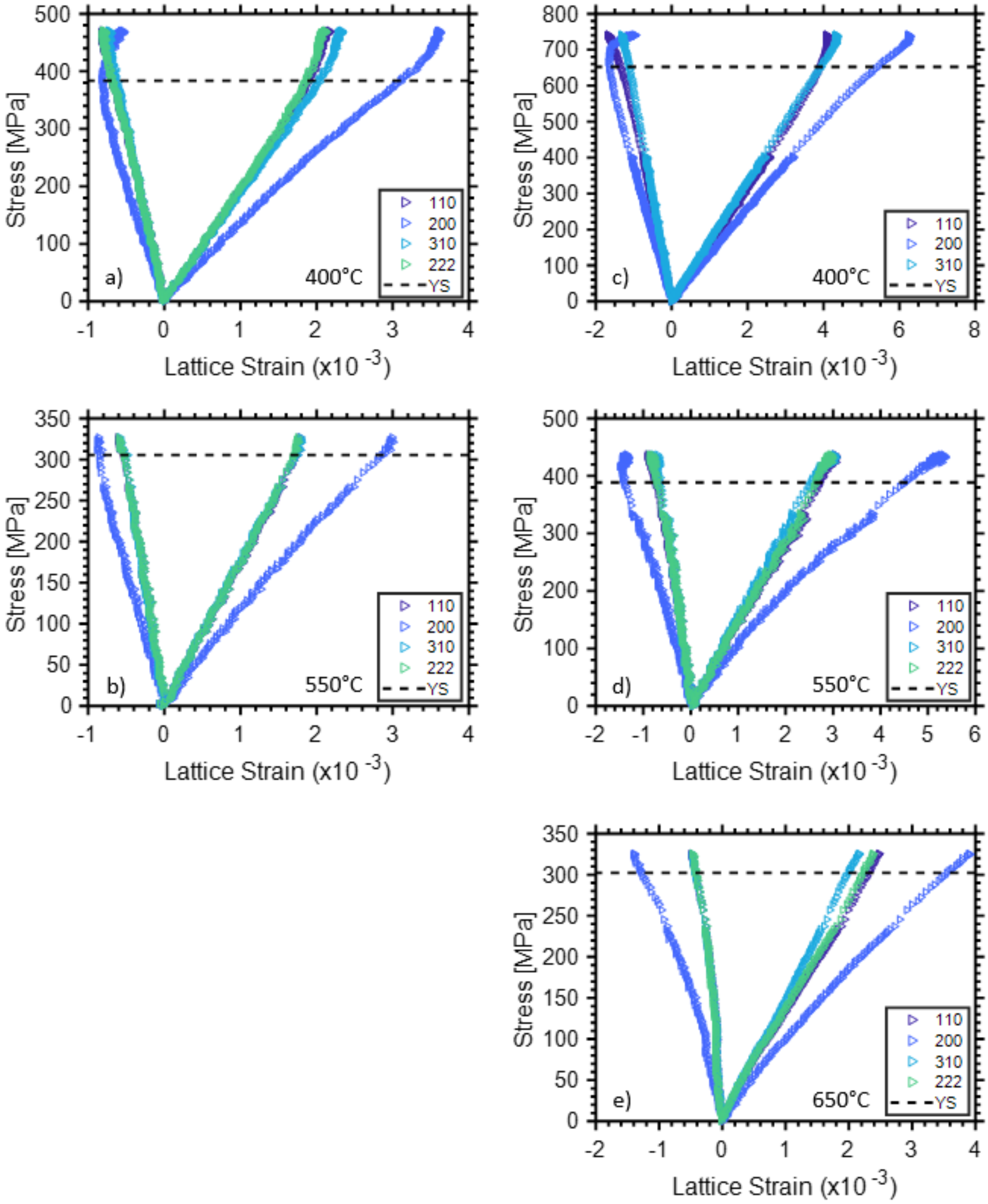

Figure 0.3 Graphs demonstrating lattice strain evolution for a)/b) EUROFER97, and c)-e) ODS EUROFER97 at elevated temperature. Test temperature is indicated on each plot.

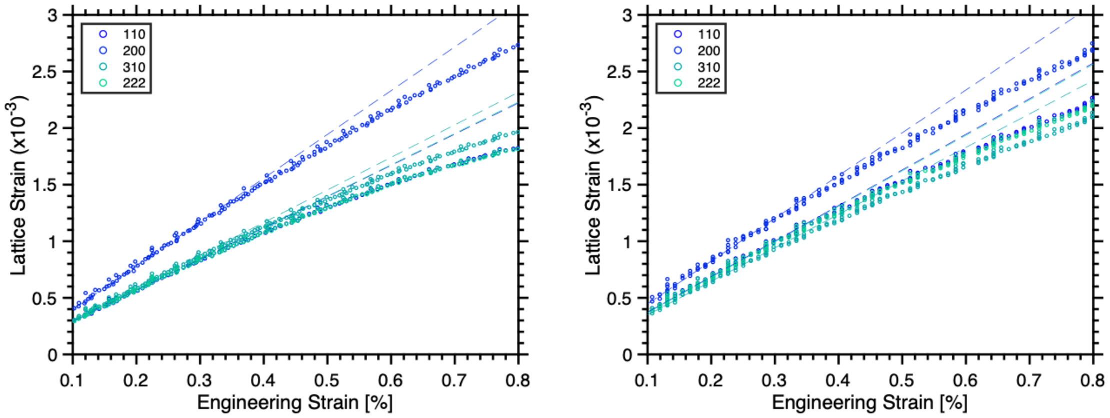

Figure 0.4 Graphs demonstrating deviation of grain family deformation from bulk deformation for a) RT EUROFER97, and b) RT ODS EUROFER97.

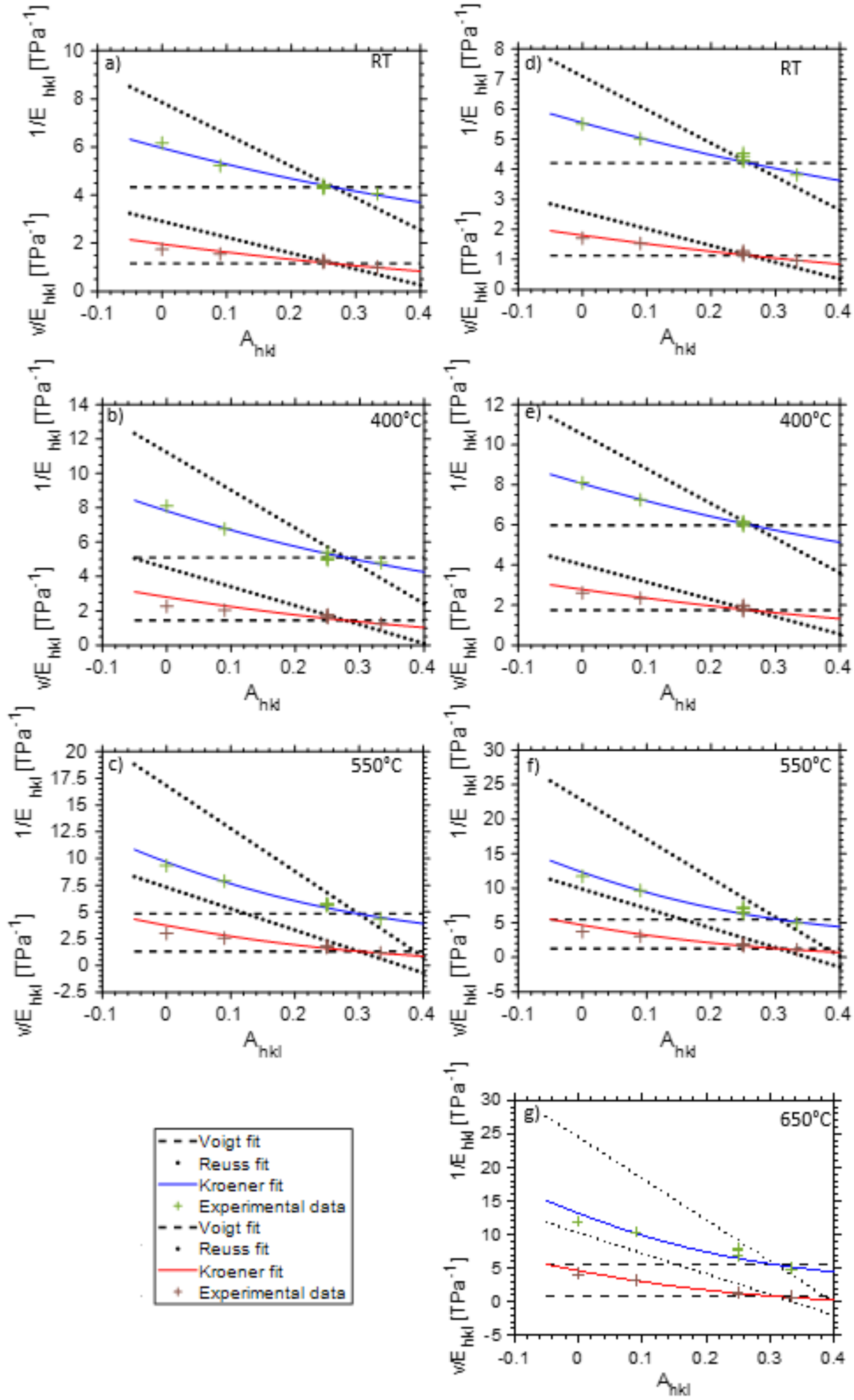

Figure 0.5 Figures demonstrating variation of diffraction elastic constants and ratio as a function of anisotropy, and accompanying Kroner model fit, used to determine single crystal elastic constants for a)-c) EUROFER97 and d)-g) ODS EUROFER97

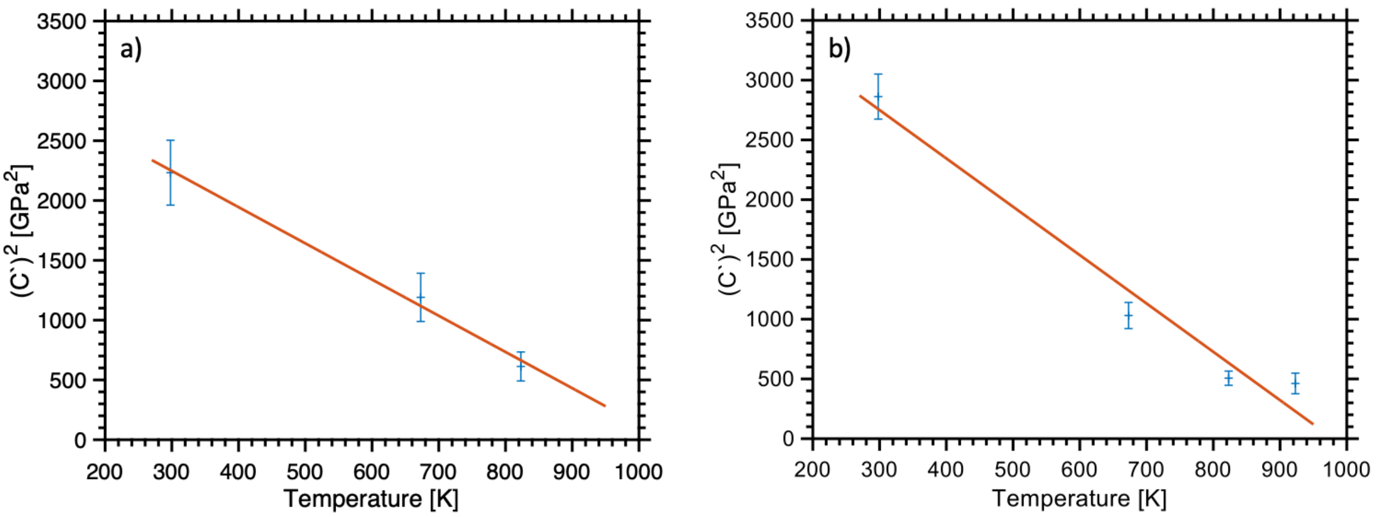

Figure 0.6 Variation of the tetragonal shear modulus with temperature of a) EUROFER97 and b) ODS EUROFER97 for the determination of the Curie temperature

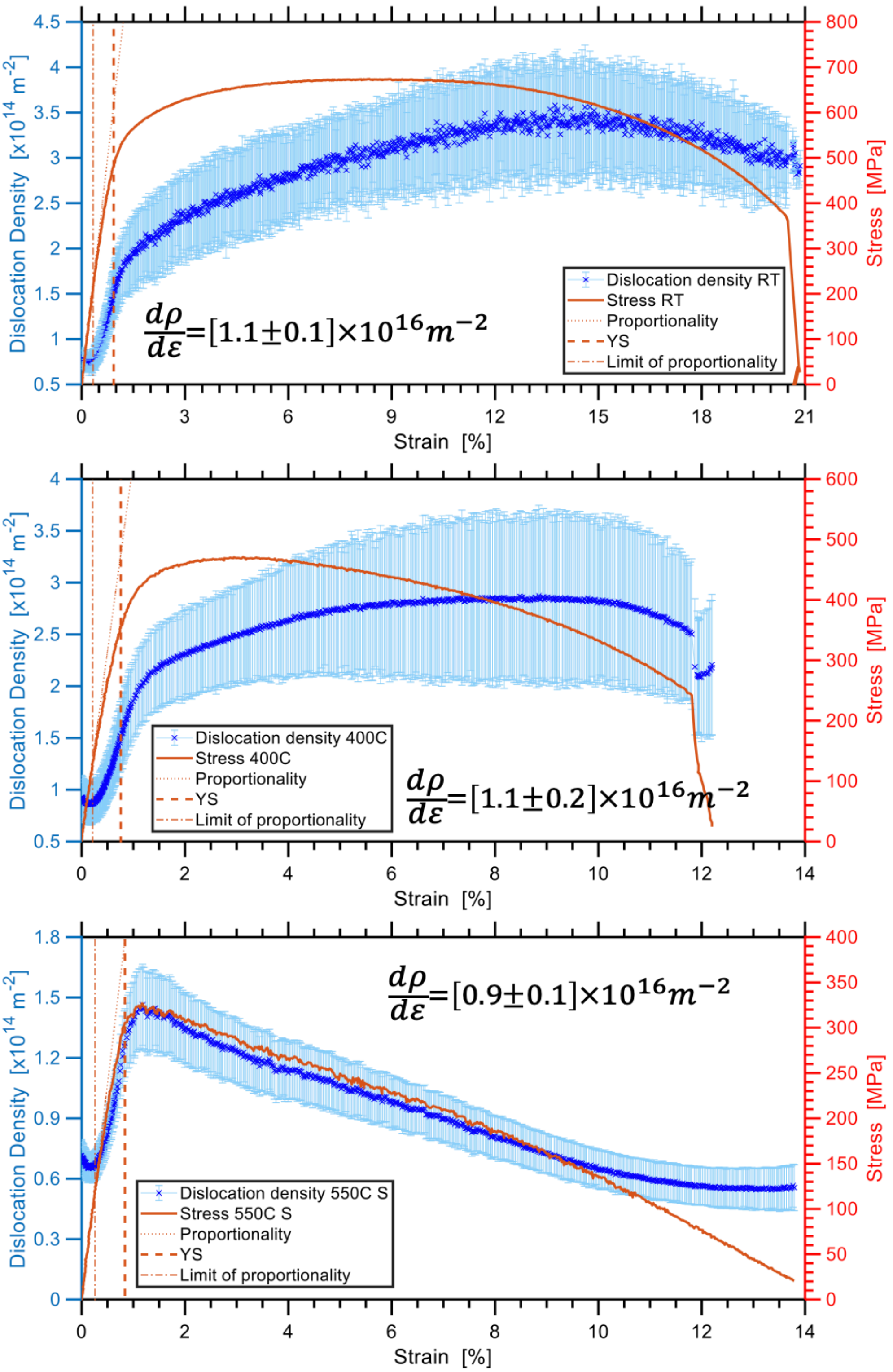

Figure 0.7 Dislocation density and stress evolution with strain during tensile testing of EUROFER97 at RT (a), 400°C (b), and 550°C (c). 0.2% offset yield stress, limit of proportionality, and Stage II net dislocation generation rate are indicated. Limit of proportionality is taken as the point at which the stress-strain curve deviates from proportional fit by more than twice the ETMT rig's noise (~1 MPa). Stage II net dislocation generation rate determined between limit of linearity and yield stress.

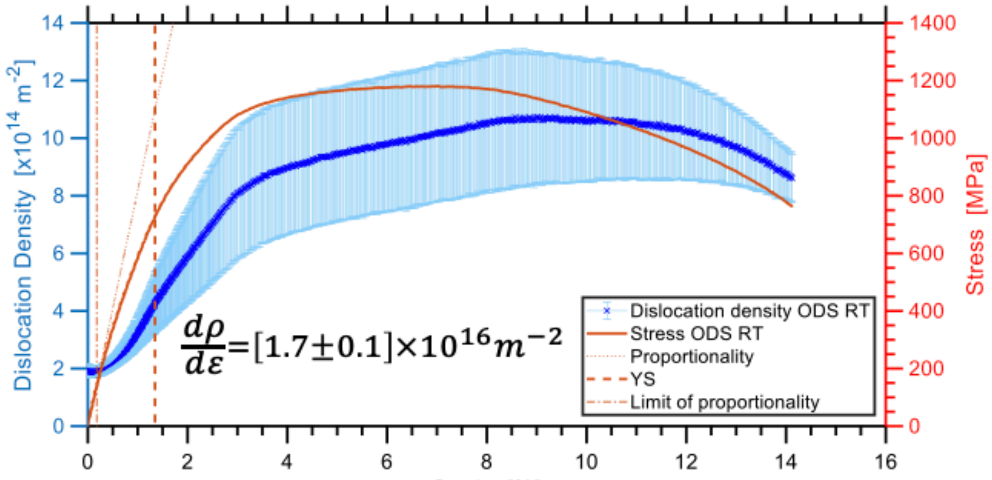
Dislocation Density [x10^{14} m^{-2}]
Stress [MPa]
Strain [%]
0
2
4
6
8
10
12
14
16
0
200
400
600
800
1000
1200
1400
$\frac{d\rho}{d\varepsilon}=[1.7\pm0.1]\times10^{16}m^{-2}$
Dislocation density ODS RT
Stress ODS RT
Proportionality
YS
Limit of proportionality

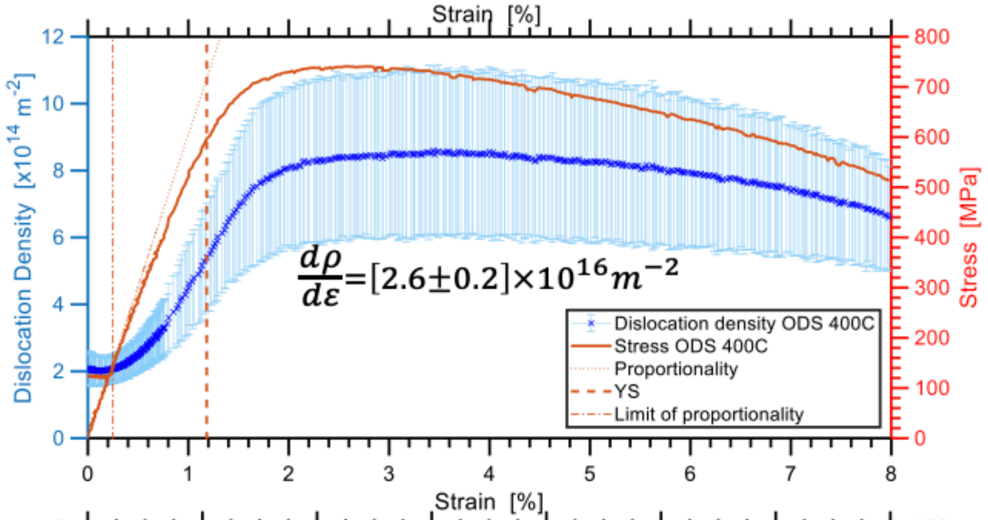
Dislocation Density [x10^{14} m^{-2}]
Stress [MPa]
Strain [%]
0
1
2
3
4
5
6
7
8
0
2
4
6
8
10
12
0
100
200
300
400
500
600
700
800
$\frac{d\rho}{d\varepsilon}=[2.6\pm0.2]\times10^{16}m^{-2}$
Dislocation density ODS 400C
Stress ODS 400C
Proportionality
YS
Limit of proportionality

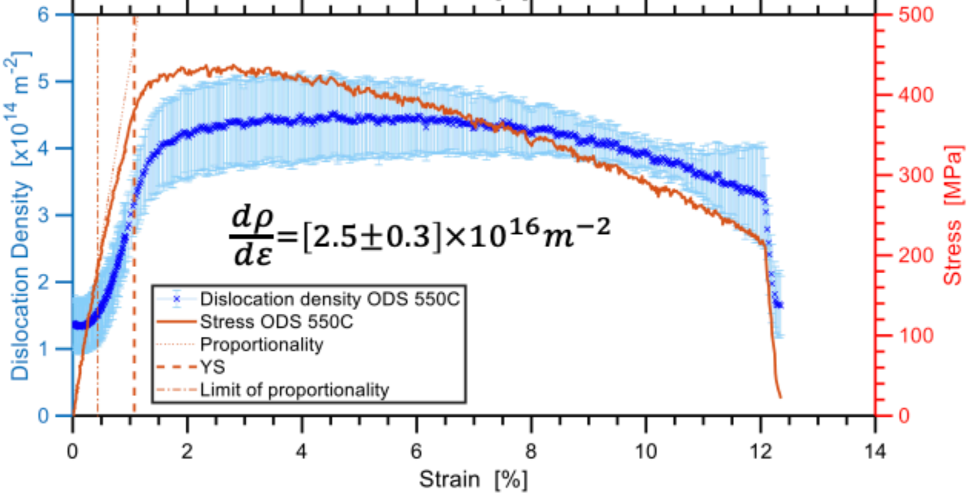
Dislocation Density [x10^{14} m^{-2}]
Stress [MPa]
Strain [%]
0
2
4
6
8
10
12
14
0
1
2
3
4
5
6
0
100
200
300
400
500
$\frac{d\rho}{d\varepsilon}=[2.5\pm0.3]\times10^{16}m^{-2}$
Dislocation density ODS 550C
Stress ODS 550C
Proportionality
YS
Limit of proportionality

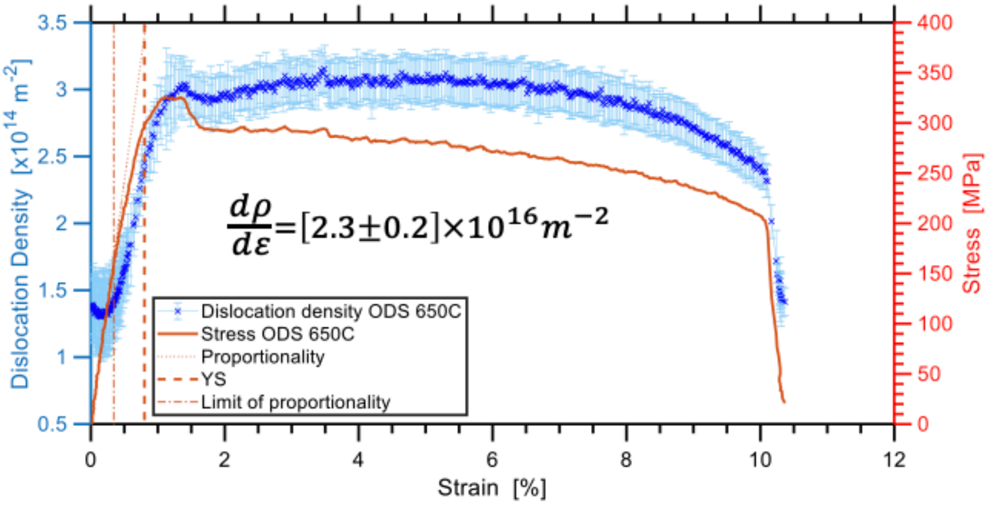
Dislocation Density [x10^{14} m^{-2}]
Stress [MPa]
Strain [%]
0
2
4
6
8
10
12
0.5
1
1.5
2
2.5
3
3.5
0
50
100
150
200
250
300
350
400
$\frac{d\rho}{d\varepsilon}=[2.3\pm0.2]\times10^{16}m^{-2}$
Dislocation density ODS 650C
Stress ODS 650C
Proportionality
YS
Limit of proportionality

Figure 0.8 [Previous page] *Dislocation density and stress evolution with strain during tensile testing of ODS EUROFER97 at RT (a), 400°C (b), 550°C (c), and 650°C (d). 0.2% offset yield stress, limit of proportionality, and Stage II net dislocation generation rate are indicated. Limit of proportionality is taken as the point at which the stress-strain curve deviates from proportional fit by more than twice the ETMT rig's noise (~1 MPa). Stage II net dislocation generation rate determined between limit of linearity and yield stress.*

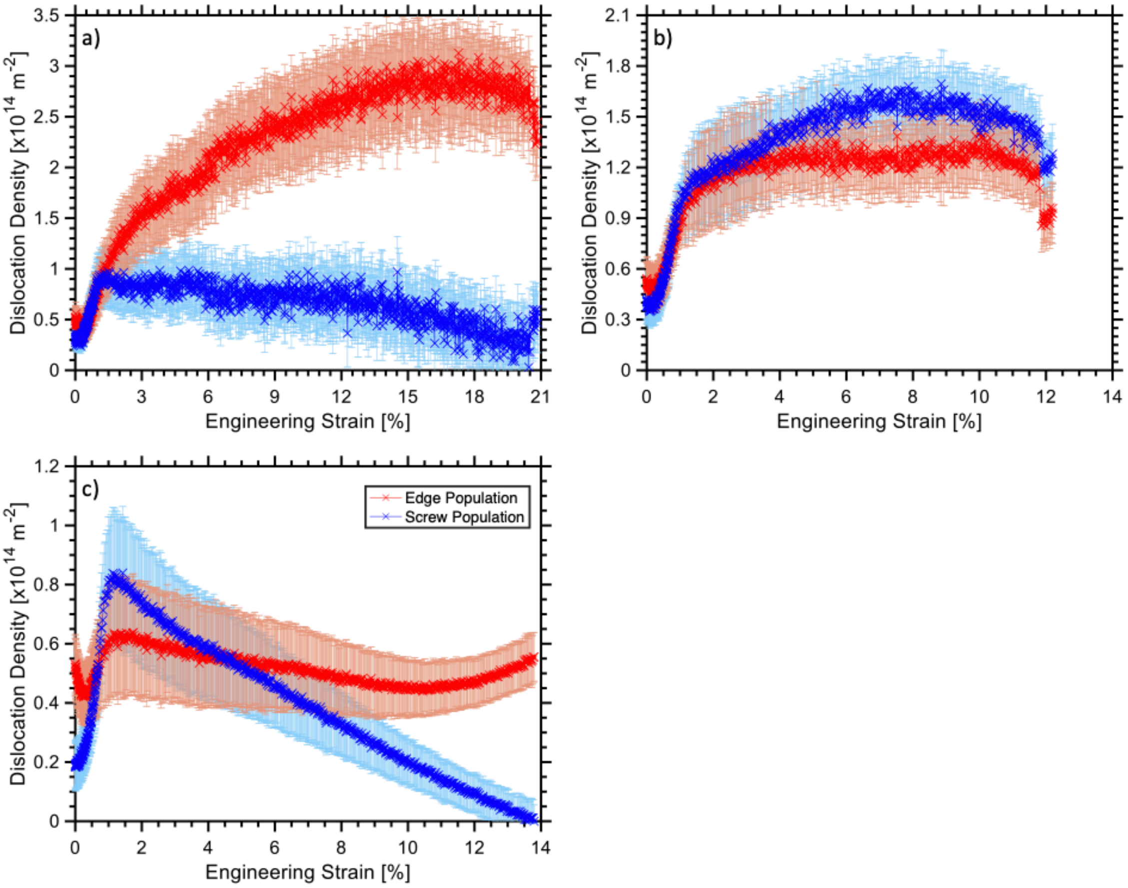

Figure 0.9 Dislocation density evolution of screw (blue) and edge (red) type dislocations with strain during tensile testing of EUROFER97 at RT (a), 400°C (b), and 550°C (c).

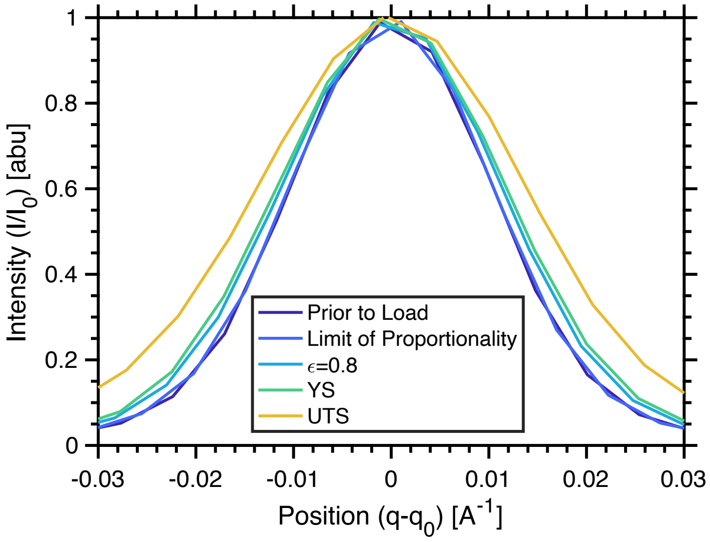

Figure 0.10 Change in peak FWHM with applied load, demonstrating consistent FWHM to the limit of stress-strain proportionality, and increase of FWHM at and prior to the point of yield. Data taken from RT testing of EUROFER97 sample, {200} peak, intensity values scaled per fitted peak intensity (I_0), peak position centred around fitted peak centroid position (q_0).

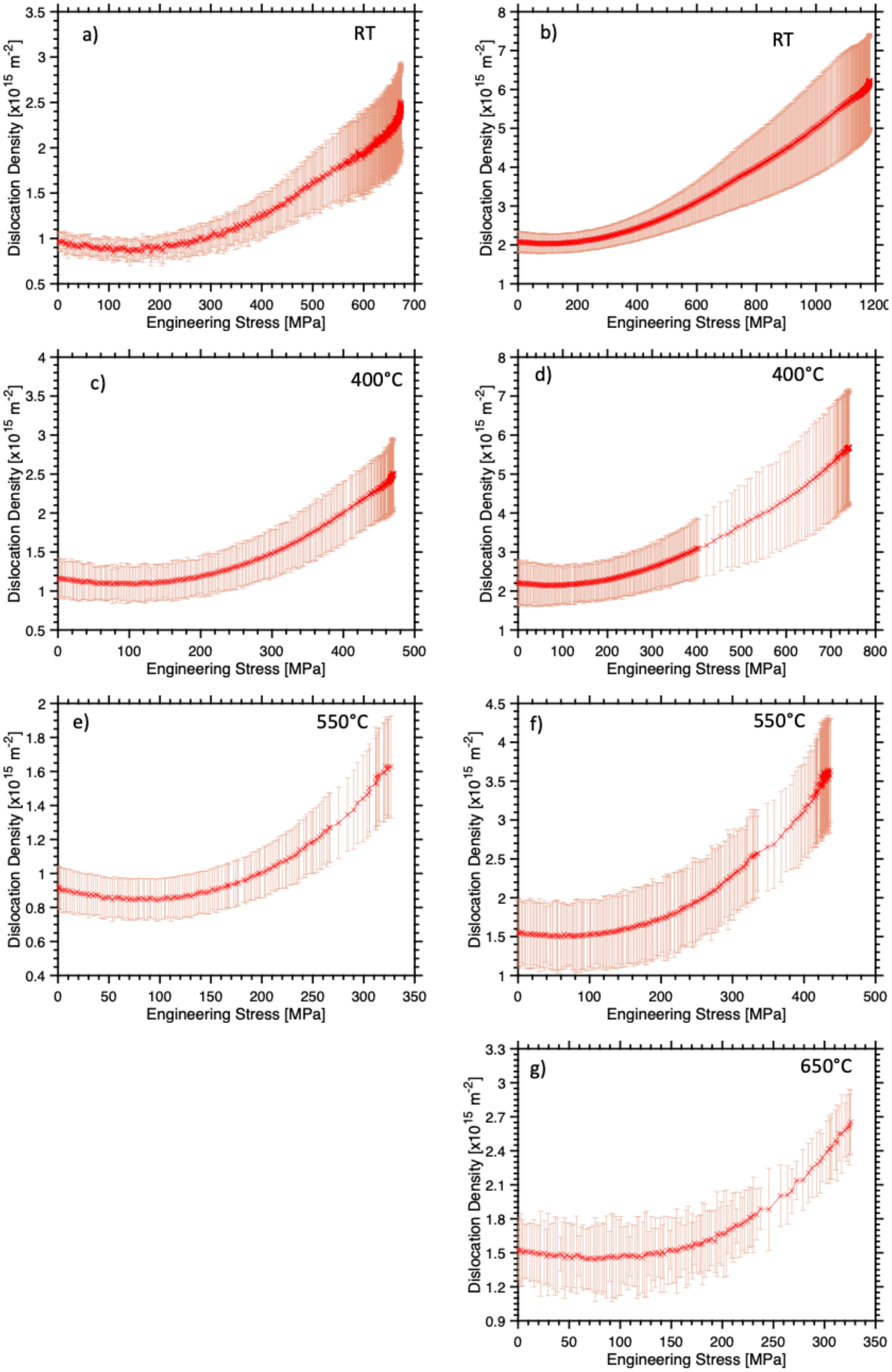

Figure 0.11 Dislocation density evolution with stress during tensile testing of EUROFER

[a), c), e)] and ODS EUROFER97 [b), d), f), g)] at RT (a/b), 400°C (c/d), 550°C (e/f), and 650°C (g).

Table 0.1 Parameters controlling grain family contrast factors of EUROFER97, and fitting parameters of these components quasi-linear temperature dependency. Grain family contrast factors are determined such that $C = C_{h00}(1 - q(\frac{h^2k^2+h^2l^2+k^2l^2}{h^2+k^2+l^2}))$ *where h,k,l are the grain family Miller indices. Parameters determined using ANIZC software from single crystal elastic constants determined at each test temperature.*

	Temperature [ºC]	C_{h00}^{Edge}	q^{Edge}	C_{h00}^{Screw}	q^{Screw}
EUROFER97	25	0.257	1.24	0.304	2.63
	400	0.352	1.89	0.340	2.74
	550	0.397	2.07	0.356	2.77
	Linear Fitting for each parameter: x=m*T+c				
	m	2.64	16.1	0.986	2.84
	c	0.250	1.21	0.301	2.63

Table 0.2 Parameters controlling grain family contrast factors of ODS EUROFER97, and fitting parameters of these components quasi-linear temperature dependency. Grain family contrast factors are determined such that $C = C_{h00}(1 - q(\frac{h^2k^2+h^2l^2+k^2l^2}{h^2+k^2+l^2}))$ *where h,k,l are the grain family Miller indices. Parameters determined using ANIZC software from single crystal elastic constants determined at each test temperature.*

	Temperature [ºC]	C_{h00}^{Edge}	q^{Edge}	C_{h00}^{Screw}	q^{Screw}
ODS EUROFER97	25	0.243	1.08	0.293	2.59
	400	0.314	1.67	0.320	2.69
	550	0.372	1.97	0.360	2.79
	650	0.366	1.91	0.374	2.81
	Linear Fitting for each parameter: x=m*T+c				
	m	2.13	14.5	1.290	3.63
	c	0.237	1.07	0.284	2.57

Table 0.3 Elastic constants of V-4Cr-4-Ti alloy obtained Monte Carlo simulations for 5x5x5 bcc-supercell

	2000K		2000K with experimental lattice constant		300K
Volume in A^3	3316.26	3316.26	3510.42	3510.42	3316.19
Relaxation	Without atomic relxation	With atomic relaxation	Without atomic relxation	With atomic relaxation	With atomic relaxation
Single crystal elastic constants in GPa					
C11	274.2	284.41	262.97	258.5	276.64
C12	139.92	136.7	136.5	131.81	139.38
C13	139.88	134.97	136.44	138.68	139.45
C22	276.53	286.24	262.07	261.26	276.55
C23	138.93	136.95	139.49	137.38	139.29
C33	276.05	284.66	257.62	257.62	276.25
C44	9.82	16.31	14.06	14.06	10.53
C55	10.29	16.94	17.48	17.48	10.14
C66	10.18	16.37	13.65	13.65	10.64
C14	0	0	0	0	-0.08
C15	0	0	0	0	-0.02
C16	0	0	0	0	-0.30
C24	0	0	0	0	-0.52
C25	0	0	0	0	0.30
C26	0	0	0	0	-0.32
C34	0	0	0	0	-0.29
C35	0	0	0	0	-0.38
C36	0	0	0	0	-1.16
C45	0	0	0	0	1.42
C46	0	0	0	0	-0.81
C56	0	0	0	0	0.33
Youngs modulus in GPa					
Emin	29.73	48.17	43.18	43.1	27.79
Emax	182.85	197.04	169.69	169.78	183.15
Eav	51.9	75.8	67.27	67.18	52.61
Emax/Emin	6.15	4.09	3.93	3.933	6.591
SD	28.22	30.87	26.09	25.96	28.47
SD/Eav (%)	54.39	40.73	38.78	38.65	54.12
Poisson ratio					
Pmin	0.336	0.3216	0.3418	0.3392	0.3351
Pmax	0.4732	0.4568	0.4598	0.4593	0.4773
Pav	0.4532	0.432	0.4371	0.4367	0.4525
Pmax/Pmin	1.408	1.421	1.345	1.354	1.425
SD	0.0261	0.0282	0.0251	0.0251	0.0264
SD/Pav (%)	5.76	6.54	5.73	5.75	5.83
Policrystalline moduli					
B (VRH) in GPa	184.91	185.86	178.59	176.99	185.04
G (VRH) in GPa	24.28	31.85	27.54	27.51	24.6
E (VRH) in GPa	69.41	90.12	78.4	78.29	70.28